ÇUKUROVA UNIVERSITY
INSTITUTE OF NATURAL AND APPLIED SCIENCES

PhD THESIS

Tural TUNAY

EXPERIMENTAL AND NUMERICAL STUDIES OF FLOW CHARACTERISTICS AROUND A GROUND VEHICLE

DEPARTMENT OF MECHANICAL ENGINEERING

ADANA, 2011

ÇUKUROVA UNIVERSITY
INSTITUTE OF NATURAL AND APPLIED SCIENCES

EXPERIMENTAL AND NUMERICAL STUDIES OF FLOW CHARACTERISTICS AROUND A GROUND VEHICLE

Tural TUNAY

PhD THESIS

DEPARTMENT OF MECHANICAL ENGINEERING

We certify that the thesis titled above was reviewed and approved for the award of degree of the Doctor of Philosophy by the board of jury on 19/08/2011.

…….....	…….....	…….....
Prof. Dr. Beşir ŞAHİN	Prof. Dr. Recep YURTAL	Prof. Dr. Hüseyin AKILLI
SUPERVISOR	MEMBER	MEMBER

…….....	……..….….....
Assoc. Prof. Dr. Ahmet PINARBAŞI	Assoc. Prof. Dr. Muammer ÖZGÖREN
MEMBER	MEMBER

This Ph.D. Thesis is written at the Department of Institute of Natural And Applied Sciences of Çukurova University.
Registration Number:

Prof. Dr. İlhami YEĞİNGİL
Director
Institute of Natural and Applied Sciences

ABSTRACT

PhD THESIS

EXPERIMENTAL AND NUMERICAL STUDIES OF FLOW CHARACTERISTICS AROUND A GROUND VEHICLE

Tural TUNAY

ÇUKUROVA UNIVERSITY
INSTITUTE OF NATURAL AND APPLIED SCIENCES
DEPARTMENT OF MECHANICAL ENGINEERING

Supervisor : Prof. Dr. Beşir ŞAHİN
Year: 2011, Pages: 185
Jury : Prof. Dr. Recep YURTAL
: Prof. Dr. Hüseyin AKILLI
: Assoc. Prof. Dr. Ahmet PINARBAŞI
: Assoc. Prof. Dr. Muammer ÖZGÖREN

Flow around ground vehicles is fully three-dimensional and turbulent. Large-scale separation and circulation regions, a complex wake flow, long trailing vortices and the interaction of boundary layer flows can be given as typical characteristics of the flow around ground vehicles. A Thorough understanding of the structure of the flow around ground vehicles is essential for the designer when developing a new road vehicle because the shape of vehicles has a strong influence on the aerodynamic drag, fuel consumption, noise production and road handling. The simplified vehicle shape employed by Ahmed et al. (1984) retains some main features of the flow around real cars including fully three-dimensional large regions of separation elongated downstream of the vehicle, large coherent vortex structures and unsteadiness.

Thus, the aim of the present study is to investigate characteristics of flow structures around ground vehicles with the help of Ahmed body using both experimental and numerical methods. Therefore, 1/4 scale Ahmed body having 25^o slant angle was employed. The Reynolds number based on the body heights, H and the free stream velocity, U was $Re_H=1.48x10^4$. Investigations were conducted in two parts. In the first part of the study, particle image velocimetry (PIV) technique was used for the measurement of the instantaneous velocity fields around the Ahmed body. In addition, measurements were performed at several planes which were selected to highlight the aerodynamic characteristics of the body. In the second part of the study, Large Eddy Simulation (LES) method was used to resolve the flow structures around the Ahmed body, numerically. Most of the flow features around the Ahmed body such as the formation of trailing vortices, separation and re-circulatory flows were well predicted. Finally the instantaneous and time-averaged velocity vectors maps, vorticity contours, streamline topology and turbulence characteristics of the flow fields were presented and discussed in details.

Key Words: Ahmed body, Flow separation, Ground vehicle aerodynamics, Large eddy simulation, Particle image velocimetry.

ÖZ

DOKTORA TEZİ

BİR KARA TAŞITI MODELİ ETRAFINDA OLUŞAN AKIŞ KARAKTERİSTİKLERİNİN DENEYSEL VE SAYISAL YÖNTEMLERLE İNCELENMESİ

Tural TUNAY

ÇUKUROVA ÜNİVERSİTESİ
FEN BİLİMLERİ ENSTİTÜSÜ
MAKİNE MÜHENDİSLİĞİ ANABİLİM DALI

Danışman :Prof. Dr. Beşir ŞAHİN
Yıl: 2011, Sayfa: 185
Jüri : Prof. Dr. Recep YURTAL
: Prof. Dr. Hüseyin AKILLI
: Doç. Dr. Ahmet PINARBAŞI
: Doç. Dr. Muammer ÖZGÖREN

Kara taşıtları etrafında oluşan akış yapısı tamamen üç boyutlu ve türbülanslıdır. Büyük ölçekli akış ayrılmaları ve sirkülasyon bölgeleri, karmaşık yapılı girdaplar, aracın arka kısmında akış yönünde oluşan girdaplar ve araç üzerinde oluşan sınır tabakasının yer ile etkileşimi kara taşıtları etrafında oluşan akış yapısının tipik karakteristik özellikleri olarak belirtilebilir. Yeni bir kara taşıtı tasarımı yapılırken, taşıt etrafında oluşan akışın karakteristik özelliklerinin tam olarak bilinmesi taşıtın dış yapısının dizaynını, aerodinamik sürtünme direncini, yakıt tüketimini, taşıt etrafında oluşan akustik gürültüleri ve yol tutuşunu doğrudan etkilediği için çok önemlidir. İlk defa Ahmed ve ark. (1984) tarafından önerilen basitleştirilmiş araç modeli, kara taşıtları etrafındaki akış yapısının genel karakteristik özelliklerini korur.

Bu çalışmanın amacı kara taşıtları etrafında oluşan akış yapısının karakteristik özelliklerini, Ahmed taşıt modelini kullanarak, sayısal ve deneysel olarak incelemektir. Bu amaç doğrultusunda çalışmalarda 1/4 ölçekli, 25^o arka eğik yüzeye sahip Ahmed taşıt modeli kullanılmıştır. Akışın, model yüksekliğine ve serbest akış hızına göre tanımlanan Reynolds sayısı $Re_H=1.48x10^4$'dır. Çalışmalar iki kısımda gerçekleştirilmiştir. Deneysel ölçümler çalışmanın birinci kısmında tamamlanmıştır. Çalışmanın bu kısmında Ahmed taşıt modeli etrafında oluşan akış yapısının ölçümü parçacık görüntülemeli hız ölçme tekniği kullanılarak yapılmıştır. Çalışmanın ikinci kısmında model etrafındaki akış yapılarının hesaplanması için Büyük Girdap Simülasyonu (LES) yöntemi kullanılmıştır. Son olarak, akış alanına ait anlık ve zaman-ortalama hız vektörleri, girdap eşdeğer eğrileri, akım çizgileri ve türbülans karakteristikleri sunularak detaylı bir şekilde anlatılmıştır.

Anahtar Kelimeler: Ahmed taşıt modeli, Akış ayrılması, Taşıt aerodinamiği, Büyük girdap simülasyonu "Large eddy simulation", Parçacık görüntülemeli hız ölçme tekniği.

ACKNOWLEDGEMENTS

I would like to express my sincere gratitude to Prof. Dr. Beşir ŞAHİN, my supervisor, for his encouragement, invaluable advice, guidance, understanding and support throughout the preparation of this thesis.

Thanks are extended to Prof. Dr. Hüseyin AKILLI and Assoc. Prof. Dr. Ahmet PINARBAŞI for providing invaluable research advice and motivation during my thesis.

I would also like to express my special thanks to all administrator and colleagues at Adana İl Özel İdaresi for their continuous support and helps. In particular I would like to thank: Mr. Salih İNCETAŞ, Mr. Uğur AKCİĞER, Mr. Oğuz ÖZNAY and Mr. Mehmet Emin ATAYAN.

Last but not the least, I have my deepest appreciation to my beloved family for their advice, understanding and endless support during the preparation of this thesis.

CONTENTS **PAGE**

LIST OF TABLES **PAGE**

LIST OF FIGURES **PAGE**

NOMENCLATURE

H	: Height of the model
L	: Length of the model
W	: Width of the model
H_w	: Depth of the water in the channel
Re_H	: Reynolds number based on model height
u	: Stream-wise velocity component
u_{rms}	: Root-mean square value of stream-wise velocity component
v	: Span-wise velocity component
v_{rms}	: Root-mean square value of span-wise velocity component
w	: Cross-stream velocity component
w_{rms}	: Root-mean square value of cross-stream velocity component
$u'v'$	: Reynolds stresses correlations
x	: Coordinate in stream-wise direction
y	: Coordinate in span-wise direction
z	: Coordinate in cross-stream direction
N	: Frame number
U	: Free stream velocity
Δt	: Time interval
ψ	: Instantaneous streamline
$\langle\psi\rangle$	: Time-averaged streamline
ω	: Vorticity magnitude
$\langle\omega\rangle$	: Time-averaged vorticity
$\Delta\langle\omega\rangle$	: Increment of the time-averaged vorticity
$\langle\omega_{max}\rangle$	: Maximum vorticity value
$\langle\omega_{min}\rangle$	: Minimum vorticity value
SP	: Saddle point
S_{ab}	: Saddle point of attachment
F	: Foci

N_a : Node of attachment

S_u : Spectra of stream-wise velocity fluctuations

f : Sampling frequency

C_D : Total drag force coefficient

C_S : Component of drag force coefficient on the rear slant surface of the body

C_B : Component of drag force coefficient on the rear vertical surface of the body

C_K : Component of drag force coefficient on the front surface of the body

φ : Slant Angle

e : Average rate of energy dissipation per unit mass

n : Kinematic viscosity

h : Kolmogorov length scale

t_h : Kolmogorov time scale

u_h : Kolmogorov velocity scale

u_τ : Friction velocity

y^+ : Dimensionless wall unit

t_w : Wall shear stress

r : Fluid density

Δx^+ : Mesh resolutions in the streamwise direction

Δz^+ : Mesh resolutions in the spanwise direction

U_c : Characteristic mean velocity

L_c : Characterizing length

t_c : Time scale

λ : Taylor micro scale

g : Ground clearance

k : von Karman constant

τ_{ij} : Subgrid-scale stress

μ_t : Subgrid-scale turbulent viscosity

$\overline{S_{ij}}$: Rate-of-strain tensor

$|\bar{S}|$: Smagorinsky constant

L_s : Mixing length for subgrid scales, Length of the slant surface

V : Control volume

1. INTRODUCTION

1.1. Ground Vehicle Aerodynamics

Ground vehicles, in view of Fluid Mechanics, can be thought as bluff bodies which move very close proximity to the ground. The flow around the ground vehicle is fully three-dimensional and turbulent (Hucho and Sovran, 1993). Large-scale separation and recirculation regions, a complex wake flow, long trailing vortices and the interaction of boundary layer flows on the vehicle and ground can be given as typical characteristics of the flow around ground vehicles.

Thorough understanding of the structure of the flow around ground vehicles is essential for the designer when developing a new road vehicle because it has strong influence on the shape of the vehicle, aerodynamic drag, fuel consumption, noise production and road handling (Robinson, 2001). Fuel efficiency is the major objective in designing the new generation road vehicles. Wood (2004) stated that 27% of the total energy used, for example, in the United States is consumed by transportation systems, and 60% of the transportation energy or 16% of the total energy consumed in the United States is used to overcome aerodynamic drag in transportation systems.

In the past, ground vehicle aerodynamics has not been interested as much as their counterpart in aeronautics by the researchers for different historical and technical reasons. The flow over the ground vehicle is much more complex than the one around an airfoil. In the case of flow through the ground vehicles the gap between the body and the ground manipulates the flow characteristics for example, vortex periodicity and the mass flux through the gap etc. Rotation of the wheels and complex geometries leading to fully three dimensional flows can be given as other difficulty of ground vehicle aerodynamics. Main difference between aeronautic aerodynamics and ground vehicle aerodynamics, apart from the take-off and landing situations, is that we are not concerned with the control of wall turbulence but with the control of separation and large coherent structures in ground vehicle aerodynamics (Beaudoin and Aider, 2008).

Flow around ground vehicles have been studied experimentally and numerically by various researchers. Measure of all unsteady flow features around ground vehicles, at the same time, is extremely difficult in a wind tunnel by using experimental techniques. Computational Fluid Dynamics (CFD) is a powerful tool to understand the flow features around ground vehicles because it can provide enormous amount of information as well as high economical efficiency. Despite all of the recent developments in computational fluid dynamics (CFD) and its constituent technologies, however, it's still not an easy task to accurately predict the flow characteristics around ground vehicles. The complex configurations and flow physics involved in ground vehicle aerodynamics require, among other things, sophisticated geometry modelling and meshing tools, advanced turbulence models and an efficient solution algorithm (Makowski and Kim, 2000). Numerical studies conducted by using Reynolds averaged Navier Stokes (RANS) modeling have poor prediction of this flow. Using the RANS model to predict the flow around ground vehicles has two fundamental problems: its strong dependence on turbulence models adopted and its difficulty of capturing the unsteady flow characteristics. It can be concluded that RANS plays only a supplementary role of a wind tunnel test at the moment. Large Eddy Simulation (LES) can be alternative to the conventional numerical methods. LES with accurately fine mesh near the wall will be an encouraging solution to the problem because it can resolves unsteady turbulence characteristics with high accuracy, but in turn it requires excessively large computational resources. As a result, only few attempts have been made so far to apply LES to predict the flow features around the ground vehicles (Tsubokura et al., 2009).

Although the automotive industry has a high demand for reliable simulation methods capable of tackling the complex turbulent airflow around ground vehicles, a real-life automobile is very complex shape to model or to study experimentally. However, the simplified vehicle shape employed by Ahmed et al. (1984) retains some main features of the flow around real cars and generates fully three-dimensional regions of separated flow which may enable a better understanding of such flows (Guilmineau, 2008). The Ahmed body which has been used frequently as

a benchmark test case for this kind of flow by other researchers has been become a generic car-type bluff body with a slant back (Hinterberger et al., 2004). The flow around the Ahmed body exhibits basic features, which are also characteristic for other bluff body vehicles, namely trucks, buses or trains: There exist large coherent vortex structures and elongated separated flow regions downstream of the Ahmed body, which give the main contributions to the drag (Ceyrowsky et al., 2009).

The original Ahmed body used in the experiments of Ahmed et al. (1984) has dimensions of length L = 1044mm, height H = 288mm and width W = 389mm. The length of the slanted surface is L_S = 222mm, whatever the angle φ. The bottom surface of the Ahmed body is located at 50mm above the ground. This geometry is represented in Figure 1.1. In the present study a ¼ scale Ahmed body geometry was employed. The model was made up of a Plexiglas material.

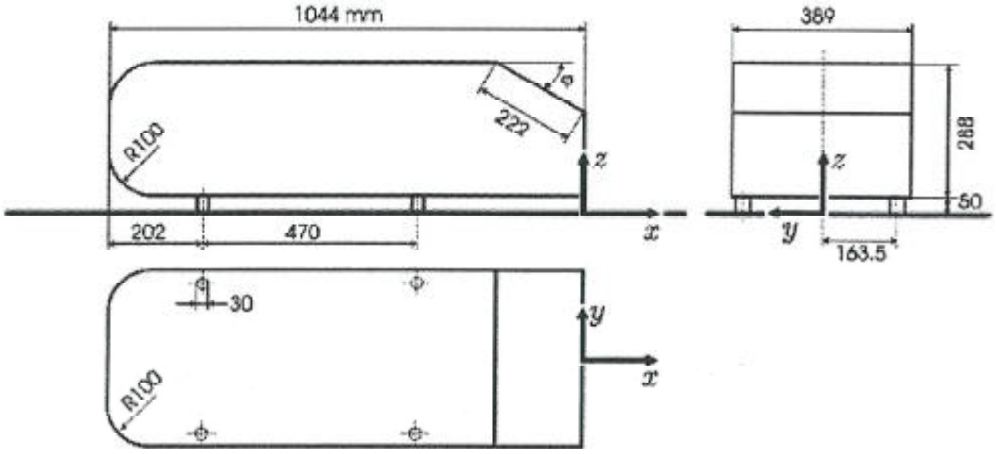

Figure 1.1. Geometry of the Ahmed body (Ahmed et al., 1984, dimensions are in millimeter)

The flow around this body is strongly influenced by the angle of the rear slant surface, which indicates that large portion of the aerodynamic drag is generated by development of three dimensional vortex separations from the rear slant surface (Guilmineau, 2008). Three main flow phenomena can be seen in the complex downstream flow of the Ahmed body. These are the recirculation bubble on the slant, the longitudinal vortices created on the side edges of the slant and the recirculation torus on the base of the body. In fact the pressure drag comes from rear part of the

body and is related to the competition between these three strong coherent structures (Beaudoin and Aider, 2008). For bluff bodies drag is mainly caused by pressure drag in contrast to streamlined bodies such as aircraft and ships which suffer primarily from the friction drag. In their experimental study, Ahmed et al. (1984) showed that up to 85% of the total drag is governed by pressure drag and in some vehicle configurations, more than 75% of the pressure drag is due solely to the averaged force applied on the rear part of the body while only 9% is due to the force applied on the fore-body (Beaudoin et al, 2004). Clearly, a more exact simulation of the wake flow and of the separation process is essential for the accuracy of drag predictions.

In the experiments of Ahmed et al. (1984), a critical rear body slant angle $\varphi_c = 30^\circ$ is found at which the drag is maximum. This drag crisis is due to a drastic change in the flow structure. The flow evolves, when increasing the angle from a quasi-two-dimensional wake to a complex three-dimensional very dissipative structure. Beyond this critical angle, the wake becomes again quasi-two-dimensional. The incidence 35° corresponds to the low-drag configuration (quasi-two-dimensional wake) while the incidence 25° is the high-drag configuration (strongly three-dimensional wake) (Guilmineau, 2008).

Due to the fact that the location at which the flow separates determines the structure of the wake flow and the size of the separation zone behind ground vehicles which presents major contribution to the ground vehicle's drag, avoidance of separation or, if this is not possible, its control is the most important objective of vehicle aerodynamics (Hucho and Sovran, 1993). Because different vortex structures can occur depending on the rear slant angle of the Ahmed body, different control strategies are required. The modern flow control techniques involve both passive and active techniques modifying behaviour of vortical structures in the wake (Uruba and Hladík, 2009). Active solutions need an external energy source in order to control the flow around the vehicle without necessarily interfering with its shape. On the other hand passive control techniques are energy free and often easier to implement.

1.2 Objectives of Present Investigation

The main objective of this study is to be the investigation of flow structures around the simplified ground vehicles, named as the Ahmed Body after the works of Ahmed et al. (1984), including large regions of separations and unsteadiness using experimental method employing Particle Image Velocimetry (PIV) technique and numerical flow modelling tools with the aid of Large Eddy Simulation (LES). All these investigations provide a detailed quantitative description of highly complex and time dependent nature of the flow around the Ahmed body. Better understanding of the physical phenomena encountered in the wake flow of the body and an identification of parameters that contribute to the aerodynamic drag of the body is aimed. Overall, understanding of the unsteady acrodynamic properties of the flow around ground vehicles; such as drag, lift, stability, wind noise and the accumulation of water and dirt on the surface of the vehicles could lead to better design of the ground vehicles (Krajnovic and Davidson, 2003). Additionally suitable application of new flow control devices capable of reducing the aerodynamic drag of the ground vehicles needs detailed knowledge about the flow characteristics around the ground vehicles.

Lienhart and Becker (2003), who conducted extensive experiments to understand the unsteady characteristics of the flow structures around the Ahmed body, state that the validation of turbulence models requires the availability of detailed experimental data which cover the most critical flow regions around the ground vehicle and they should give physical quantities that can directly be correlated to the results of numerical simulations. So that a secondary but also important goal in this study is to obtain quantitative data sets for validation of numerical simulations of the flows around ground vehicles.

A ¼ scale Ahmed body geometry (Ahmed et al., 1984) is employed as a test case. The geometry of the body is given in Figure 3.1. The flow geometry employed in the present LES calculations fit to the geometrical features of the Ahmed body employed in the present PIV measurements.

Experimental results obtained by using the Particle Image Velocimetry (PIV) technique are compared with three dimensional flow structures resolved with the aid of Large Eddy Simulation (LES) method. Our numerical and experimental results are also compared with the results from literature. Benefits and shortcomings of the LES method and the PIV method with respect to other methods are discussed.

In the present work, investigations were conducted in two parts. In the first part of the study, experimental measurements were completed. Particle image velocimetry (PIV) technique was used for the measurement of the instantaneous velocity fields around the Ahmed body. In the second part, Large Eddy Simulation (LES) method was used to resolve the flow structures around the Ahmed body. Finally, quantitative results obtained with the aid of experimental measurements and numerical calculations were presented in terms of important turbulent flow properties. Hence, flow visualization and turbulent coherent structures observed around the Ahmed body were discussed in detail.

1.3. Outline of Dissertation

The outline of the thesis is as follows. It is structured in five chapters. The background and objectives of the present investigation have been presented in Chapter 1.

Chapter 2 summarizes the literature survey and unresolved issues for the ground vehicle aerodynamics.

Chapter 3 describes the experimental setup and numerical method employed throughout the investigation. The simulation details, for example, computational setup and grids employed are described.

Results and discussion of the experimental measurements (using PIV) and numerical calculations (using LES method) of the flow around the Ahmed body are presented in Chapter 4. Flow visualisations and turbulent coherent structures are discussed.

Finally, Chapter 5 summarizes the main findings and conclusion of the present work and provides recommendations for further investigations as future works.

2. PREVIOUS STUDIES

In the beginning of twentieth century, when the motorized ground vehicles had been introduced to the people's life, nobody cared about their aerodynamics. In the past, ground vehicle aerodynamics has not been interested as much as their counterpart in aeronautics by the researchers. Application of aerodynamic principles to the ground vehicles has initiated much after the significant development had been done in the area of aeronautic aerodynamics. Initial efforts to improve ground vehicle aerodynamics were performed with respect to progress achieved in aeronautical aerodynamics. Streamlined body shapes employed in aeronautics was directly used in ground vehicle aerodynamics with almost no change. In those days, due to the bad road conditions and limited technology in automotive industry, the benefits of aerodynamics on the design of ground vehicles could not be attained and moreover were not needed. Additionally unwanted aesthetic issues arisen by using streamlined body shapes in the design of ground vehicles (Hucho and Sovran, 1993).

Critical events in the development of ground vehicle aerodynamics have been summarized in chronological order by Bayraktar (2002) as follow:

1. First, Klemperer (1922) recognized that the pattern of flow around half a body of revolution is significantly changed when that half body is brought close to the ground in 1922 (Figure 2.1).

2. Kamm et al. (1934) and Koenig-Fachsenfeld (1951) conducted rear body end truncation studies.

3. Hucho et al. (1976) introduced "detail-optimization" into vehicle development by modifying small components on the vehicle. Details such as radii of edges and pillars, camber of panels and size and location of spoilers were changed and significant results were obtained.

4. Morel (1978) and Ahmed et al. (1984) investigated detailed flow patterns at car rear ends.

5. Han (1989) implemented CFD methods to ground vehicle aerodynamics.

6. Today, aerodynamic design analysis on "add-on" devices such as mirrors, air dams, fairings and wings to passenger cars, trucks, and race cars are getting attention.

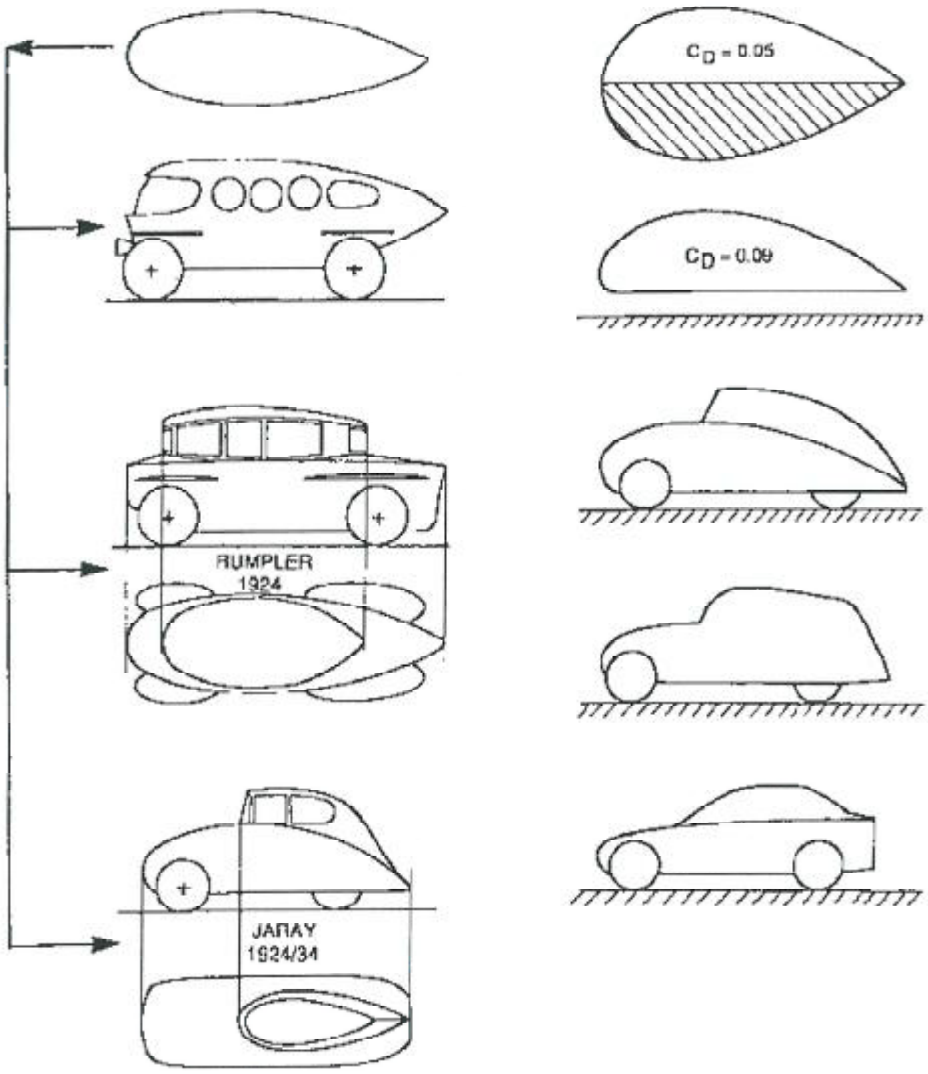

Figure 2.1. Historical development of ground vehicle aerodynamics (Hucho and Sovran, 1993)

In the 1930s, investigations were conducted on the characteristics of flow around front and rear end configurations of ground vehicles and their interactions. Strong interactions between front and rear end design were revealed in those studies. In the 1960s, detail optimization strategy based on subsequent detail modifications to

achieve substantial drag reductions was introduced. In detail optimization, a stylistic design is made first and the modification of details such as radii, taper, spoilers, etc., are carried out wherever required and significant results were obtained (Bayraktar, 2002). The two oil crises of the 1970s generated great pressure for improving fuel economy and provided a breakthrough for ground vehicle aerodynamics. In those days, another design strategy named as shape optimization method has been started to be used by vehicle designers. In this optimization process, shape design of the ground vehicles starts from a low-drag streamlined body with the same overall dimension as the final car and then converted into a real car step-by-step, applying the optimization technique for each detail (Elankumaran, 1997). Common applications of these two optimization strategies in developing new ground vehicles increase day by day. Actually, today both detail and shape optimization strategies are successfully used on the aerodynamic vehicle development process (Hucho and Sovran, 1993).

On the other hand, due to the fact that there is no significant reduction of

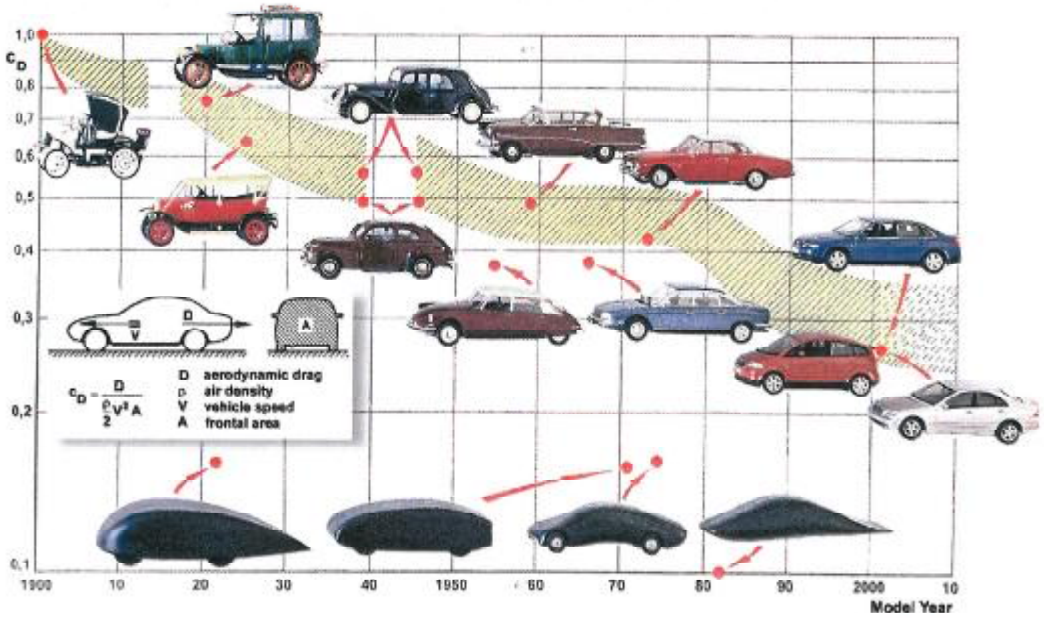

Figure 2.2. Development of drag coefficient c_D versus time (Hucho, 2009)

production car drag values for nearly two decades, strategies used so far have been exhausted (Hucho, 2009). Hucho (2009) has proposed the "limit value" strategy in order to overcome this stagnation to obtain lower drag values with models of various shapes shown at the bottom of Figure 2.2. He has stated that while developing this strategy, it became evident that considerable gaps in the science of vehicle aerodynamics still exist and require filling. He has shown the regions of a car that require more attention in Figure 2.3. They include the following:

- The underbody: Devices must be developed to improve the flow passing the wheels. Further measures must be adopted to smooth the underbody flow;
- The rear: Control of the near (and far) wake, and perhaps a rear diffuser;
- Windshield, A-pillar, and mirrors;
- Interference between the different regions, notably the front and rear parts of the car.

Figure 2.3. Regions for further improvement (Hucho, 2009)

Hucho and Sovran (1993) emphasize that the shape of cars has changed in an evolutionary rather than a revolutionary manner over the years, and at first for reasons other than aerodynamic ones. Research in road-vehicle aerodynamics has always been far ahead of practical application. Nevertheless, they also indicate that blaming the automobile industry for not taking advantage of the full potential of aerodynamics is not justified, since the "concept" of any car is influenced by a variety of factors (Figure 2.4) which, collectively, are summarized by the term "market". However, according to Hucho and Sovran (1993), the long-known potential for reducing drag (which relates to one of these factors) is now being

exploited more and more. How far this trend will go depends on the future course of fuel prices and, perhaps, of emissions regulation.

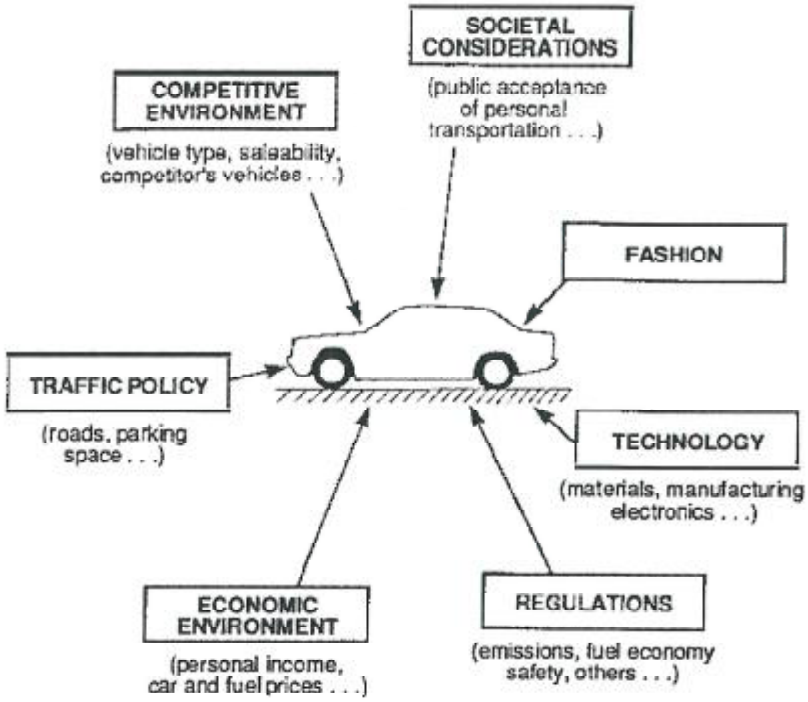

Figure 2.4. Factors that influence the concept of a car (Hucho and Sovran,1993)

2.1. Ground Vehicle Aerodynamics

A real-life automobile is very complex shape to model or to study experimentally. Therefore simplified vehicle shape which retains primary behavior of the vehicle aerodynamics should be employed. When the history of the ground vehicle aerodynamics is reviewed, one can see that there are two common bluff body geometries that have been used as a benchmark case in the literature. Morel (1978) has proposed the first generic bluff body case for ground vehicle aerodynamics, and then this bluff body geometry was revised by Ahmed et al. (1984). Ahmed et al. (1984) conducted extensive research about the characteristics of flow around this generic bluff body. Both Morel (1978) and Ahmed et al. (1984) have investigated the characteristics of flow through the rear end of the bluff body model and reported drag coefficient change. Afterwards, various types of bluff body geometry have also

been studied by scientific community (Ludwieg (1984), Jenkins (2000), Krajnovic and Davidson (2001), Barlow et al. (2001), Alam et al. (2003), Lawson et al. (2006)). But still the bluff body model which was used in the study of Ahmed et al. (1984) is the most preferred bluff body model for the studies in ground vehicle aerodynamics. It has been used in several experimental (Ahmed et al. (1984), Lienhart et al. (2000), Spohn and Gillieron (2002), Beaudoin et al. (2004), Vino et al. (2004, 2005), Strachan et al. (2007)) and numerical studies (Gilliéron and Chometon (1999), Makowski and Kim (2000), Howard and Pourquie (2002), Kapadia et al. (2003a,b), Hinterberger et al. (2004), Krajnovic and Davidson (2004a,b, 2005a,b,c), Bernard et al. (2005), Fares (2006), Guilmineau (2008)).

Le Good and Garry (2004) reviewed the design characteristics and use of several key reference models which have been used in both experimental and computational researches on the subject of automotive aerodynamics. They discussed the advantages and disadvantages of these designs and also the applicability of the results in providing guidelines for the development of production vehicles. They grouped the reference vehicle shapes into three categories based on the published papers. These are: 1- *Simple Bodies;* such as the Ahmed model, NRCC/SAE model and Rover Bluff Body model, which are used mainly for research. 2- *Basic Car Shapes;* such as the MIRA Reference Car, SAE Reference Car, which have been used for calibration, correlation and research. 3- *Production (series) Cars* – which have been used in both small-scale and full-size versions for a variety of specific investigations and correlation studies. They concluded that the use of simple reference models has provided an extensive insight into the fundamental aerodynamic characteristics of automobiles. They also concluded that using the same reference model have contribute to the development of experimental techniques, providing systematic data sets for the development of wind tunnel blockage correction theories and the calibration and correlation of wind tunnels. Moreover reference models can be used as test cases in the validation of CFD codes.

Ahmed body is 1044mm long (L), 288mm high and 389mm width. The slant part is 222mm long, whatever the angle. The bottom surface of the Ahmed body is located at 50mm above the ground. Although its forms are free from all accessories

as well as from wheels, it still retains the primary behavior of the vehicle aerodynamics. This geometry is represented in Figure 1.1. The flow around this body is strongly influenced by the angle of the rear slant surface, which indicates that the large portion of aerodynamic drag is generated by the development of three-dimensional vortex separation from the rear slant surface. The wind tunnel experiments on this model (Ahmed et al., 1984, Lienhart et al., 2000) show critical slant angle of 30° where the total drag on the body become maximum.

Ahmed et al. (1984) have carried out experiments with several slant angles φ and described the characteristics of the flow for various angles. The most important finding driven from their studies can be stated as the most of the drag of the body is due to pressure drag which is generated at the rear end. This can be seen from Figure 2.5. Various contributions to the drag coefficient as a function of the slant angle are shown on the right of this figure. As Rodi (2004) reported sudden drop in drag occurs above the slant angle of 30° at which the maximum drag was occurred. Drastic change in the wake flow is also occurred beyond this angle, which is also called as critical angle. He summarized the flow characteristics after the Ahmed body for the angles below and above the critical angle as follow. Below this angle, strong counter-rotating vortices emanating from the sloping edges of the body are present and the flow separates in the middle region of the top edge and reattaches at the sloping surface. For angles above the critical angle, the counter-rotating vortices are much weaker, the separation occurs along the entire top and the side edges, and there is no reattachment on the sloping surface. The main differences between the flow characteristics, which are occurred in the wake after the Ahmed body, before and after the slant angle of 30° are illustrated in the left of Figure 2.5.

Han (1989) investigated flow around the Ahmed body using steady Reynolds-averaged Navier-Stokes solver with k-ε model. Due to the lack of accuracy of the turbulence modeling used, calculations of pressure coefficient on the base did not match the corresponding value in the literature. His calculations predicted the location of separation and trailing vortices as in the literature.

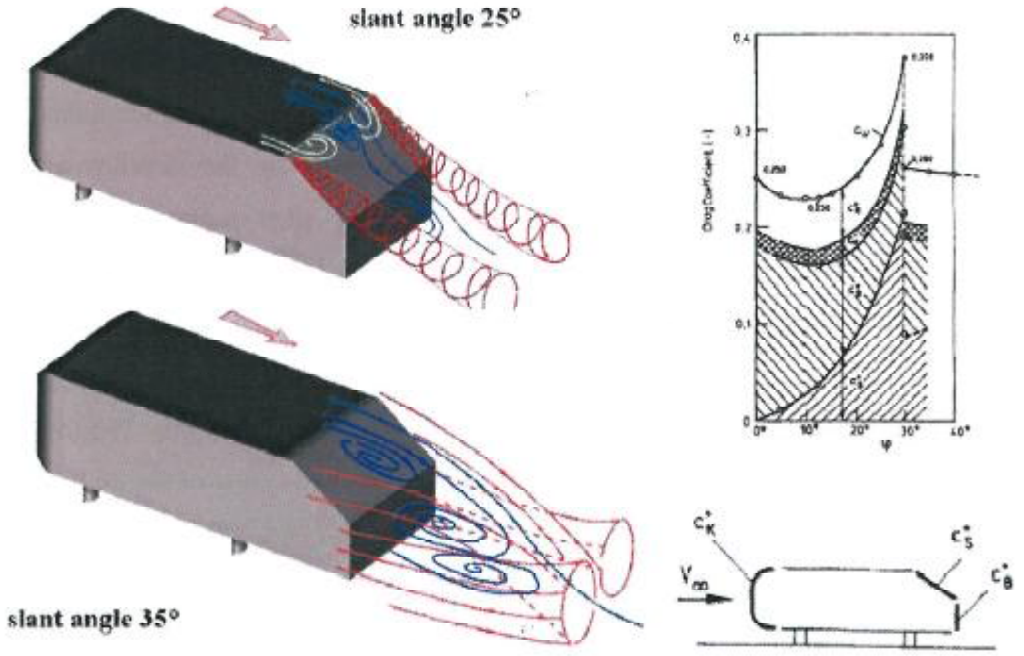

Figure 2.5. Development of the flow in the rear of the Ahmed body for two slant angles (left; Lienhart et al., 2000) and dependence of drag coefficient on slant angle φ (right; from Ahmed et al., 1984)

Basara and Alajbegovic (1998) presented an attempt to validate and test the ability of turbulent closures in flow simulations of the flow around the Morel Body by assessing two different models, standard k-ε model and full Reynolds-stress model. Their paper examines the validity of using steady state approach for this type of flows. Their results show that the measured values of drag and lift coefficients for various back slant angles by steady state calculations and standard k-ε or Reynolds-stress model can't be predicted correctly. Calculations confirm that the vortex shedding is present for this geometry and therefore, transient approach is only appropriate for such simulations.

In aerodynamic design, computational fluid dynamics (CFD) methods are slowly superseding empirical methods and design engineers are spending more and more time applying CFD tools to analyze and predict (Van Dam, 1999). Van Dam (1999) studied on the CFD-based drag prediction with an emphasis on flow solutions governed by the Euler and Reynolds-averaged Navier-Stokes equations. For these types of flow solutions, various drag analysis methodologies have been outlined and

applied to determine the drag of components of as well as whole-body airplanes, helicopters, and ground-based vehicles at subsonic and transonic flow conditions. Although many advances have been made, his review shows that the physical modeling of turbulence in boundary layers and free shear layer limits the useful application of CFD-based drag prediction, particularly for flows about multi-element lifting surfaces with strong viscous interactions and flows over bluff bodies.

Gilliéron and Chometon (1999) used Fluent software to compute the flow field variables around the Ahmed reference model. They compare computed results against experimental findings for different angles of rear window inclination, and offer qualitative analysis, chiefly concerning aerodynamic drag coefficient and the behavior of vortex wake flows. Their results are in agreement with experimental results of Ahmed et al. (1984). They found that the agreement of the time-averaged quantities was good although some discrepancies were present, especially in the lower part of the slant back with experimental data.

Makowski and Kim (2000) studied various aspects of applying modern computational fluid dynamics (CFD) to the prediction of aerodynamic flows around ground vehicles using the unstructured-mesh-based solver technology in the FLUENT code. Their study was in the framework of an unstructured mesh finite-volume method applied to the steady-flow RANS equations. The main issues in their paper include numerical details and turbulence modeling.

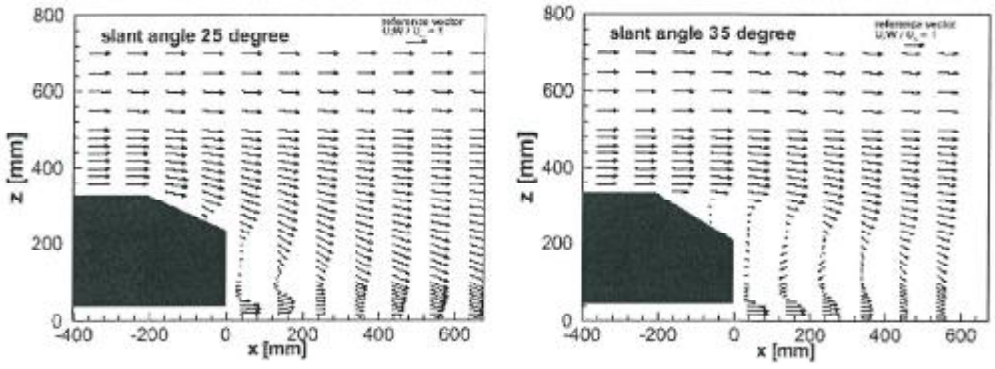

Figure 2.6. Comparison of the recirculating wake region and attached/detached flow for the two different rear slant angles (Lienhart et al., 2000)

Lienhart et al. (2000) showed oil-flow pictures for the sloping surface and visualization of the wake flow with smoke injection for the slant angles 25° and 35°. Lienhart et al (2000) also measured the mean and fluctuating velocities by 2-component laser-Doppler anemometer (LDA) mounted on a traversing system and a simplified model of a car (Ahmed model). Measurements were made for two rear vehicle body slant angles (25° and 35°) at a bulk air velocity of 40 m/s. These quantitative data cover the most critical flow regions around a bluff car-shaped body and they give physical quantities that can directly be correlated to the results of numerical simulations.

More recently (within the last 10 years), computational fluid dynamics (CFD) has matured sufficiently as a technology to enable it to calculate such quantities as drag and lift for a road vehicle without resort to wind tunnel testing. (Robinson, 2001). Robinson's study is concerned with the application of a cubic non-linear k-ε model to flows pertinent to road-vehicle aerodynamics. Three simple test cases were initially considered and the Ahmed body was used as a final test case. He compared the performance of the non-linear k-ε model with the linear k-ε model. He conclude that for the body with the 25° rear-slant, the linear *k*-ε model calculates the attached flow with the strong side-edge vortices reasonably well; the non-linear *k*-ε model does not calculate this flow well. On the other hand, over the 35° rear slant both the linear and non-linear *k*-ε models produce separated flow.

Spohn and Gillieron (2002) have investigated both the structure of flow separations on the Ahmed body and the vortical structures in the near wake of the body. For that purpose they employed the low-speed water tunnel which allows to use visualizations techniques in combination with ordinary video acquisition equipment. Their experiments were carried out at Reynolds numbers of about $8x10^3$. Their results indicate that although the dimensions of the front part separation zones which are open with periodic vortex shedding tend to decrease with increasing Reynolds number, the shedding will persist and cause detrimental effects like sound generation and unsteady interaction with the vortical structures arising from the hatch panel. They recognized that the rear part separation zone appears to be more complex than previously found by Ahmed et al (1984). They found an additional region of

attachment in agreement with previous numerical simulations of Gilliéron and Chometon (1999). Furthermore the central detached flow region is not closed but contains two separation foci, which slowly evacuate the fluid above the panel into the wake.

Kapadia et al. (2003) have conducted numerical studies on the characteristics of the flow structure around the Ahmed reference model with 25° and 35° slant angle by using Spalart-Allamaras based detached eddy simulation hybrid model. They also employed one-equation RANS model for the same simulation. Both techniques were compared by showing the capability of each technique in capturing the minor flow details and in predicting the coefficient of drag (C_D). As a result of this comparison the strong ability of DES in capturing unsteady structure of the flow with minor flow details than RANS was showed. The Reynolds number based on body length $2.78x10^6$ was used in their study. They indicated that the flow over the base slant in the experiments was attached at 25° and separated at 35°. This causes a large drop in the drag with the increased slant angle as the vortices on the side of the slant are weakened due to the separation. They also compared their DES results with the experimental data available in the literature. They saw that DES predicted separation at 25° slant angle, in contrast to the experiments. Drag was relatively close to the experiments, but the distribution of drag was more on the rear than on the slant due to the separation. At the 35° slant angle, DES was in good agreement to the experimental drag, with the correct distribution, while RANS over-predicts the drag.

Beaudoin et al. (2004) studied the wake after the Ahmed body in a hydrodynamic flow. A cavitation technique is proposed to identify the lowest pressure regions. They showed that the lowest pressure regions in the flow over a simplified road vehicle correspond to the longitudinal vortices produced at the rear part. They concluded that cavitation technique is the powerful tool to characterize the flow structures by using a non-intrusive technique which provides both visualization and pressure measurements of flow structures at high Reynolds numbers.

The latest improvements in computation power have introduced more sophisticated numerical methods into bluff body aerodynamics. For example, LES and Direct Numerical Simulation methods which are powerful numerical methods could not be

applied on the real industrial problems through past decades. But, nowadays, it can be said that there are numerous studies that are being conducted by using LES method.

Initial successful application of LES to solve the flow around the Ahmed reference model was conducted by Howard and Pourquie (2002). They shown wide range of flow results such as: time averaged mean profiles, time-dependent traces, flow spectra and a number of two-dimensional and three-dimensional animations of the flow field. The body geometry was analyzed at a slant angle of 28°. They used a non-structured tetrahedral grid which enables accurate modeling of the body geometry while avoiding the need for a prohibitively expensive mesh. Their simulation revealed complex time dependence of the flow around the body. Visualizations of the Q criterion showed a series of horseshoe vortices being shed in the wake where previous studies indicated that the wake structure was made up of discrete contra-rotating vortices.

Rodi (2004) studied the flow around the Ahmed body. LES was presented there for the case with $\varphi = 25^{\circ}$ and the Reynolds number is $Re = 2.8 \times 10^6$ (based on the length of the body). A Smagorinsky SGS model was employed in the LES with a model constant of $C_s = 0.13$. The calculations were performed on two multi-block grids. The coarser one consists of 93 blocks and 8.8×10^6 cells and the finer one of 214 blocks and 18.5×10^6 cells. He observed that for high Reynolds number situation with large regions of thin attached boundary layers on the body a detached eddy simulation (DES) approach or in general a coupled LES/RANS calculation would be more suitable in which the development of the attached boundary layer is simulated by the RANS mode.

Hinterberger et al. (2004) performed the LES of the flow around the Ahmed body with a slantback angle of 25°. Their configuration has been specifically chosen to match the experiment of Lienhart et al. (2000). The bulk velocity was 40 m/s. This results in a Reynolds number $Re = 2.8 \times 10^6$ (based on the length of the body). Hinterberger et al. (2004) stated that the flow around the Ahmed body was a very challenging problem because of the complex geometry and the high Reynolds number.

Krajnovic and Davidson have applied LES to the different type of bluff bodies with ground proximity successfully. They presented LES of the flow around a bus-like body (Krajnovic and Davidson, 2001). Flow around a simplified bus was further analyzed by Krajnovic and Davidson (2003) using large-eddy simulation with different type of grids in detail. At the Reynolds number of 0.21×10^6, based on the model height and the incoming velocity, the flow produced features and aerodynamic forces relevant for the higher Reynolds number. The large-eddy simulation used in this study predicted not only large-scale coherent structures that agree with previous knowledge but also some new, smaller structures. Krajnovic and Davidson (2004) also studied flow around the Ahmed body by using LES. In that study, they used a new approach for LES of the flows around ground vehicles. It was based on the character of the flow with large regions of recirculations rather than on traditional resolution requirements for the LES of wall bounded flows. Krajnovic and Davidson (2004) confirmed their hypothesis of the partial Reynolds number independence of some vehicle flows and also shown that LES had a large potential in external vehicle aerodynamics. Krajnovic and Davidson (2005) was investigated the effect of a moving floor on the flow around the Ahmed body. They performed two large eddy simulations of the flows with stationary and moving floors and compared both instantaneous and time-averaged results. It was found that the floor motion reduces drag by 8% and lift by 16%. The wake flow was found to be relatively insensitive to the floor movement, in agreement with previous experimental observations. Krajnovic (2009) made a brief review of LES applications conducted by him and his co-workers for different bluff-body flows at the past. Examples of flows range from simple cube flows to flows around ground vehicles. He indicated that an increase of the Reynolds number towards the operational speeds of ground vehicles requires accurate near-wall modeling for a successful LES. He concluded that his review proves the applicability of LES for various bluff body flows.

Franck and d'Elia (2004) employed LES turbulence model to investigate the flow around the Ahmed model with a slant angle of 12.5°. Flow visualizations through streamlines, isosurfaces and isolines were presented on the forebody part, rear end and neighboring wake. Franck et al. (2007) further investigate the near-wake

structure of the flow around the Ahmed model with the same slant angle by applying LES method. In their study, the Reynolds number (based on the model length) was 4.25 million. The coherent macro structures in the near-wake were estimated through the second invariant of the velocity gradient applied on the time-average flow. Their results are in agreement with experimental results. They indicated that the turbulent eddies up to the Taylor length scale were well resolved and this can be mainly attributed to the fact that the normal mesh-spacing on the body surface (at its first layer) was smaller than such length scale. They stated that the flow around this bluff-body is dominated by large coherent macro structures formed by a massive flow separation. The mean drag coefficient they obtain agrees quite well the experimental one. They concluded that according to the current computational resources LES may be used as a feasible turbulence model for real vehicles aerodynamics.

Vino et al. (2004) and (2005) investigated the time-averaged and time-dependant nature of the wake region behind the Ahmed model with a slant angle of 30° experimentally. They employed a new multi-hole probe allowed for measurement in regions including flow reversals, and high levels of unsteadiness. Their time-averaged results of the far-wake showed good agreement to previously published work, although the near-wake structure was found to be somewhat different. Their time-dependant analysis indicate that the shedding behind the model is analogous to vortex shedding behind simple bluff bodies, with most of the fluctuations confined to the axial and vertical directions. They have illustrated all their time-averaged and transient results as shown in Figure 2.7. Vino et al. (2005) have also investigated the complex nature of the near- and far-wake of the Ahmed model geometry along with Reynolds number behavior. They have found that although the model is quite bluff, drag coefficients exhibited some sensitivity to changes in Reynolds number; up to 15% reduction over the test speed range. They have concluded that Reynolds number effects on spectral characteristics revealed that a drop in drag was accompanied by an increase in Strouhal number.

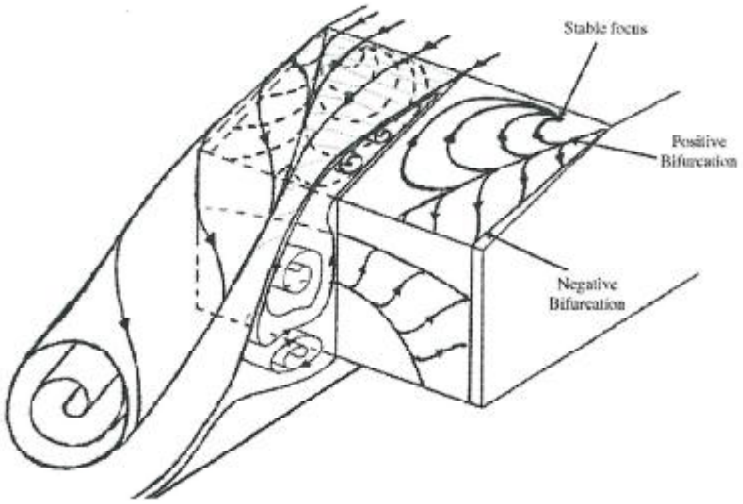

Figure 2.7. Proposed topological flow structure of the Ahmed model with 30° rear slant by Vino et al. (Vino et al., 2005)

Bernard et al. (2005) applied the grid-free vortex method to predict the turbulent aerodynamic flows produced by road vehicles. They indicated that grid-free vortex method has the character of a large eddy simulation and incorporates a fast technique for evaluating the mutual interactions of several million vortex elements needed in describing the dynamically significant structure of the turbulent field. Their study demonstrated that quantitatively accurate predictions of velocity statistics can be obtained as long as appropriate wall resolution is maintained. The wall resolution issue reflects the fact that with the absence of a turbulence model per se, the Reynolds number is a real parameter in this method and its effect on the physics has to be taken into account where necessary. Main advantage of grid-free vortex method was stated as the difficulties of grid generation that typically affect LES schemes are avoided in this method.

Mavuri and Watkins (2005) have conducted studies on the simulation of relative motions of the wheels and moving ground for road vehicle aerodynamics. Their method involves the application of double symmetry concept on Ahmed model geometry with the slant angle of 30° as shown in Figure 2.8. They indicated that this technique was useful for experimental examination of local flows in wheel, wheel housing, underbody and other similar areas of a test vehicle. Working with simple measurement mechanism, requiring only single model and simulating the moving

ground while rotating the wheels can be given other advantages of this technique. As a result of their studies, they found that drag coefficients exhibited almost insensitive to changes in Reynolds number, based on body length, nearly between 800.000 and 2.000.000.

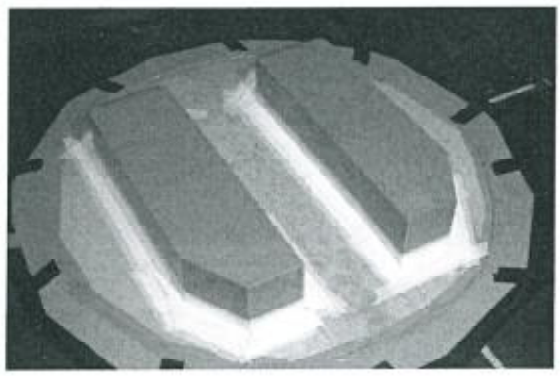

Figure 2.8. Experimental model of split Ahmed body in double symmetry arrangement (Mavuri and Watkins, 2005)

Fares (2006) investigated the unsteady flow at the rear slant of Ahmed body for two slant angles 25° and 35° using the lattice Boltzmann numerical model approach. He presented results containing the discussion of the flow of the wake and comparison of the distributions of averaged pressure and velocities with available experimental findings. He also investigated the resolution requirement in terms of computational requirement and accuracy achieved. He stated that the resolution requirement represents a key issue in the simulation process. As a result of his effort on applying different resolutions based on the Taylor microscale λ_h, well captured separation region was achieved using $\Delta x_{min} = \lambda_h/1.5$ and a fair prediction was also achieved using $\Delta x_{min} = \lambda_h$. He concluded that the approximation of λ_h for different flow regions based on the relevant local Re number can be used to determine the requirements in other simulations. He indicated that qualitative and quantitative comparisons with experiments show excellent agreement with experimental findings.

Strachan et al. (2005) presented computational and experimental data for the Ahmed reference model in near side wall proximity. During the experiments Laser Doppler Anemometry (LDA), force and moment data was recorded. The aim of the

study was to investigate the ability of both the k-ε and Reynolds Stress viscous model to predict the characteristics of flow around the model when in wall proximity in comparison with the isolated case. They concluded that the Reynolds Stress viscous model provides a more accurate simulation of the Ahmed body than the k-ε RNG model. Both models significantly over predicted the pressure drag over the front end, and thus cannot be used for accurate pressure drag force predictions. Strachan et al. (2007) also study the vortex structure behind the Ahmed body in the presence of a moving ground plane by using Laser Doppler anemometry (LDA) for various backlight angles. LDA velocity measurements were taken in a number of planes around and downstream of the model at a free-stream velocity of 25 m/s. They found that the inclusion of the ground simulation and the consequent supporting strut produces a reduction in the size and strength of the vortices shed from the back end of the Ahmed model when compared with previous analysis. They further concluded this effect is primarily a result of the overhead strut, and that the rolling road has little effect on these upper vortices.

Hoessler et al. (2007) performed unsteady numerical simulations of the flow around the Ahmed body using both LES and Lattice Boltzmann Method (LBM) in order to evaluate their ability to predict the mean and fluctuating flow produced by this complex geometry at high Reynolds number. Their aim was analyzing both the steady and unsteady effects of the coherent structures produced in this 3D flow on the drag and lift forces applied on the body. The Ahmed bluff body on its 25° slant angle configuration was chosen for that purpose as it presents a separation line and two intense and stable counter-rotating vortices on the rear slant that contribute for most of the total drag. The inlet velocity was $U_0 = 40$m/s with a zero turbulence rate. The time step was set to $\Delta t = 5 \times 10^{-5}$ s for the LES and $\Delta t = 3.9 \times 10^{-6}$ s for the Lattice Boltzmann simulation. They showed that the results obtained were in good agreement in terms of mean flow prediction with the Laser Doppler Anemometer (LDA) measurements performed by Lienhart et al. (2000).

Guilmineau (2008) investigated numerically, with several turbulence models, the flow around the Ahmed body for the base slant angles 25° and 35°. He compared his results with experimental data of Lienhart and Becker (2003). He resulted that all

turbulence models used predict the topology of the flow correctly. On the other hand, the EASM (quadratic explicit algebraic stress model) model gives a better estimate of the drag. The two-dimensional behavior of the flow, for the slant angle 35°, is well predicted. At the 25° slant angle, all simulations predict massive separation, whereas the experiment shows reattachment about half-way down the center of the face. He concluded that the flow around the Ahmed body with 25° slant angle can be considered as an open challenge for turbulence modeling.

Rouméas et al. (2008) carried out a 3D numerical simulation based on the lattice Boltzmann method on the Ahmed body with 25° slant angle to analyze and establish a method for controlling the near-wake flow topology of a generic blunt body model. Their results indicate the existence of a complex flow topology consisting of transverse and longitudinal vortices emanating from flow separations that occur on the top and the lateral edges of the slanted rear window, respectively. They gave the detail of the topology of each structure and compared their numerical results with the experimental results in the literature. They concluded that the results obtained constitute a validation of the computation code for the representation of bluff body near-wake flow characteristics of automotive vehicle wake and lattice Boltzmann method can therefore be used to develop and parameterize active control solutions.

Uruba and Hladik (2009) conducted studies on both stationary and dynamical behavior of structures in the wake of Ahmed body. Two configurations with slant angles of 25° and 35° were considered as the test-cases. The small variant model of Ahmed body, scale 3/20 relative to original Ahmed body was subjected to experimental study, mean flow velocity about 6.5 m/s resulting in Reynolds number 54000. For the measurements, the stereo time-resolved PIV technique was used. As a result of their measurements. angle 25° showed more or less attached flow, while angle 35° generated fully detached flow from the ramp.

Ceyrowsky et al. (2009) investigated the flows around the Ahmed body with different rear geometries (slant angles of 25° and 35°) with the aid of numerical simulations based on the unsteady Reynolds-averaged Navier-Stokes (URANS) equations. They concluded that the numerical efforts for the URANS simulations are

much lower than the efforts for LES or lattice Boltzmann simulations. They suggest that URANS models should be applied in early-stage optimization simulations, whereas large-eddy or lattice Boltzmann simulations should be employed in late stage final tuning simulations.

Several other studies investigated similar bluff body structures for the variables other than backlight angle. Jenkins (2000) conducted an experimental investigation of the flow over the rear end of a 0.16 scale notchback automobile configuration. His objective was to investigate the flow separation that occurs behind the backlight and obtain experimental data that can be used to understand the physics and time-averaged structure of the flow field. He used a three-component laser velocimeter to make non-intrusive, velocity measurements in the center plane and in a single cross-flow plane over the decklid. In addition to off-body measurements, flow conditions on the car surface were documented via surface flow visualization, boundary layer measurements, and surface pressures. He concluded that his experimental data show several features previously identified by other researchers, but also reveal differences between the flow field associated with his particular configuration and the generally accepted models for the flow over a notchback rear end.

Alam et al. (2003) performed mean and time-varying flow measurements on the surface of a family of idealized road vehicles. They stated that modern vehicles experience strong surface pressure fluctuations on the side windows due to flow separation around the A-pillar. So that they investigated how these fluctuations vary with speeds and also studied the effects of local A-pillar and windshield geometry and yaw angles on the nature of the fluctuations. Their studies showed that Reynolds number sensitivities (based on free-stream flow velocities and body width) in the range of $6.4x10^5$–$1.5x10^6$ were minimal. They concluded that the magnitudes of the fluctuating pressure coefficients depend largely on local A-pillar radii and can be reduced significantly with the increase of local corner radii.

Kozaka et al. (2004) investigated turbulent structure of three-dimensional flow behind a model car exposed to uniform approach flow. Their results showed that two counter-rotating helical vortices, which are formed within the inner wake region, play a key role in determining the flux of kinetic energy.

Jindal et al. (2005) investigated the flow field around two vehicle geometries using the Immersed Boundary (IB) technique in conjunction with a steady RANS CFD solver. They reported that the IB approach allows the computation of the flow around objects without requiring the grid lines to be aligned with the body surfaces. Their simulations were carried out for a SUV and a pickup truck models at a Reynolds number of $8x10^5$. The comparisons between the their simulation results and the time-averaged measurements revealed that their CFD simulations predicted the drag coefficients for the SUV and the pickup truck models within 6% of the measured values.

Guilmineau (2006) performed numerical simulations for a new vehicle model, created to analyze the behavior of unsteady wakes on bluff bodies. RANS equations were solved on unstructured grid using a near-wall low-Reynolds number turbulence closure model. In the paper, only a large yaw angle (β=30°) was investigated and the Reynolds number was close to 10^6. He reported that his numerical results show an excellent agreement when compared with experimental data.

Lawson et al. (2006) investigated the flow characteristics in the boot-deck region of 36 per cent scale model notch-back saloon vehicle and presented the results of an experimental investigation of the bootdeck flow structure together with a general review of advanced laser diagnostic techniques suitable for large-scale wind tunnel flow measurement. The tests were used to characterize the flow behaviour over the Reynolds number range $0.74\times10^6 - 4.93\times10^6$. Their experiments involved flow visualization, rear boot-deck and backlight three-dimensional stereoscopic particle image velocimetry (PIV) measurements, and mean static and unsteady static pressure measurements. It was reported that their flow visualization results indicated flow asymmetries in the backlight region which appear to be sensitive to changes in free-stream speed.

d'Apollonia et al. (2007) performed RANS and LES of a semi realistic vehicle shape under crosswind conditions. Their model was the simplified fifth scale mock-up of a Citroën C5. They compared aerodynamic force and torque components, wall pressure coefficient and mean velocity profiles of the flow. They

reported that LES can be a suitable tool for studying vehicle aerodynamics in crosswind conditions. Finally, they indicated that in their study, only an un-detailed and 1:5 scale reduced size macro-shape of a vehicle was considered. This resulted in a lower Reynolds number and thus larger turbulence eddy scales and less constraints on the volume mesh. In order to address more realistic situations such as full scale models, they recommend more resolution.

Tsubokura et al. (2009) conducted one of the largest-scale unstructured LES of flow around a full-scale road. The main objective of their study was to look into the validity of LES for the assessment of vehicle aerodynamics, especially in the context of its possibility for unsteady or transient aerodynamic forces. They reported that LES will be a powerful tool for the vehicle aerodynamic assessment in the foreseeable future, because it can provide precious aerodynamic data which conventional wind tunnel tests or RANS simulations are difficult to provide. They concluded that more attention is going to be paid to understand unsteady flow structures around vehicles and the physical mechanism of their generation and interaction with the solid body. Reduction of the aerodynamic noise generated around the front pillar was given as a typical problem. Accordingly, Tsubokura et al. (2010) investigated unsteady aerodynamic response of a road vehicle subjected to transient crosswinds with the aid of LES method based on a fully unstructured finite volume method. They reported that typical transient responses of the aerodynamic forces and moments such as phase shifting and undershooting or overshooting were observed. They discussed their dependence on the frequency and amplitude of the input perturbation. As a result they demonstrated the utility and validity of the LES in the context that such transient aerodynamic forces are difficult to measure using a conventional wind tunnel.

Ortega et al. (2002) indicated that significant amount of effort has been put forth to reduce the aerodynamic drag of heavy vehicles over the past several decades. A reduction in the total aerodynamic drag will have a significant improvement on the fuel economy of a heavy vehicle. In recent years, the pressure drag on the front of a heavy vehicle has been successfully reduced by streamlining the tractor, installing air shields on the tractor roof, or optimizing the relative height of the tractor and trailer.

However, the pressure drag on the rear of a heavy vehicle, also known as base-drag, yet remains to be reduced on a widespread basis. There are numerous efforts in the scientific community to fully understand the characteristics of flow structures around the heavy vehicle and trains, for example, Ortega et al. (2002), Bayraktar (2002), Wood (2004), Maddox et al. (2004), Diedrichs et al. (2004) and Hemida et al. (2005). There are also numerous concepts have been proposed in the effort to reduce the total drag of heavy vehicles, for example, Englar (2001), McCallen et al. (2000), Wood and Bauer (2003), McCallen et al. (2004).

According to the Hucho and Sovran (1993) location at which the flow separates determines the structure of the wake flow and the size of the separation zone behind the ground vehicle which presents the major contribution to a car's drag. Because of this fact, avoidance of separation or, if this is not possible, its control is the most important objective of vehicle aerodynamics. Because different vortex structures can occur depending on the rear slant angle of Ahmed body, different control strategies are required. The modern control methods involve both passive and active techniques modifying behaviour of vortical structures in the wake (Uruba and Hladík, 2009).

Wood et al. (2003) have developed three simple, low cost aerodynamic drag reduction devices for application to the trailer of a tractor-trailer truck. The three devices have undergone extensive operational testing where they have amassed over 85,000 miles of use. Technologies developed by Wood et al. (2003) have shown a combined fuel savings of 10% at an average speed of 47.5 mph. This improvement in fuel economy correlates to an equivalent drag reduction of approximately 30% with a corresponding drag coefficient of 0.45. Observations and anecdotal evidence from their test activity have shown that the addition of these devices to the trailers has not had a negative impact on either the operational utility of the trailers or the maintenance procedures and requirements.

There are numerous studies conducted on the flow control of ground vehicles using both passive and active techniques in the literature. Khalighi et al. (2001), Verzicco et al. (2002), Beaudoin and Aider (2008), Bruneau et al. (2008) have performed studies on the flow control of ground vehicles using passive control

techniques. Nisugi et al. (2004), Beaudoin et al. (2006), Brunn and Nitsche (2006), Rouméas et al. (2009a,b), Krajnovic and Fernandes (2010) have performed studies on the flow control of ground vehicles using active control techniques. Grosche and Meier (2001) Bruneau et al. (2010) have performed studies on the flow control of ground vehicles using both active and passive control techniques at the same time.

As presented above, previous experimental studies conducted on the investigation of the flow around the Ahmed body have largely employed intrusive and single point traditional measurement techniques, for example Pitot tubes, hotwire anemometry and laser Doppler anemometry techniques. Thus, they do not reveal instantaneous spatial structures of the flows. Whereas, particle image velocimetry (PIV) technique which is employed in this study, is capable of measuring the entire flow field simultaneously, without disturbing the flow. Using PIV technique, significant advantages over other methods for examining and quantifying fluid flows is gained. When considering previous studies presented above another remarkable point ascertained is that Reynolds number employed in almost all previous studies conducted on the Ahmed body is the same. There is a little studies conducted at lower Reynolds number on the order of 10^4. At these level of Reynolds number, characteristics of flow around ground vehicles are not known thoroughly. For example, in this study, Reynolds number of the flow is nearly 80 times lower than the Reynolds number employed in the study of Ahmed et al. (1984). In fact, there is a little experimental and numerical study conducted to investigate characteristics of the flow around the Ahmed body at lower Reynolds number as aimed in the present study ($Re=1.48x10^4$).

3. MATERIAL AND METHOD

The flow around the ground vehicle is fully three-dimensional and turbulent (Hucho and Sovran, 1993). Large-scale separation and recirculation regions, a complex wake flow, long trailing vortices and the interaction of boundary layer flows on the vehicle and ground can be given as typical characteristics of flow around road vehicles. Thorough understanding of the structure of the flow around the ground vehicle is essential for the designer when developing a new road vehicle because it has strong influence on the shape of the vehicle, aerodynamic drag, fuel consumption, noise production and road handling (Robinson, 2001). Although the automotive industry has a high demand for reliable simulation methods capable of tackling the complex turbulent airflow around ground vehicles, a real-life automobile is very complex shape to model or to study experimentally. However, the simplified vehicle shape employed by Ahmed et al. (1984) retains some main features of the flow around real cars and generates fully three-dimensional regions of separated flow which may enable a better understanding of such flows (Guilmineau, 2008). The Ahmed reference model which has been used frequently as a benchmark test case for this kind of flow by other researchers has been become a generic car-type bluff body with a slant back (Hinterberger et al., 2004). The flow around the Ahmed body exhibits basic features, which are also characteristic for other bluff body vehicles, namely trucks, buses or trains: There exist large coherent vortex structures and elongated separated flow regions downstream of the Ahmed body, which give the main contributions to the drag (Ceyrowsky et al., 2009).

In this study, flow around the Ahmed body having 25^0 slant angle was investigated both experimentally and numerically. Experimental and numerical methods employed during the studies are explained in the following chapters, respectively.

3.1. Geometrical Details of the Model

The original Ahmed body used in their experiments of Ahmed et al. (1984) has dimensions of length L=1044mm, height H=288mm and width W=389mm. The length of the slant part is L_S=222mm, whatever the angle φ. The bottom surface of the Ahmed body is located at 50mm above the ground. This geometry is represented in Figure 1.1. In the present study ¼ scale Ahmed body geometry was employed as shown in Figure 3.1. The model used in our experiments was made up of a Plexiglas material.

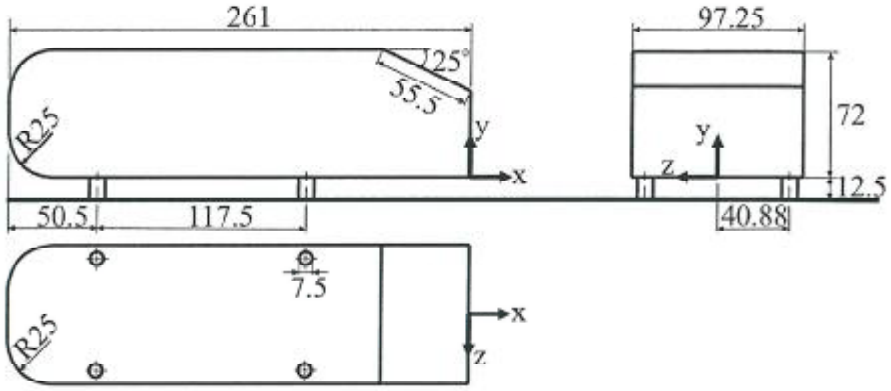

Figure 3.1. A ¼ scale Ahmed body geometry (Dimensions are in millimeter)

3.2. Experimental Methods

3.2.1. Particle Image Velocimetry (PIV) Technique

Particle Image Velocimetry (PIV) is a non-intrusive measurement technique to investigate flow structures with the aid particles inserted in the flow. The medium is seeded with some sort of tracer particles and then illuminated periodically by a high power laser light source. The idea is to obtain successive digital images from charged coupled device (CCD) cameras. These images can then be analyzed by a computer, which determines the velocities of the tracer particles, which can be used to understand the velocity of the given medium. In the PIV technique there is no need for measurement probe placed in the medium which could affect the overall

flow. PIV also can return information about the entire flow field. These are the main advantages of PIV technique over traditional techniques which use measurement probe.

When we look at the history, it is seen that quantitative flow field measurements were initially obtained in aerodynamic studies using Pitot static probes, which were suitable for measuring the time-average or low frequency response flow field properties at a single point in the flow. Hot wire anemometry proved to be a significant improvement over pitot probes by providing high frequency response velocity measurements. Adding more wires enabled multi-component flow measurements. Similar to pitot probes, hot wire anemometers were invasive and disturbed the flow field under study. The first non-invasive point velocity measurement technique was Laser Doppler Velocimetry (LDV), which used a crossed pair of laser beams to measure the velocity of seed particles entrained in the flow. Additional advantages of the LDV technique were the high frequency response and high measurement accuracy (Gürlek, 2008). According to Raffel et al. (1998) coherent structures in shear flows or wake flows are extremely unsteady, for example near- and far-wake structure formed after the Ahmed body. So, in this type of flow both spatial and temporal information of the entire flow field are required in order to capture instantaneous flow fields and thus to allow the detection of spatial structures in unsteady flows quantitatively, which is not possible with other experimental techniques. For this type of flow measurements, PIV technique is extremely convenient. This technique has the ability to achieve higher accuracy, higher spatial and temporal resolution and larger observation areas and volumes of experimental data. Hucho (1998) also indicates that the most of the velocity-measuring techniques such as LDV, hot wire anemometry, or measurements with the Pitot-static tube have the disadvantages of collecting values at one point or position at a time. Thus the determination of the velocity and turbulence characteristics of a whole flow field turns out to be a very time-consuming task. PIV technique overcomes this shortfall.

The development of PIV has begun in the eighties of the last century. The early work of Meynard (1983) established the foundations of its present form. The

theory of PIV was introduced by Adrian (1988) in the late 1980s with the first experimental implementations following shortly afterwards (Keane and Adrian, 1990, 1991). The time since then was characterized by a rapid development of hard- and software for the PIV technique. Improved cameras, lasers, optics and software lead to a significant increase in performance. The development of particle image velocimetry during the past 20 years is characterized by the fact that analog recording and evaluation techniques have been replaced by digital techniques. At present, PIV is widely used in fluid mechanics in the investigation of air and water flows. New areas of application are continuously reported (Raffel et al., 2007). Comprehensive reviews of PIV techniques were given by Rockwell and Lin (1993), Rockwell et al. (1993). Adrian (1991, 2005) and (Raffel et al., 2007).

3.2.1.1. Principles of PIV Technique

A typical setup for PIV technique is sketched briefly in Figure 3.2. The experimental setup of PIV system typically consists addition of tracer particles to the flow. A plane within the flow which is investigated is illuminated twice by means of a laser. It is assumed that the tracer particles move with local flow velocity between the two illuminations. The light scattered by the tracer particles is recorded via high performance digital cameras. The output of the digital sensor is transferred to the memory of a computer directly. For evaluation, the digital PIV recording is divided in small subareas called "interrogation areas". The local displacement vector for the images of the tracer particles of the first and second illumination is determined for each interrogation area by means of statistical methods (auto- and cross-correlation). It is assumed that all particles within one interrogation area have moved homogeneously between the two illuminations. The projection of the vector of the local flow velocity into the plane of the light sheet (two-component velocity vector) is calculated taking into account the time delay between the two illuminations and the magnification at imaging. The process of interrogation is repeated for all interrogation areas of the PIV recording (Raffel et al., 2007).

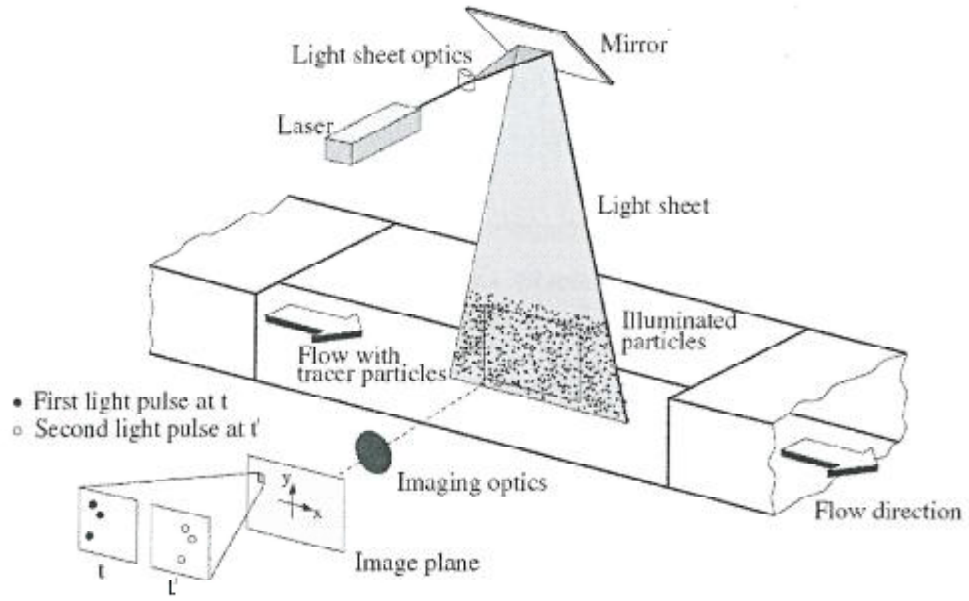

Figure 3.2. Illustration of seeding, illuminating and capturing of the image process in PIV measurement technique (Raffel et al, 2007)

A CCD (Charge Coupled Device) digital camera, a laser system, a synchronizer, a frame grabber and a computer compose the main components of the PIV system. In general, the technique of PIV contains two stages; image acquisition and image evaluation as shown in Figure 3.3. Contents of these two stages are explained in the following sections.

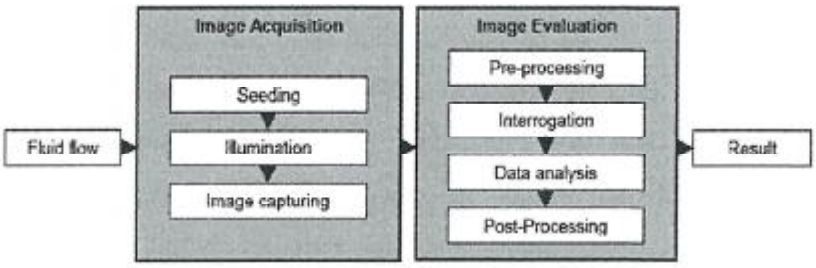

Figure 3.3. Flowchart of the PIV measurement (Tonddast-Navaei and Sharp, 2001)

3.2.1.2. Image Acquisition

3.2.1.2.(1). Particle Seeding

Partical Image Velocimetry technique essentially determines two fundamental dimensions of the flow velocity with the aid of measurements of velocity of tracer particles. Therefore, properties of the tracer particles used in the measurements are very important in PIV. These tracer particles should be carefully selected in order to avoid significant discrepancies between fluid and particle motion. The seeding particles can be seen in Figure 3.4.

Figure 3.4. Seeding particles in the water channel

Tracer particles should have a density value almost nearly the fluid in which they added. These particles should be small enough to track the flow accurately. Besides, they should be large enough to scatter sufficient light for the camera in order to be detected precisely. For water, fluorescent, polystyrene, silver-coated particles or other highly reflective particles must be used to seed the flow; while olive oil or alcohol droplets are generally used for wind tunnels.

The camera images of seeding particles should have a diameter of at least 2 pixels, preferably 3 pixels or more. This will allow the system to estimate particle positions and displacements to sub-pixel accuracy, effectively increasing the resolution of the technique. The number of the particles in the flow is also important to obtain a good signal peak in the cross-correlation. As a rule of thumb, 10 to 25 particles should be seen in each interrogation area (Karakuş, 2007).

3.2.1.2.(2). Illumination

The PIV technique can use any light source to illuminate the flow field under study. The range of potential light sources includes: continuous wave lasers, pulsed lasers, laser diodes and Xenon flash lamps. On the other hand, to obtain successful images of tracer particle in the flow, experimental system should be provided with illumination source having sufficient energy density. For the illumination, it is preferable to use a laser since the laser beam is easy to form into a sheet by a cylindrical lens. Lasers provide a highly directional, intense collimated laser beam, well suited for producing an intense light sheet down to a thickness from one-two millimetres to one centimetre. Most PIV illumination systems are based on a pulsed laser light source. Nd:YAG (Neodymium-Doped Yttrium Aluminum Garnet) lasers is the most widely used in PIV due to the high output energy (25 to 400 mJ/pulse), short pulse duration (6 to 10 ns) and 532 nm emission. The nominal pulse repetition rate of Nd:YAG lasers is 10 to 15 Hz (Gürlek, 2008).

The illumination system employed in PIV experiments should compensate the following basic criteria for the successful measurements:

- The light budget should be sufficiently high to ensure the intensity of scattered light from the seeding particles is such that images of them can be recorded on the PIV camera,
- The duration of the light pulse should be such that the particle does not move significantly during its exposure to the light-pulse,
- The time between successive light pulses should be such that the flow field does not move significantly,
- The location and dimensions of the measurement plane should be well-defined.

3.2.1.2.(3). Image Capturing

The light scattered by the tracer particles with the aid of double pulsed laser sheet is imaged and recorded by a CCD camera. The term CCD stands for charge-

coupled device. The processes of laser illumination of tracer particles and image capture are illustrated schematically in Figure 3.2. The purpose of the camera is to capture the initial and final positions of seeding particles in the flow fields and from these particle positions the displacement vector can be produced. The CCD camera comprises an array of detectors called pixels. There are several types of CCD cameras. Basically, the architecture of the CCD array influences whether the particular camera can be used for auto- or cross-correlation image capture. Historically, auto-correlation has been the most commonly used method of image capture in PIV initially because photographic film was used as an image capturing medium. Now, cameras are available which can have a very short time between double frames so cross-correlation image capture is now possible.

The laser pulse for the illumination and camera for the image capturing must be triggered with the correct sequence and timing to capture the flow field images in the right way. For that purpose, a synchronizer is employed to control all of the components which are initiated at the exact moment necessary.

3.2.1.2.(4). Image Evaluation (Correlation Process and Post Process)

In the PIV, particle images are correlated to obtain vector displacement information. Generally, there are three types of techniques used to process PIV image data: auto-correlation, cross-correlation and particle tracking. The choice of the processing technique depends primarily on the available equipment used to record the particle image data and the seed particle concentration. The recorded image frame is divided into small sub-regions, each containing particle images. By processing the image over a regular grid of small sub-regions, a velocity vector map is generated. Both auto and cross-correlation operations are implemented using Fast Fourier Transforms (FFT). Auto-correlation processing is the oldest of the PIV processing techniques. In the auto-correlation technique a single image frame is exposed multiple times and processed over a regular grid of small sub-regions, essentially due to the fact that film based recording systems were incapable of recording independent particle image records at two closely spaced instances in time.

In cross-correlation of PIV, two single exposure image frames must be recorded. The cross-correlation operation is similar to auto-correlation where again the image frames are divided into small sub-regions. However, now a sub-region from image 1 (recorded at the first laser pulse) is cross-correlated with a sub-region from image 2 (recorded at the second laser pulse). The direction of the displacement is determined unambiguously because the images from exposures 1 and 2 are recorded separately (Gürlek, 2008). The fundamental principle of Adaptive correlation is an iterative procedure: From an initial guessed offset value, an offset is introduced from the first window (the interrogation area in the image frame from laser pulse one) to the second window. The obtained vector is validated and is used as a new estimate for the window offset. A new run is made, but this time with a smaller window (interrogation area). The main benefit derived from using the shifted window is capturing the particle images that left the interrogation area during the time between the two light pulses. Loss of these particle images is known as the "in-plane dropout", which reduces signal strength and, as a result, the number of successful vectors that can be obtained. Capturing more particle images for each vector permits the interrogation area to be refined while still obtaining an adequate number of successful vectors without increasing the seeding density in the flow (Canpolat, 2008).

The post-processing of the raw velocity field involves vector validation, removal of spurious vectors, replacement of the removed vectors, and data smoothing and filtering. General procedure for the image processing is presented in Figure 3.5.

After the velocity field was calculated, the vectors were validated using CleanVec (CleanVec is a PIV vector validation program written by Ron Adrian's group in Theoretical and Applied Mechanics at the University of Illinois). It has absolute range filter, RMS tolerance filter, magnitude difference filter and quality filter methods. Three of these four filters were used for purposes of eliminating incorrect vectors. Following the process of removing incorrect vectors, a bilinear least-square fit technique was used to fill in the areas of missing vectors, scale the image field to the actual flow field, and compute the vorticity distribution. The

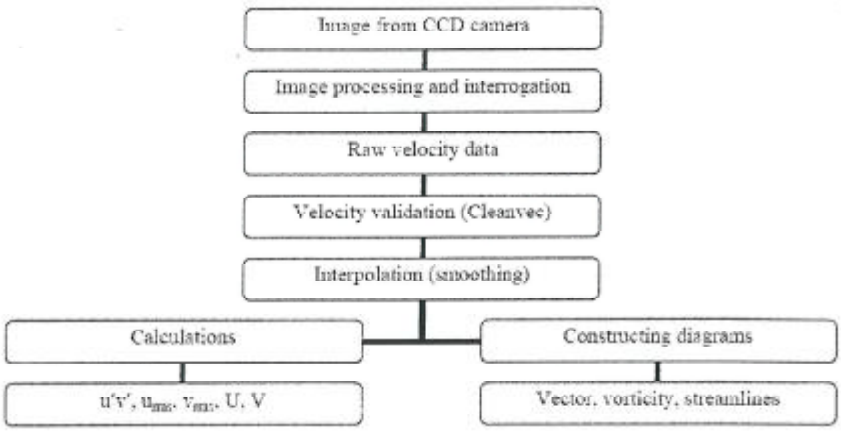

Figure 3.5. General procedure for image processing

resulting velocity field was also smoothed by using a Gaussian-weighted technique based on the work Landreth and Adrian (1989). A suggested smoothing parameter of 1.3 was used.

3.2.2. Experimental Arrangement

3.2.2.1. Water Channel System

Experiments were conducted in a recirculating, open surface water channel located in the Çukurova University Fluid Mechanics Laboratory shown in Figure 3.6. The water channel test section has a width of 1000 mm, a depth of 750 mm, and a length of 8000 mm. Side and bottom walls of the test section were equipped with 15 mm thick Plexiglas for optical access. The flow was driven by a 15 kW centrifugal pump having a variable speed controller. Before entering the test chamber, the flow passes through a settling reservoir, a honeycomb and a 2:1 contraction. The mean velocity is uniform and average turbulent intensity is less than 0.5% in an empty test section. The flow speeds vary linearly according to free stream velocity ranging from 0 to 297mm/sec and are calibrated for a test section water depth, H_w= 400mm.

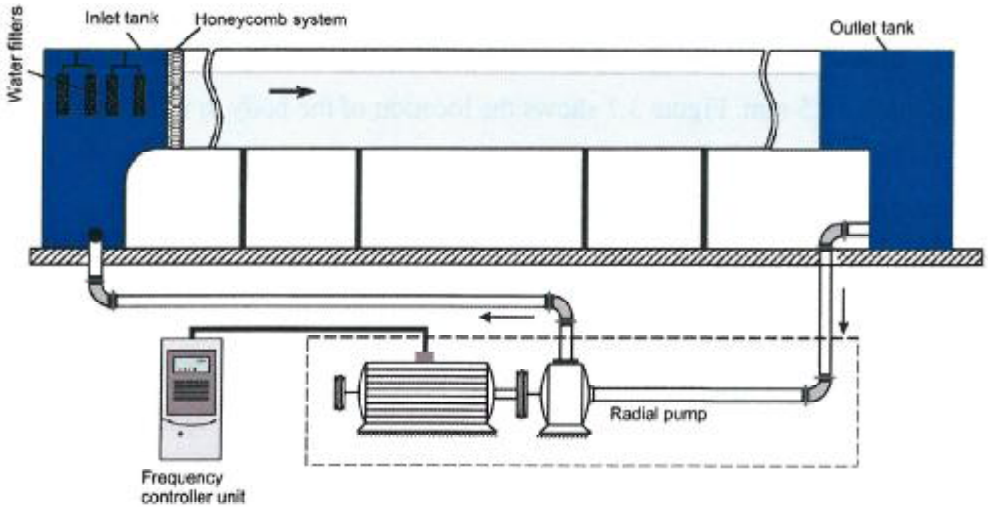

Figure 3.6. Schematic representation of water channel

The experiments were performed at a free stream velocity of U=207 mm/s which corresponds to the Reynolds number $Re_H=1.48x10^4$ based on the model height. The velocity profile and boundary conditions between the real road and the wind tunnel conditions looks different and modifies the flow field around a vehicle. One of the approaches to reproducing or simulating the road is to equip the wind tunnel with an elevated ground plate that creates a much thinner boundary layer than the wind tunnel floor (Hucho, 1998). For the present experiments, a 2 m long ground plate mounted 0.1 m above the bottom wall of the test section was used as a ground. The ground plate spans the cross section of the tunnel and has a rounded leading

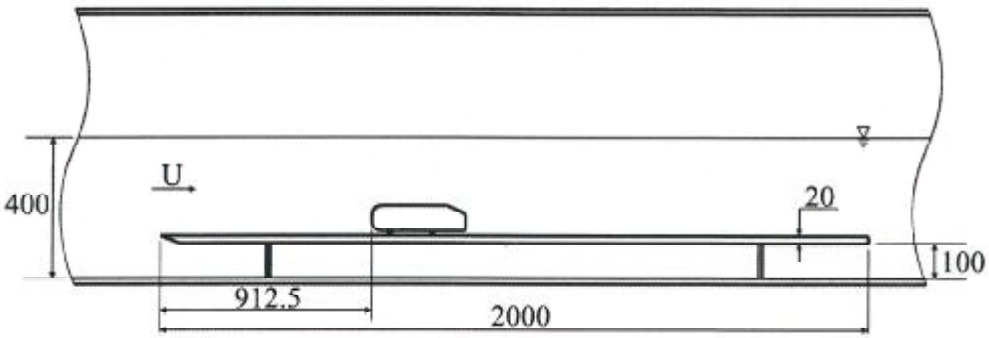

Figure 3.7. Location of the Ahmed body in the water channel (Side view, dimensions are in milimeter)

edge to avoid flow separation. During the experiments model were fixed to the ground plate. The gap between the ground plate and the bottom surface of the model was 12.5 mm. Figure 3.7 shows the location of the body in the water channel.

3.2.2.2. PIV Instrumentation

The velocity fields were measured by Dantec PIV system which consisted of a dual-head Nd:YAG laser, a high resolution CCD (Charge Coupled Device) digital camera, a synchronizer and optics. Schematic of the PIV system used in this study is shown in Figure 3.8. The measuring planes were illuminated by a thin and intense laser sheet by using a pair of double-pulsed Nd:YAG laser units each having a maximum energy output of 120 mJ/pulse at 532 wavelength. The time interval between pulses was 1.2 ms. The thickness of the laser sheet was approximately 2 mm. The time interval and the laser sheet thickness were selected such that the maximum amount of particle displacement in the interrogation window was obtained.

PIV measurements were performed at several vertical, horizontal and cross planes which were selected to highlight the aerodynamic characteristics of the models. Location of the laser sheet and the view of camera for measurement planes as well as the coordinate system are shown in Figures 3.9(a), (b) and (c). In the present study, coordinate system x, y and z are respectively the streamwise, vertical and spanwise directions. The origin of this system was located in the symmetry plane and downstream bottom edge of the models. For the side view, the laser sheet was oriented vertically, parallel to the flow direction through the center of the models as shown in Figure 3.9(a). For the end view, the laser sheet was oriented perpendicular to the flow direction, and a surface mirror was installed downstream of the models to reflect the image of the end view laser sheet to the recording CCD camera. The angle between the mirror and the free-stream was 45°. The distance between the model's base and the front edge of the mirror was kept approximately 8.5 H to eliminate the interference with the wake of the body as shown in Figure 3.9(b). For the plan view, the laser sheet was parallel to the bottom surface of the water channel and the axis of

the camera lens has a right angle intersection with the laser sheet as shown in Figure 3.9(c).

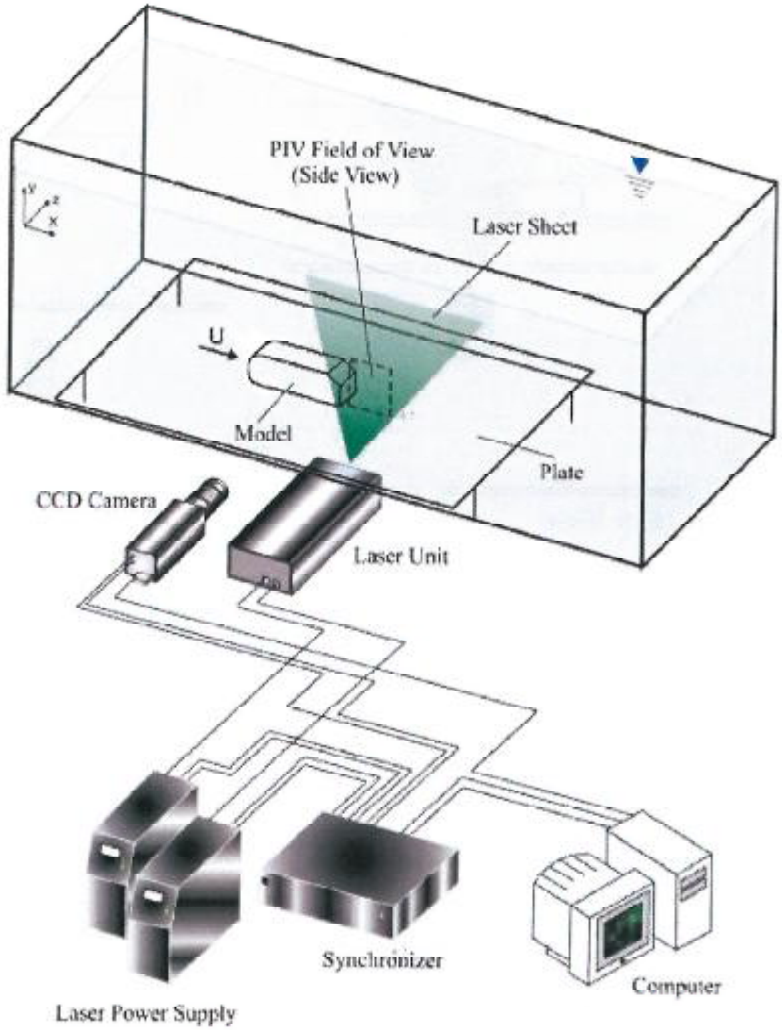

Figure 3.8. Schematic representation of the experimental setup and PIV system

In the present experiments, patterns of particle images were acquired by a model MEGAPLUS ES 1.0 8-bit series charge-coupled device (CDD) camera. The camera was equipped with a Nikon AF Micro 60 f/2.8D lens of a focal length of 60 mm. The camera was placed at right angles to the light sheet. The resolution of the CCD camera was 1008x1016 pixels for image recording. The Nd:YAG laser and CCD camera were connected using a Dantec FlowMap Processor synchronizer to control the timing of data acquisition. The flow was seeded with silver-coated spherical particles of 12 μm in average diameter. These particles are very close to

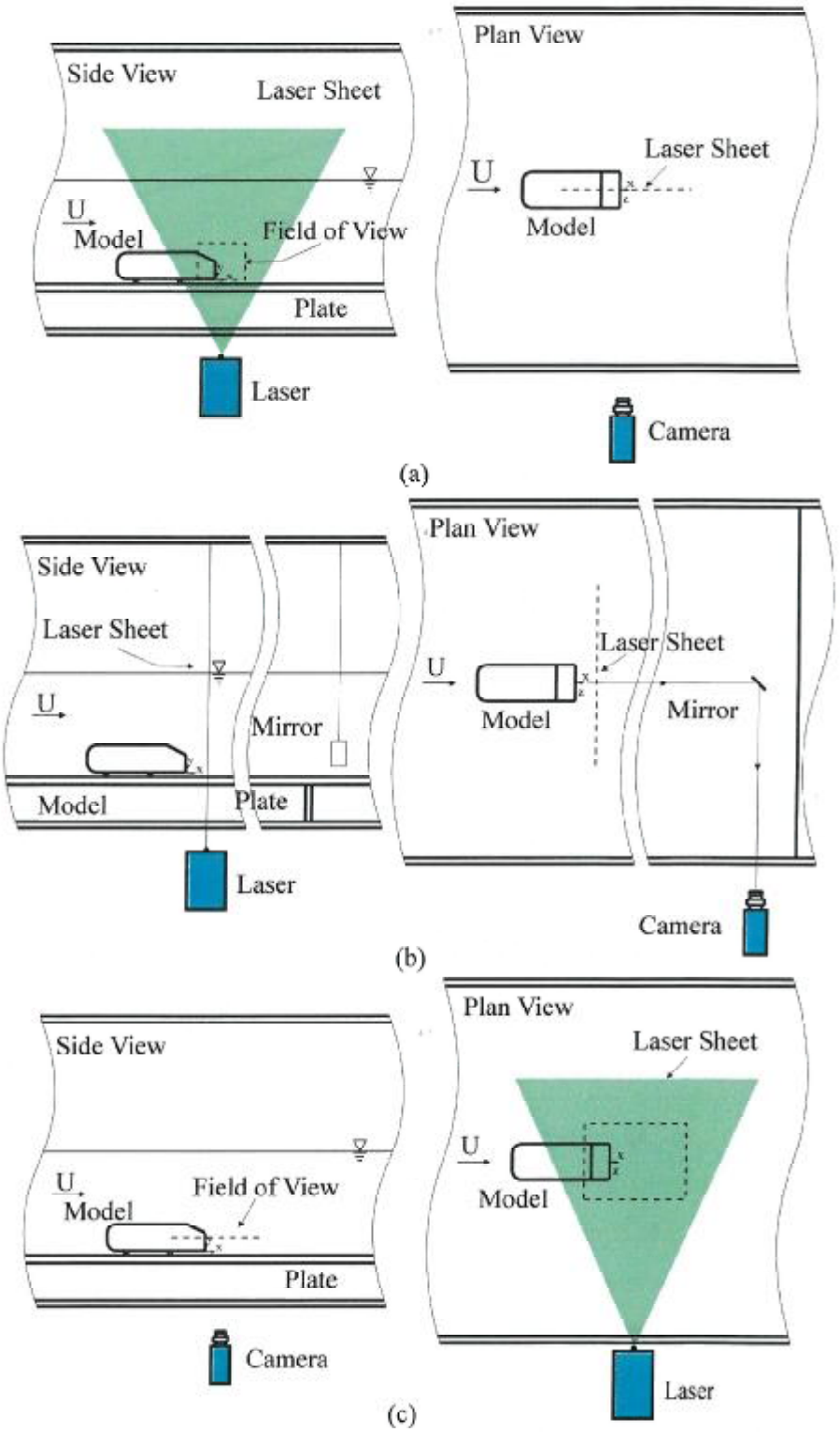

Figure 3.9. Location of the laser sheet and the view of camera for (a) side view, (b) end view, (c) plan view

being neutrally buoyant. The silver coated hollow particles were mixed in a container and poured in to the water channel. Then, the water channel was run at maximum speed for a period of several minutes in order to ensure that particles were uniformly dispersed through the water. To determine the time-averaged mean flow structure, 350 instantaneous velocity fields were recorded successively for one series of image capturing with an acquisition frequency of 15Hz for each continuous run. Instantaneous velocity vector fields were generated using adaptive correlation technique between successive particle images. The dimensions of the interrogation area employed throughout were 32x32 pixels with 50% overlap providing 3844 velocity vectors over the entire field of view plane. These instantaneous velocity fields were averaged to obtain the corresponding time-averaged patterns of vorticity $\langle w \rangle$ and streamline $\langle \psi \rangle$ topology.

3.3. Numerical Methods

According to Wesseling (2001) turbulence is a fact of nature that for sufficiently large Reynolds numbers, flows show rapid apparently random fluctuations, even when the controlling factors of the flow, such as body geometry and upstream conditions, are stationary. He stated that turbulent flow is a complicated example of a chaotic dynamical system. Irregularity or randomness, diffusivity, having large Reynolds numbers, having three dimensional vorticity fluctuations, being dissipative and continuum are given as the characteristics of turbulent flows by Tennekes and Lumely (1972). The nonlinear and stochastic properties of the turbulence remain it as the great unsolved problems of physics. However, analytical solutions to the Navier-Stokes equations exist for only the simplest flows under ideal conditions. Solutions for real fluid flow cases need a numerical approach, where the equations are replaced by algebraic approximations, which can be solved using a numerical method. Over the past thirty years, mathematical models for turbulence with varying levels of complexity have been developed. These models can be broadly categorised into four groups: Direct Numerical Simulation (DNS), Large Eddy Simulation (LES), Second-Moment

Closure and Eddy-Viscosity Models (EVM). From the mathematical models given above, only Direct Numerical Simulation calculates the flow without resorting to a numerical model. It resolves the flow to sufficiently fine detail to capture the motion of the smallest eddies and the briefest time-scales (Robinson, 2001). The computational costs of DNS can be roughly estimated based on the analysis of the physical scales involved in a fluid flow, using the concept of Kolmogorov microscales. Kolmogorov microscales are the smallest scales in turbulent flows. They are defined by

$$\text{Kolmogorov length scale } \eta = \left(\frac{\nu^3}{\varepsilon}\right)^{1/4} \tag{3.1}$$

$$\text{Kolmogorov time scale } \tau_\eta = \left(\frac{\nu}{\varepsilon}\right)^{1/2} \tag{3.2}$$

$$\text{Kolmogorov velocity scale } u_\eta = (\nu\varepsilon)^{1/4} \tag{3.3}$$

where ε is the average rate of energy dissipation per unit mass and ν is the kinematic viscosity of the fluid. In a DNS, all the spatial scales, ranging from the smallest dissipative scales (Kolmogorov microscales) to the integral scale of the flow are associated with the motions containing most of the kinetic energy and need to be resolved directly in the computational mesh. To illustrate the number of mesh points requirements of DNS, we consider an integral scale L and number of discretized points N along a given mesh direction with uniform increments h, where the resolution has to satisfy $Nh > L$ so that the integral scale is contained within the computational domain. In the meantime, $h \leq \eta$ needs to be satisfied so that the smallest dissipative scales can be resolved. Since $\varepsilon \approx u'^3/L$, where u' is the root mean square (rms) of the velocity, the previous relations imply that a three-dimensional DNS requires a number of mesh points N^3 satisfying $N^3 \geq \mathrm{Re}^{9/4}$, where $\mathrm{Re} = \frac{u'L}{\nu}$ is the turbulent Reynolds number. Therefore, the requirement for computing resources including CPU and memory storage requirement in a DNS

grows very fast with the Reynolds number due to a significant increase in the required number of mesh points (Jiang and Lai, 2009). As a result, using DNS to solve turbulent flows is too computationally expensive to simulate directly in practical engineering calculations. DNS is currently feasible for very simple geometries (pipes, channels) at moderate Reynolds numbers or complex geometries with low Reynolds number flows ($Re \approx 10^2$). In ground vehicle flow the Reynolds number is typically between $Re \approx 10^5$-10^6 and DNS cannot be used to calculate the flow at road going speeds (Robinson, 2001). Instead, the instantaneous (exact) governing equations can be time-averaged, ensemble-averaged, or otherwise manipulated to remove the small scales, resulting in a modified set of equations that are computationally less expensive to solve. However, the modified equations contain additional unknown variables, and turbulence models are needed to determine these variables in terms of known quantities. It is an unfortunate fact that no single turbulence model is universally accepted as being superior for all classes of problems. The choice of turbulence model depend on considerations such as the physics encompassed in the flow, the established practice for a specific class of problem, the level of accuracy required, the available computational resources, and the amount of time available for the simulation (Fluent User's Guide, 2006).

The complex unsteady turbulent flow characterized by eddies with a wide range of length and time scales on the slant back of the Ahmed body leads to high fluctuation intensities which are very difficult to predict. The largest eddies are typically comparable in size to the characteristic length of the mean flow. The smallest scales are responsible for the dissipation of turbulent kinetic energy. Basically, in LES, large eddies are resolved directly, while small eddies are modeled. One area of application for LES is the wake behind a three-dimensional bluff body. The physics of such a wake is not possible to predict with RANS methods because of the unsteady nature of wakes. These unsteadiness can easily be captured using the LES technique (Krajnovic and Davidson, 2000).

In the present study, the Large Eddy Simulation (LES) method has been used to investigate turbulent flow around the Ahmed body having 25° slant angle with the

aid of FLUENT package program. Details of the Large Eddy Simulation (LES) method employed in this study are given in Section 3.3.2.

3.3.1. Numerical Setup and Computational Geometry

In this study, a ¼ scaled geometry of Ahmed vehicle model was employed. The geometry of the computational domain is given in Figure 3.10. All the geometric quantities which are normalized with the body height, H=0.072 m., are as follow. The size of the computational domain in terms of body height is 29H×5H×5H. The values of the geometric quantities are L/H = 3.625, L_S/H=0.771, W/H =1.347. The radius of the front face is R/H =0.347. The channel cross section is B x F =5H x 5H (width x height). The Ahmed body is located in the channel such that the upstream length between its front face and inlet of the channel is 7.25H and the downstream length between the rear face and outlet of the channel is 18.125H. The ground clearance between the body and floor is c/H=0.174. The Reynolds number, based

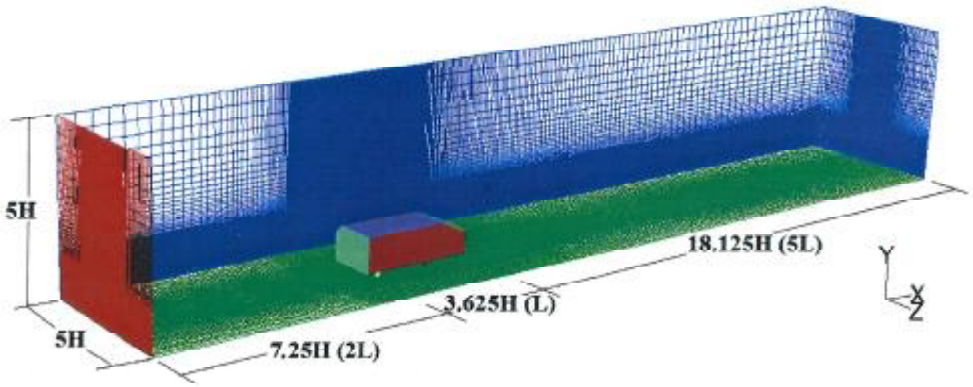

Figure 3.10. Representation of the computational domain with the Ahmed body

on the incoming velocity U=0.207 m/s and the body height H=0.072 m, is Re_H =1.5x10^4 corresponding to the Reynolds number employed in the PIV experimental studies.

Krajnovic and Davidson (2004) stated that providing the optimal structured mesh for the detailed passenger car would be quite a challenge. Our approach while constructing mesh was to concentrate most of the cells in the region around the

Ahmed body. Computational grid was contained 6573867 nodes. In Figure 3.11, structure of the computational mesh employed around the Ahmed body in view of vertical symmetry plane, z/H=0 is presented.

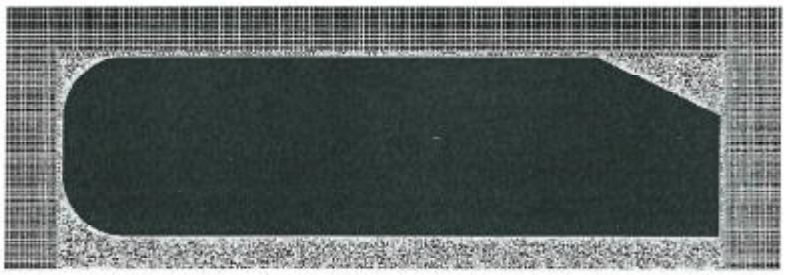

Figure 3.11. The structure of the computational mesh employed around the Ahmed body in view of symmetry plane, z/H=0

3.3.1.1. Spatial and Temporal Resolution

Flow around the ground vehicle is wall-bounded, meaning that the coherent motions in the boundary layer are responsible for the maintenance of turbulence. Krajnovic and Davidson (2004) indicated that unlike channel or the flat plate flows, flows around bluff bodies contain a number of separating regions with large coherent structures that contain much more turbulent energy than the near-wall structures. In the regions of the separated flow behind the ground vehicle, transport of momentum is dominated by large recirculating motions of the flow and the influence of the small near wall structures is limited. Thus the structures that must be resolved in this region are the smallest "large" (recirculating) structures. They concluded that, although the influence of the geometry on the flow characteristics is much larger than that of the upstream history of the flow in the case of ground vehicles, their effects cannot be neglected. Therefore the flow through the near wall region should be tried to predict as good as possible. On the other hand, the near wall coherent structures decrease in size with the Reynolds number and the task of resolving these structures is overwhelming.

For simulations of near-wall flows using LES with near-wall modelling, an important parameter is the wall unit, which is defined as

$$y^+ = \frac{u_\tau y}{\nu} \tag{3.4}$$

where the friction velocity is defined as $u_\tau = \sqrt{\tau_w / \rho}$ with τ_w standing for the wall shear stress and ρ for the fluid density, y for the distance to the nearest wall, and ν for the kinematic viscosity of the fluid (molecular viscosity). In LES, both the accuracy of the numerical scheme and the mesh size are of importance to the accuracy of the results. For a given numerical scheme, the mesh size used in a practical simulation is the major factor determining the accuracy of the results. In LES of near-wall flows, the quality of the results can exhibit a dependence on the size of mesh.

For the characterization of the mean flow field, a characteristic mean velocity U_c, a characterizing length L_c and a time scale t_c should be introduced. In this study, L_c is taken as the length of the Ahmed body, U_c is taken as the free stream velocity of the flow field and for the characteristic time $t_c = L_c/U_c$ ratio is used. Smallest dissipative micro-scales or Kolmogorov scales are given in the introduction part of this section. The length, velocity and time scales introduced by Kolmogorov are determined in such a way that they characterize that part of the spectrum of the turbulent velocity fluctuations in which the energy production of the turbulent vortices is equal to the dissipation. The characteristic turbulent eddy quantities, determined by Kolmogorov's scales of turbulence, are those that represent the viscous effects which damp the turbulent velocity fluctuations. These smallest eddies are assumed to convert the kinetic energy of turbulence into heat. The Reynolds number resulting on the basis of the micro-length scale and micro-velocity scale is, $\mathrm{Re}_K = \frac{u_K l_K}{\nu} = 1$. Another flow scales characterizing the smallest vortices of a turbulent flow can be given as the Taylor micro-scale. Taylor micro-scale defines an eddy size which is located between the smallest viscous eddies and the large eddies having quantities of the dimension of the geometric extension of the mean flow. Schematic presentation of different scales mentioned above is illustrated in Figure 3.12 (Durst, 2008).

In order to characterize the complex nature of turbulent flows, the following Reynolds numbers are employed.

$$\mathrm{Re}_K = \frac{u_K l_K}{\nu} = 1 \ , \ \mathrm{Re}_{K\varepsilon} = \frac{U_c l_K}{\nu} \ , \ \mathrm{Re}_\lambda = \frac{U_c l_T}{\nu} \tag{3.5}$$

$$\mathrm{Re}_K = \frac{U_c l_c}{\nu} = \mathrm{Re} \tag{3.6}$$

Additonally, for the relationships of the characteristic length scales, the following expression also considered.

$$\frac{l_K}{L_c} = \mathrm{Re}_L^{-3/4} = \mathrm{Re}_\lambda^{-3/2} \ , \ \frac{\lambda_T}{L_c} = \mathrm{Re}_L^{-1/2} = \mathrm{Re}_\lambda^{-1} = \left(\frac{l_K}{l_T}\right)^2 \ ,$$

$$\frac{l_K}{l_T} = \mathrm{Re}_L^{-1/4} = \mathrm{Re}_\eta^{-1} = \mathrm{Re}_\lambda^{-1/2} \tag{3.7}$$

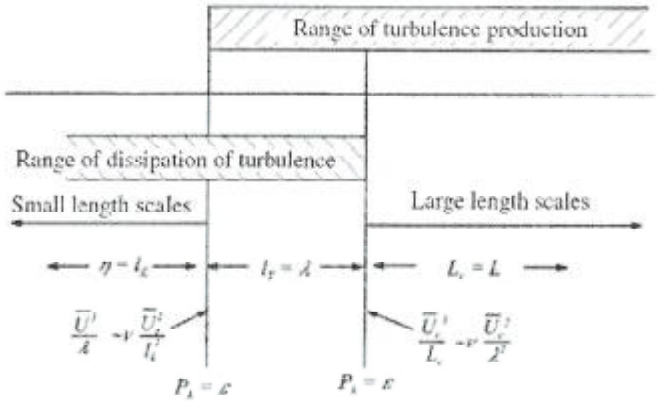

Figure 3.12. Length scales of turbulence and contributions to production and dissipation (Durst, 2008)

The above derivations indicate the differences in the structure of turbulent flows at small and high Reynolds numbers. For flows with the same integral dimensions, the flow at a large Reynolds number proves to be "micro-structured", whereas for the small Reynolds number the flow appears "macro-structured". The Taylor length scale proves always to be larger than the Kolmogorov micro length scale and the difference between them becomes larger with increasing Reynolds

number. From the above relationships, one can compute $l_T / l_K = \mathrm{Re}^{1/4}$. For a Reynolds number of approximately $Re = 10^4$, l_T is approximately 10 times larger than l_K. These relationships are often employed when considering turbulent flows, in order to carry out order of magnitude considerations regarding the characteristic properties of turbulence (Durst, 2008).

Fares (2006) summarized all relevant length and time scales associated with the flow over a vehicle. Accordingly, in the case of ground vehicles, there are several geometrical and turbulent length scales. For the flow around Ahmed vehicle model, there are mainly two geometrical length scales, the length l and the height H. The Reynolds number based on the length of the body can be crudely considered the determining parameter for the boundary layer around the vehicle whereas Reynolds number based on the height of the body describes the unsteady separation at the rear of the vehicle. In this study body height is considered to be the relevant flow feature. Similarly, he treated the flow in the underbody region as a channel flow with the determining characteristic integral length as the ground clearance, g. The flow over the cylinder type stilts are characterized accordingly by the diameter, d. He also referred flow dependent turbulent length scales as follow. Turbulent boundary layer thickness at the end of the vehicle is estimated using the 1/7th wall law $\delta/l \approx 0.37\mathrm{Re}_l^{-0.2}$, the wall unit $y^+ = 1$ as a measure for the viscous boundary sublayer at the end of the vehicle $y_{y^+}/l \approx 5.9\mathrm{Re}_l^{-0.9}$, the Taylor microscale associated with the integral motions in the wake estimated similar to $\lambda_H/H \approx 5.5\mathrm{Re}_H^{-0.5}$ and the Kolmogorov length scale describing the smallest turbulent scales of the wake $\eta_H/H \approx 1.2\mathrm{Re}_H^{-0.75}$. Table 4.1 summarizes the length scales revealed in the present simulation.

Davidson (2011) indicated that large scale eddies extract kinetic energy from the mean flow. The kinetic energy of the large scales is lost to slightly smaller scales with which the large scales interact. Through the *cascade process* the kinetic energy is in this way transferred from the largest scale to the smallest scales. At the smallest scales the frictional forces (viscous stresses) become large and the kinetic energy is transformed (dissipated) into thermal energy. The smallest scales where dissipation occurs are called the Kolmogorov scales. It is often convenient to use Fourier series

to analyze turbulence. The spectrum of kinetic energy of turbulent flow is illustrated in Figure 3.13. Davidson (2011) have made following explanations for regions I, II and III in Figure 3.13.

I. In region I: the large eddies exist and they carry most of the energy. These eddies interact with the mean flow and extract energy from the mean flow. The energy of the largest eddies is transferred to slightly smaller scales. In this region, velocity and length scales of eddies are denoted by U_e and L_e, respectively.

II. Inertial subrange: The existence of this region requires that the Reynolds number is high (fully turbulent flow). This region is a "transport region" (in wavenumber space i.e.) in the cascade process. Energy per time unit, $P^k = \varepsilon$, is coming from the large eddies at the lower part of this range and is given off to the dissipation range at the higher part (note that the relation $P^k = \varepsilon$ is given by the concept of the cascade process). One can argue that the eddies in this region

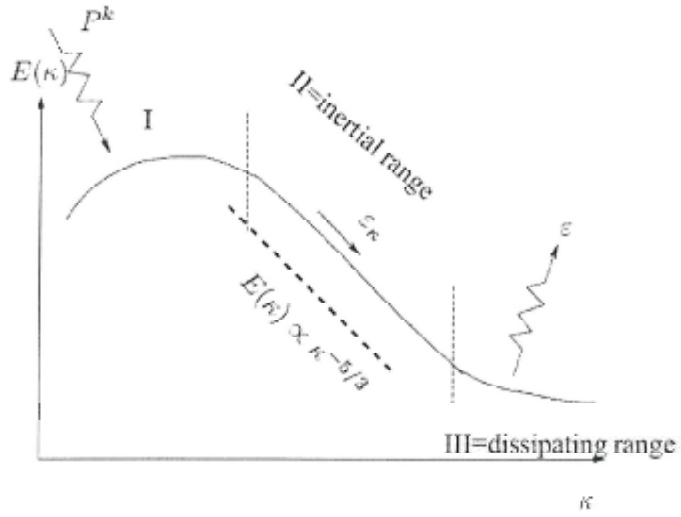

Figure 3.13. Spectrum for turbulent kinetic energy, k. I: Range for the large, energy containing eddies. II: the inertial subrange. III: Range for small, isotropic scales (Davidson, 2011)

should be characterized by the spectral transfer of energy (ε) and the size of the eddies $1/\kappa$. By using dimensional analysis, we get $E(\kappa) = \text{const.}\varepsilon^{2/3}\kappa^{-5/3}$. This is a very important law (Kolmogorov spectrum law or the -5/3 law) which states that, if the flow is fully turbulent (high Reynolds number), the energy spectra should exhibit

a −5/3-decay in the inertial region. Above it is assumed that the small eddies are *isotropic*. In the inertial subrange region, it is found that the ratio of the velocity, length and time scales of the energy-containing eddies to the Kolmogorov eddies increases with increasing Reynolds number. This means that the eddy range (wave number range) of the intermediate region, (region II, the inertial region), increases with increasing Reynolds number. Hence, the larger the Reynolds number, the larger the wave number range of the intermediate range where the eddies are independent of both the large scales and the viscosity.

III. Dissipation range: In this region eddies are small and isotropic and dissipation occurs. The scales of the eddies formed in this region are described by the Kolmogorov scales.

Pope (2000) suggests that a grid that can resolve 80 % of the turbulent energy everywhere in the domain including the viscous wall region is needed for LES with wall resolution. On the other hand, Davidson (2009) presented that the energy spectra is not a good measure of LES resolution; neither is the ratio of the resolved turbulent kinetic energy to the total one (i.e. resolved plus modelled turbulent kinetic energy). He suggested that two-point correlations are the best measures for estimating LES resolution.

The smallest timescale associated with turbulence can be approximated based on the Kolmogorov timescale $\Delta t_k \sim (H/U)Re_H^{-0.5}$, where Re_H represents the Reynolds number based on the characteristic velocity U and the characteristic length, H (Fares, 2006). The corresponding maximum timestep size in this study associated with Kolmogorov timescale is 2.86×10^{-3} second. The time step employed in this sudy was 1×10^{-3} second. Numerical time steps in LES are short to retain accuracy. The short time steps lead to large number of time steps for resolving the low frequency events and the time averaging. Krajnovic and Davidson (2004) indicated that the number of time steps required for resolving the low frequency events is larger than that needed for obtaining of the time-averaged results. They used the symmetry of the flow around the symmetry plane as an indication for the proof of long enough averaging time. This approach was adopted in the present study.

3.3.1.2. Boundary and Initial Conditions

In this work, a uniform velocity profile constant in time, $U_0 = 0.207$ m/s with a zero turbulence rate, was used as the inlet boundary condition. The level of turbulence at the inflow boundaries is assumed to be negligible. Therefore, fluctuating velocity components of the flow at the inlet boundaries are neglected and individual instantaneous velocity components are simply set equal to their mean velocity counterparts. At the outlet, where the diffusion fluxes for all flow variables in the exit direction are zero, outflow boundary condition was employed. Walls of the ground vehicle and lateral and bottom (ground) walls of the channel were treated as no-slip surfaces. Upper surface of the channel were treated as symmetry boundary condition.

Krajnovic and Davidson (2004) stated that the results of LES are dependent on the time where it is started to monitor results. The initial fully developed flow is often computed from a previous solution of RANS simulation as did in the present study.

3.3.1.3. Reynolds number dependence

Krajnovic and Davidson (2004) presented two main findings for the flow around ground vehicles. First findings can be stated as the geometry of the model rather than the upstream flow defines the structure of flow in the wake and second one can be stated as the magnitude of the Reynolds number is less important for the recirculating flow in the wake than for the boundary layer. According to these evaluations, we have attempted to reduce the Reynolds number in the present LES to obtain a flow similar to that obtained in the experiments conducted at higher Reynolds number. Additionally, reducing the Reynolds number makes it easier to resolve coherent structures exist around ground vehicle. Furthermore, Rodi et al (1997) presented results from the simulations of flow around the cube with ground effect at two different Reynolds numbers, 3000 and 40000, based on the incoming velocity and cube height. They found a great similarity in the results for these two

flows. Time-averaged coherent structures had almost identical shapes and sizes in the two flows. Thus it seems likely that the qualitative knowledge about the flow around a three dimensional bluff bodies (such as a car) can be extracted from the flow at lower Reynolds number (Krajnovic and Davidson, 2002).

3.3.2. Large Eddy Simulation

In a highly turbulent flow it is possible to categorize the eddies into two classes with distinct characteristics. Firstly, there are the large eddies which contain most of the energy, interact with the mean flow, are diffusive, anisotropic, long-lived, inhomogeneous, ordered, dependent on boundaries and difficult to model analytically. Secondly, there are small eddies which are dissipative, isotropic, short-lived, homogeneous, random and lend themselves to theoretical modelling. The structure of the small eddies is to a large extent independent of the particular geometry at hand, and largely universal. Therefore there is some hope of obtaining a universal model for the small eddies, but this matter is still not completely settled (Wesseling, 2001). A reasonable approach would therefore be to calculate only the large eddies in the flow and to model the effects of the small eddies in order to diminish the demands put on computer resources. This method is known as Large Eddy Simulation (LES).

In Large Eddy Simulation (LES) method, large eddies are explicitly computed (resolved) in a time-dependent simulation using the "filtered" Navier-Stokes equations. The rationale behind LES is that by modeling less of turbulence (and resolving more), the error introduced by turbulence modeling can be reduced. It is also believed to be easier to find a "universal" model for the small scales, since they tend to be more isotropic and less affected by the macroscopic features like boundary conditions, than the large eddies. Filtering procedure of governing equation is essentially a mathematical manipulation of the exact Navier-Stokes equations to remove the eddies that are smaller than the size of the filter, which is usually taken as the mesh size when spatial filtering is employed. Like Reynolds-averaging, the

filtering process creates additional unknown terms that must be modeled to achieve closure (Fluent User's Guide, 2006).

There are two major steps involved in the LES analysis: filtering and subgrid scale modeling. Traditionally, filtering is carried out using the box function, Gaussian function, or Fourier cutoff function. Subgrid modeling includes eddy viscosity model, structure function model, dynamic model, scale similarity model, and mixed model, among others (Chung, 2002).

3.3.2.1. Filtered Navier-Stokes Equations

The governing equations employed for LES are obtained by filtering the time-dependent Navier-Stokes equations. The filtering process effectively filters out the eddies whose scales are smaller than the filter width or grid spacing used in the computations. The resulting equations thus govern the dynamics of large eddies. A filtered variable (denoted by an overbar) is defined by

$$\bar{\phi}(x) = \int_D \phi(x')G(x,x')dx' \tag{3.12}$$

where D is the fluid domain, and G is the filter function that determines the scale of the resolved eddies.

The finite-volume discretization itself implicitly provides the filtering operation:

$$\bar{\phi}(x) = \frac{1}{V}\int_V \phi(x')dx', \qquad x' \in V \tag{3.13}$$

where V is the volume of a computational cell. The filter function, G(x,x') implied here is then

$$G(x,x') = \begin{cases} 1/V & \text{for } x' \in V \\ 0 & \text{otherwise} \end{cases} \tag{3.14}$$

Filtering the incompressible continuity and Navier-Stokes equations, one obtains

$$\frac{\partial \bar{u}_i}{\partial x_i} = 0 \tag{3.15}$$

and

$$\frac{\partial \bar{u}_i}{\partial t} + \frac{\partial}{\partial x_j}\left(\bar{u}_i \bar{u}_j\right) = -\frac{1}{\rho}\frac{\partial \bar{p}}{\partial x_i} + \nu \frac{\partial^2 \bar{u}_i}{\partial x_j \partial x_j} - \frac{\partial \tau_{ij}}{\partial x_j} \tag{3.16}$$

where τ_{ij} is the subgrid-scale stress defined by

$$\tau_{ij} \equiv \rho\overline{u_i u_j} - \rho\bar{u}_i \bar{u}_j \tag{3.17}$$

3.3.2.2. Subgrid-Scale Models

The subgrid-scale stresses resulting from the filtering operation are unknown, and require modeling. The majority of subgrid-scale models in use today are eddy viscosity models of the following form:

$$\tau_{ij} - \frac{1}{3}\tau_{kk}\delta_{ij} = -2\mu_t \bar{S}_{ij} \tag{3.18}$$

where μ_t is the subgrid-scale turbulent viscosity, The isotropic part of the subgrid-scale stresses τ_{kk} is not modeled, but added to the filtered static pressure term and $\bar{S}_{ij}$ is the rate-of-strain tensor for the resolved scale defined by

$$\overline{S_{ij}} = \frac{1}{2}\left(\frac{\partial \bar{u}_i}{\partial x_j} + \frac{\partial \bar{u}_j}{\partial x_i}\right) \tag{3.19}$$

In the present study, the Smagorinsky-Lilly model is employed for the calculation of μ_t.

3.3.2.2(1) Smagorinsky-Lilly Model

This simple model was first proposed by Smagorinsky (1963). In this model, the eddy viscosity is modelled by

$$\mu_t = \rho L_s^2 \left|\bar{S}\right| \tag{3.20}$$

where L_s is the mixing length for subgrid scales and $\left|\bar{S}\right| \equiv \sqrt{2\bar{S}_{ij}\bar{S}_{ij}}$. L_s is computed using

$$L_s = \min(\kappa\, d, C_s V^{1/3}) \tag{3.21}$$

where $\kappa = 0.42$, d is the distance to the closest wall, and V is the volume of the computational cell. The value of C_s=0.1 is used in the simulations.

3.3.3. Numerical Implementation

In the present study, governing integral equations for the conservation of mass and momentum were discretized using finite control volume method. Continuity and momentum equations in integral form can be given as follows, respectively:

$$\frac{\partial}{\partial t}\int_V dV + \int_A U_i dA_i = 0 \tag{3.22}$$

$$\underbrace{\frac{\partial}{\partial t}\int_V \rho U_j dV}_{\text{I}} + \underbrace{\int_A \rho U_i U_j dA_i}_{\text{II}} = \underbrace{-\int_A P dA_j}_{\text{III}} \underbrace{-\int_A \tau_{ij} dF_i}_{\text{IV}} + \underbrace{\int_V \rho g_j dV}_{\text{V}} + \underbrace{\sum F_j}_{\text{VI}} \tag{3.23}$$

Physical meanings of terms in Equation (3.23) are stated as follow:

I: Temporal change of the *j* momentum in the interior of a control volume.

II: Sum of inflows and outflows of flow momentum per unit time in the direction *j* summed up over the entire surface surrounding the considered control volume. The momentum over $i = 1, 2, 3$ represents this.

III: Resulting pressure force in the direction *j*, obtained by integration over the entire *j* components of the surface elements surrounding the considered control volume.

IV: Sum of the *j* momentum inflows and outflows occurring per unit time by molecular momentum transport over the entire surface of the control volume. The double index *i* expresses the summation over 1, 2, 3.

V: The *j* component of the mass force acting on the control volume.

VI: Sum of all external (not fluid mechanically induced) forces acting in the *j* direction on the boundaries of the control volume (Durst, 2008).

Finite volume method consists of: *i*) Division of the domain into discrete control volumes using a computational grid, *ii*) Integration of the governing equations on the individual control volumes to construct algebraic equations for the discrete dependent variables such as velocities, pressure, and conserved scalars, *iii*) Linearization of the discretized equations and solution of the resultant linear equation system to yield updated values of the dependent variables (Fluent User's Guide, 2006).

The numerical method employed to linearize and solve the discretized governing integral equations was rely on the pressure-based segregated algorithm. In this algorithm the momentum and continuity equations are solved sequentially wherein the constraint of mass conservation (continuity) of the velocity field is achieved by solving a pressure correction equation. The pressure equation is derived

from the continuity and the momentum equations in such a way that the velocity field, corrected by the pressure, satisfies the continuity. The SIMPLEC (Semi-Implicit Method for Pressure-Linked Equations-Consistent) algorithm was used for introducing pressure into the continuity equation. In simulations, a co-located scheme was used, whereby pressure and velocity are both stored at cell centres. PRESTO (PREssure STaggering Option) pressure interpolation scheme was used to compute required face values of pressure from the cell values. In simulations, face values of scalars required for the convection terms in the discretized governing equation were interpolated from the discrete values of the scalar stored at the cell centers. This was accomplished by using a Bounded Central Differencing Scheme. The gradients of the flow variables at cell faces are computed by using node based Green-Gauss theorem, when discreatizing secondary diffusion terms and velocity derivatives in the flow conservation equations. The time derivative was discretized using the second-order discretization implicitly. A point implicit (Gauss-Seidel) linear equation solver was used in conjunction with an Algebraic Multigrid (AMG) method to solve the resultant scalar system of equations for the dependent variable in each cell.

4. RESULTS AND DISCUSSIONS

In this study, flow around the Ahmed body (Ahmed et al., 1984) having 25° slant angle was analyzed using both experimental and numerical methods which are particle image velocimetry (PIV) and Large Eddy Simulation (LES) methods, respectively. The numerical simulations were run on 8 number 2.8 GHz Xeon CPU workstation under Windows 7. Experimental measurements were conducted in a recirculating, open surface water channel located in the Çukurova University Fluid Mechanics Laboratory.

This section presents comparison of the mean and turbulent quantities of the present LES calculation results and PIV measurement results with some open literature data at different locations over the slant, in the wake and at the front part of the Ahmed body. The Reynolds number based on the body heights, H and the free stream velocity, U was about $Re_H=1.48x10^4$. Experimental and numerical investigations were performed at several vertical, horizontal and cross planes at the rear and front part of the body which were selected to highlight the aerodynamic characteristics of the model. These PIV measurements were; at z/H=0, 0.34, -0.34 in the vertical planes (side-view planes, xy-planes); at elevations of y/H=0, 0.07, 0.14, 0.35, 0.67, 0.78, 0.89 and 1.00 in the horizontal planes (plan-view planes, xz-planes); at x/H=-0.70, -0.56, -0.42, -0.28, -0.14, 0, 0.21, 0.28, 0.35, 0.70, 1.04, 1.39, 1.74, 2.08 and 2.43 locations in the cross planes (end-view planes, yz-planes). Figure 4.1 shows the PIV measurement planes. In addition to the PIV measurements, numerical solution of the flow with the aid of Large Eddy Simulation (LES) method were also carried out and numerical results corresponding to the experimental measurement planes were presented. The PIV and LES results provided instantaneous and time averaged velocity vector maps, vorticity contours, streamline topology and turbulence characteristics of the flow. Most of the features of the flow around the generic Ahmed body were predicted, such as the formation of trailing vortices, separation and circulatory flows.

Various visualization techniques (Krajnovic and Davidson, 2000) were used throughout the study. These are: 1- streamlines 2- vorticity contours, 3- velocity

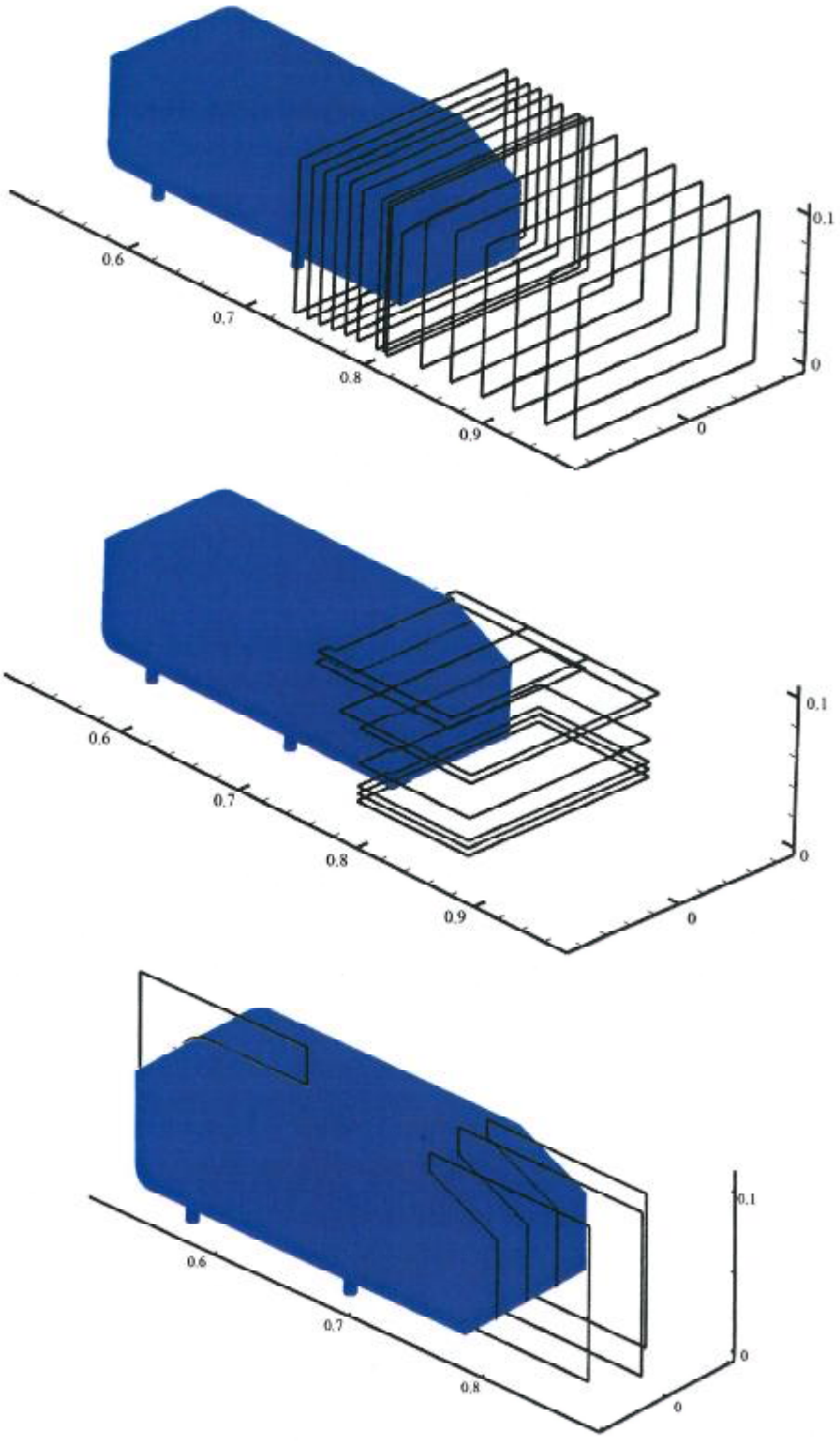

Figure 4.1. PIV measurement planes

vectors, 4- contours of pressure coefficient and surface pressure, 5- iso-surfaces of second invariant of the velocity gradient, Q defined as

$$Q = -\frac{1}{2}\frac{\partial \bar{u}_i}{\partial x_j}\frac{\partial \bar{u}_j}{\partial x_i} \tag{4.1}$$

and 6- trace lines.

Streamlines are used to visualize separations and re-attachments in the mean in front of, on the top of, at the lateral sides and behind the Ahmed body. Velocity vector planes and iso-surfaces of second invariant of the velocity gradient are used in identifying the coherent structures. Contours of pressure coefficient are also useful in visualizing large-scale coherent structures.

Since the formulation of the governing equations is fully implicit, there is no stability criterion that needs to be met in determining time step, Δt. However, to model transient phenomena properly, it is necessary to set Δt accordingly. A good way to judge the choice of Δt is to observe the number of iterations needed by the solver to converge at each time step. The ideal number of iterations per time step is 5-10 (Fluent User's Guide, 2006). In this study, number of iterations needed by the solver to converge at each time step was between 8-10 and time step was $1x10^{-3}$ second. On the other hand, as explained in section 3, the smallest timescale associated with turbulence can be approximated based on the Kolmogorov timescale $\Delta t_k \sim (H/U)Re_H^{-0.5}$, where Re_H represents the Reynolds number based on the characteristic velocity U and the characteristic length, H (Fares, 2006). The corresponding maximum time-step size in this study associated with Kolmogorov timescale is $2.86x10^{-3}$ second. The time step employed in this study was $1x10^{-3}$ second. Additionally, to check the convenience of time step, contours of the cell Courant number on the model is plotted in Figure 4.2. In this figure, maximum value of cell Courant number is about 3. According to the Fluent User's Guide (2006), for a stable, efficient calculation, the Courant number should not exceed a value of 20-40

in most sensitive transient regions of the domain. Therefore time step size used throughout the simulation can be considered as suitable.

Krajnovic and Davidson (2004) stated that time used for the averaging of the solution must be sufficiently long to produce the mean solution that is not a function of time. This can be a problem in LES where the size of the time step in the simulations is limited by the stability requirements and the resolution in time. They recommended to use some kind of test to find out if the averaging time was sufficient in the simulations. In their studies, they used the symmetry of the flow around a symmetry plane (z/H=0 plane) as a proof of long enough averaging time. The averaging time, tU_∞/H, in our simulation was 66.13 (185000 time steps). This time interval is equal the time interval used in our PIV experiments and its much larger than the one used in the study of Krajnovic and Davidson (2004).

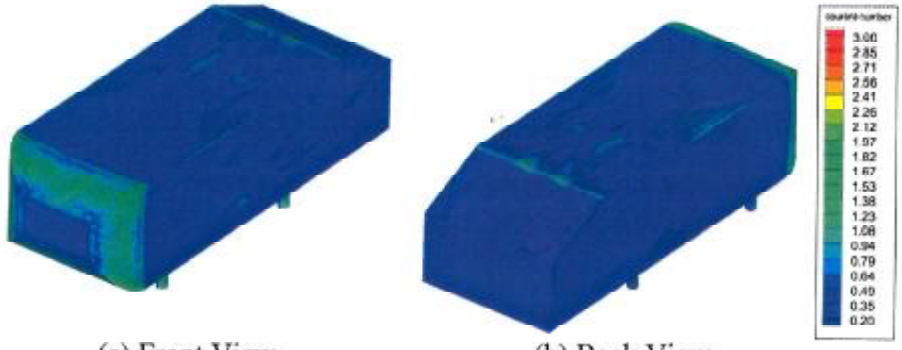

(a) Front View (b) Back View

Figure 4.2. Contours of the cell Courant number on the Ahmed body

For simulations of near-wall flows using LES with near-wall modelling, an important parameter is the wall unit, y^+. Details and formulations of y^+ are given in section 3. In this study, the spatial resolution has a resolution of $y^+<6.6$ in the wall normal direction as shown in Figure 4.3.

For the characterization of the mean flow field, all relevant characteristic length scales associated with the flow over the Ahmed body should be introduced. According to Fares (2006), in the case of ground vehicles, there are several geometrical and turbulent length scales. For the flow around Ahmed body, there are mainly two geometrical length scales, the length (L) and the height (H). Similarly, he

treated the flow in the under-body region as a channel flow with the determining characteristic integral length as the ground clearance (g). The flow over the cylinder

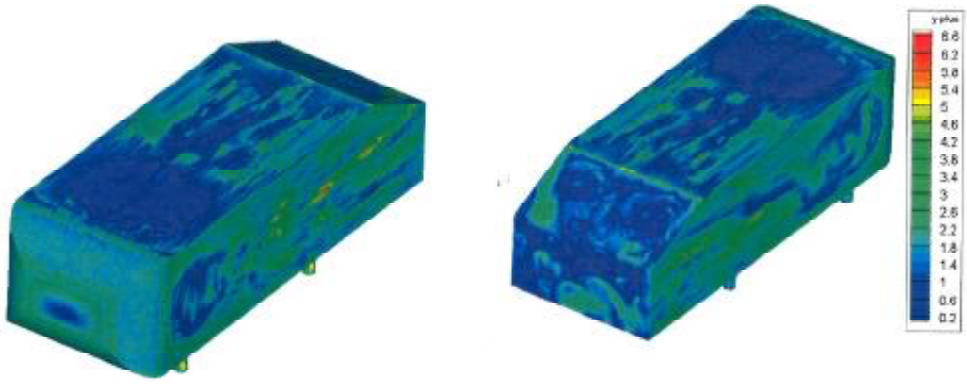

(a) Front View (b) Back View

Figure 4.3. Contours of the dimensionless wall unit (y^+)values on the Ahmed body

type stilts are characterized accordingly by the diameter (d). He also referred flow dependent turbulent length scales as follow. The wall unit $y^+ = 1$ as a measure for the viscous boundary sublayer, the Taylor microscale associated with the integral motions in the wake and the Kolmogorov length scale describing the smallest turbulent scales of the wake. In Table 4.1, relevant length scales of this simulation are summarized. In the present study, approximate maximum and minimum cell distance normalized with body height are $3.30x10^{-1}$ and $9.14x10^{-4}$, respectively.

Table 4.1. Selected approximate length scales of the simulation compared to the body height, H.

l/H	g/H	d/H	λ_H/H	η_H/H
3.625	0.174	0.104	$4.52x10^{-2}$	$8.93x10^{-4}$

For bluff bodies drag is mainly caused by pressure drag in contrast to streamlined bodies. According to the Ahmed et al. (1984), in some vehicle configurations, more than 75% of the pressure drag is due solely to the averaged force applied on the rear part of the model while only 9% is due to the force

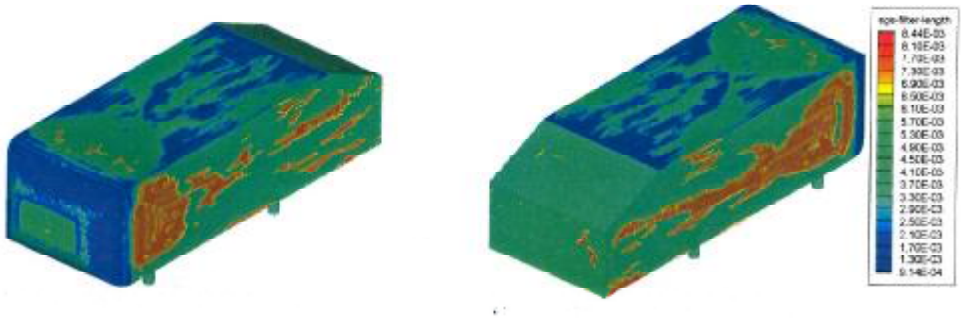

(a) Front View (b) Back View

Figure 4.4. Contours of values of the subgrid-scale filter length of cells on the wall of the Ahmed body

applied on the fore-body. Clearly, a more exact simulation of the wake flow and of the separation process is essential for the accuracy of drag predictions. Therefore, in this study, we have mainly emphasized on the investigation of the flow characteristics at back of the ground vehicle model. With this in mind, comparison of our LES results and the experimental data for the flow around the rear part of the body is essential.

The number of investigations conducting on the flow characteristics at the front of the Ahmed body is relatively low by comparing the number of investigations conducting on the flow characteristics at the rear and wake of the Ahmed body. Ahmed et al. (1984) who conducted pioneer work on the Ahmed body stated that the interference between the rear end and the fore body flow is weak. They also declared that this could be a consequence of the relatively long midsection of Ahmed body. This statement of Ahmed et al. (1984) may be given as reason for the low number of studies conducted on the front of the Ahmed body in the previous literature. Four descriptions of the front part of the flow are given by Spohn and Gillieron (2002), Krajnovic and Davidson (2005), Franck and d'Elia (2004) and Minguez et al. (2008). Experimental study of Spohn and Gillieron (2002) and numerical study of Krajnovic and Davidson (2005) at lower Reynolds number ($Re=8.3x10^3$ and $Re=2x10^5$, respectively) and numerical studies of Franck Franck and d'Elia (2004) and Minguez et al. (2008) at higher Reynolds number ($Re=4.25x10^6$, $Re=7.68x10^5$) have recovered these recirculations on the front part of the body. They also observed

similar recirculation regions on the lateral sides of the front part. Spohn and Gillieron (2002) investigated the flow at a Reynolds number of $8.3x10^3$, based on the incoming velocity and the height of the body, which is close to the Reynolds number employed in our study. They found that the flow separates at the leading edge, forming vortical structures similar to Kelvin-Helmholtz vortices with their axes parallel to the separation line on the leading edge of the front of the body. Numerical study of Krajnovic and Davidson (2005), which is conducted at a Reynolds number of $2x10^5$, shown that the instantaneous vortices formed on the upper front surface of the Ahmed body are more of the hairpin-like type. Instantaneous vortices they found do not extend between the two foci as found in the study of Spohn and Gillieron (2002). Franck and d'Elia (2004) observed that there are detachments on the curved surfaces at the front part as well as on the intersection between front and top middle surfaces. In their observation, the transversal Kelvin-Helmholtz vortices are convected downstream from the front side and converted into the hairpin vortices. On the other hand, in the work of Minguez et al. (2008), flow separations and then reattachments on the leading edge of the body front were observed. Minguez et al. (2008) stated that occurrence of thin bubble on the front part of the body at Re=768000 remains an open question and may be artifact of the numerical computations. They also emphasized on the fact that most of the studies conducted on the investigation of flow through the Ahmed body only focus on the slant part and on the near wake of the bluff body and consequently do not provide any available data for the upstream flow. Therefore, to identify the structure and formation mechanism of recirculation region at the front of the body, detailed discussion of the present numerical and experimental results at the front of the body is also performed.

4.1. TIME-AVERAGED VELOCITY FIELD

4.1.1. Flow Structures at the Front Part of the Ahmed Body

Time-averaged velocity vectors map <V>, the patterns of streamlines <ψ> and the corresponding vorticity contours <ω> at the front part of the Ahmed body in the vertical plane for z/H=0 are presented in Figure 4.1.1. In the figures, minimum and incremental values of the vorticity contours are $<\omega_{min}> = \pm 2s^{-1}$ and $<\Delta\omega> = 2s^{-1}$. Contours of positive and negative vorticity are indicated by solid and dashed lines. In this work, focus, saddle points, node, negative and positive bifurcation lines are designated as F, SP, N and NBL and PBL respectively. "S" and "U" notations used in front of the focus and node representations also means "stable" and "unstable" respectively. In velocity vectors maps <V> shown in Figure 4.1.1, the magnitude of velocity vectors can be observed to have decreased gradually as the free-stream flow approaches to the model, hence a stagnation point appears almost at the central point of the model in both numerical and experimental results. Additionally, division of approaching flow into two main flow streams in which one part of the flow is oriented towards the bottom surface and the other part towards the roof surface of the model is evidenced in the time-averaged patterns of streamlines as the free-stream flow get close to the front surface of the model. The division of the flow starts from the half-saddle point of attachment, S_{ab} is indicated by a small arrow in Figure 4.1.1, and located on the upstream surface of the model.

The upper part of the flow is separated after the rounded part of the front face, thereby a separated flow region is formed. Distance of the separation point from the frontal leading edge on the upper surface of the body is founded to be x/H=0.167 in numerical computations and x/H=0.108 in experimental measurements. Dimensions of the separated flow region estimated by numerical investigation are much larger than the ones measured in the experimental investigations. The differences in dimensions of the separated flow region on the roof surface of the model obtained by the experimental measurements are resulted from the insufficient laser sheet, which is essential for the accurate measurement, due to the thick Plexiglas material used to

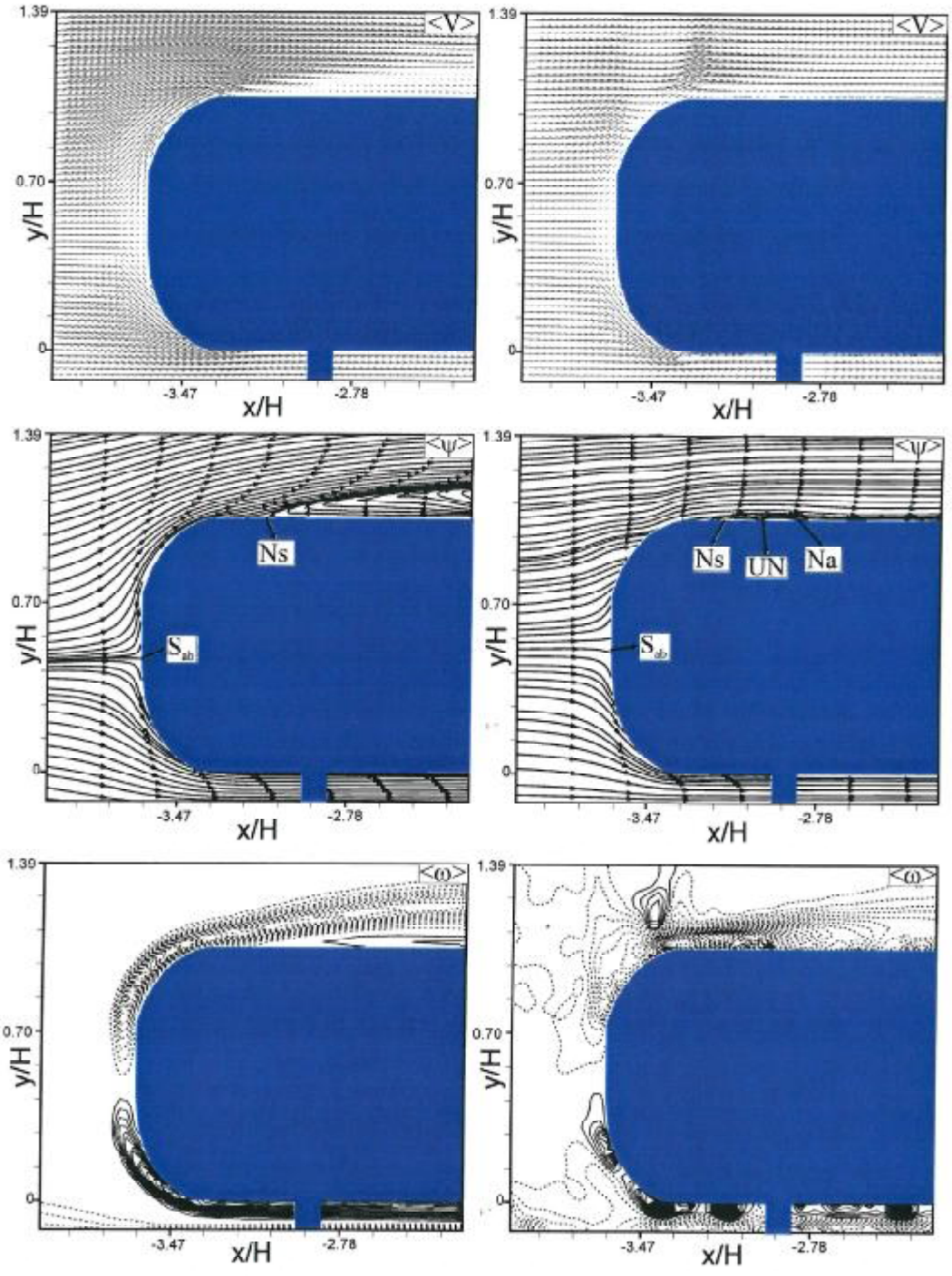

Numerical Experimental

Figure 4.1.1. Patterns of time-averaged velocity vectors map <V>, streamlines <ψ> and vorticity contours <ω> in the vertical symmetry plane z/H=0. Minimum and incremental values of vorticity are $<\omega_{min}>=\pm 2s^{-1}$ and $\Delta<\omega>=2s^{-1}$, respectively

construct model vehicle. In the experimental measurements, patterns of streamlines along the vertical symmetry plane indicate an unstable node occurring on the roof surface of the model at a distance x/H=0.274 from the frontal leading edge of the body. Similar unstable node is observed on the roof surface of the body in the numerical computations, but its location is at a distance of x/H=1.316 away from the frontal leading edge of the body. Its dimensions are somewhat larger than the one in experimental measurements as shown in Figure 4.1.9. However, the leading–edge shear layer reattach to the model roof surface at a point x/H=1.815 and 0.426 away from the frontal leading edge in numerical investigations and experimental measurements, respectively. Similar separated flow structures experimentally at a Reynolds number of $8x10^3$ based on the height of the model were reported by Spohn and Gillieron (2002). Although there are very limited number of experimental investigations on the characteristics of the flow around the front part of the Ahmed body, it is reasonable to expect that the separation region at the front part of the model becomes thinner as the Reynolds number is increased. Krajnovic and Davidson (2004) state that character of the flow (i.e. attached or detached) around the front part of the body depends on the Reynolds number and the curvature of the front of the body. Normally the lower the Reynolds number, the rounder leading edge is needed to prevent the separation. In our study, while the curvature of the front of the body is the same with the one employed in the study of Krajnovic and Davidson (2004), Reynolds number employed is around 13 times lower than the Reynolds number employed in their study. Large separation region estimated in our numerical investigation on the roof surface of the model also correspond to the findings of Krajnovic and Davidson (2004).

Figure 4.1.2 presents the patterns of time-averaged streamlines $\langle\psi\rangle$ obtained by numerical calculations in the horizontal xz-plane for y/H=-0.17, y/H=-0.09, y/H=0, y/H=0.35, y/H=0.67, y/H=0.78, y/H=0.89 and y/H=1.0 . In Figure 4.1.2 (a), (b) and (c), flow structures under the Ahmed body for horizontal xz-planes y/H=-0.17, y/II=-0.09, y/II=0 are shown. Various types of flow structures are observed in the plane y/H=-0.17. There are two unstable nodes one of which is at the front part of the body, and the other one is at the back of the body. In addition, there are saddle

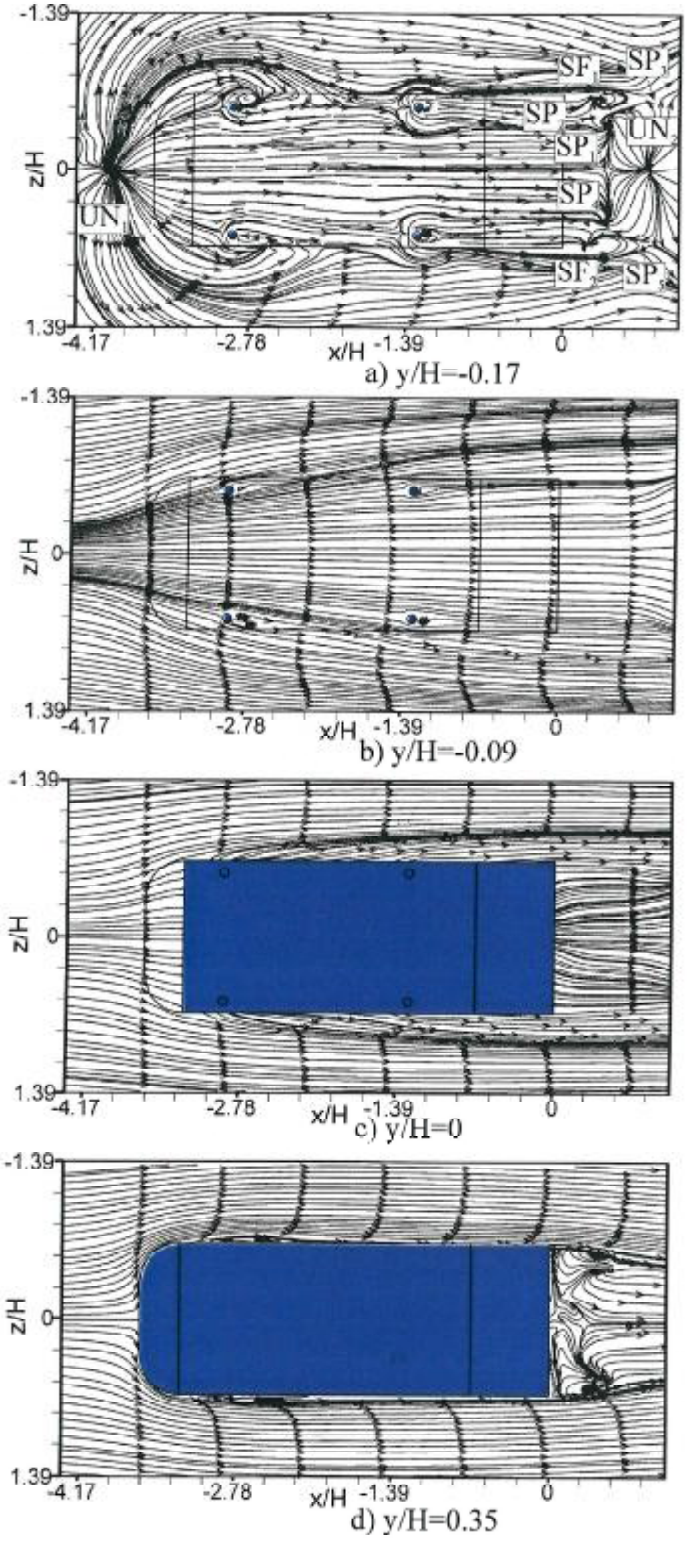

Figure 4.1.2. Patterns of time-averaged streamlines <ψ> obtained from numerical calculations in the horizontal xz-plane for different positions of y/H

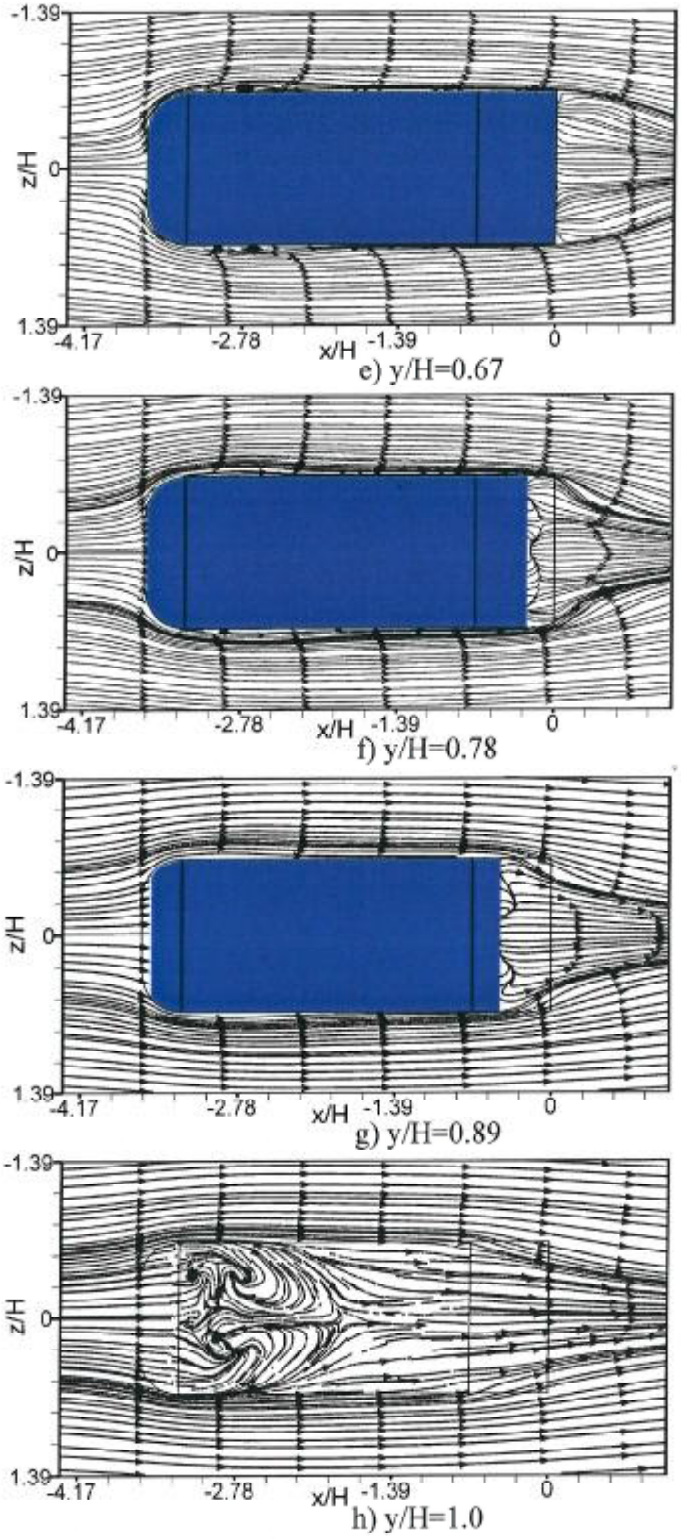

Figure 4.1.2. Patterns of time-averaged streamlines <ψ> obtained from numerical calculations in the horizontal xz-plane for different positions of y/H (Continued)

part of the body, and the other one is at the back of the body. In addition, there are saddle points just at the front of these unstable nodes. As shown in figures, the model stands on stilts. Flow structures formed around these stilts are similar to the flow structures formed around cylinder. Similarly, there is one saddle point at the front of the stilt and a recirculation region at the back of the stilt. This flow situation is valid for all stilts of the model. Flow coming from upstream shows vortex structure similar to the horse shoe vortex just at the front region of the model. Horse shoe type vortex structures at the front of the model can also be observed with the aid of iso-surfaces of second invariant of the velocity gradient presented in Figure 4.2.10. Stable focus and saddle point pairs are also observed at each lateral side of the body, symmetrically, on the bottom surface of the near wake region of the body. As the observation level increases under the body, complex flow structures seen on the bottom surface become to disappear. Upstream flow coming at the front part of the body spread out towards the lateral side of the body as a result of separations occurred around the stilts. Additionally, on each lateral side of the body, separated flow regions are observed as shown in Figures 4.1.2 (d), (e) and (f). Length of the separated flow region observed on the lateral sides of the body decreases as the observation level increases. In Figures 4.1.2 (g) and (h), this separated flow regions observed on the lateral surfaces disappear, and complex flow structures are observed on the upper surface of the body.

Figures 4.1.3 to 4.1.6 display the patterns of time-averaged velocity vectors map $\langle V \rangle$, streamlines $\langle \psi \rangle$ and the corresponding vorticity contours $\langle \omega \rangle$ obtained by numerical computations in the transversal yz planes for x/H=-3.63, x/H=-3.53, x/H=-3.28, x/H=-2.93, x/H=-2.58, x/H=-2.24, x/H=-1.54, x/H=-0.85. In Figure 4.1.3, one unstable node which is almost at the center of the vertical front face of the model vehicle and four positive bifurcation lines which move from the center of the vertical front face to the corners of the body are observed. In the velocity vectors map, we can detect that the velocity of the flow becomes minimum at the region about the unstable node and half stagnation point. In addition, magnitude of the velocity vectors increases in the direction of the upper, lower and lateral sides of the body. In Figure 4.1.3, no separation point is observed on the vertical and rounded

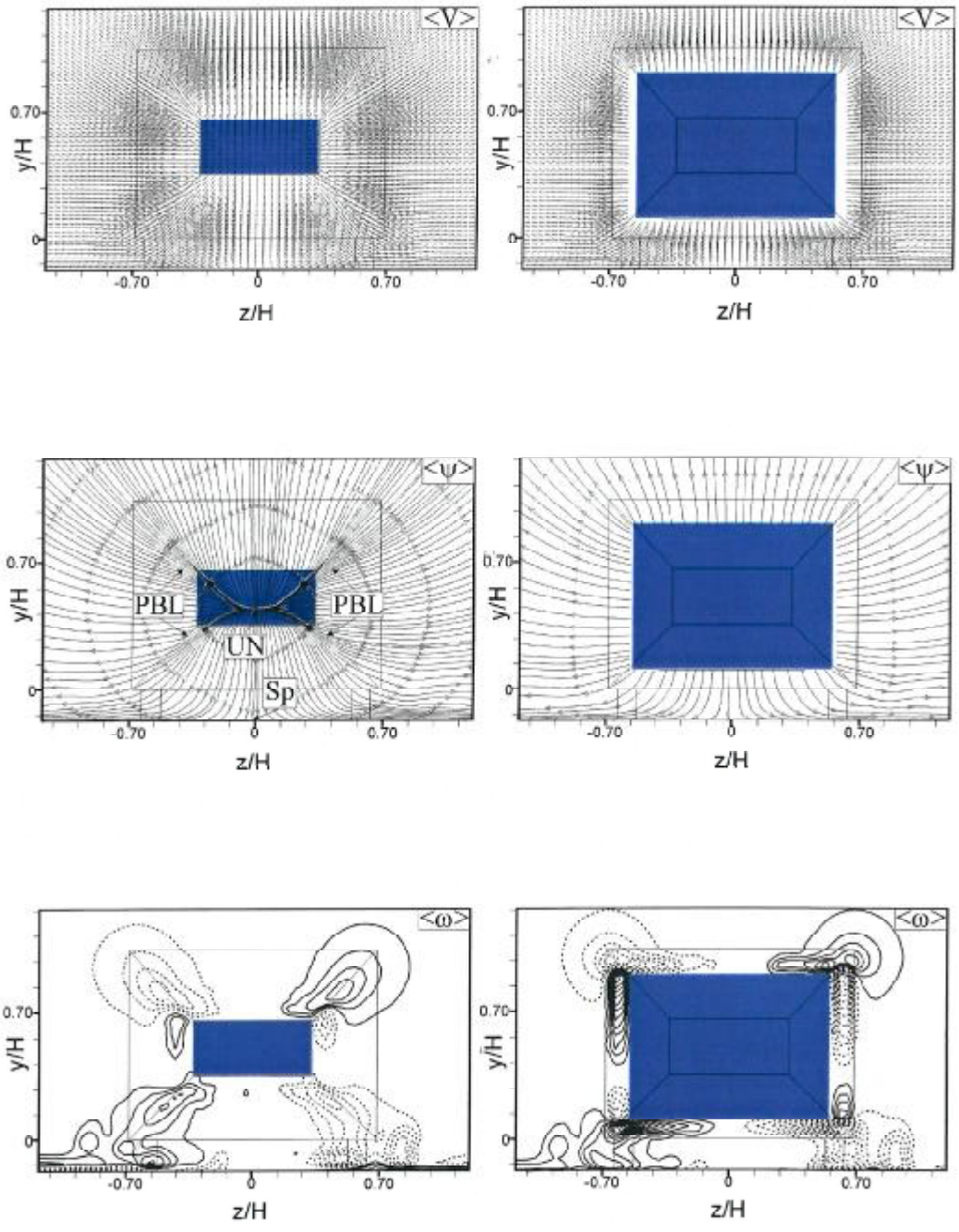

x/H=-3.63 x/H=-3.53

Figure 4.1.3. Patterns of time-averaged velocity vectors map <V>, streamlines <ψ> and vorticity contours <ω> in the transversal yz-planes for x/H=-3.63 and -3.53. Minimum and incremental values of vorticity are $<\omega_{min}>=\pm 2s^{-1}$ and $\Delta<\omega>=2s^{-1}$, respectively

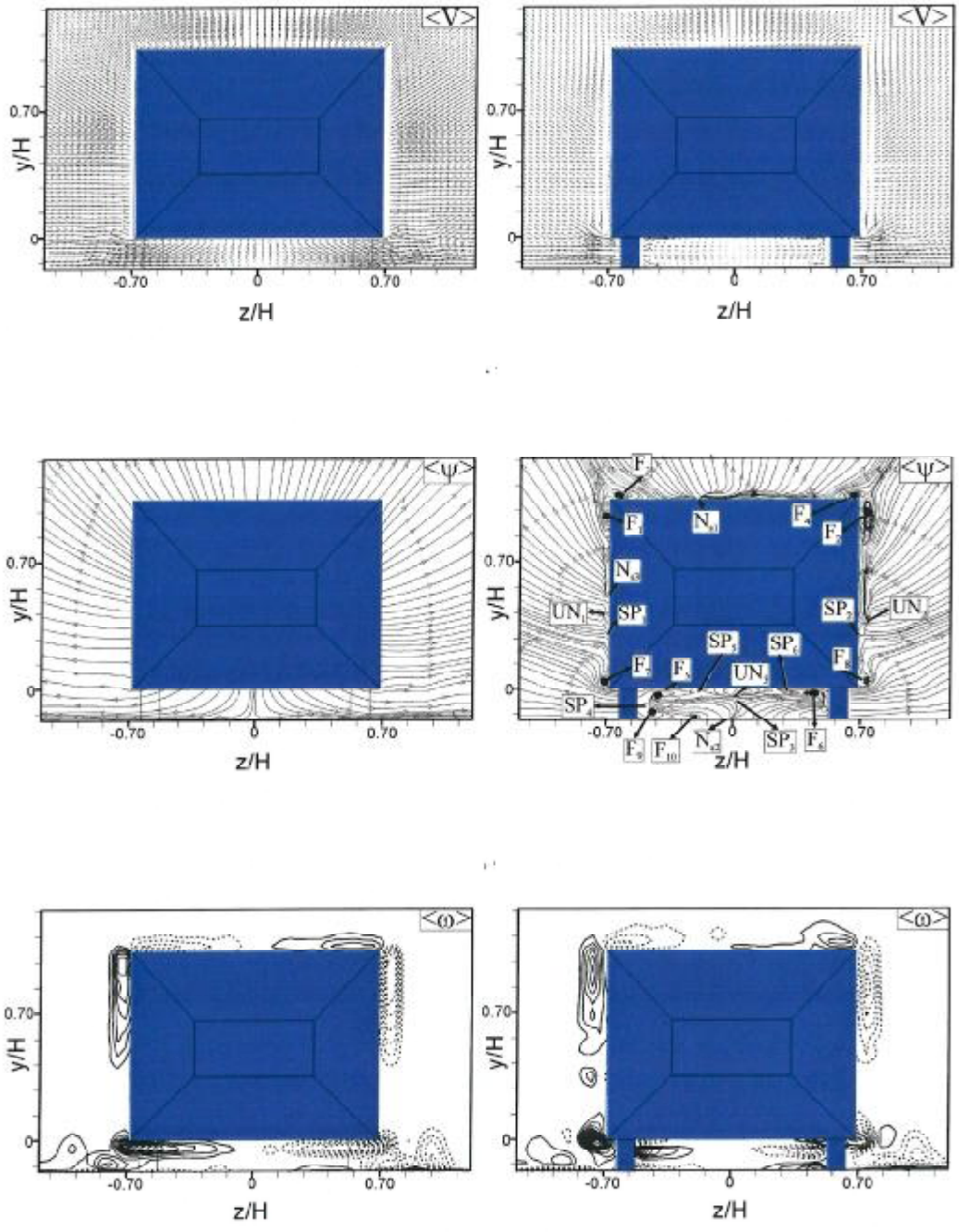

x/H=-3.28 x/H=-2.93

Figure 4.1.4. Patterns of time-averaged velocity vectors map <V>, streamlines <ψ> and vorticity contours <ω> in the transversal yz-planes for x/H=-3.28 and -2.93. Minimum and incremental values of vorticity are $<\omega_{min}>=\pm 2s^{-1}$ and $\Delta<\omega>=2s^{-1}$, respectively

part of the front surface of the model vehicle. Front-view figures of the upper, lower and lateral surfaces starts with Figure 4.1.4. In this figure, there is highly uniform flow structures at the plane of x/H=-3.28 where the leading edge of the upper, lower and lateral surface exist. The magnitude of the velocity vectors in the plane is almost the same and varied uniformly except at the critical points. On the other hand, if we consider other plane at a downstream x/H=-2.93, we can see that flow becomes very complex and unstable.

In general, two trailing vortices are formed at each side of the upper lateral edges of the body. One of them is on the horizontal (roof) side of the edge and the other is on the vertical side of the edge. These trailing vortices are first seen on the transversal plane x/H=-2.93. Trailing vortices, on the upper (roof) surfaces, are seemed to have disappeared after a distance of x/H=-2.24. Their positions vary with the condition of the flow as shown in Figures 4.1.4 and 4.1.5. Nodes, N_1 and N_2, develop symmetrically in the vicinity of both lateral sides, which means that upstream flow diverges at this point. Furthermore, incoming flow passing through the underbody and flow comes from these nodes form free shear layers at the lower part of both lateral surfaces. Another pair of trailing vortices is also developed around each lower lateral edge of the body. Due to the small gap between the body and ground, the size of the vortices on the under-body side is lower than those on the lateral sides. The right hand side and left hand side vortices on the lower lateral sides rotate counter-clockwise and clockwise, respectively. The flow at the bottom of the model vehicle can be considered to be fully three dimensional because of the complex flow developed. Flow incoming underbody diverges at the saddle point, SP_3 and move in both directions of the lateral surfaces of the body. In addition, throughout the gaps under the model in the stream-wise direction, the flow is complex and three dimensional. On the upper surface of the model, separated flow region is also observed in the transversal direction. Boundary of this separated flow region can also be seen in Figure 4.1.13 presented as a three dimensional view.

Further downstream of the flow, in Figures 4.1.5 and 4.1.6, development of the flow formed around the Ahmed body are shown in the transversal yz-planes at distances of x/H=-2.58, x/H=-2.24, x/H=-1.54 and x/H=-0.85 in the flow direction. In

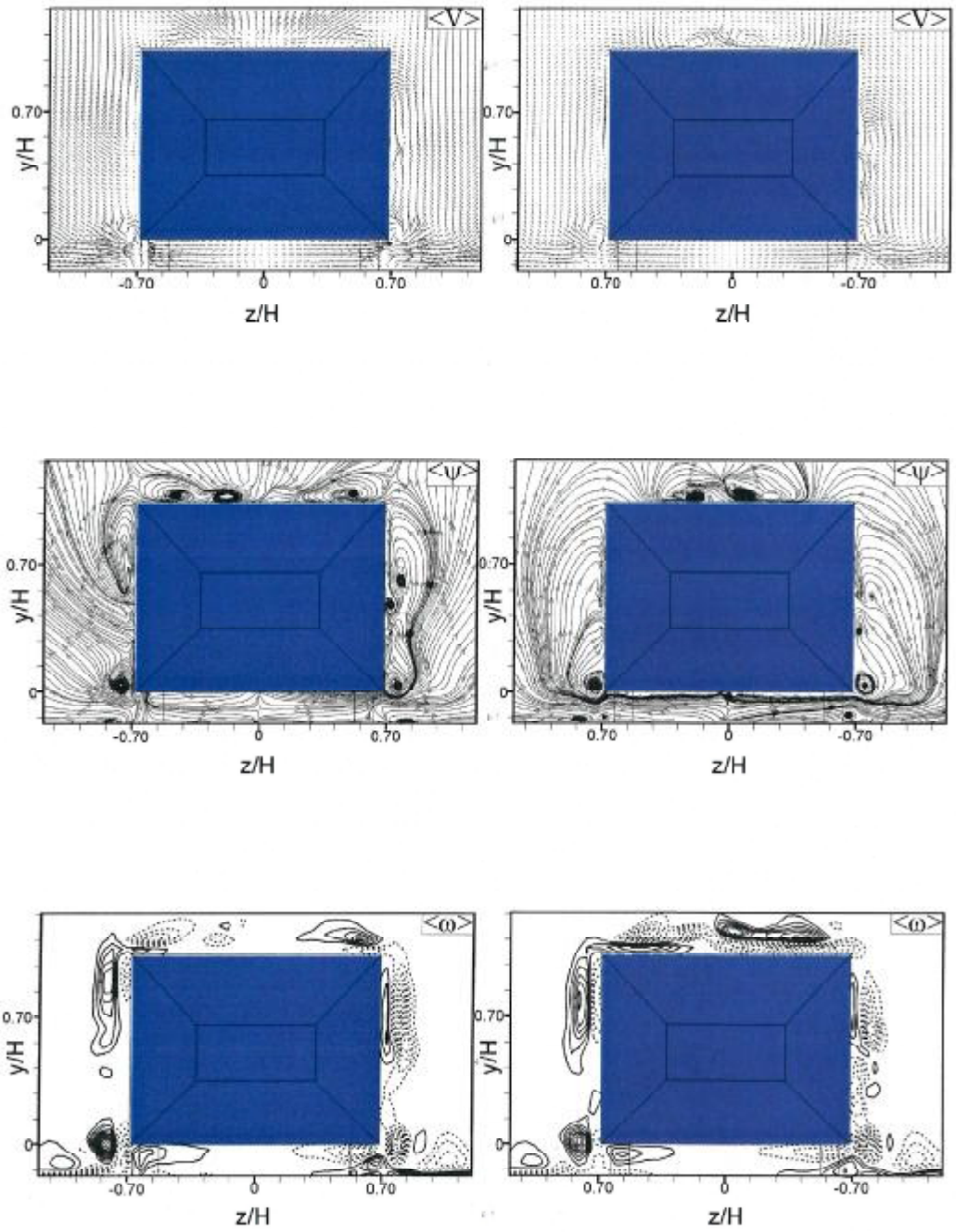

Figure 4.1.5. Patterns of time-averaged velocity vectors map <V>, streamlines <ψ> and vorticity contours <ω> in the transversal yz-plane for x/H=-2.58 and -2.24. Minimum and incremental values of vorticity are $<\omega_{min}>=\pm 2s^{-1}$ and $\Delta<\omega>=2s^{-1}$, respectively

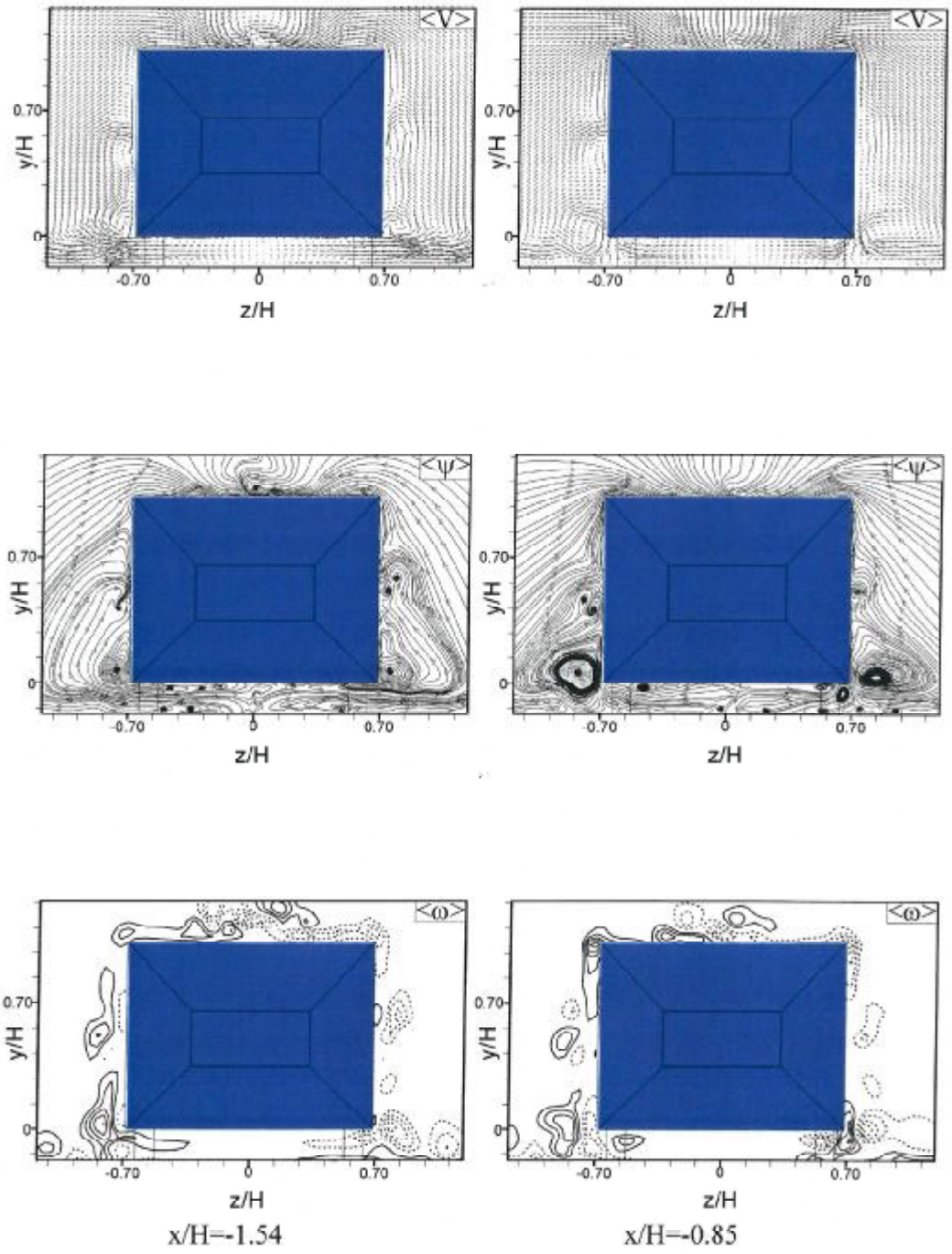

Figure 4.1.6. Patterns of time-averaged velocity vectors map <V>, streamlines <ψ> and vorticity contours <ω> in the cross yz-planes for x/H=-1.54 and -0.85. Minimum and incremental values of vorticity are $<\omega_{min}>=\pm 2s^{-1}$ and $\Delta<\omega>=2s^{-1}$, respectively

these figures, the domain of the trailing vortices situated on the upper part of the lateral surfaces becomes lower and they move downward. They are finally combined with other trailing vortices at the lower part of the lateral surfaces. On the other hand, the size of vortices at the lower part of the lateral surfaces becomes bigger and bigger as the flow goes down and reaches its highest value at x/H=-0.85. Flow stream which comes from the underbody becomes dominant on the lateral surfaces of the model. Furthermore, span-wise length of the separated flow region on the upper part of the model first enlarges and then shrinks in size after a distance of x/H=-2.58. Similarly, Spohn and Gillieron (2002) observed these vortices in a vertical transversal plane at a distance of 70 mm (x/H=-2.74) downstream of the frontal face of the Ahmed body. Vortical structures developed on the upper part of the model seem to have disappeared at the transversal plane x/H=-0.85.

Time-averaged velocity patterns obtained by using LES computations and PIV measurements in vertical symmetry plane, z/H=0 at the front face of the Ahmed body are presented in Figures 4.1.7 and 4.1.8. In the figures, time-averaged normalized velocity profiles at the front face of the model for positions between x/H=-3.889 and x/H=-2.361, where space difference between the two profiles is $\Delta x/H=0.139$, are presented. Here, velocity components are normalized with the free stream velocity, U. Figure 4.1.7 shows the stream-wise velocity profiles, $\langle u \rangle/U$ and Figure 4.1.8 shows the normal velocity profiles, $\langle v \rangle/U$. In these figures, all velocity profiles results of the LES calculation are in good agreement with the PIV experimental data at almost all positions at the front face of the model except at the separated flow region occurred on the roof surface. In Figure 4.1.7, the velocity profiles of the flow coming from upstream start to deteriorate as they approach the body. The rate of decrease in magnitude of the stream-wise velocity approaching the model is due to the stagnation point occurred at the front face of the body. Due to this stagnation point, one part of the flow is oriented towards the bottom surface, and the other part is oriented towards the roof surface of the model. Stream-wise velocity results of PIV measurements on the upper surface of the body show negative values only at x/H=-3.056, which means that PIV can measure the separated flow as a small region nearly at a position just after the frontal leading edge of the body in the

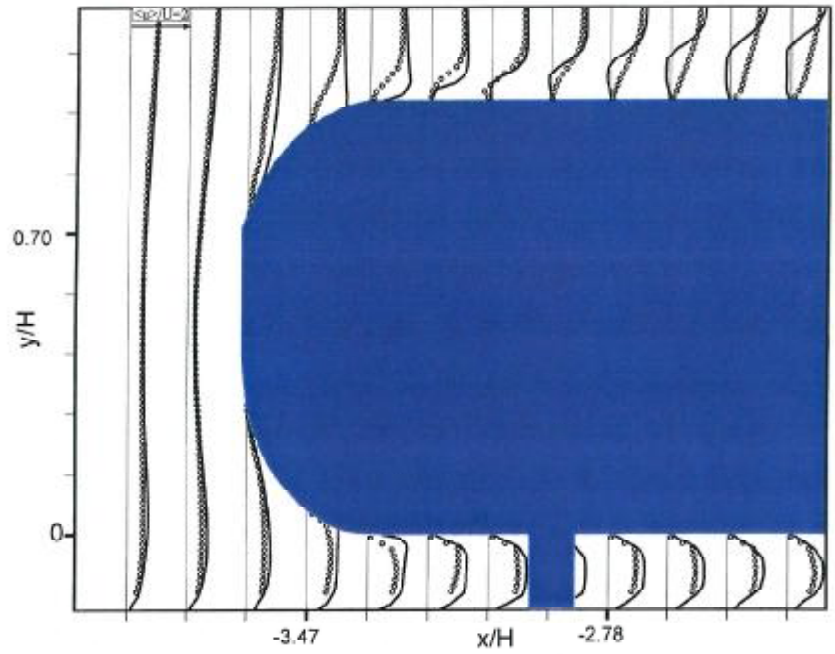

Figure 4.1.7. Time-averaged stream-wise velocity, <u>/U profiles in the symmetry plane z/H=0 on the forward face of the Ahmed body. Numerical results (solid curve), experimental results (symbols)

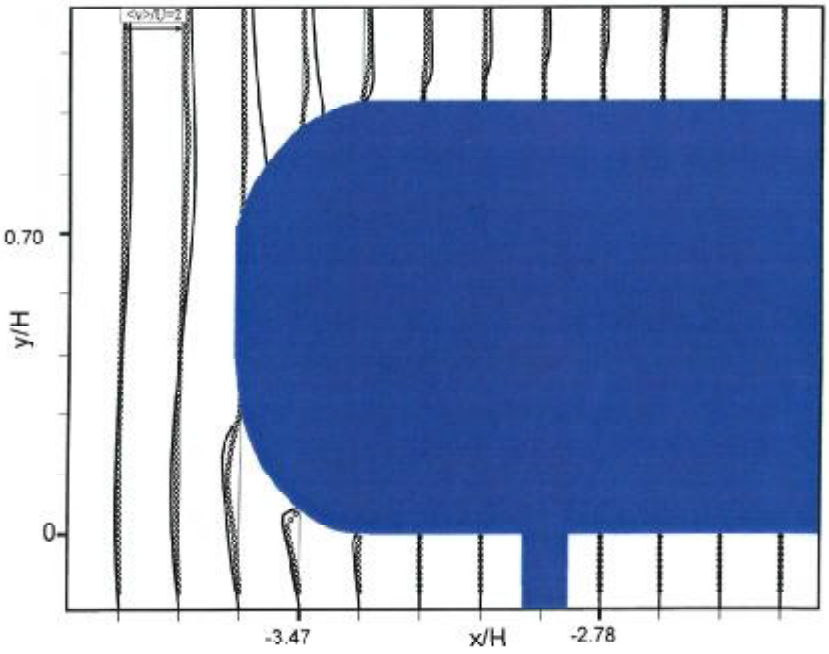

Figure 4.1.8. Time-averaged normal velocity, <v>/U profiles in the symmetry plane z/H=0 on the forward face of the Ahmed body. Numerical results (solid curve), experimental results (symbols).

symmetry plane. The stream-wise velocity results of LES computations on the upper surface show negative values between x/H=-3.06 and -2.36. This means that LES computed a larger separated flow region than the PIV measurements on the upper surface of the body. Because of the jet flow occurring between the ground and the bottom surface of the model, the magnitude of stream-wise velocity increases in the lower part of the wake region. The PIV measurements have smaller stream-wise velocities under the body. Figure 4.1.8 displays the time-averaged normal velocity profiles of the flow, <v>/U in the vertical symmetry plane. Rapid changes in velocity profiles occur at the beginning of the rounded part of the front surface both in the direction of upper and lower part of the body. The computed velocity, <v>/U profiles show the striking differences among the measured velocity, <v>/U results in these region. Positive velocity, <v>/U results in the approaching flow indicate the upsweep flow. The maximum upsweep velocity is 0.228 and 0.832 times the free-stream velocity, U for the results of PIV measurements and LES computations, respectively. The locations of the maximum upsweep velocity are nearly at x/H=-3.33 and y/H=1.10 for the experimental results and at x/H=-3.61 and y/H=0.82 for the numerical results. Negative velocity, <v>/U results in the approaching flow indicates the downward flow. The maximum downward velocity is -0.392 and -0.584 times the free stream velocity, U for the results of PIV measurements and LES computations, respectively. Locations of the maximum down-sweep velocity in the stream-wise direction are nearly at the same point in both experimental and numerical results which is about x/H=-3.61. On the other hand, locations of the maximum down-sweep velocity in the normal direction are nearly y/H= 0.104 and 0.177 for the results of PIV measurements and LES computations, respectively.

Time-averaged velocity vectors map <V>, corresponding streamlines <ψ>, vorticity contours <ω> and pressure coefficient contours obtained numerically in the vertical symmetry plane (z/H=0) through the full-length of the Ahmed body are presented in Figures 4.1.9 and 4.1.10, respectively. These figures help our understanding of the flow structures exposed throughout the model. In Figure 4.1.9, the flow separates and then reattaches after the frontal leading edge of the body. The distance of the reattachment point to the frontal leading edge is x/H=1.9 which

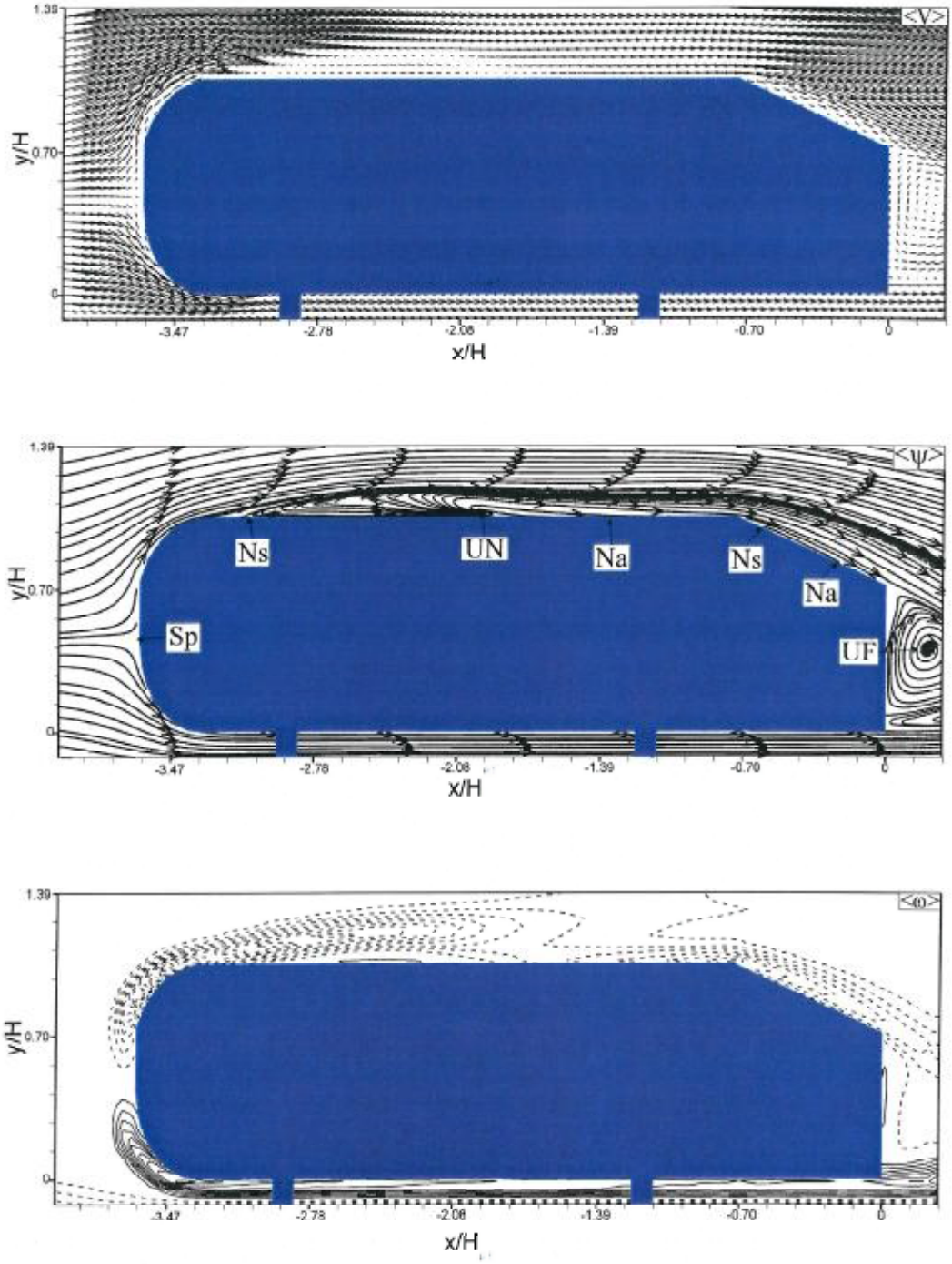

Figure 4.1.9. Time-averaged velocity vectors map <V>, streamlines <ψ> and corresponding vorticity contours <ω> in the vertical symmetry plane z/H=0 through full length of the Ahmed body.

corresponds to 53% of the model length. Patterns of streamlines, $\langle\psi\rangle$ along the vertical symmetry plane indicates that unstable node, UN occurs on the upper surface of the model. The distance of the unstable node, UN to the frontal leading edge of the model is x/H=1.32. In the downstream of the model, separation occurs and two shear layers are developed, which then interact with each other in the wake region. In Figure 4.1.10, positive pressure coefficient values are seen only at some part of the front face of the body and rest of the body exposed to negative pressure coefficient values. After the large change in mean pressure coefficient gradient exhibited at the beginning of the rounded part of the front face of the body, one of the lowest pressure region on the model vehicle body was observed. This region ends nearly at the frontal leading edge of the body. From this region and further on, positive changes in pressure gradient is observed around the Ahmed body until reaching the rear slanted surface of the body.

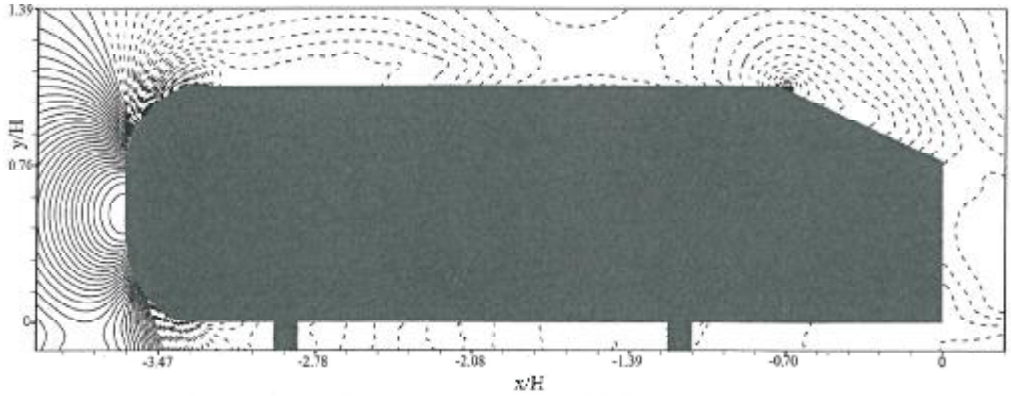

Figure 4.1.10. Time-averaged mean pressure coefficient contours in the vertical symmetry plane z/H=0. Minimum and incremental values of mean pressure coefficient are $\langle C_{p,min}\rangle$=0.02 and $\Delta\langle C_p\rangle$=0.02

Time-averaged numerically computed trace lines projected on the front, upper and lateral sides of the Ahmed body are shown in Figure 4.1.11. On the front face of the body, flow is directed into upper, lower and lateral sides of the body. These flow streams are separated by four positive bifurcation lines which start at the stagnation point and end at the corners of the front face. Highly unsteady flow structures on the upper and lateral surfaces are observed. The flow separates and then reattaches both on upper and lateral surfaces of the body. Differently from previous literature

conducted at the higher Reynolds number, large flow separation regions observed on the front part of the Ahmed body in our numerical study may be the results of the effect imposed by the boundary conditions, i.e. occurrence of first increased flow velocity on the rounded part of the body and then, after this region, decreased flow velocity around the frontal leading edge of the body due to the subsequent adverse pressure gradient and a weak level of turbulence which support the detachment due to the low Reynolds number.

Negative bifurcation lines presented in Figure 4.1.11 show separation line of the flow. Separated flow region on the upper surface of the model vehicle is nearly symmetric about the symmetry axis of the body. Along the downstream of the flow separation, there are two stable focus, SF_1 and SF_2, on each side of the symmetry axis and further two saddle points, SP_1 and SP_2, exist on the symmetry axis as shown in Figure 4.1.11. Distances of saddle points, SP_1 and SP_2 from the frontal leading edge of the body are x/H=0.222 and 1.45 respectively. The focus points SF_1 and SF_2 indicating the positions where the origin of two counter rotating longitudinal vortices linked by transversal vortices similar to Kelvin- Helmholtz vortices are attached to the surface of the body and they are also shown in Figure 4.2.11. Spohn and Gillieron (2002) and Krajnovic and Davidson (2005) also identified similar flow structures. In the study of Krajnovic and Davidson (2005) the flow separates as it reaches the top, the lateral, and the bottom sides of the body. However, the results of our study reveal differences from those of Krajnovic and Davidson (2005). For example, in the present work, flow separates after some distance from the frontal leading edge of the body and formation of negative bifurcation lines which shows the separation of the flow is more complex and unsteady. In addition, during the downstream of the flow separation, the length of the recirculating flow region observed in our study is much more than the length of the recirculating flow region observed in the study of Krajnovic and Davidson (2005). There are also positive bifurcation lines through the downstream of the recirculating flow region. These positive bifurcation lines ending up with the saddle point, SP_2, show reattachment of the flows on the upper surface of the body.

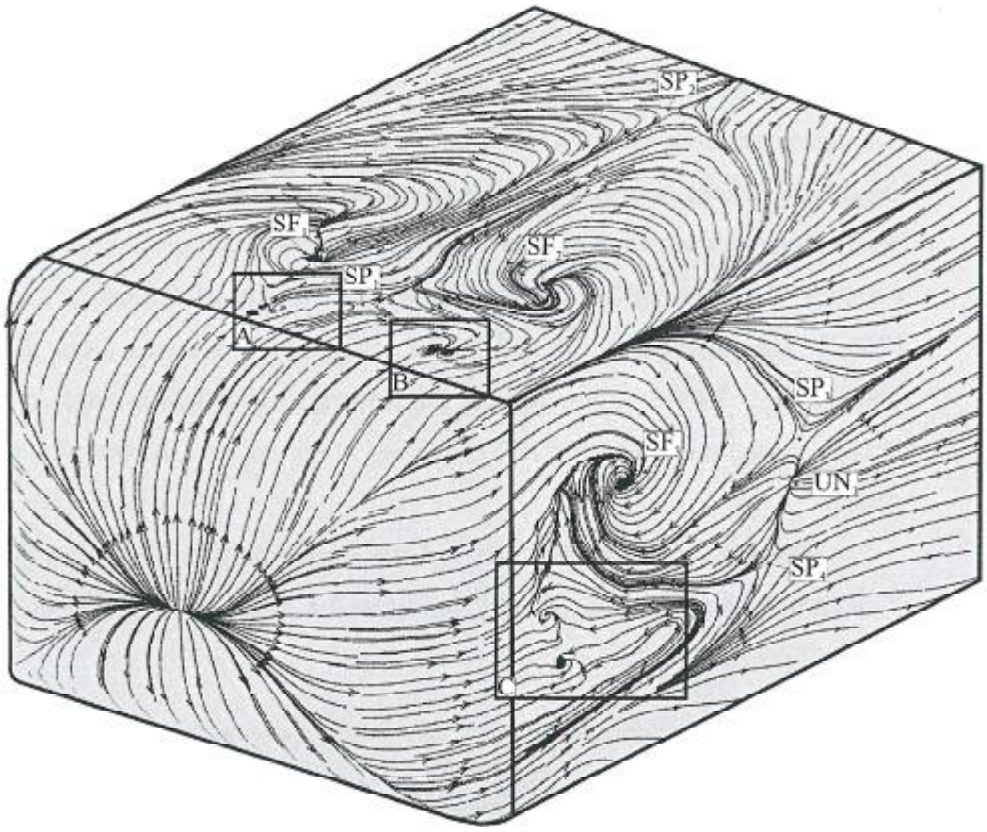

Figure 4.1.11. Time-averaged trace lines projected on the surface of the Ahmed body. View of the front, upper and lateral sides of the body

It can be said that nearly the same flow topology occur on the upper and lateral surfaces of the front part of the body. On the other hand, symmetric flow structures observed on the lateral surfaces deteriorate due to the ground effect, and the length of the separated flow region becomes shorter on the lateral sides of the body. The effects of the ground to the structure of separated flow region are formed on the lateral sides of the body plays an important role.

There are very complex and unstructured flow structures on the negative bifurcation line formed on the lateral side of the body. Details of the lower part of the flow structures found on the negative separation line, NBL_4, are shown in Figure 4.1.12(c). At the end of the separated flow region observed on the lateral side, there are two saddle points, SP_3 and SP_4, and one unstable node, UN_1. Distances of saddle

points, SP_3 and SP_4 from the frontal leading edge of the body are x/H=1.0 and 0.892 respectively. The findings of the present study differ from those of Krajnovic and Davidson (2005) in two important ways. First, the separated flow region on the upper and lateral surfaces of the Ahmed body does not extends between two sides of the upper and lateral surfaces in the span-wise direction. The other is that negative bifurcation lines which show starting point of separated region of the flow are more tentative and unstable than those found in the study of Krajnovic and Davidson (2005). The differences are thought to mainly have resulted from the Reynolds number, $Re_H=1.48x10^4$, employed in the present study which is nearly thirteen times lower than the one's ($Re_H=2x10^5$) employed in the study of Krajnovic and Davidson (2005).

Detailed view of time-averaged trace lines projected on the surfaces of the Ahmed body for region A, B and C in Figure 4.1.11 are shown in Figures 4.1.12 (a), (b) and (c) respectively.

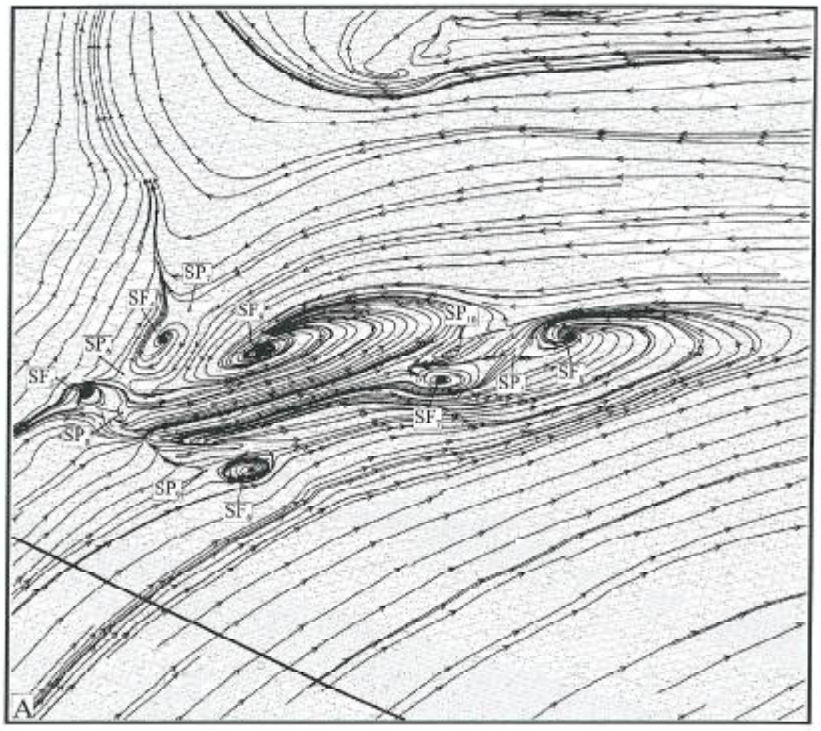

(a)

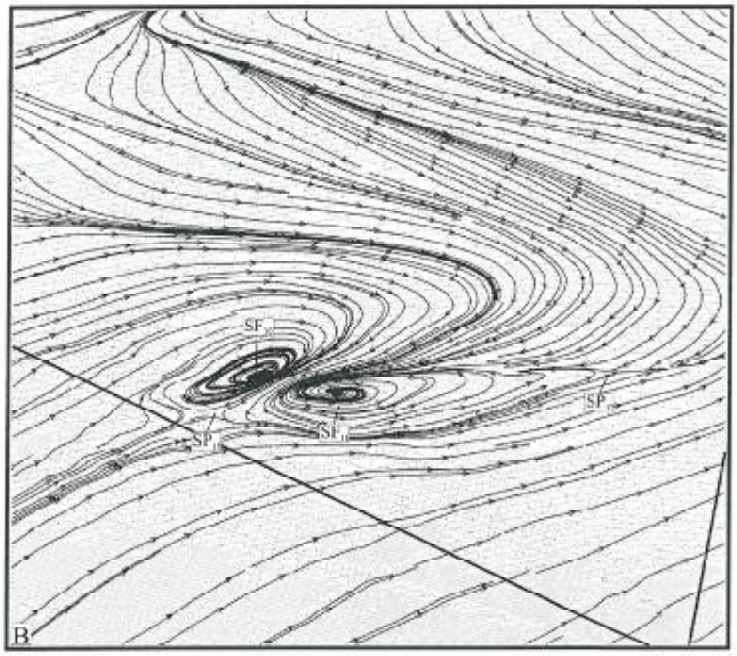

(b)

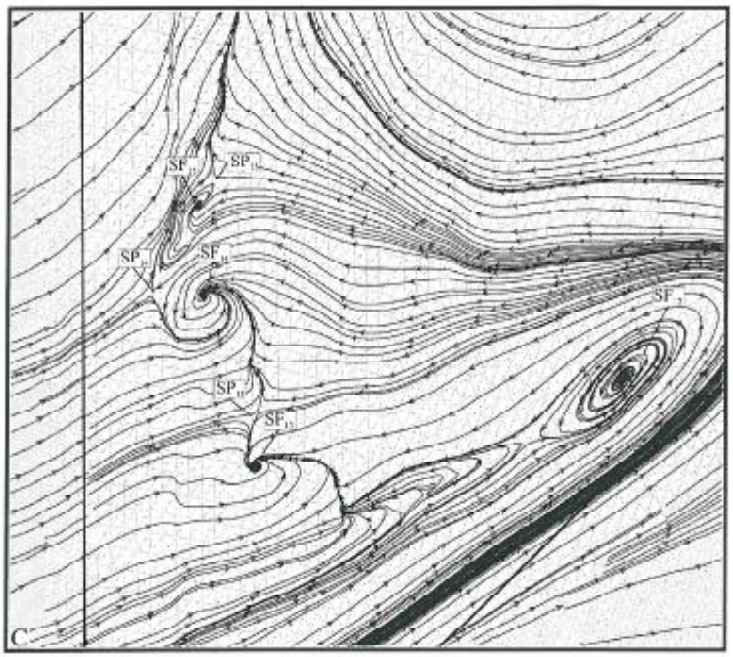

(c)

Figure 4.1.12. Time-averaged trace lines projected on the surfaces of the Ahmed body. Zoom of region A, B and C in Figure 4.1.11 are shown in (a), (b) and (c) respectively.

In Figure 4.1.13, mean wall shear stress contours and contours of du/dy=0 on the upper and slanted surface of the Ahmed body are presented. The occurrence of separated flow region is observed on the upper surface of the model. The boundary of this separated flow region can be seen in Figure 4.1.13 in three dimensional views.

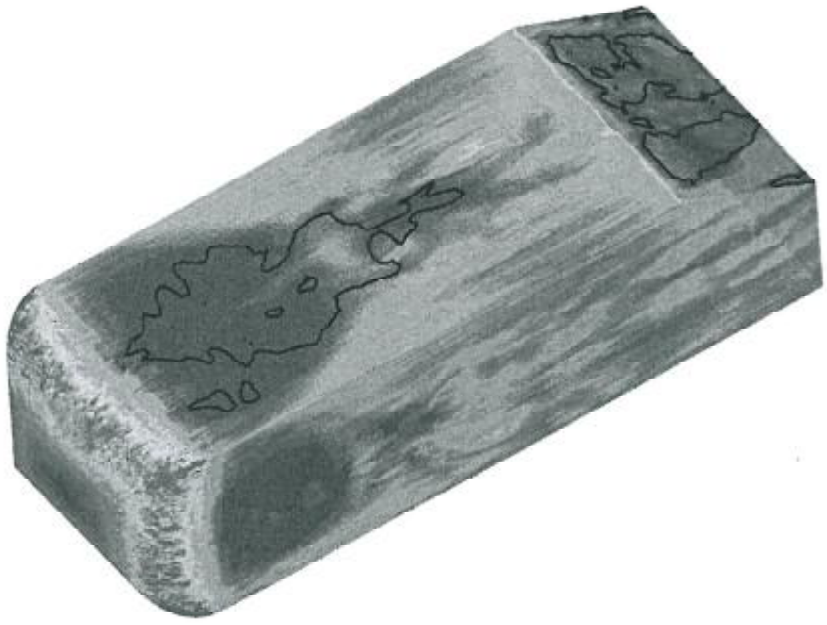

Figure 4.1.13. Mean wall shear stress contours and contours of du/dy=0 on the upper and slanted surface

4.1.2. Flow Structures on the Rear Surfaces and in the Wake Region of the Ahmed Body

The flow topology downstream of the Ahmed body having 25° slant angle is illustrated with the sketch given in Figure 2.5. The previous studies have revealed that two strong counter-rotating vortices emanating from lateral edge of the slant surface are present, and the flow separates in the middle region of the top edge and reattaches to the slant surface(Ahmed et al. (1984), Lienhart et al. (2000), Spohn and Gillieron (2002), Hinterberger (2004), Krajnovic and Davidson (2005a,b), Fares (2006), Guilmineau (2008), Minguez et al. (2008)). Accordingly, at the beginning of the study ,we expected that the present PIV measurements and LES calculations should predict the same separation and reattachment on the slant surface, although the Reynolds number employed in the present study was very small compared with Reynolds number employed in previous studies. However, the results of the present study revealed noteworthy agreement of the flow characteristics with the results of previous literature in the wake region downstream of the Ahmed body, whereas the differences were found on the slant surface of the body.

4.1.2.1. Time-averaged Patterns of Velocity Vectors Map, Streamlines and Vorticity Contours

Time-averaged velocity vectors map $\langle V \rangle$, the patterns of streamlines $\langle \psi \rangle$ and the corresponding vorticity contours $\langle \omega \rangle$ along the Ahmed body in the vertical planes for z/H=0, 0.34 and -0.34 are presented in Figures 4.1.14, 4.1.15 and 4.1.16, respectively. In these figures, minimum and incremental values of vorticity contours are $\langle \omega_{min} \rangle = \pm 4s^{-1}$ and $\langle \Delta\omega \rangle = 2s^{-1}$. Contours of positive and negative vorticity are indicated with solid and dashed lines, respectively. The flow recirculation region formed downstream of the body is composed of two counter-rotating vortices. Size and centre location of numerically computed results corresponds well with the experimental measurements. Regions of negative and positive vorticity contours are created with the upper-body shear layer and the under-body shear layer, respectively.

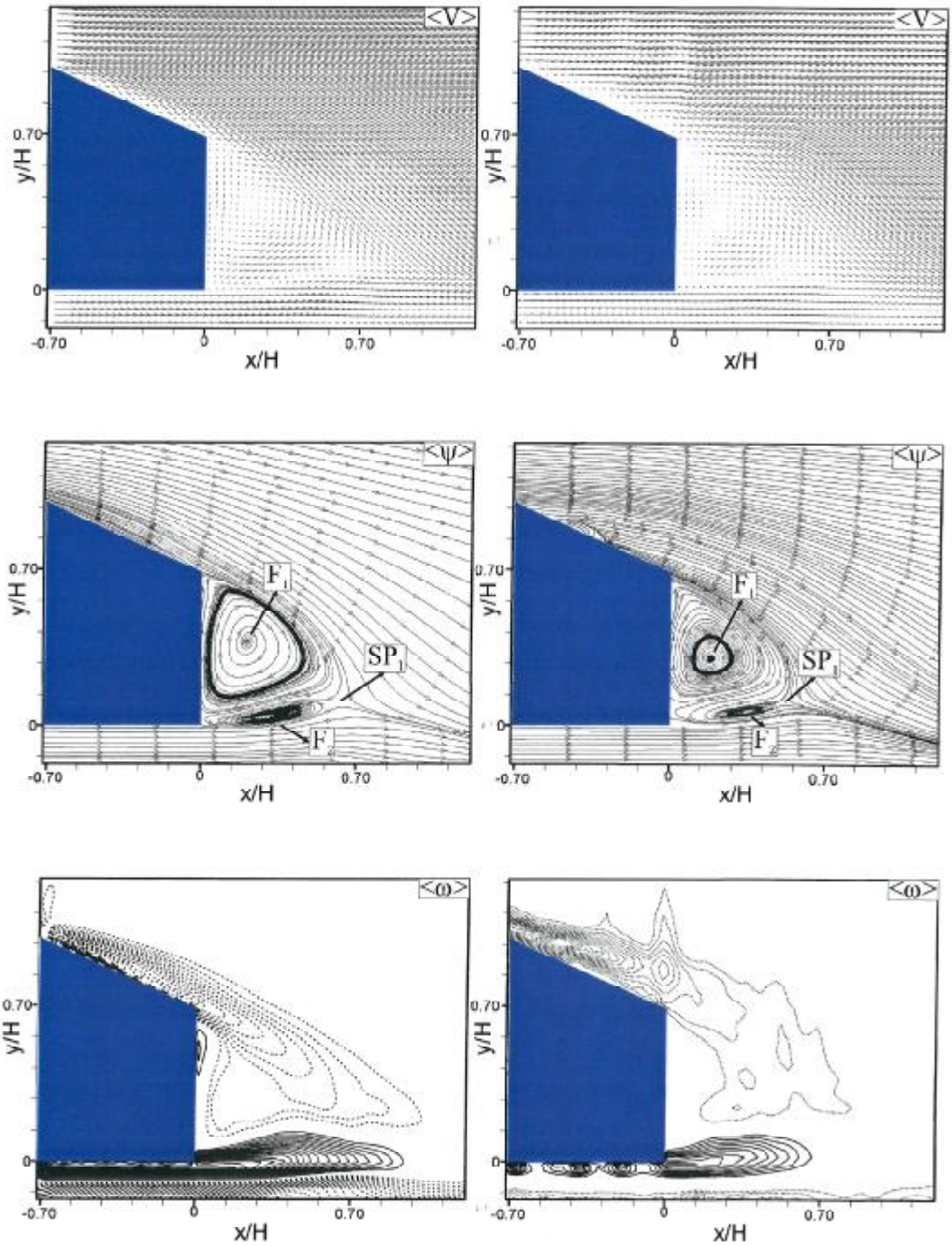

Figure 4.1.14. Patterns of time-averaged velcity vectors map <V>, streamlines <ψ> and vorticity contours <ω> in the vertical symmetry plane, z/H=0. Minimum and incremental values of vorticity are $<\omega_{min}>=\pm 4s^{-1}$ and $\Delta<\omega>=2s^{-1}$, respectively

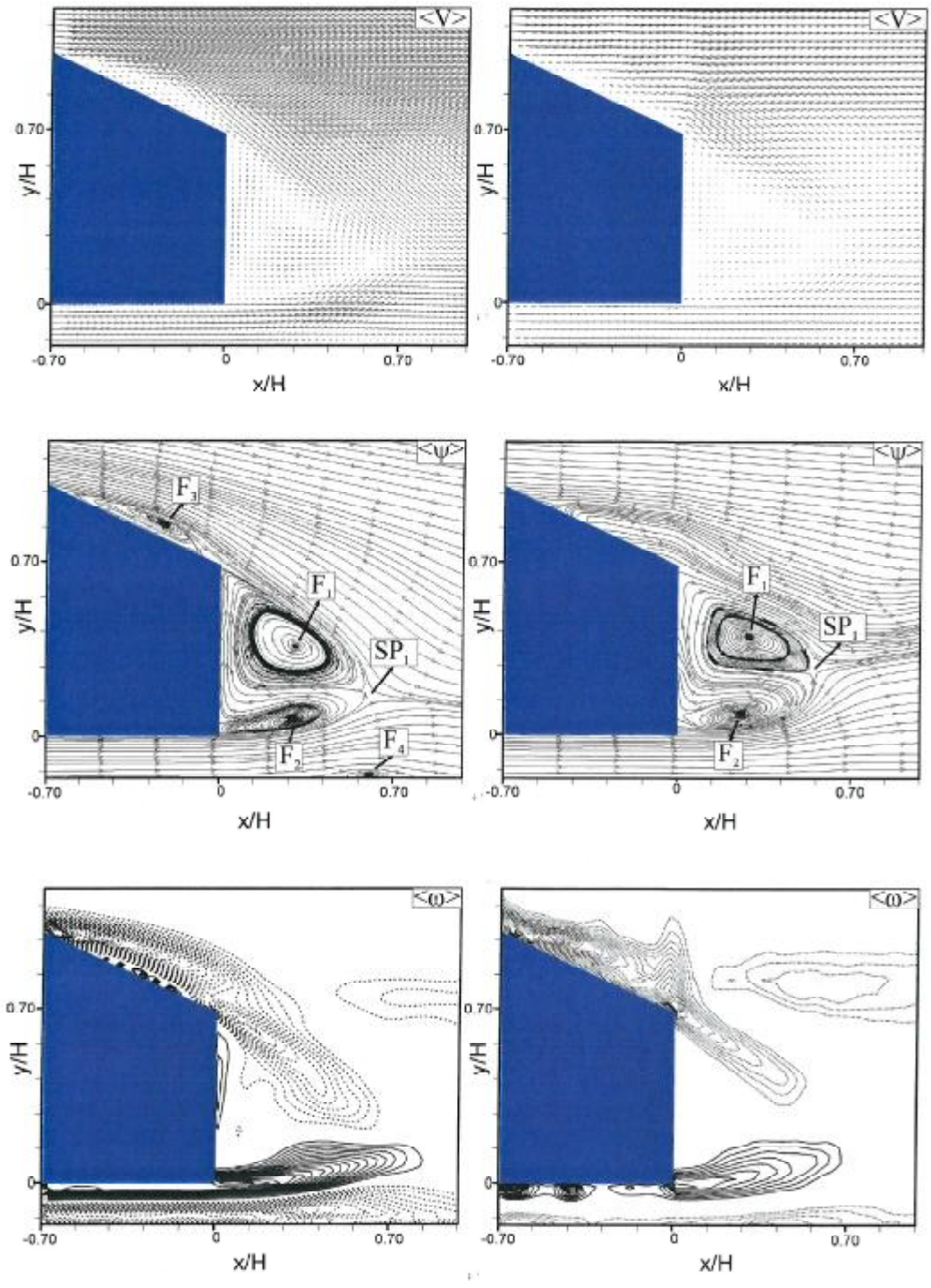

Numerical Experimental

Figure 4.1.15. Patterns of time-averaged velocity vectors map <V>, streamlines <ψ> and vorticity contours <ω> in the vertical plane, z/H=0.34. Minimum and incremental values of vorticity are $<\omega_{min}>=\pm 4s^{-1}$ and $\Delta<\omega>=2s^{-1}$, respectively

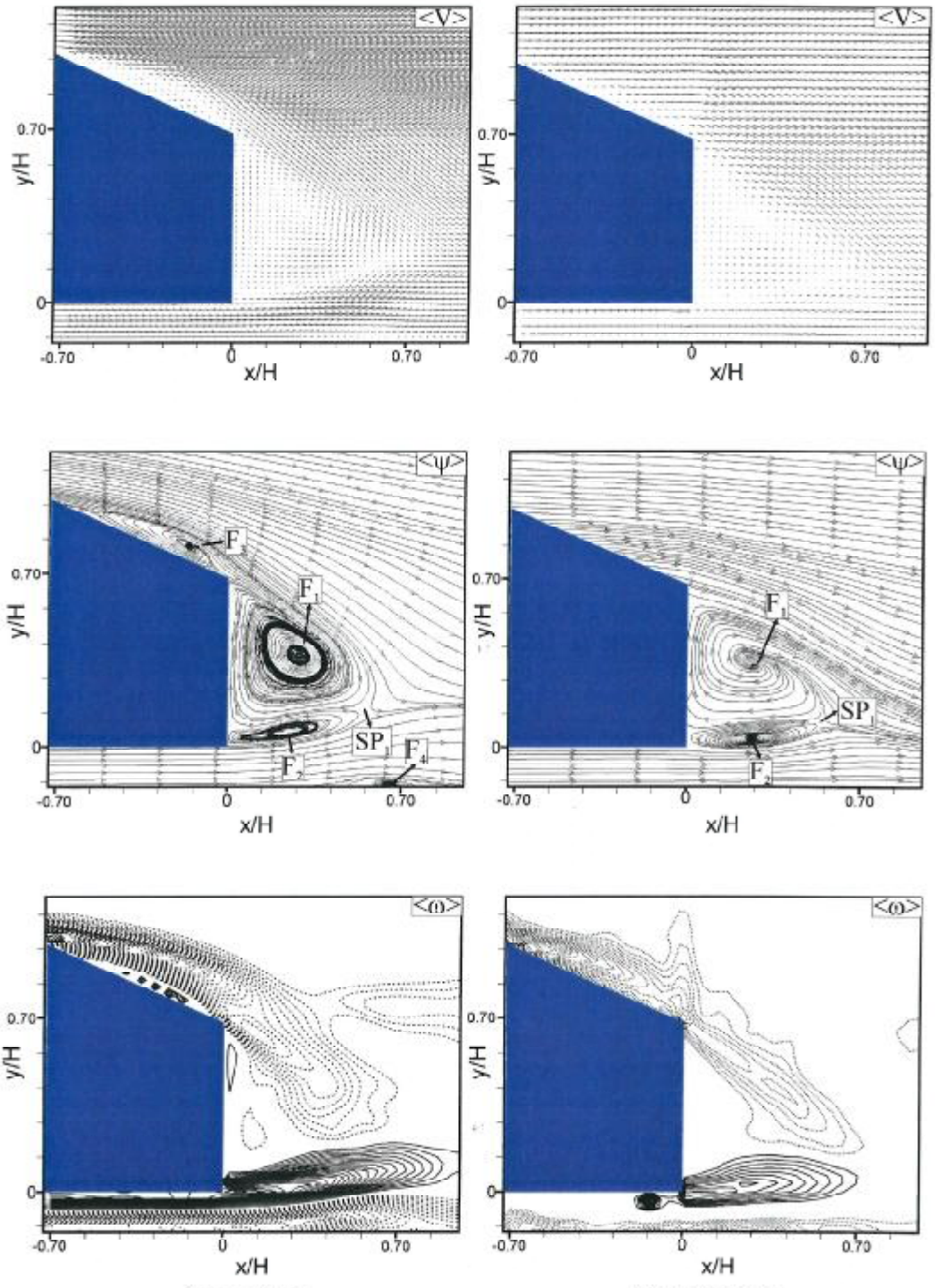

Numerical Experimental

Figure 4.1.16. Patterns of time-averaged velocity vectors map <V>, streamlines <ψ> and vorticity contours <ω> in the vertical symmetry plane, z/H=-0.34. Minimum and incremental values of vorticity are $<\omega_{min}>=\pm 4s^{-1}$ and $\Delta<\omega>=2s^{-1}$, respectively

The under-body shear layer becomes smaller than the upper-body shear layer as a result of the ground effect. Jet like flow emerging from the narrow gap between the bottom of the body and ground surface creates the base corner vortex. In the wake region, two circulatory bubbles are observed, one located above the other, and they rotate in the sense of opposite directions. The bubble rotating in clockwise direction interacts with the upper region of the slant surface of the model, while the lower bubble which rotates in the opposite direction covers the bottom surface. A very small recirculation region on the slant surface of the body is observed. This recirculation region is more distinctive in the experimental results than the numerical results. The flow separates at a point nearly half of the slanted surface from the beginning. Beyond this region, the flow then reattaches to the slanted surface, and then develops into a second, larger recirculation region along the rear vertical surface of the body. The saddle point, SP_1 defines the size of the wake region. The time-averaged velocity vectors map, $\langle V \rangle$ and the corresponding patterns of streamline, $\langle \psi \rangle$ figures clearly indicate the location of the saddle point SP_1, focus F_1 and F_2, which are in the near wake region of the body. Numerically computed and experimentally measured locations of the saddle point 1 (S_1), focus 1 (F_1) and focus 2 (F_2) in the vertical symmetry planes for z/H=0, 0.34 and -0.34 are shown in Figures

Table 4.1.1. Comparison of the numerically computed and experimentally measured location of the saddle point 1 (S_1), focus 1 (F_1) and focus 2 (F_2) in the vertical planes at locations of z/H=0, z/H=0.34 and z/H=-0.34.

		z/H=0 Plane		z/H=0.34 Plane		z/H=-0.34 Plane	
		X (x/H)	Y (y/H)	X (x/H)	Y (y/H)	X (x/H)	Y (y/H)
Saddle Point (SP_1)	Computed	0.63	0.11	0.59	0.16	0.55	0.13
	Measured	0.51	0.11	0.54	0.25	0.53	0.08
Focus 1 (F_1)	Computed	0.18	0.38	0.30	0.35	0.29	0.36
	Measured	0.21	0.30	0.29	0.39	0.27	0.32
Focus 2 (F_2)	Computed	0.36	0.05	0.29	0.06	0.24	0.05
	Measured	0.35	0.06	0.25	0.09	0.26	0.02

4.1.14, 4.1.15 and 4.1.16 are presented in Table 4.1. In the table, distances are normalized with body height, H. Analysing the table, it can be seen that the LES calculations well captures the locations of the all flow structures such as saddle point and focuses in the near wake region ($0<x/H<0.694$) with differences less than 12% over the height of the Ahmed body. Maximum difference in stream-wise direction occurs between the computed and measured locations of the saddle point in z/H=0 plane with a value of %12. Maximum difference in the normal direction of the flow occur again between the computed and measured location of the saddle point in z/H=0.34 plane with a value of %9.

The present LES calculations predict massive separation at vertical planes z/H=0.34 and -0.34 on the slant, whereas PIV measurements show no separation at these planes. These differences in the velocity field on the slant surface of the body are also seen in the trace-line Figures 4.1.48 and 4.1.49. In addition, as previously mentioned, a good agreement is not observed between the LES results and the PIV results through the upstream part of the flow at the front of the body This discrepancy in the velocity field on the slant and front surface of the body is thought to have resulted from the insufficient laser sheet, which is essential for the accurate measurement due to the thick Plexiglas material used to construct the Ahmed body. As a result, large flow separation observed in the LES calculations at the front of the body increases the turbulence production around the symmetry plane, and thereby effects all flow structure on the upper part of the body. The process is shown more clearly in Figures 4.2.11 (a) (b) and (c).

The time-averaged patterns of velocity vectors map $\langle V \rangle$, the streamline patterns, $\langle \psi \rangle$ and the corresponding vorticity contours, $\langle \omega \rangle$ are presented in the horizontal xz-plane for locations of y/H=0, 0.07, 0.14, 0.35, 0.67, 0.78, 0.89 and 1.00 through the wake region downstream of the Ahmed body in Figures from 4.1.17 to 4.1.24. Symmetrical pattern of flow field can be observed in all of these figures. The present results indicate that the flow structures in the wake region vary significantly with the elevation level. Therefore, the flow can be investigated in three category according to the interaction of upstream flow coming from bottom, upper and lateral surfaces of the model as the observation levels increase from bottom to top.

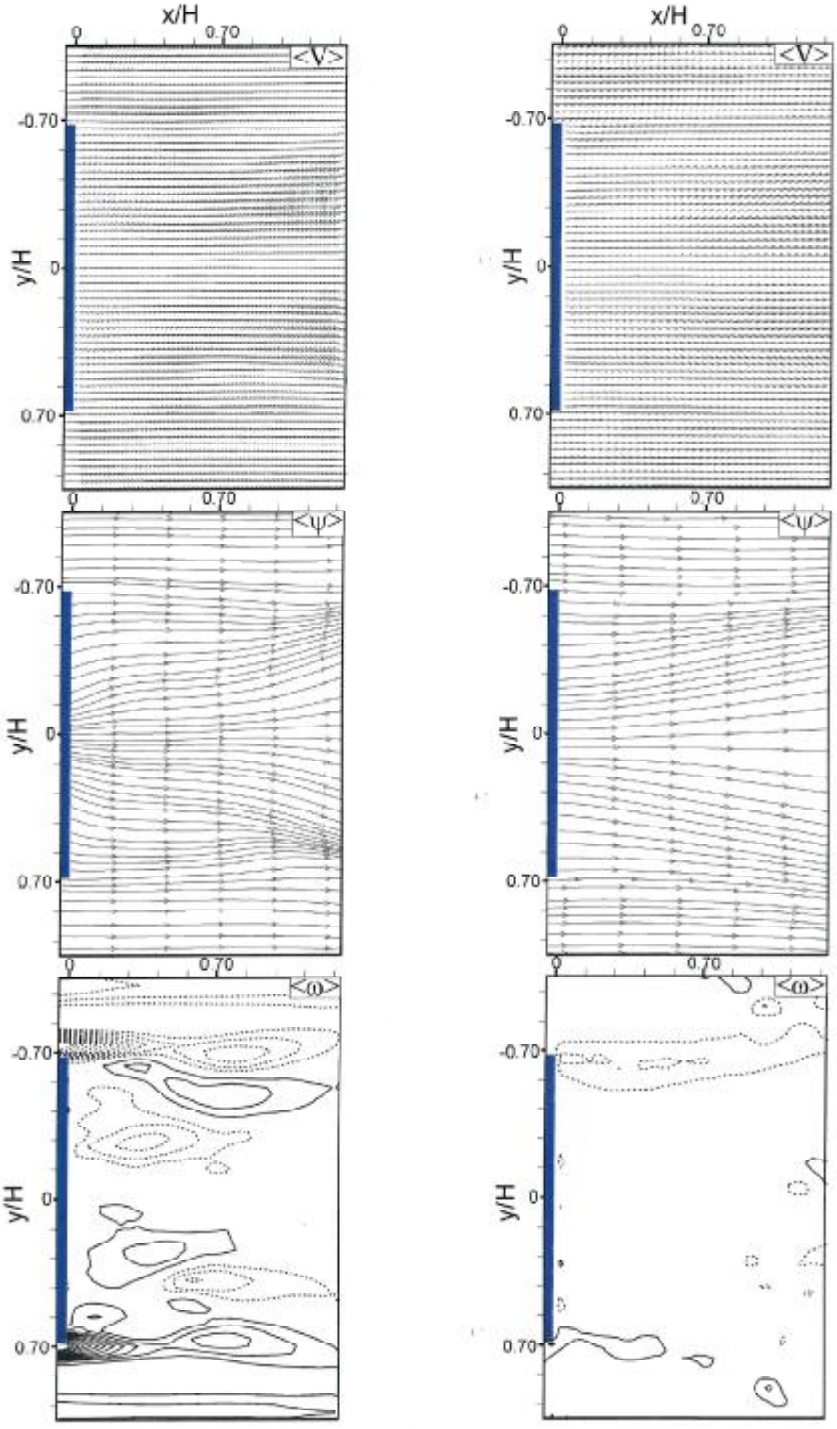

Numerical Experimental

Figure 4.1.17. Patterns of time-averaged velocity vectors map <V>, streamlines <ψ> and vorticity contours <ω> in the horizontal xz-plane for y/H=0. Minimum and incremental values of vorticity are $<\omega_{min}>=\pm 2s^{-1}$ and $\Delta<\omega>=2s^{-1}$, respectively

Furthermore, it can be observed on planes at the locations of y/H=0, 0.07, 0.14, 0.35, that the flow stream coming from the bottom surface of the model dominates the flow structure in the near wake of the body. The main features of the flow in Figures 4.1.18 and 4.1.19 are reversed flow region downstream of the body due to the flow coming from under-body and two shear layers originated from the sharp trailing vertical side edges. In the wake region after the body, a pair of shear layer regions is identified. Regions of high vorticity contours define the shear layers. These two shear layers extend approximately to the same downstream location. In Figures 4.1.18 and 4.1.19, some discrete structures between the numerical and experimental results appear in the flow. For example, the numerical results presented in Figure 4.1.18 for y/H=0.07 while two nodes, N_1 and N_2 and one saddle point, SP_1 appear in the centre of the wake, only one node, N_1 appear in the experimental results for the same plane. Similarly, in the experimental results presented in Figure 4.1.19 for y/H=0.14 while one node, N_1 one saddle point, SP_1 and one focus, F_1 appear in the wake, only one node, N_1 appear in the numerical results for the same plane. Although the flow field presented in these figures are time averaged, because the near-wake flow structure after the body is very complex and unstable, the discrepancies observed between numerical and experimental results may appear. Therefore, the general flow structures in the near wake after the body can be approved to be the same for both numerical and experimental results and in the mean, one node and two shear layers are observed in the wake region presented in Figures 4.1.18 and 4.1.19. The distances of nodes to the vertical surface of the body at the location of y/H=0.07 are x/H=0.489 and 0.515 for the LES results and x/H=0.492 for the PIV results as shown in Figure 4.1.18. Similarly, the distance of nodes to the vertical surface of the body at the location of y/H=0.14 are x/H=0.686 for the LES results and x/H= 0.608 for the PIV results as shown in Figure 4.1.19. Span-wise length of the wake region between the two shear layers at the point of node is the same for both numerical and experimental results, which is z/H=1.35 and does not change as the observation level changes between planes of y/H=0.07 and 0.14. On the other hand, as noted above, stream-wise length of the reversed flow

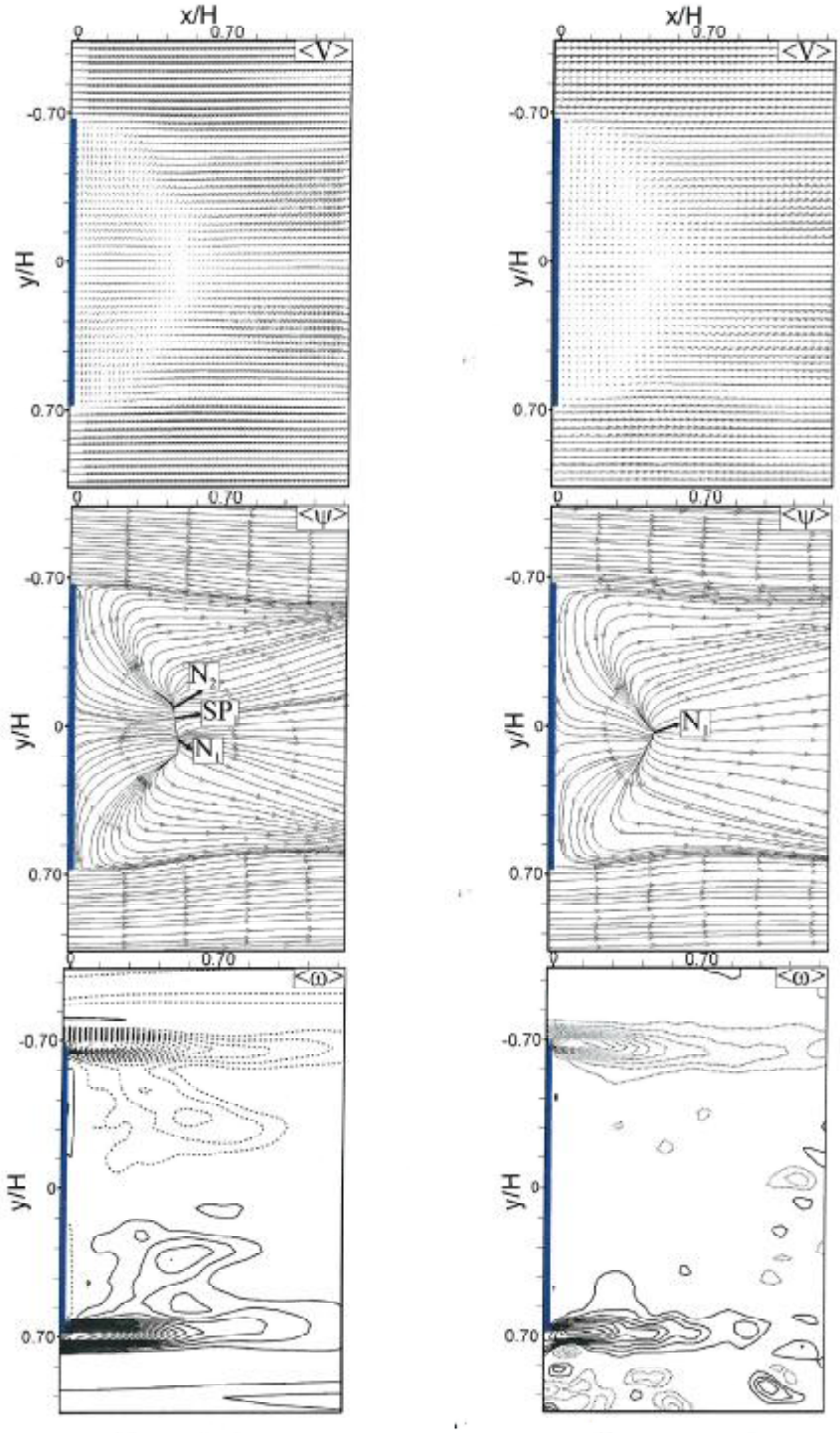

Figure 4.1.18. Patterns of time-averaged velocity vectors map <V>, streamlines <ψ> and vorticity contours <ω> in the horizontal xz-plane for y/H=0.07. Minimum and incremental values of vorticity are $<\omega_{min}>=\pm 2s^{-1}$ and $\Delta<\omega>=2s^{-1}$, respectively

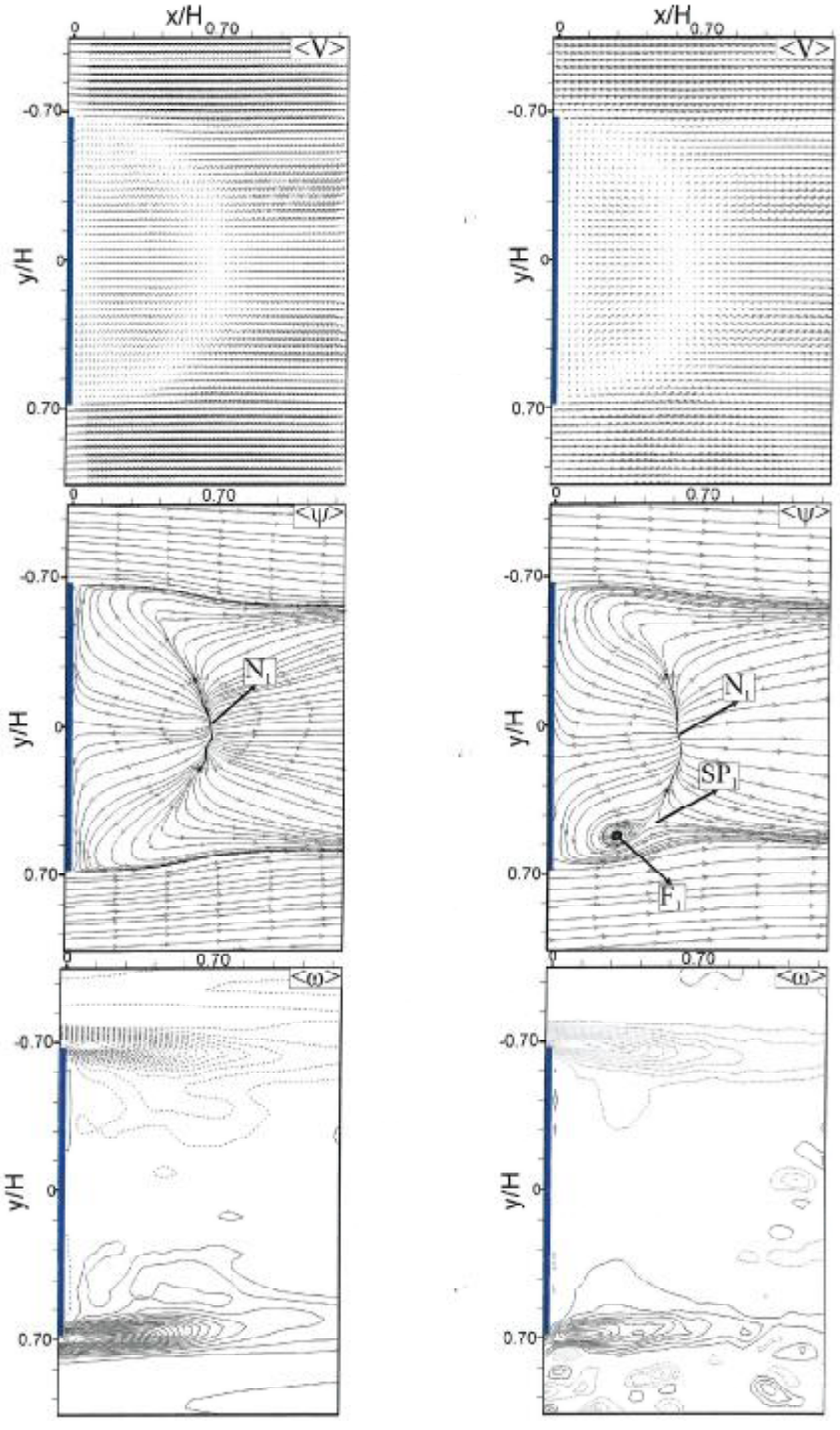

Numerical Experimental

Figure 4.1.19. Patterns of time-averaged velocity vectors map <V>, streamlines <ψ> and vorticity contours <ω> in the horizontal xz-plane for y/H=0.14. Minimum and incremental values of vorticity are $<\omega_{min}>=\pm 2s^{-1}$ and $\Delta<\omega>=2s^{-1}$, respectively

region formed in the near wake flow after the model enlarge between planes of y/H=0.07 and 0.14.

In the region between planes of y/H=0.35 and 0.67, i.e. between the half line of the rear vertical surface and transversal trailing edge of the slant surface, flow got affected by both upstream flow coming from upper and lower parts of the body. The most complex flow structures among all other horizontal xz-planes occur in the plane of y/H=0.35 presented in Figure 4.1.20. In this plane, flow structures, which do not exist in the lower planes arise, and wake flow are reshaped symmetrically about the symmetry axis of the body. Focus F and bifurcation lines, BL arise in newly formed flow structure. Relatively uniform structure of the reversed flow region seen at the lower planes is completely deformed in this plane. Although, two focus points are resolved close to the shear layers at each side of the wake in the LES results, only one well defined focus point is captured in the experimental measurements as shown in Figure 4.1.20.

Above the level of transversal trailing edge of the body, as a primary effect, flow streams coming from upper surface of the body becomes dominated. At these observation levels, trailing vortices which move from the lateral sides to the slanted surface can also be observed. Actually, in all horizontal planes (xz-planes) above the level of transversal trailing edge of the body, effects of the flow coming from the lateral surfaces of the body are observed, but its effects on the flow structures are considered to be a secondary. Shear layers emanating from the lateral surfaces of the body tends to remove wake flow region in the transversal direction, in other words, through the rear vertical surface of the model starting from the level of y/H=0.67. Above the levels of y/H=0.67 (on the slant surface of the body), flow streams coming from the lateral surfaces have additional effects on the flow structure in that they tend to create longitudinal vortices on the side edges of the slant as seen in Figures from 4.1.21 to 4.1.24.

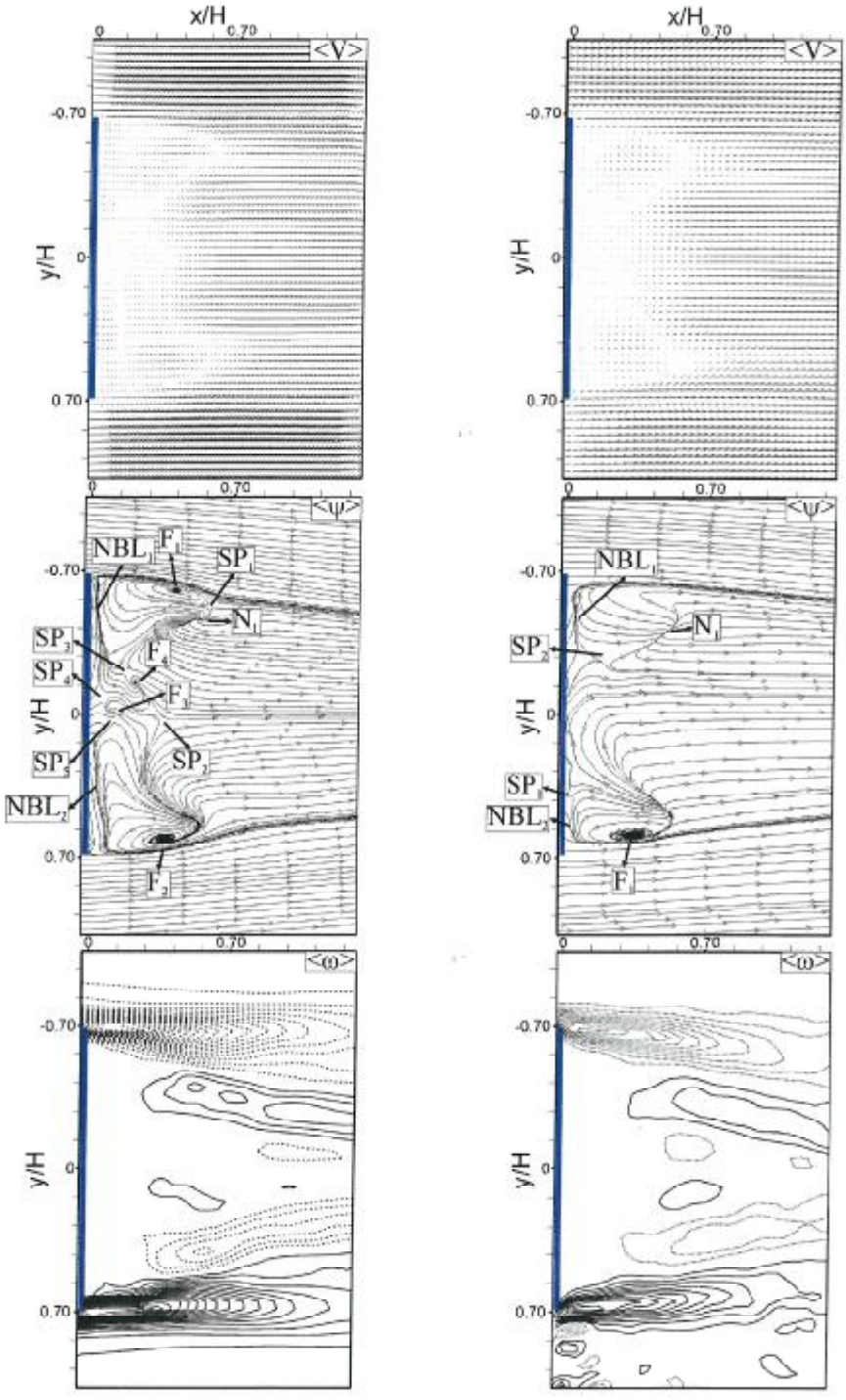

Numerical Experimental

Figure 4.1.20. Patterns of time-averaged velocity vectors map <V>, streamlines <ψ> and vorticity contours <ω> in the horizontal xz-plane for y/H=0.35 . Minimum and incremental values of vorticity are $<\omega_{min}>=\pm 2s^{-1}$ and $\Delta<\omega>=2s^{-1}$, respectively

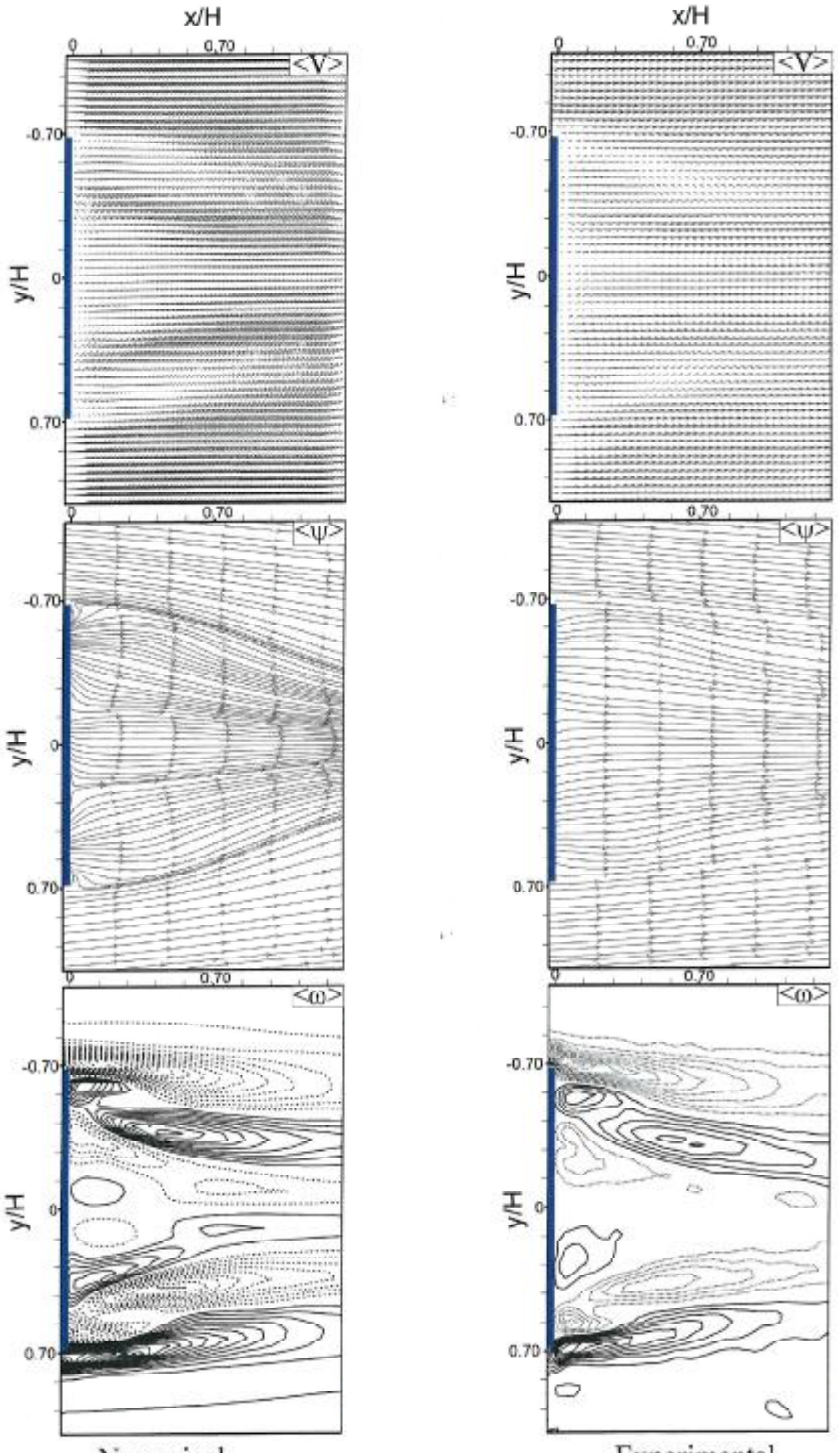

Figure 4.1.21. Patterns of time-averaged velocity vectors map <V>, streamlines <ψ> and vorticity contours <ω> in the horizontal xz-plane for y/H=0.67. Minimum and incremental values of vorticity are $\langle\omega_{min}\rangle=\pm 2s^{-1}$ and $\Delta\langle\omega\rangle=2s^{-1}$, respectively

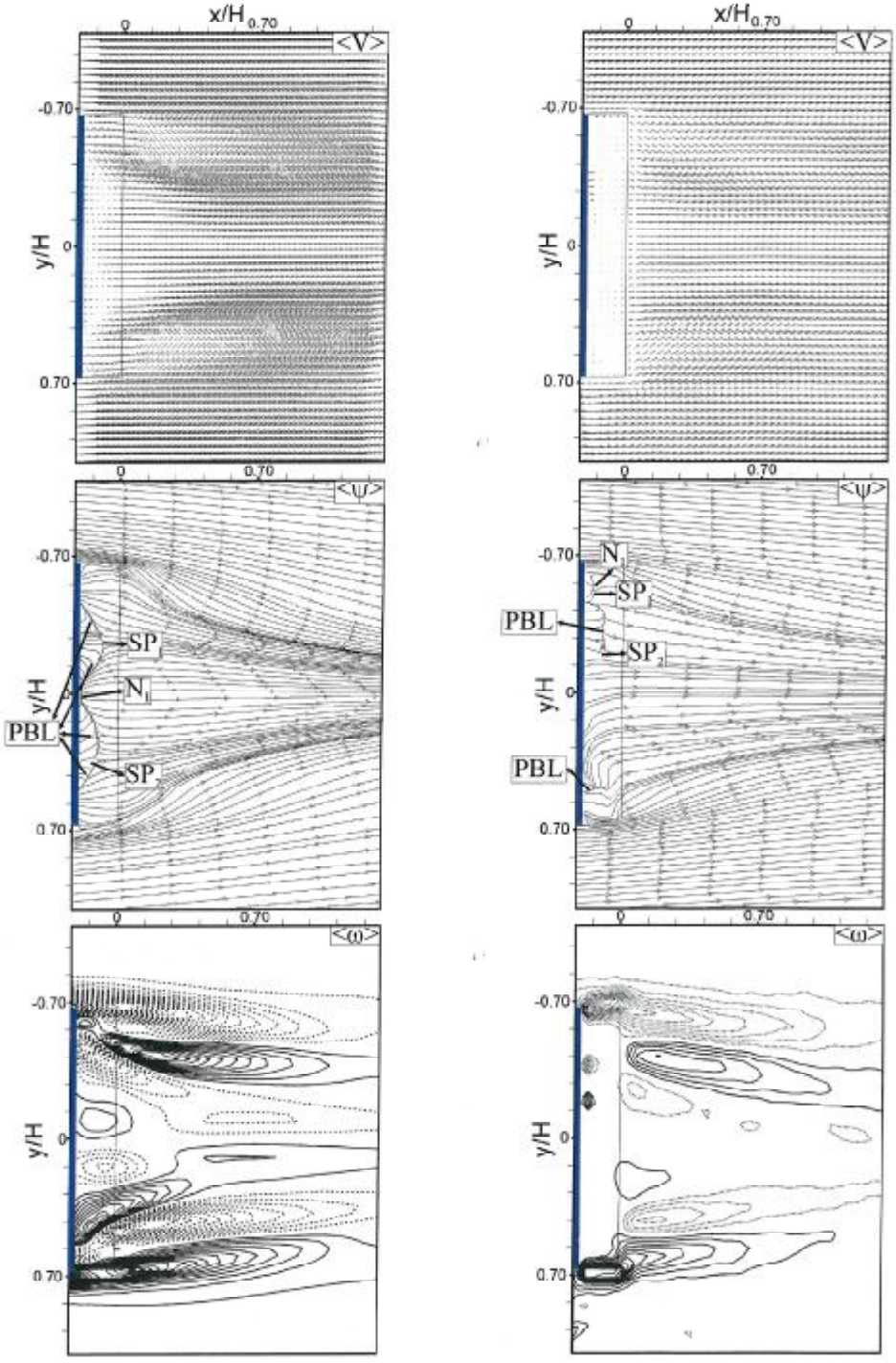

Numerical Experimental

Figure 4.1.22. Patterns of time-averaged velocity vectors map <V>, streamlines <ψ> and vorticity contours <ω> in the horizontal xz-plane for y/H=0.78. Minimum and incremental values of vorticity are $<\omega_{min}>=\pm 2s^{-1}$ and $\Delta<\omega>=2s^{-1}$, respectively

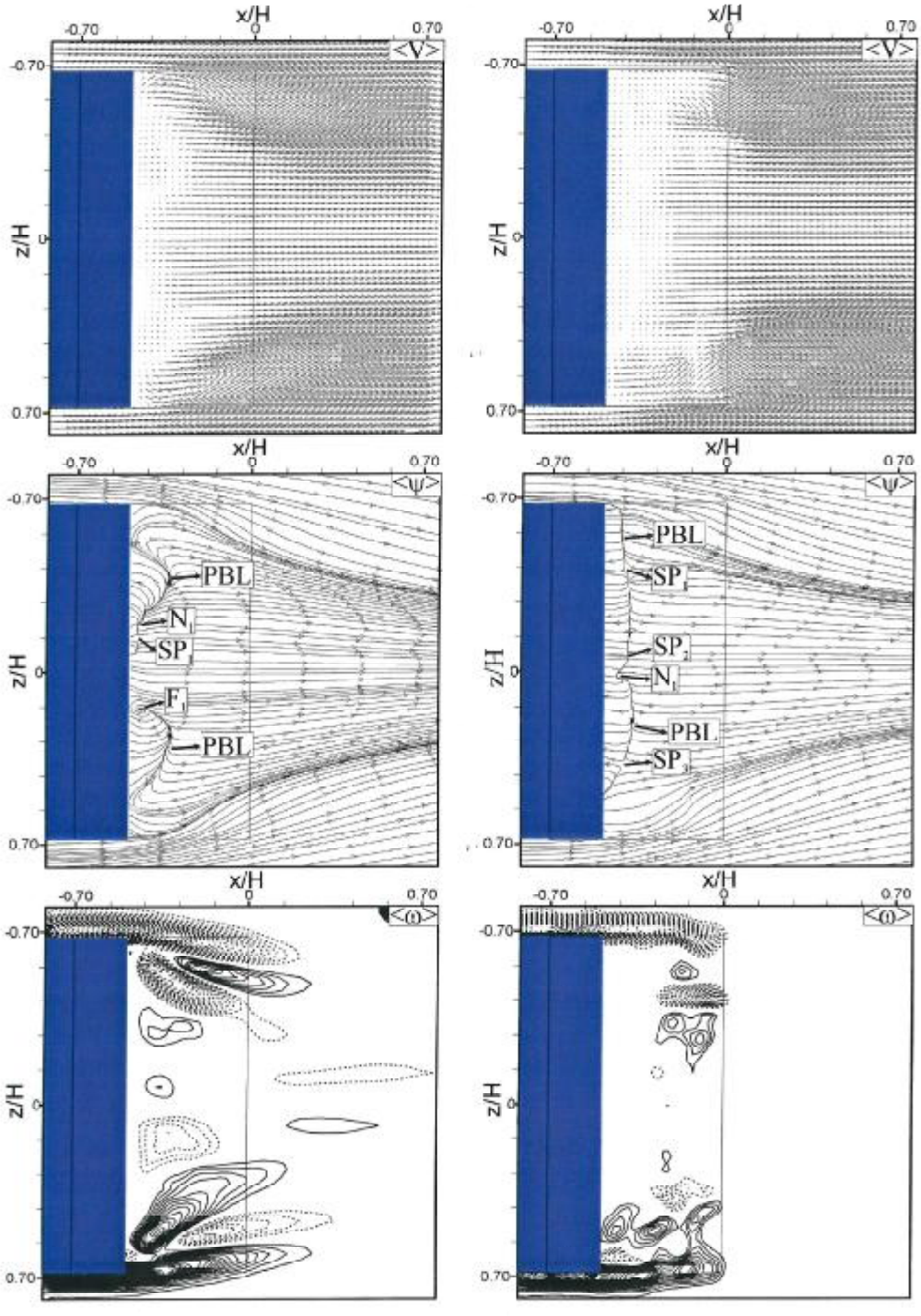

Numerical Experimental

Figure 4.1.23. Patterns of time-averaged velocity vectors map <V>, streamlines <ψ> and vorticity contours <ω> in the horizontal xz-plane for y/H=0.89 . Minimum and incremental values of vorticity are $<\omega_{min}>=\pm 4s^{-1}$ and $\Delta<\omega>=2s^{-1}$, respectively

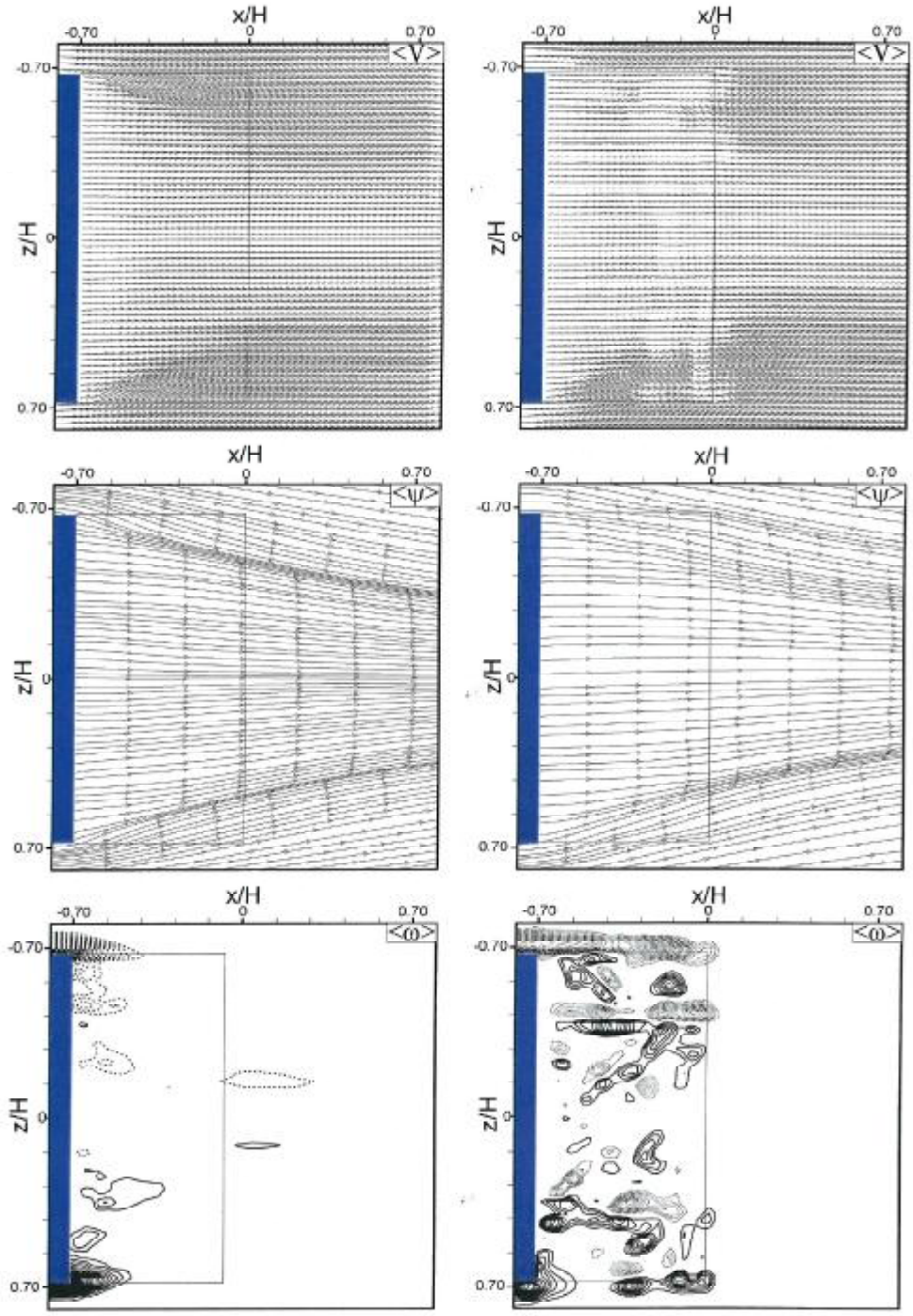

Numerical Experimental

Figure 4.1.24. Patterns of time-averaged velocity vectors map <V>, streamlines <ψ> and vorticity contours <ω> in the horizontal xz-plane for y/H=1.0 . Minimum and incremental values of vorticity are $<\omega_{min}>=\pm 4s^{-1}$ and $\Delta<\omega>=2s^{-1}$, respectively

In Figures from 4.1.25 to 4.1.39, the time-averaged patterns of velocity vectors map <V>, the streamline patterns, <ψ> and the corresponding vorticity contours, <ω> are presented in the transversal yz-planes for locations of x/H=-0.69, -0.56, -0.42, -0.28, -0.14, 0, 0.21, 0.28, 0.35, 0.69, 1.04, 1.39, 1.74, 2.08 and 2.43 through the wake region downstream of the body. When experimental results compared with the numerical results by considering all transversal yz-plane figures, locations and size of the main flow structures are well predicted in the simulation especially in the wake region downstream of the body. The dimensions of the recirculation zone are well predicted. Development of counter-rotating vortices estimated by the LES calculations is also closely similar to the PIV measurements. It is also observed that longitudinal vortices emanating from lateral sides of the slant develop near the halfway of the slant surface as presented in Figure 4.1.27. They grow while they approach end of the body, and they are strong and fully developed in the near wake. These cross-section of the longitudinal vortex pairs disappear at positions between x/H= 0.35 and 0.69 as depicted in Figures 4.1.33 and 4.1.34. The flow emanating from the gap between the body and ground has three dimensional characters as presented in the transversal planes shown in Figures from 4.1.25 to 4.1.29, which concurs with results of the study carried out by Krajnovic and Davidson (2004). Flow stream coming from the underbody and travelling to the lateral sides forms two trailing vortices close to each of the lower lateral edges of the body as seen in Figures from 4.1.25 to 4.1.29. These left and the right lateral trailing vortices rotate clockwise and counter-clockwise, respectively and they stretch locations between x/H=-2.79 and x/H=0.35. They first grow and later shrink in size as they move downstream.

In addition, the size and the location of the trailing vortices obtained by using LES calculations are consistent with the results obtained by using PIV measurements in the wake region of the Ahmed body. While the wake flow travels further downstream, the size of rotating vortices become larger and their centre lines moves gradually downward. The major difference in the near-wake and far-wake flow fields downstream the Ahmed body is the shape of vortices formed. In the near-wake region, effects of vortices emanating from the slant, lateral and bottom surfaces

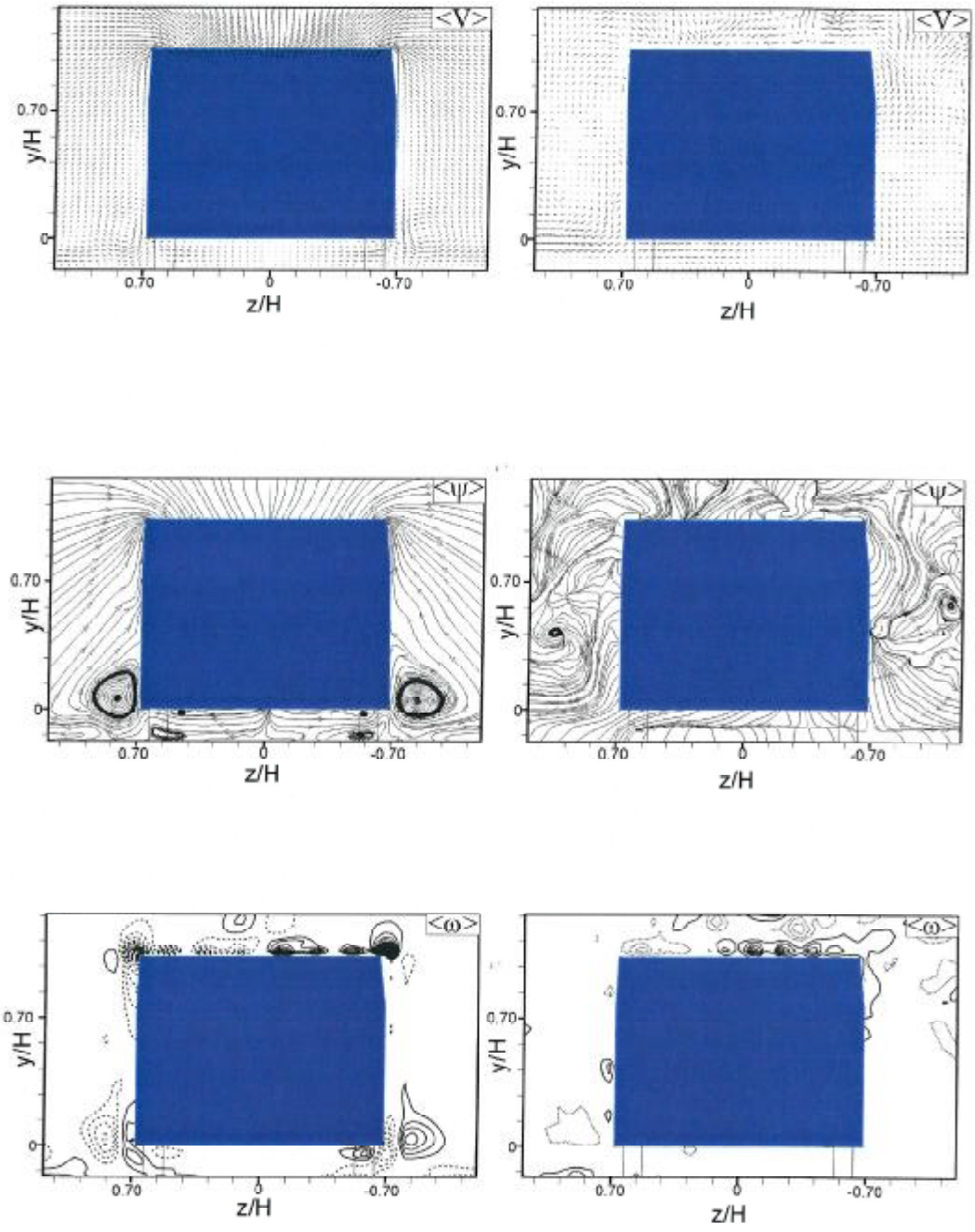

Numerical Experimental

Figure 4.1.25. Patterns of time-averaged velocity vectors map <V>, streamlines <ψ> and vorticity contours <ω> in the transversal yz-plane for x/H=-0.69 . Minimum and incremental values of vorticity are $<\omega_{min}>=\pm 1s^{-1}$ and $\Delta<\omega>=1s^{-1}$, respectively

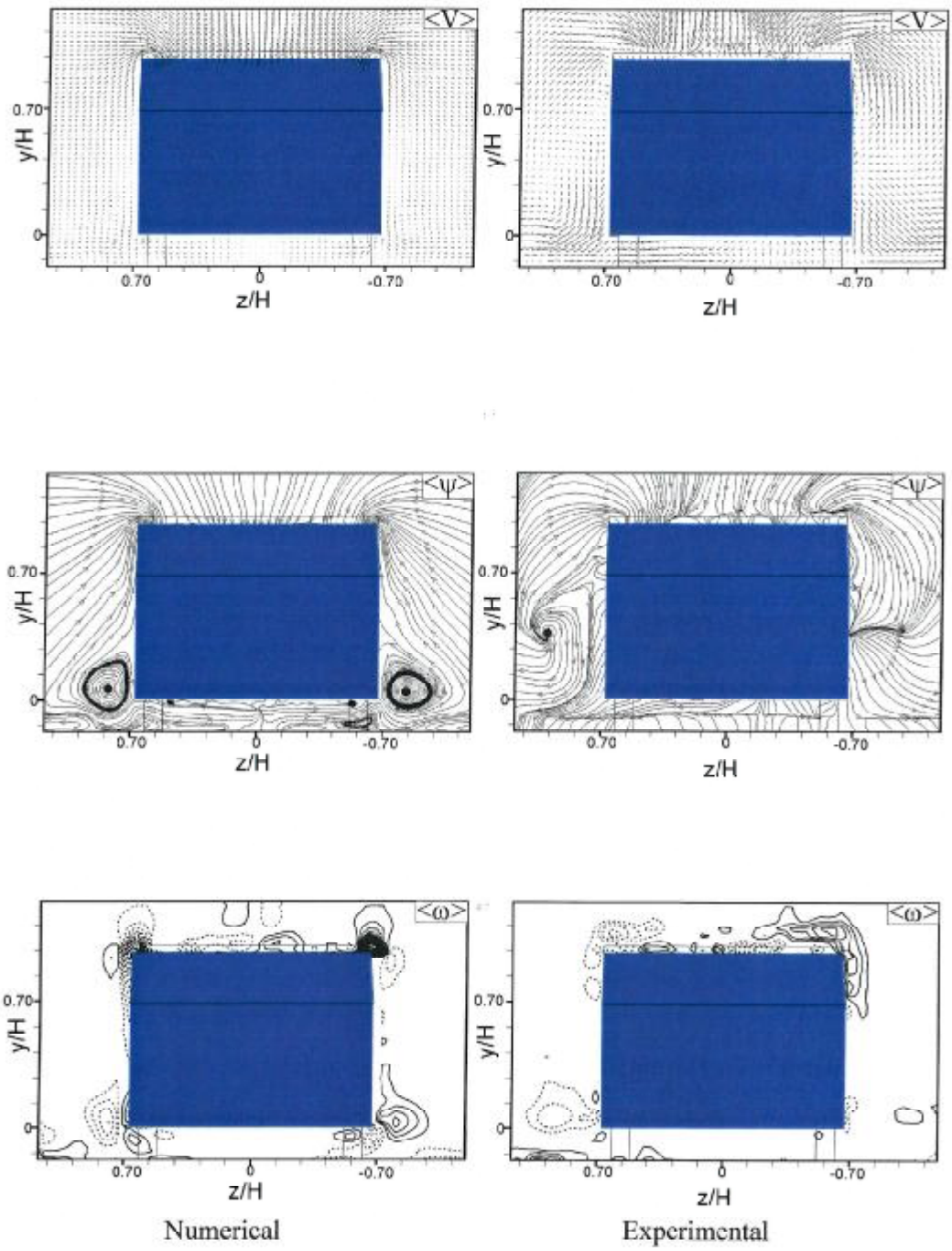

Figure. 4.1.26. Patterns of time-averaged velocity vectors map <V>, streamlines <ψ> and vorticity contours <ω> in the transversal yz-plane for x/H=-0.56. Minimum and incremental values of vorticity are $<\omega_{min}>=\pm 1s^{-1}$ and $\Delta<\omega>=1s^{-1}$, respectively

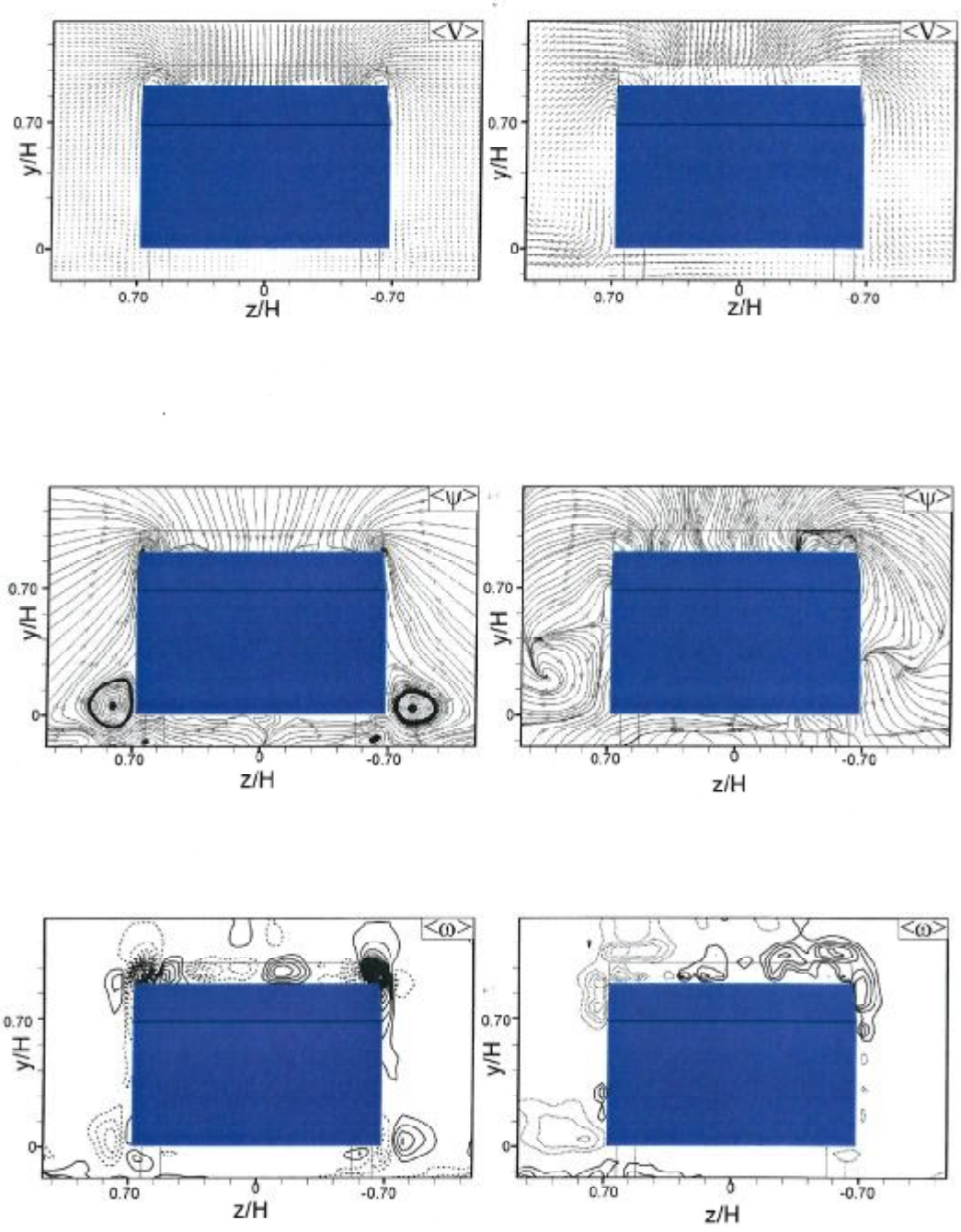

Figure 4.1.27. Patterns of time-averaged velocity vectors map <V>, streamlines <ψ> and vorticity contours <ω> in the transversal yz-plane for x/H=-0.42 . Minimum and incremental values of vorticity are $<\omega_{min}>=\pm 1 s^{-1}$ and $\Delta<\omega>=1 s^{-1}$, respectively

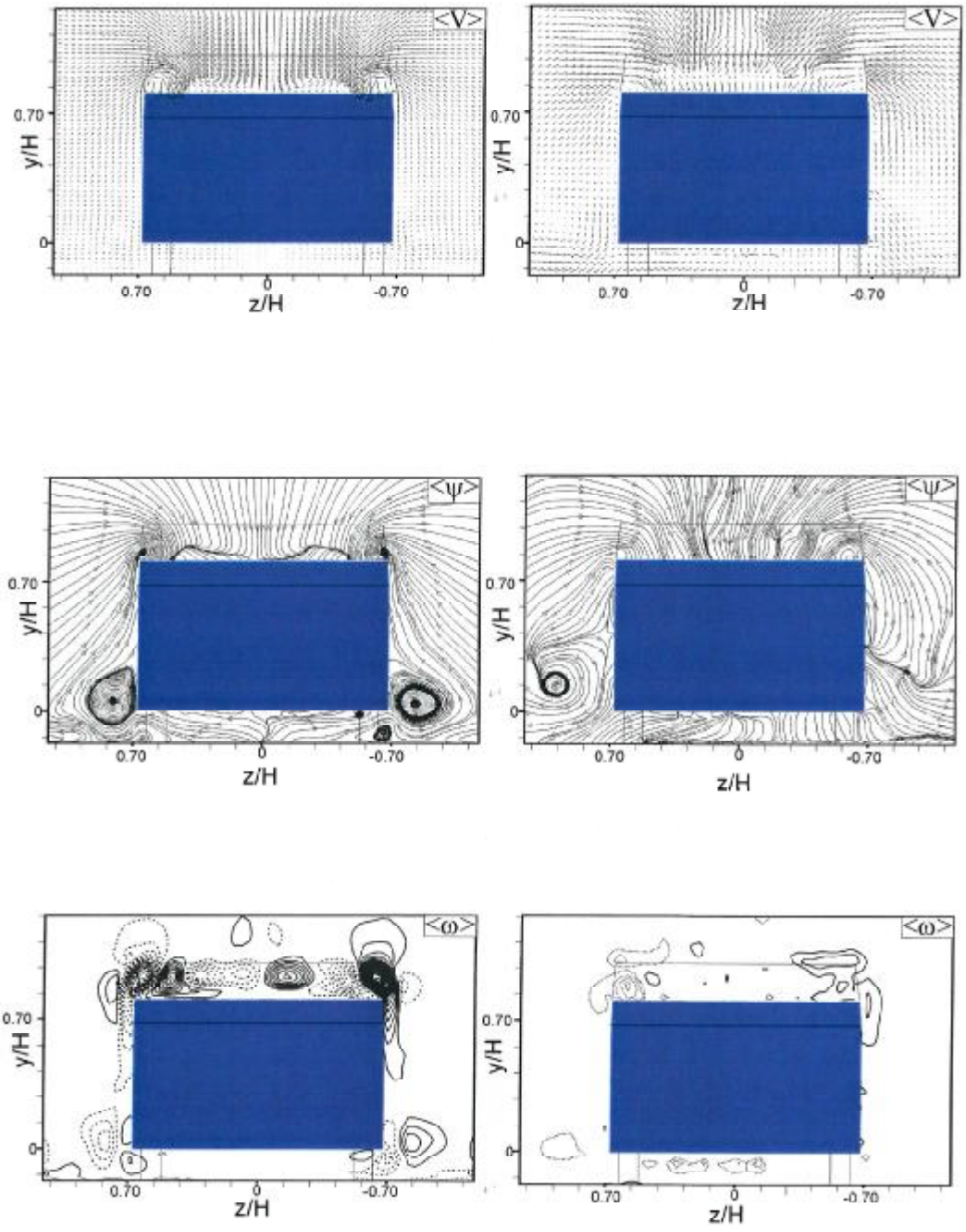

Numerical Experimental

Figure 4.1.28. Patterns of time-averaged velocity vectors map <V>, streamlines <ψ> and vorticity contours <ω> in the transversal yz-plane for x/H=-0.28. Minimum and incremental values of vorticity are $<\omega_{min}>=\pm 1 s^{-1}$ and $\Delta<\omega>=1 s^{-1}$, respectively

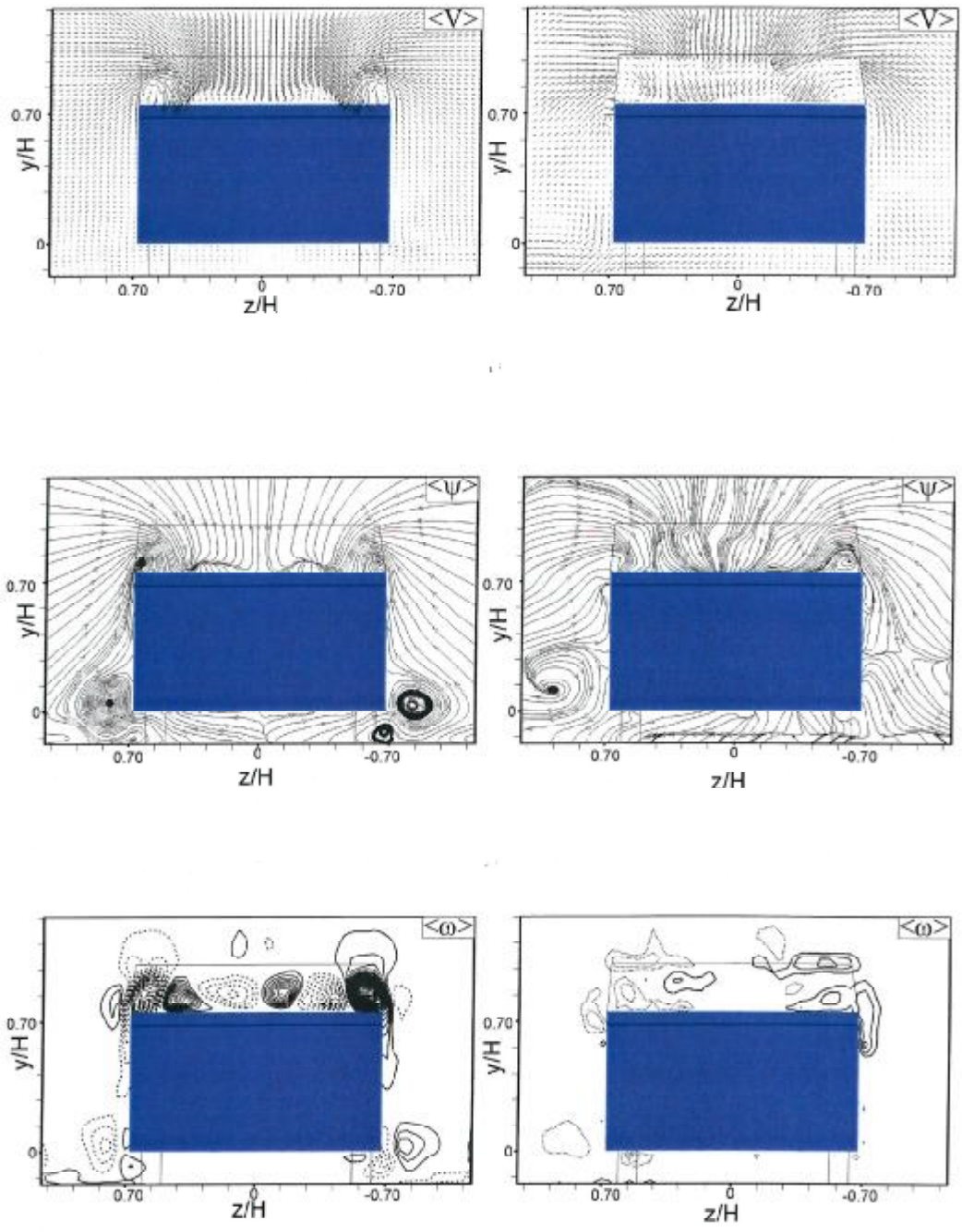

Numerical Experimental

Figure 4.1.29. Patterns of time-averaged velocity vectors map <V>, streamlines <ψ> and vorticity contours <ω> in the transversal yz-plane for x/H=-0.14. Minimum and incremental values of vorticity are $<\omega_{min}>=\pm 1 s^{-1}$ and $\Delta<\omega>=1 s^{-1}$, respectively

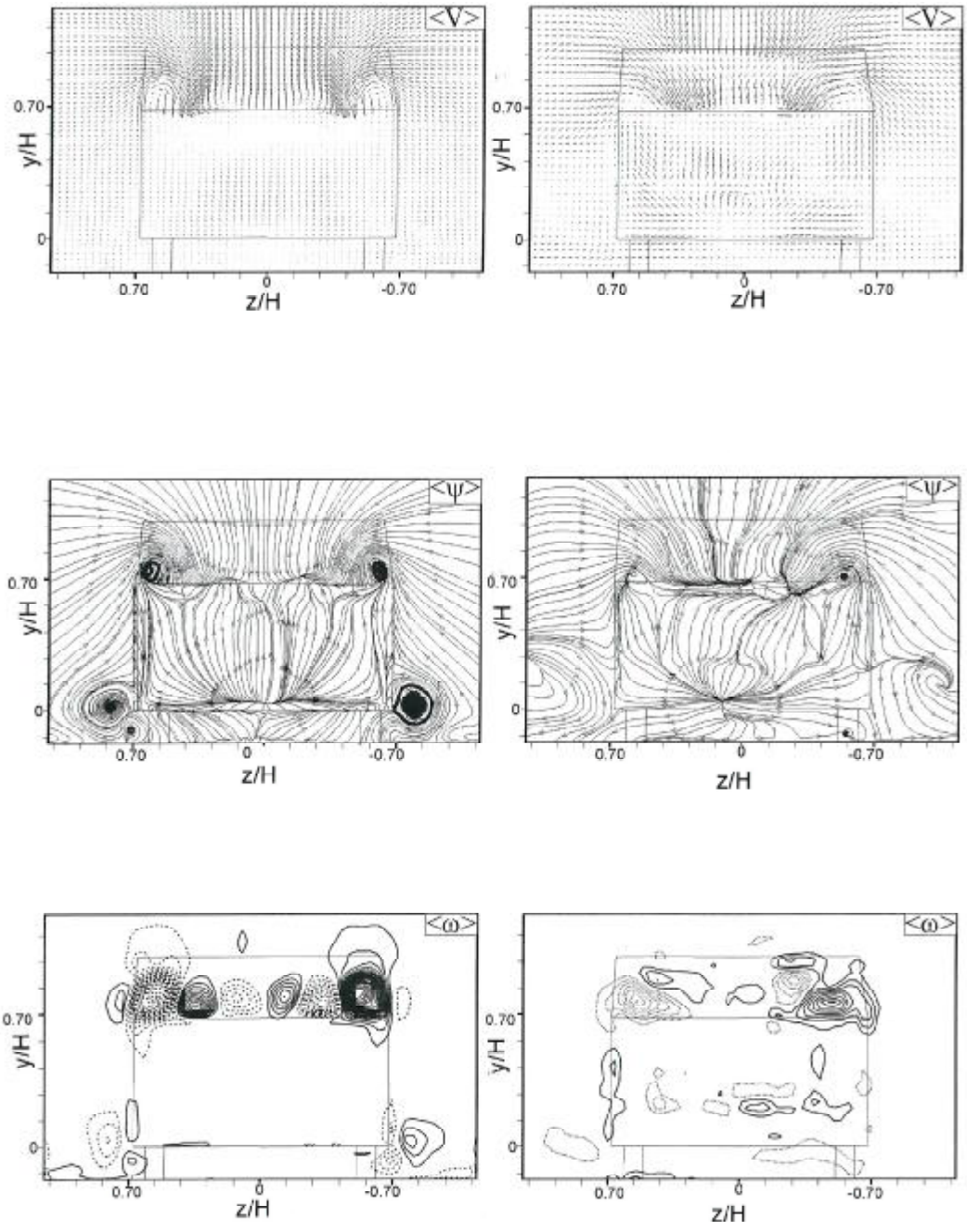

Numerical Experimental

Figure 4.1.30. Patterns of time-averaged velocity vectors map <V>, streamlines <ψ> and vorticity contours <ω> in the transversal yz-plane for x/H=0. Minimum and incremental values of vorticity are $<\omega_{min}>=\pm 1 s^{-1}$ and $\Delta<\omega>=1 s^{-1}$, respectively

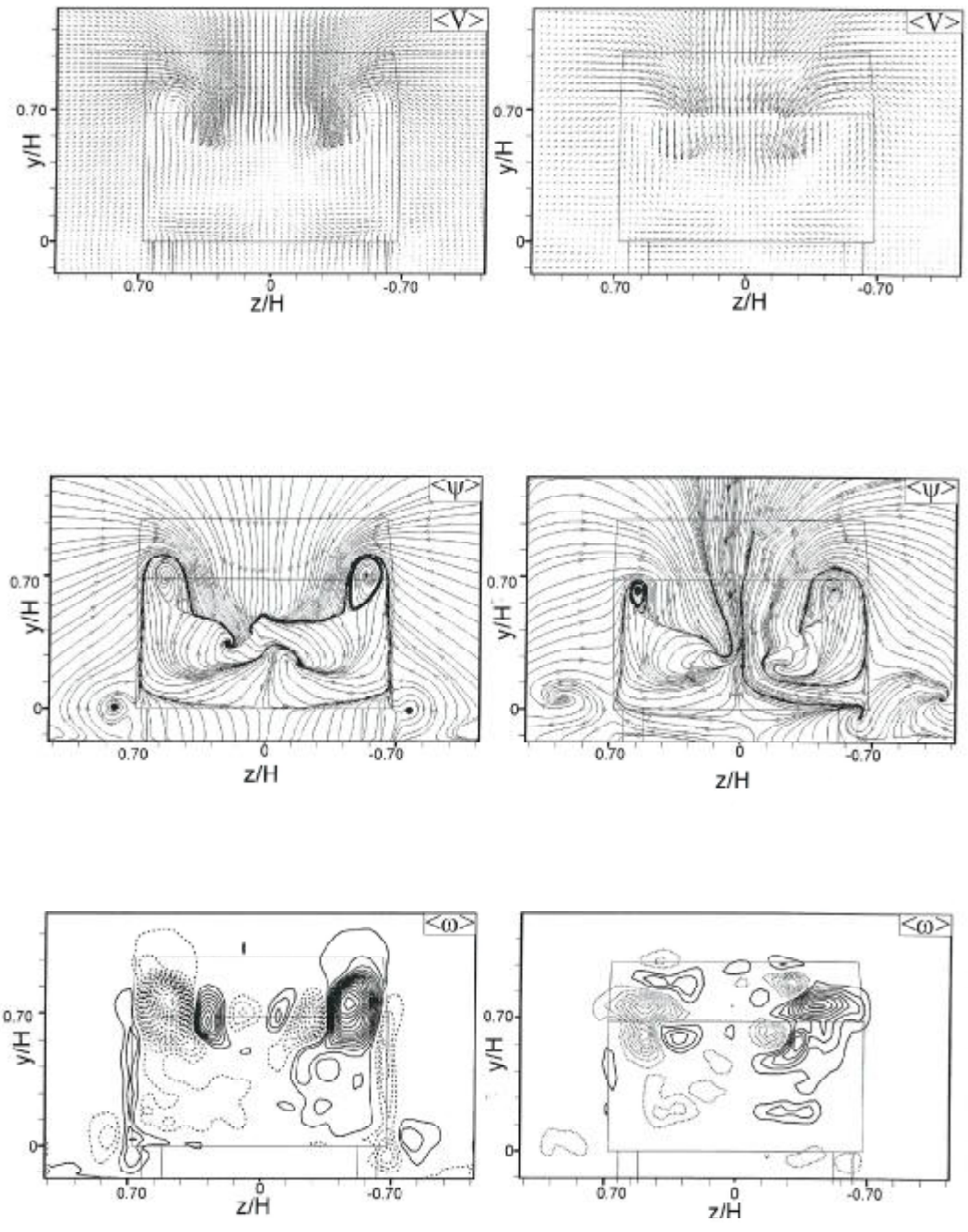

Numerical Experimental

Figure 4.1.31. Patterns of time-averaged velocity vectors map <V>, streamlines <ψ> and vorticity contours <ω> in the transversal yz-plane for x/H=0.21. Minimum and incremental values of vorticity are $<\omega_{min}>=\pm 1 s^{-1}$ and $\Delta<\omega>=1 s^{-1}$, respectively

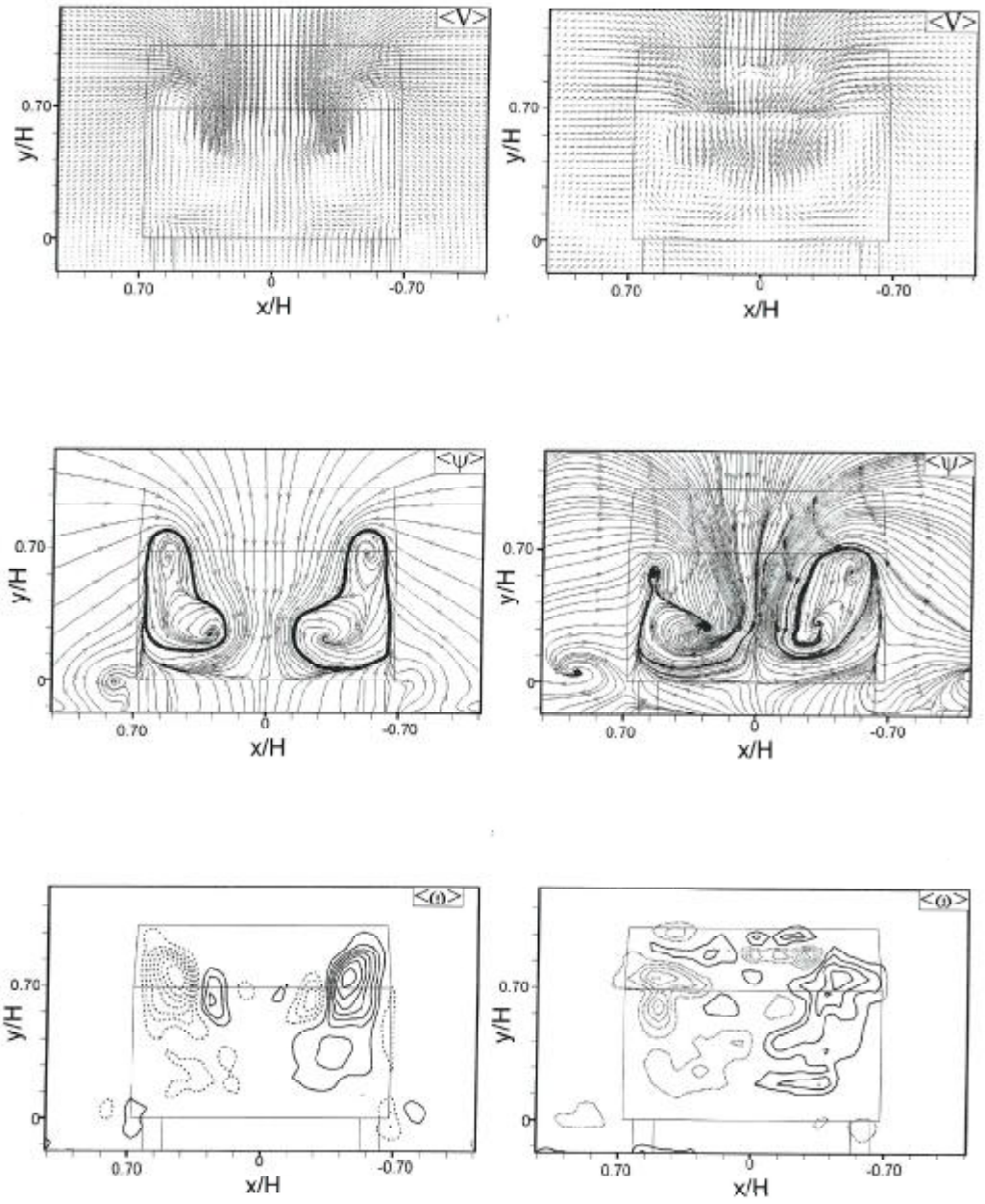

Figure 4.1.32. Patterns of time-averaged velocity vectors map <V>, streamlines <ψ> and vorticity contours <ω> in the transversal yz-plane for x/H=0.28. Minimum and incremental values of vorticity are $<\omega_{min}>=\pm 1s^{-1}$ and $\Delta<\omega>=1s^{-1}$, respectively

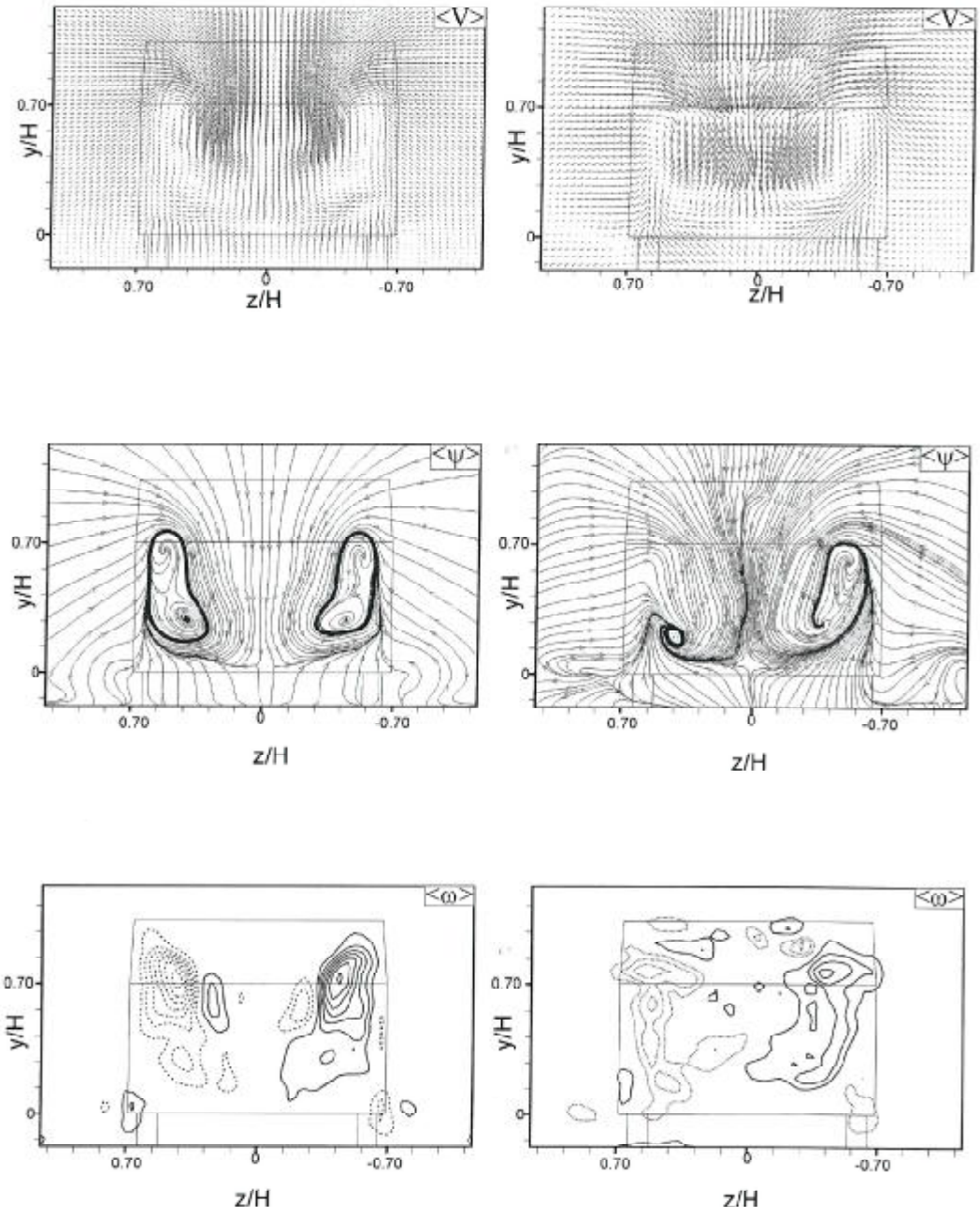

Numerical Experimental

Figure 4.1.33. Patterns of time-averaged velocity vectors map <V>, streamlines <ψ> and vorticity contours <ω> in the transversal yz-plane for x/H=0.35. Minimum and incremental values of vorticity are $<\omega_{min}>=\pm 1 s^{-1}$ and $\Delta<\omega>=1 s^{-1}$, respectively

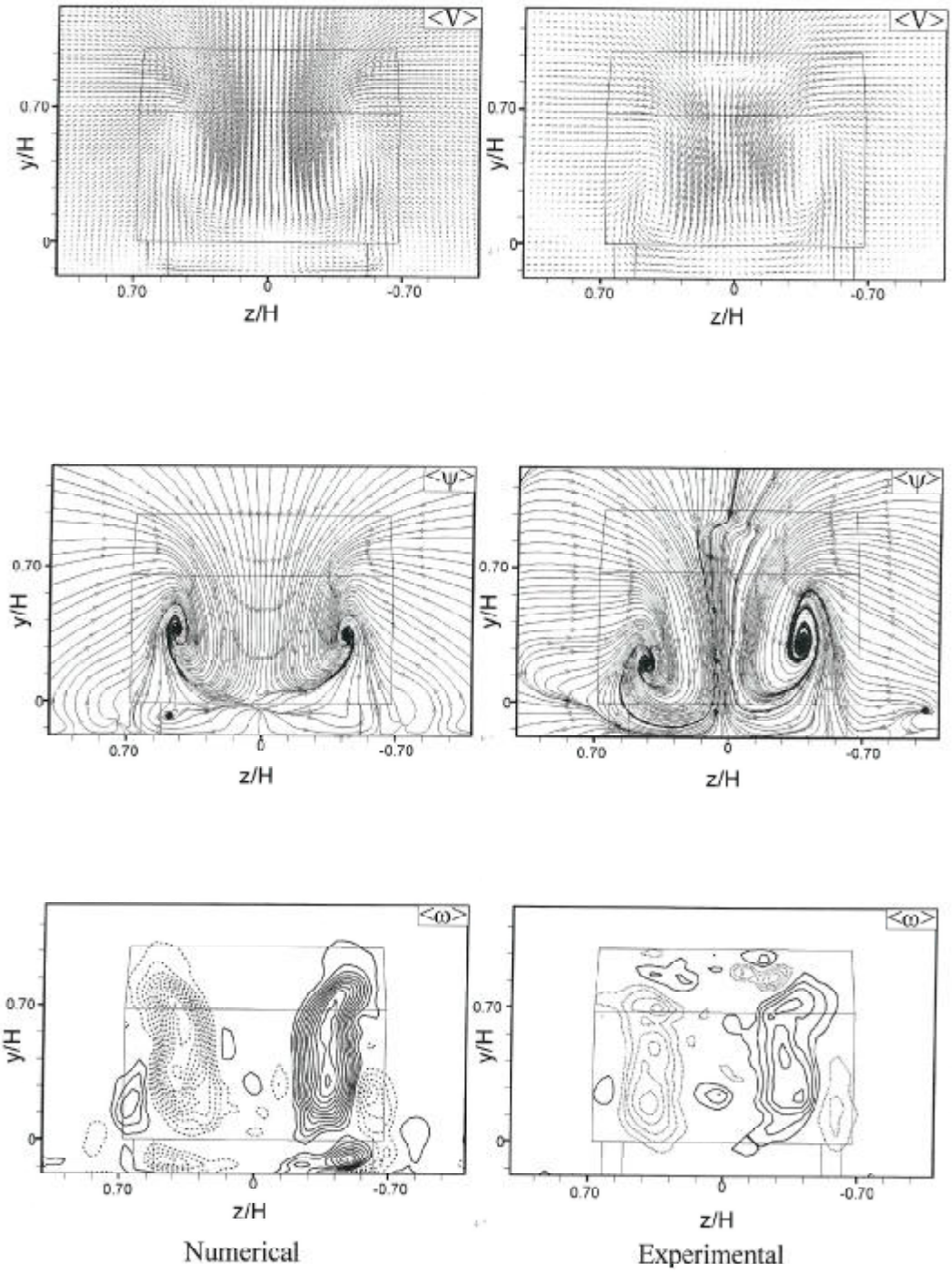

Figure 4.1.34. Patterns of time-averaged velocity vectors map <V>, streamlines <ψ> and vorticity contours <ω> in the transversal yz-plane for x/H=0.70. Minimum and incremental values of vorticity are $<\omega_{min}>=\pm 1 s^{-1}$ and $\Delta<\omega>=1 s^{-1}$, respectively

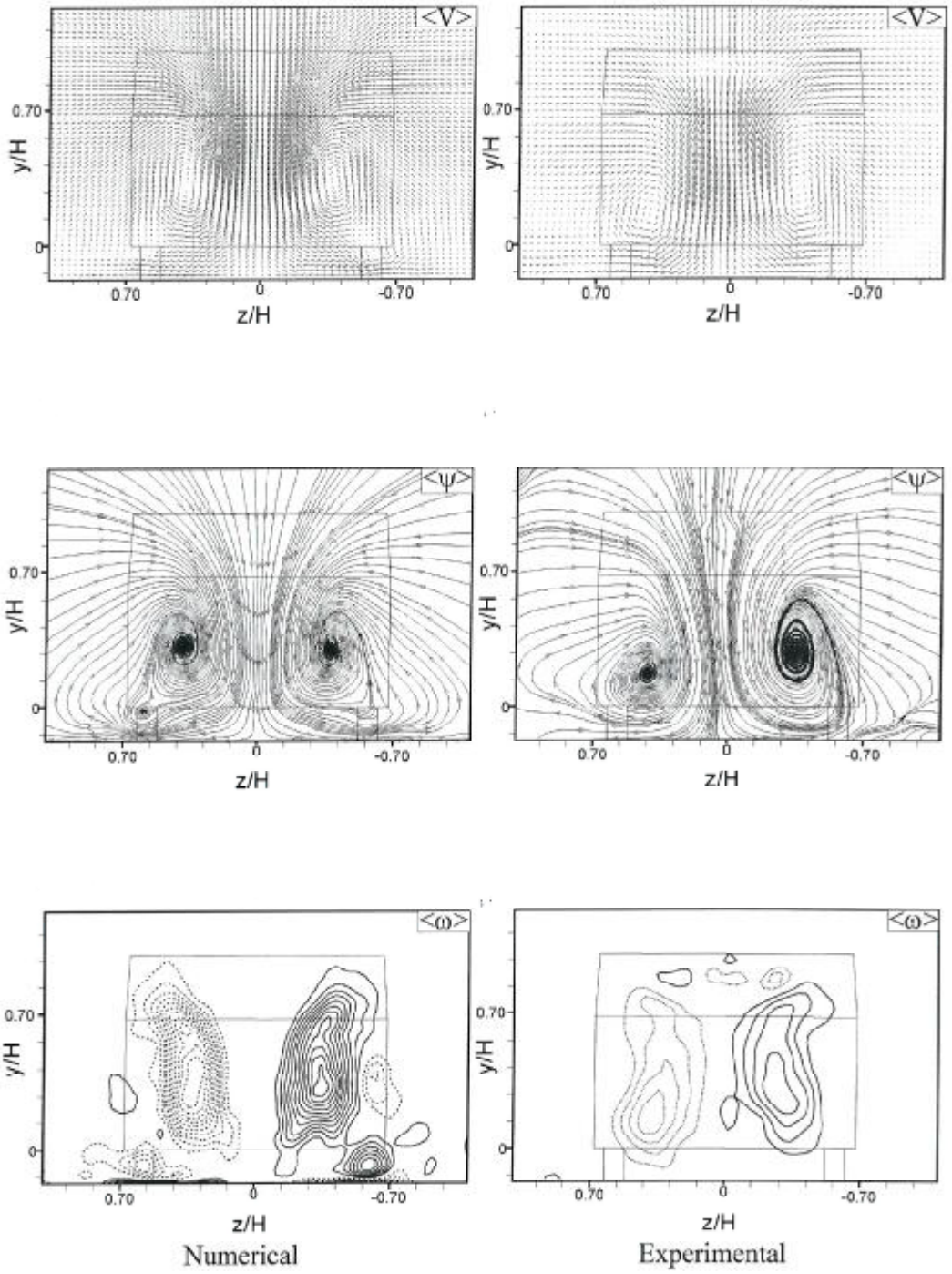

Figure 4.1.35. Patterns of time-averaged velocity vectors map <V>, streamlines <ψ> and vorticity contours <ω> in the transversal yz-plane for x/H=1.04 . Minimum and incremental values of vorticity are $<\omega_{min}>=\pm 1 s^{-1}$ and $\Delta<\omega>=1 s^{-1}$, respectively

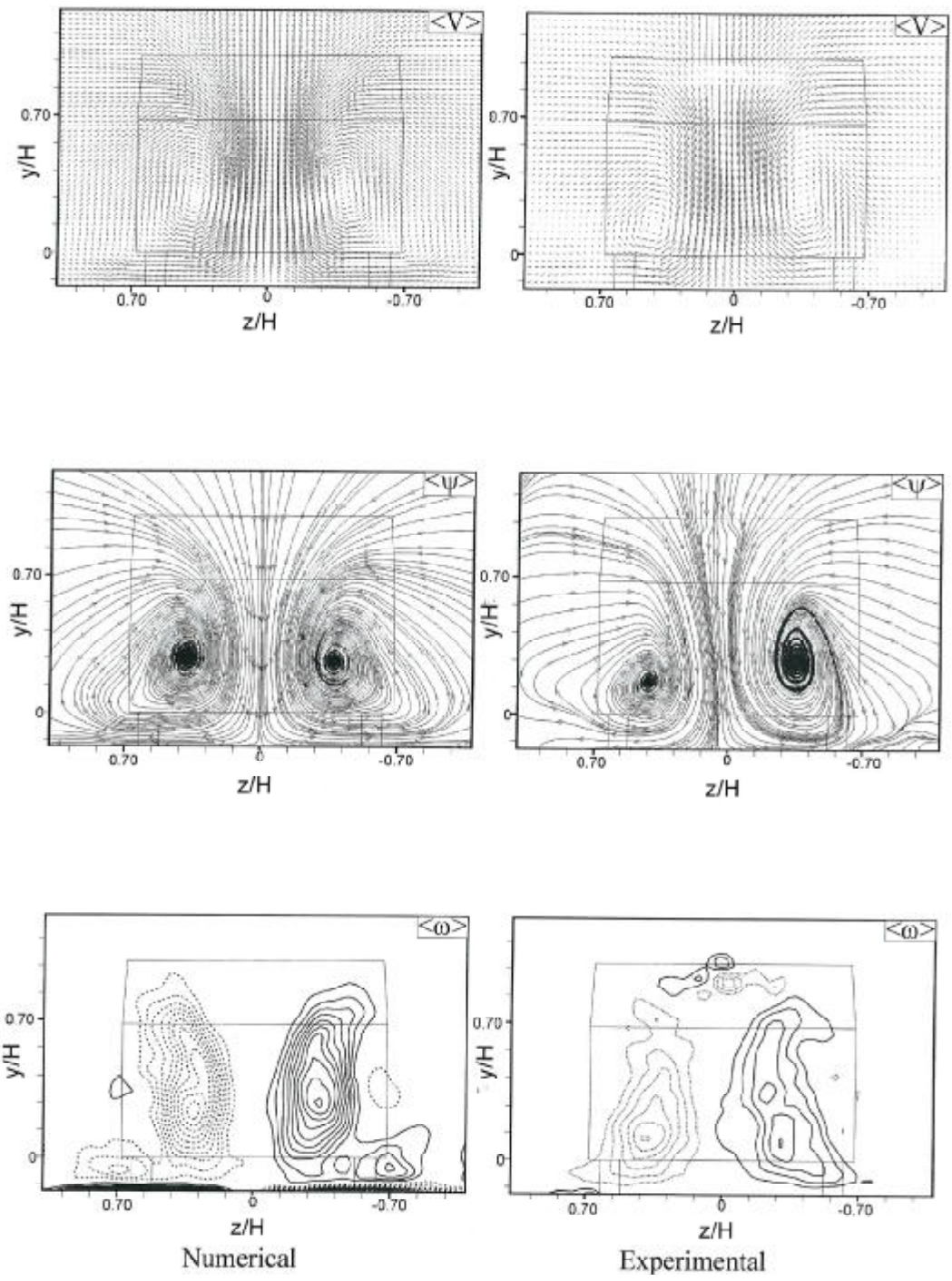

Figure 4.1.36. Patterns of time-averaged velocity vectors map <V>, streamlines <ψ> and vorticity contours <ω> in the transversal yz-plane for x/H=1.39. Minimum and incremental values of vorticity are $<\omega_{min}>=\pm 1 s^{-1}$ and $\Delta<\omega>=1 s^{-1}$, respectively

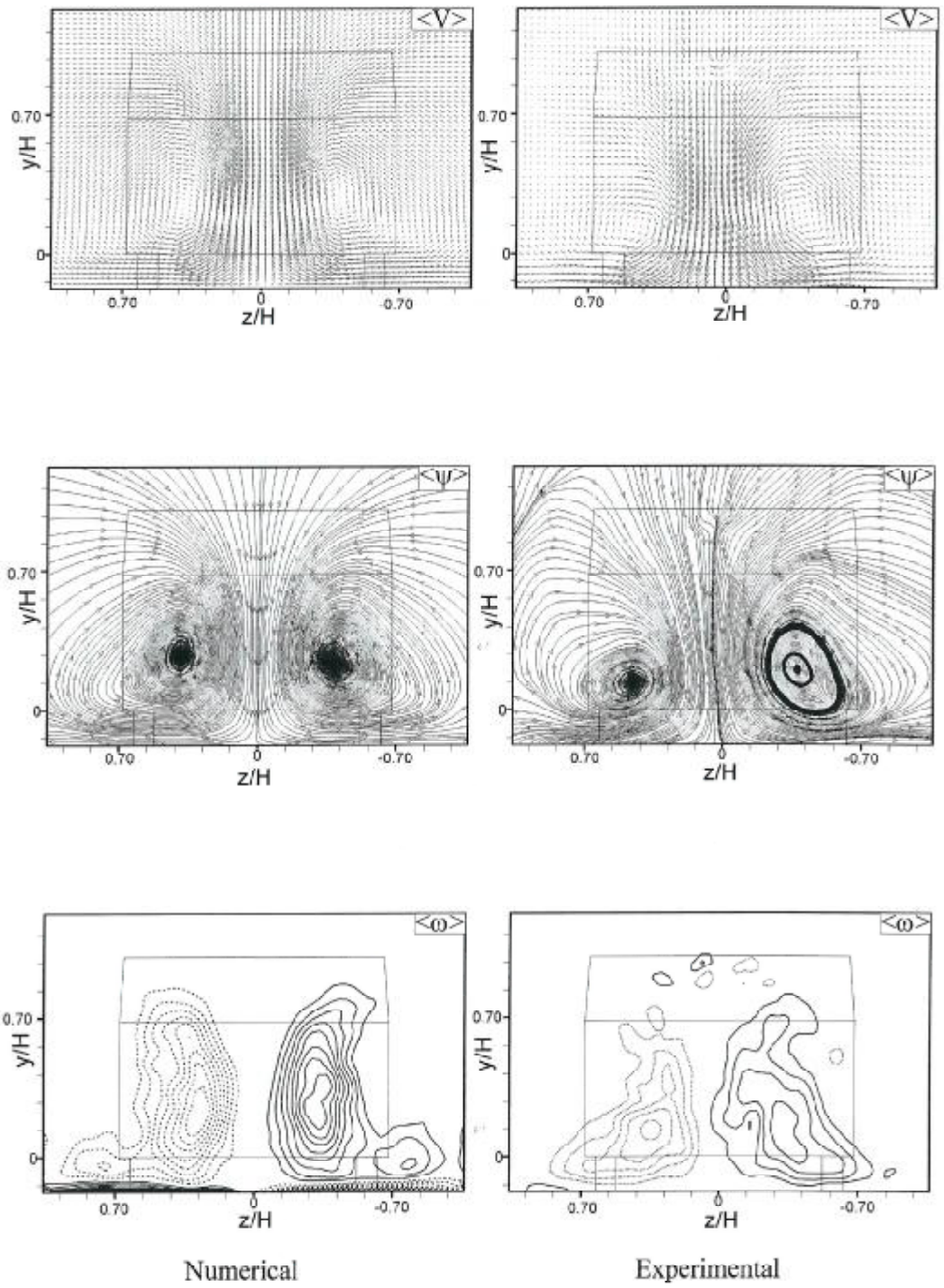

Figure 4.1.37. Patterns of time-averaged velocity vectors map <V>, streamlines <ψ> and vorticity contours <ω> in the transversal yz-plane for x/H=1.74. Minimum and incremental values of vorticity are $<\omega_{min}>=\pm 1 s^{-1}$ and $\Delta<\omega>=1 s^{-1}$, respectively

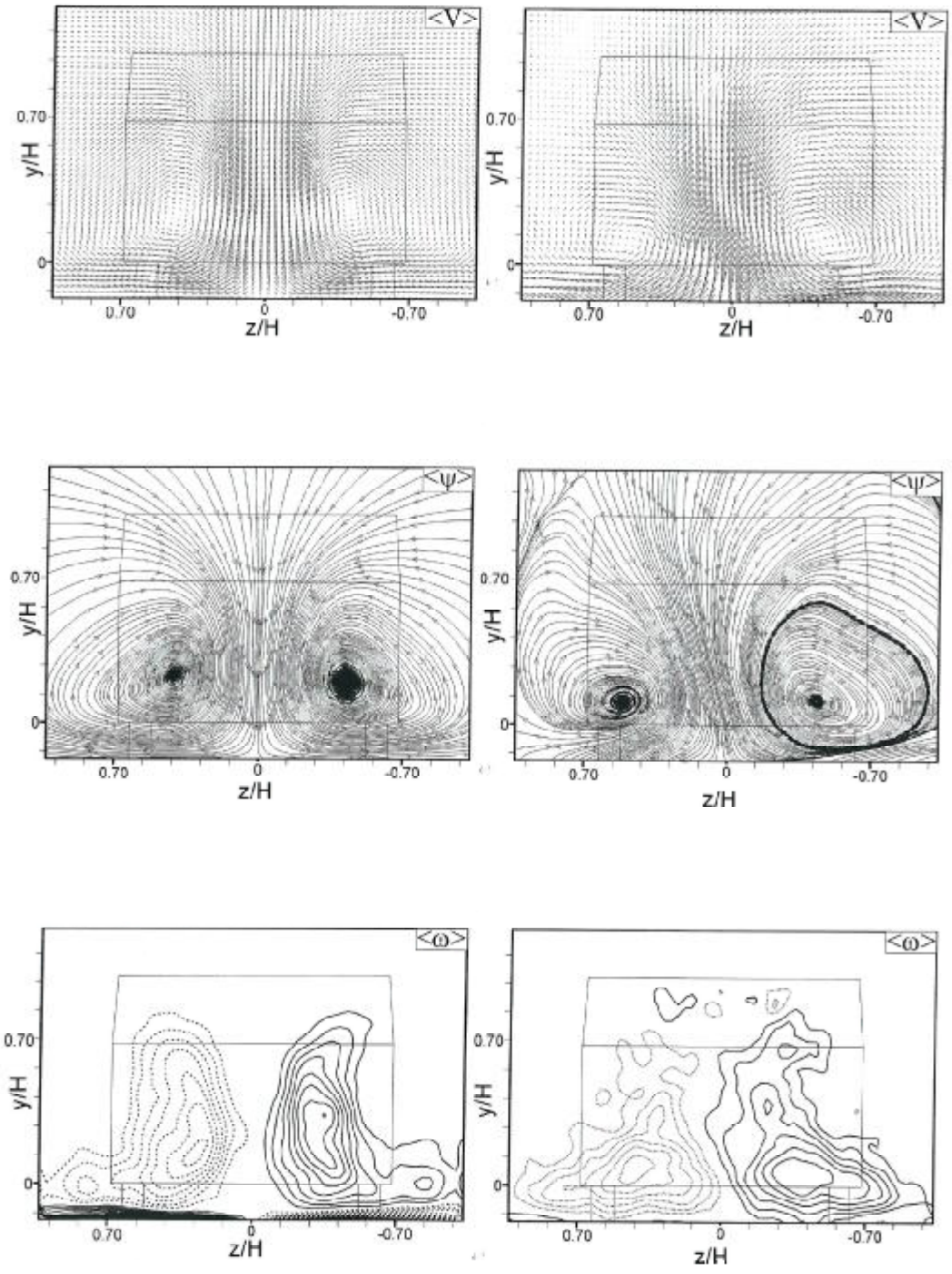

Numerical Experimental

Figure 4.1.38. Patterns of time-averaged velocity vectors map <V>, streamlines <ψ> and vorticity contours <ω> in the transversal yz-plane for x/H=2.08. Minimum and incremental values of vorticity are $<\omega_{min}>=\pm 1 s^{-1}$ and $\Delta<\omega>=1 s^{-1}$, respectively

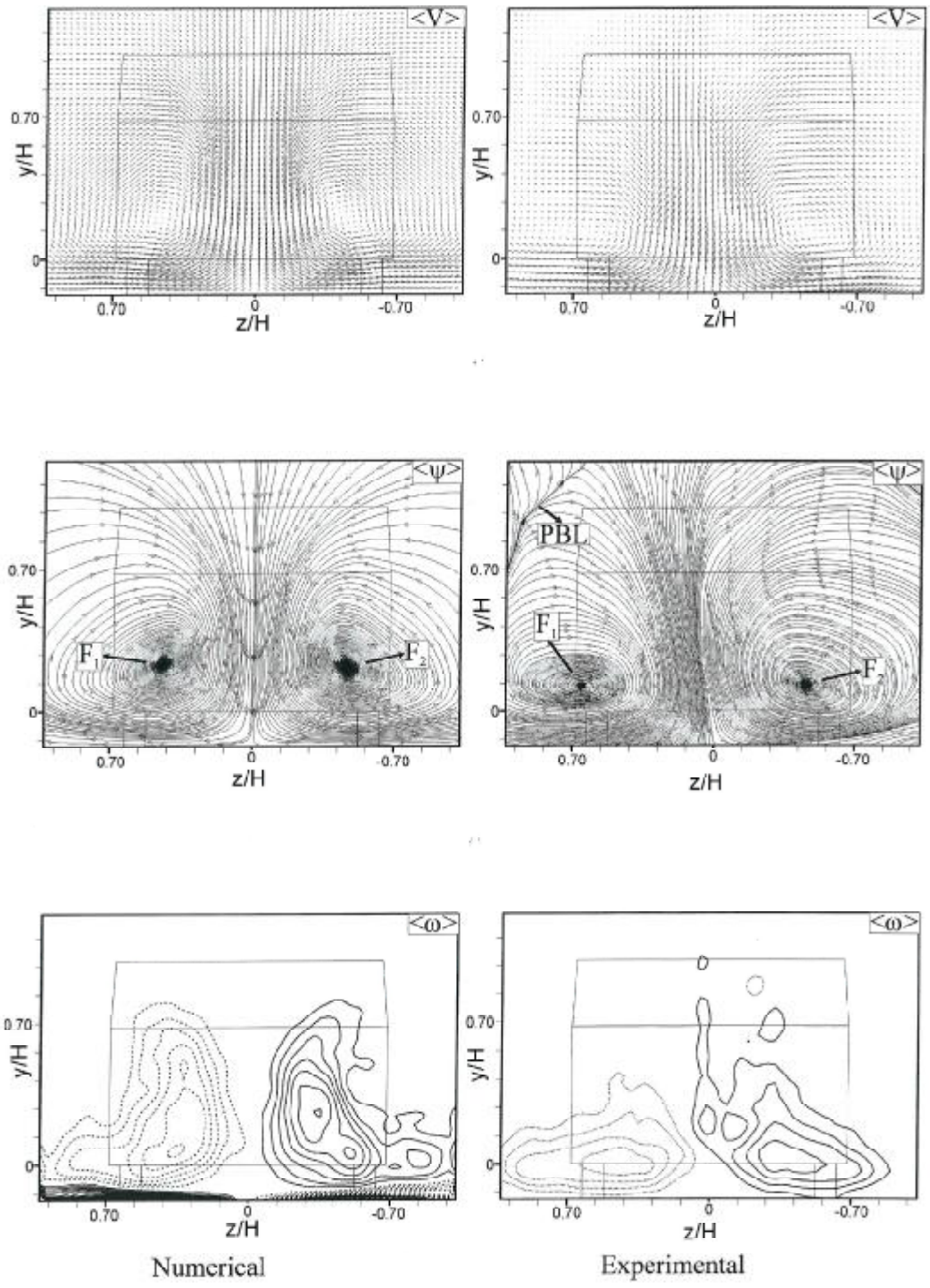

Figure 4.1.39. Patterns of time-averaged velocity vectors map <V>, streamlines <ψ> and vorticity contours <ω> in the transversal yz-plane for x/H=2.43. Minimum and incremental values of vorticity are $<\omega_{min}>=\pm 1 s^{-1}$ and $\Delta<\omega>=1 s^{-1}$, respectively

of the Ahmed body are observed individually. Furthermore, as the flow moves in the stream-wise direction through the far-wake, effects of all vortices emanating from different part of the Ahmed body become weaker, and then they are replaced by the counter rotating trailing vortices. The flow fields downstream of the body at locations between x/H=0.69 and 1.39 are dominated by this pair of counter rotating trailing vortices. In addition, two counter rotating longitudinal vortices can clearly be observed downstream at the location of x/H=2.43 as shown in Figure 4.1.39. There is a strong down-wash flow between the counter rotating longitudinal vortices in all transversal planes presented through the wake of the Ahmed body.

4.1.2.2. Time-Averaged Velocity Profiles

In Figures 4.1.40 and 4.1.41, time-averaged normalized velocity profiles, <u>/U and <v>/U obtained in the present LES calculations and PIV measurements on the slanted surface and in the wake region downstream of the Ahmed body in the vertical symmetry plane (z/H=0) are presented, respectively. They are also compared with the experimental data of Lienhart et al. (2000) at the corresponding locations on the slant and in the wake region downstream of the Ahmed body. In these figures, the velocity profiles are presented for positions between x/H=-0.694 and x/H=1.25, where the intervals between two velocity profiles are $\Delta x/H$=0.069 and 0.139 on the slant and through the wake region downstream of the body, respectively. Velocity components are normalized with the free-stream velocity, U. When the literature is reviewed, all profiles of flow data are generally provided in the symmetry plane, z/H=0. Almost all velocity profiles found in the present LES calculations agree well with the present PIV measurements and LDA measurements reported by Lienhart et al. (2000) both on the slant and in the wake. Stream-wise velocity profiles, <u>/U results of the LES calculation are in good agreement with the experimental data at almost all positions on the slant and in the near wake as shown in Figure 4.1.40. On the other hand, profiles of normal velocity of the flow, <v>/U obtained using LES calculations are also in good agreement with the experimental data in the near wake region but they show some discrepancies on the slant. The PIV measurement results

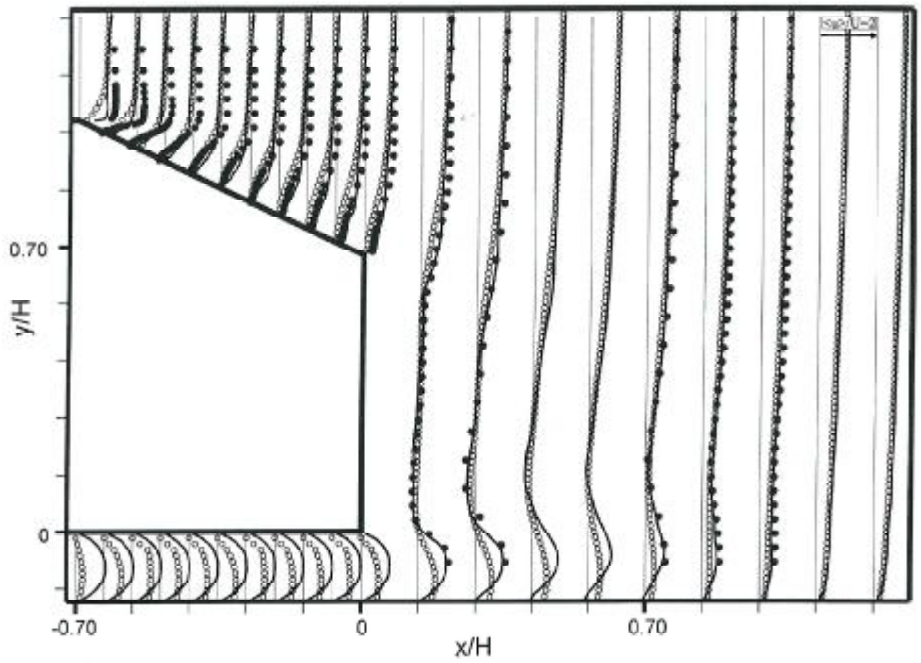

Figure 4.1.40. Time-averaged streamwise velocity, <u>/U profiles in the vertical symmetry plane z/H=0 on the slant surface and wake region of the Ahmed body. LES results (solid curve), PIV results (empty circles) and results of Lienhart et al.(2000) (filled circles)

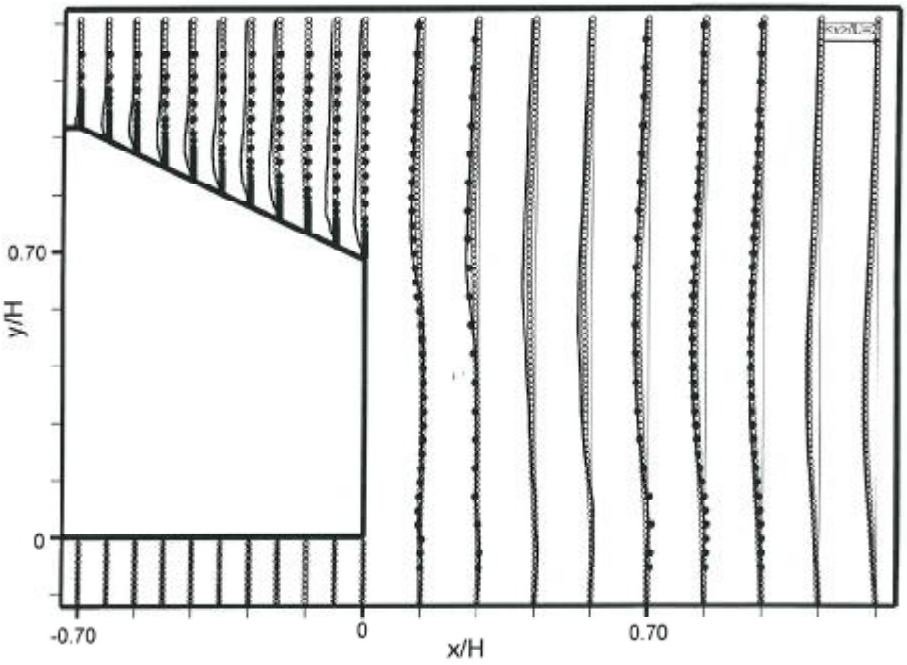

Figure 4.1.41. Time-averaged normal velocity, <v>/U profiles in the the vertical symmetry plane z/H=0 on the slant surface and wake region of the Ahmed body. LES results (solid curve), PIV results (empty circles) and results of Lienhart et al. (2000) (Filled circles)

have smaller stream-wise velocities under the body and through the shear layer occurred at the lower part of the near wake. Stream-wise velocity results of Lienhart et al. (2000) show negative values between x/H=-0.625 and x/H=-0.347 which means that flow separates just after the beginning of the slant surface and re-attaches almost at the half of the slant surface. On the other hand, stream-wise velocity results of PIV measurements on the slant surface show negative values only at x/H=-0.347, which is approximately half of the slant surface. In other words PIV can measure the separated flow as a small region nearly at a position about the half of the slant surface in the symmetry plane. In addition, stream-wise velocity results of the LES computations on the slant surface show negative values between x/H=-0.0694 and -0.208 and at x/H=-0.556. This means that LES computations can compute a small separated flow region after the beginning of the slant surface, and then relatively large separated flow region between the half point and end point of the slant surface. However, flow is reattached on the slant surface prior to the end of the body in both our computational and experimental results as also seen in the experiments of Lienhart et al. (2000). The wake flow downstream of the body is reversed causing a negative velocity between positions of x/H=0.139 and x/H=0.556. The maximum reversed velocity in the recirculatory flow region is approximately 0.193, 0.280, 0.369 times the free-stream velocity, U as seen in the results of the present PIV measurements and LES calculations and Lienhart et al. (2000) measurements. It is noteworthy that the locations of the maximum reversed velocity are nearly at the same point in both experimental and numerical results, which are about x/H=0.278 and y/H=0.278 in the stream-wise and normal direction of the flow, respectively. In the first measuring plane at a position of x/H=0.139, stream-wise velocity components take negative values between y/H=0.0126, 0.0150, 0.0278 and y/H=0.256, 0.378, 0.271 for the results of the present PIV measurements and LES computations and Lienhart et al. (2000) measurements, respectively. Stream-wise velocity components also take negative values through three locations at x/H=0.278, 0.417 and 0.556 with decreasing amount. Because of the jet flow occurring between the ground and the bottom surface of the body, the value of stream-wise velocity increases in the lower part of the wake region. The rate of increase in the stream-wise

velocity across the shear layer at the upper part of the body is due to the entrainment between wake and the core flow regions. The jet flow emanating from the narrow gap between the ground board and the bottom surface of the model travels towards the mid-section of the model and later interacts with the flow coming from the slant surface of the body. As a result of this interaction, a negative velocity region also called as near wake region occurs downstream of the body between the measuring section of x/H=0.139 and 0.556. Since the fifth measuring section, x/H=0.694 correspond to just after the saddle point, stream-wise velocity distribution profiles after position of x/H=0.694 do not indicate any negative velocity value.

Figure 4.1.41 displays the time-averaged profiles of normal velocity component of the flow, <v>/U in the vertical symmetry plane. Rapid changes in velocity profiles occur on the slant and through the upper shear layers. The computed normal velocity, <v>/U profiles show some differences as compared with the measured velocity, <v>/U results on the slanted surface and near wake region. These velocity profiles reveal that there is an intense shear throughout the velocity field. Positive normal velocity, <v>/U results in the near wake indicates upsweep flow. The maximum upsweep velocities are 0.0428, 0.111, 0.180 times the free stream velocity, U for the results of the present PIV measurements and LES calculations and Lienhart et al. (2000) measurements, respectively. The locations of the maximum upsweep velocity are nearly at the same point in both experimental and numerical results which are about x/H=0.417 and y/H=-0.0447. Furthermore, the maximum down-sweep velocities are -0.413, -0.492, -0.478 times the free stream velocity, U for the results of the present PIV measurements and LES calculations and Lienhart et al. (2000) measurements, respectively. The locations of the maximum down-sweep velocities in the stream-wise direction are x/H=0.69 for both LES results and results of Lienhart et al. (2000) and 1.11 for the PIV results. The locations of the maximum down-sweep velocities in the normal direction are also y/H=0.588, 0.664 and 0.757 for the results of the present PIV measurements and LES computations and Lienhart et al. (2000) measurements, respectively. The velocity field viewing both distributions of the velocity components, <u> and <v> present that, the flow field is not symmetric in the vertical symmetry plane due to the ground effect.

4.1.2.3. Profiles of the RMS of Stream-wise and Normal Velocity Components, and Reynolds Stress Correlations

Figures 4.1.42, 4.1.43 and 4.1.44 present profiles of the root mean square of stream-wise and normal velocity components, $\langle u_{rms} \rangle/U$ and $\langle v_{rms} \rangle/U$ normalized by free stream velocity, U and Reynolds stress correlation, $\langle u'v' \rangle/U^2$ normalized by square of the free stream velocity in the vertical symmetry plane, z/H=0. In these figures, profiles are presented on the slant and in the wake region downstream of the body for positions between x/H=-0.69 and x/H=1.25, where the space differences between two profiles are $\Delta x/H=0.069$ and 0.139 on the slant and through the wake region, respectively. The locations of peak values of $\langle u_{rms} \rangle/U$ and $\langle v_{rms} \rangle/U$ hold places along the upper-body and under-body shear layers. The magnitude of the root mean square of stream-wise velocity fluctuations, $\langle u_{rms} \rangle/U$ shown in Figure 4.1.42 is higher in the under-body shear layer than that of in the upper-body shear layer. The peak values and their locations of $\langle u_{rms} \rangle$ in the upper-body and under-body shear layers through the vertical symmetry plane of z/H=0 for the results of the

Table 4.1.2. Peak values and their locations of $\langle u_{rms} \rangle$ in the upper-body and under-body shear layers through the vertical symmetry plane of z/H=0

	Upper-body Shear Layer			Under-body Shear Layer		
		Locations of Peak Value of $\langle u_{rms} \rangle/U$			Locations of Peak Value of $\langle u_{rms} \rangle/U$	
	Peak Value of $\langle u_{rms} \rangle/U$	In the Stream-wise Direction (x/H)	In the Normal Direction (y/H)	Peak Value of $\langle u_{rms} \rangle/U$	In the Stream-wise Direction (x/H)	In the Normal Direction (y/H)
LES Results	0.159	0.139	0.658	0.306	0.417	-0.0130
PIV Results	0.156	0.139	0.715	0.194	0.556	-0.0160
Lienhart et al. (2000)	0.178	0.139	0.757	0.315	0.480	-0.0111

present LES computations and PIV measurements and Lienhart et al. (2000) measurements are given in Table 4.1.2.

The results presented in Table 4.1.2 show that the maximum $<u_{rms}>$ value found in the upper-body shear layer is formed just after the vehicle body in the stream-wise direction and aligned slightly above the trailing edge of the slant surface of the body in the vertical direction. Maximum deviation of $<u_{rms}>$ values of LES results from that of the PIV results is 0.3% and from the results of Lienhart et al.(2000) is 1.9% in the upper-body shear layer region of the symmetry plane z/H=0. In this region, maximum deviation of the location of peak $<u_{rms}>$ values of LES results from the PIV results and the results of Lienhart et al.(2000) coincide in the stream-wise direction and it deviates 5.7% from the PIV results and 9.9% from the results of Lienhart et al.(2000) in the vertical direction. But maximum deviation of peak $<u_{rms}>$ values of the present LES results from PIV results is 11.2% and from the results of Lienhart et al.(2000) is 0.9% in the under-body shear layer region. These results show that the maximum $<u_{rms}>$ value found in the under-body shear layer is formed at nearly half length of the model height after the body in the stream-wise direction and aligned slightly below the bottom end of the body in the vertical direction. Maximum deviation of the location of peak values of $<u_{rms}>$ between the present LES results and the PIV results are 13.9% in the stream-wise direction and 0.3% in the vertical direction. Maximum deviation of the location of peak values of $<u_{rms}>$ between the present LES results and the results of Lienhart et al.(2000) are 6.3% in the stream-wise direction and 0.19% in the vertical direction in the under-body shear layer region.

Profiles of the root mean square of $<v_{rms}>/U$ presented in Figure 4.1.43 show similar trend with profiles of $<u_{rms}>/U$. The maximum values of $<v_{rms}>/U$ are approximately 0.15, 0.26 at a position of x/H=0.694 for the results of our PIV measurements and LES computations, respectively. These values of $<v_{rms}>/U$ are smaller than the corresponding value of $<u_{rms}>/U$ at the same location. The magnitude of the root mean square of the stream-wise velocity fluctuations, $<v_{rms}>/U$ shown in Figure 4.1.43 are higher along the under-body shear layer than that of the upper-body shear layer. The peak values and their locations of $<v_{rms}>$ in the upper-

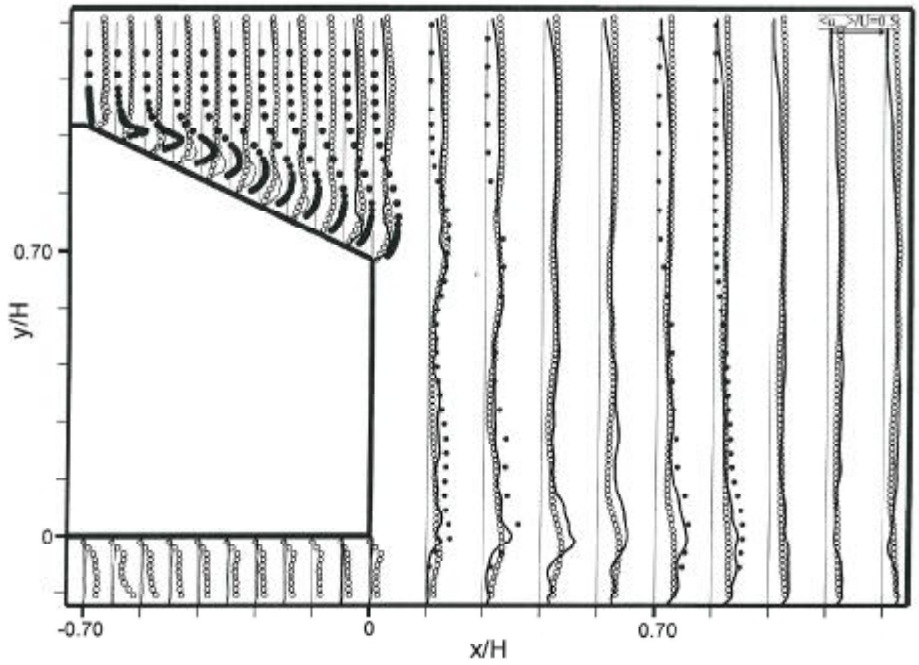

Figure.4.1.42. Time-averaged root mean square of $<u_{rms}>/U$ profiles in the symmetry plane z/H=0 on the slant surface and wake region of the Ahmed body. LES results (solid curve), PIV results (empty circles) and results of Lienhart et al. (2000) (filled circles)

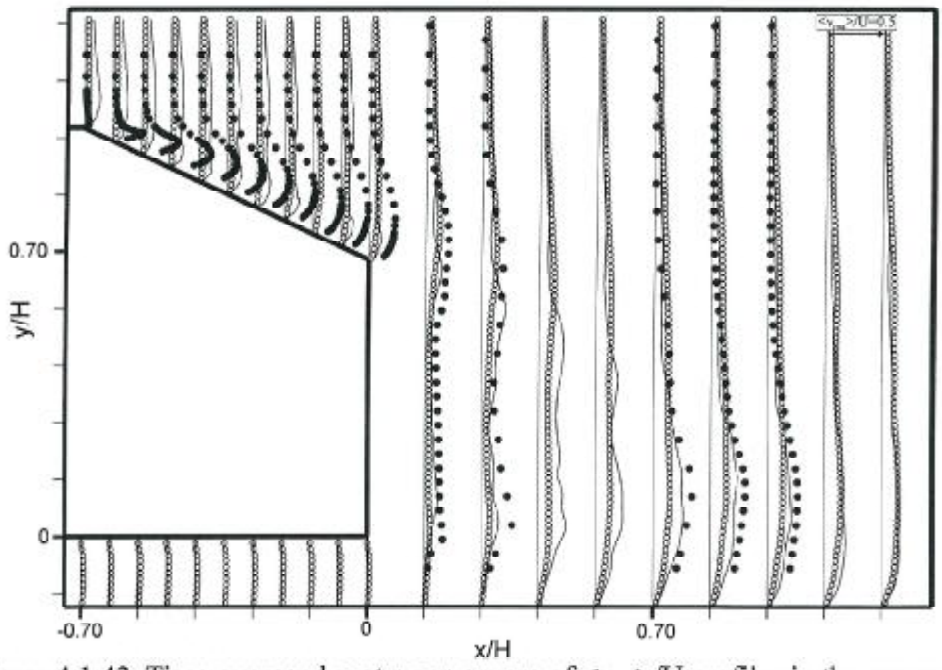

Figure.4.1.43. Time-averaged root mean square of $<v_{rms}>/U$ profiles in the symmetry plane z/H=0 on the slant surface and wake region of the Ahmed body. LES results (solid curve), PIV results (empty circles) and results of Lienhart et al. (2000) (filled circles)

body and under-body shear layers through the vertical symmetry plane of z/H=0 for the results of the present LES computations and PIV measurements and Lienhart et al. (2000) measurements are given in Table 4.1.3.

Table 4.1.3. Peak values and their locations of $<v_{rms}>$ in the upper-body and under-body shear layers through the vertical symmetry plane of z/H=0

	Upper-body Shear Layer			Under-body Shear Layer		
	Peak Value of $<v_{rms}>/U$	Locations of Peak Value of $<v_{rms}>/U$		Peak Value of $<v_{rms}>/U$	Locations of Peak Value of $<v_{rms}>/U$	
		In the Stream-wise Direction (x/H)	In the Normal Direction (y/H)		In the Stream-wise Direction (x/H)	In the Normal Direction (y/H)
LES Results	0.221	0.417	0.462	0.262	0.694	0.0569
PIV Results	0.134	0.417	0.614	0.152	0.694	0.113
Lienhart et al. (2000)	0.200	0.139	0.722	0.339	0.694	0.0972

The results presented in Table 4.1.3 show that the maximum $<v_{rms}>$ value found in the upper-body shear layer is formed in the near wake of the body in the stream-wise direction and aligned slightly below the end of the slant surface in the vertical direction. Maximum deviation of peak values of $<v_{rms}>$ between the present LES results and PIV results is 8.7%. On the other hand, this deviation between presently obtained LES results and the results of Lienhart et al.(2000) is 2.1% in the upper-body shear layer region. In this region, deviation of locations of peak values of $<v_{rms}>$ predicted by LES from PIV experimental results is 15.2% in the vertical direction. Additionally, its deviation from the results of Lienhart et al.(2000) is 27.8% in the stream-wise direction and 26.0% in the vertical direction. Deviation of peak values of $<v_{rms}>$ between LES calculations and PIV measurements is 11.0% and the results of Lienhart et al.(2000) is 7.7% in the under-body shear layer region of the symmetry plane, z/H=0. Furthermore, these results show that the maximum

$\langle v_{rms} \rangle$ value found in the under-body shear layer is formed at the region in which transition from near wake to far wake occurs downstream of the vehicle body in the stream-wise direction and aligned slightly above the bottom end of the vehicle body in the vertical direction. Maximum deviation of the location of peak values of $\langle v_{rms} \rangle$ between the LES calculations and PIV measurements and the results of Lienhart et al.(2000) coincides in the stream-wise direction in the under-body shear layer. On the other hand maximum deviation of the location of peak values of $\langle v_{rms} \rangle$ between the LES calculations and PIV measurements is 5.6% and the LES results differ from the results of Lienhart et al.(2000) as 4.0% in the normal direction in the under-body shear layer region of the symmetry plane.

Profiles of the Reynolds stress correlation, $\langle u'v' \rangle / U^2$ are shown in Figure 4.1.44. The magnitude of the Reynolds stress correlation, $\langle u'v' \rangle / U^2$ shown in this figure are higher in the under-body shear layer than that of in the upper-body shear layer. The peak values and their locations of $\langle u'v' \rangle / U^2$ in the upper-body and under-body shear layers through the vertical symmetry plane of z/H=0 for the results of the present LES computations and PIV measurements and Lienhart et al. (2000) measurements are given in Table 4.1.4. They indicate that the maximum $\langle u'v' \rangle$ value found in the upper-body shear layer is formed in the near wake of the body in the stream-wise direction and aligned slightly below the trailing edge of the slant in the vertical direction. The peak values of $\langle u'v' \rangle$, obtained by using LES calculations deviating from the PIV results and those of Lienhart et al. (2000) are 1.2% and 0.6%, respectively, in the upper-body shear layer region. In this region, deviation of the location of peak values of $\langle u'v' \rangle$ calculated by LES from the PIV results and those of Lienhart et al.(2000) is the same, which is 13.9% in the stream-wise direction, and it deviates 16.9% from the PIV results and 19.7% from the results of Lienhart et al.(2000) in the vertical direction. In addition, pertaining to the data given in Table 4.1.4 deviation of peak $\langle u'v' \rangle$ values obtained by using LES from the PIV results is 3.5% and from the results of Lienhart et al. (2000) is 1.5% in the shear layer emanating from the gap between underneath of the body and ground surface. Deviation of the location of peak $\langle u'v' \rangle$ values of LES results coincides with the results of Lienhart et al. (2000) in the stream-wise direction of the flow. On the other

hand, deviation of the location of peak <u'v'> values of LES results is 13.8% from the PIV results in the stream-wise direction. Its deviation from the PIV results is also 4.5% and from the results of Lienhart et al.(2000) is 0.1% in the vertical direction in the under-body shear layer region of the symmetry plane. These results show that the maximum <u'v'> value found in the under-body shear layer is formed in the region at the end of the near wake after the vehicle body in the stream-wise direction and is aligned to the bottom end of the body in the vertical direction.

Table 4.1.4. Peak values and their locations of $\langle u'v' \rangle / U^2$ in the upper-body and under-body shear layers through the vertical symmetry plane of z/H=0

	Upper-body Shear Layer			Under-body Shear Layer		
	Peak Value of $\langle u'v' \rangle / U^2$	Locations of Peak Value of $\langle u'v' \rangle / U^2$		Peak Value of $\langle u'v' \rangle / U^2$	Locations of Peak Value of $\langle u'v' \rangle / U^2$	
		In the Stream-wise Direction (x/H)	In the Normal Direction (y/H)		In the Stream-wise Direction (x/H)	In the Normal Direction (y/H)
LES Results	-0.0223	0.278	0.560	0.0479	0.694	0.0289
PIV Results	-0.0106	0.139	0.729	0.0133	0.556	-0.016
Lienhart et al. (2000)	-0.0163	0.139	0.757	0.0626	0.694	0.0278

Reynolds stress correlation, $\langle u'v' \rangle / U^2$ values are also well captured on the slanted surface of the Ahmed body. Its values outside the boundary layer are well predicted, whereas they are slightly underestimated within the boundary layer according to the present LES results. The peak values of $\langle u'v' \rangle / U^2$ on the slant are approximately -0.00757, -0.0268, -0.0804 times the square of the free-stream velocity, U^2 for the results of the present PIV measurements and LES calculations and Lienhart et al. (2000) measurements, respectively. Their locations are nearly x/H= -0.139, -0.347, -0.497 in the vertical symmetry plane of z/H=0 for the results of

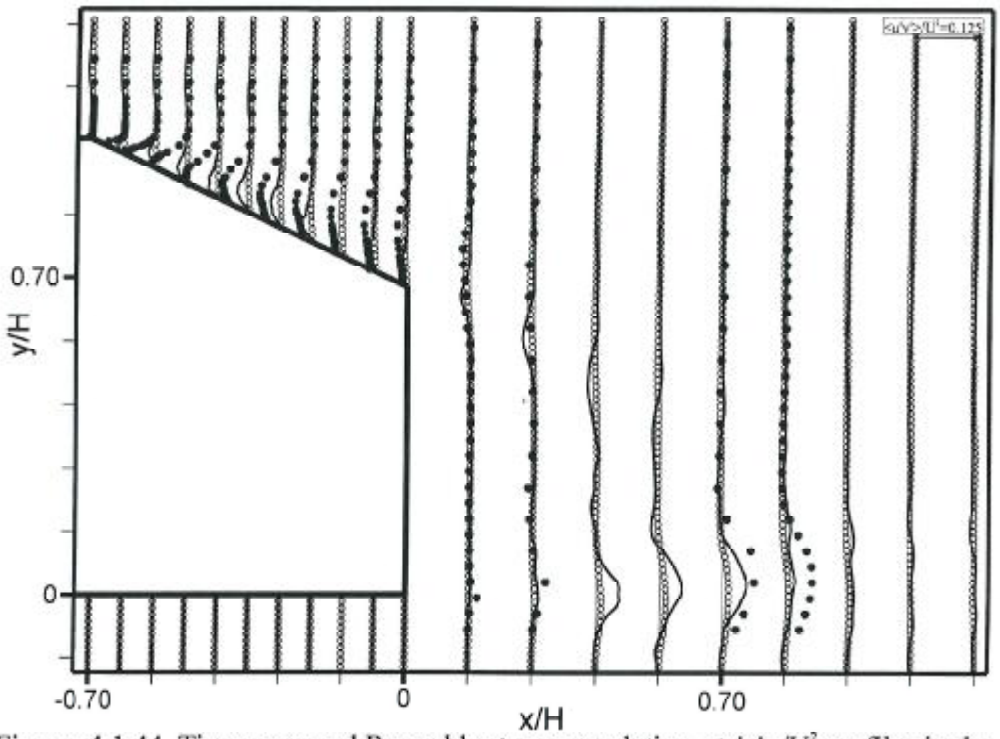

Figure. 4.1.44. Time-averaged Reynolds stress correlation, $\langle u'v' \rangle / U^2$ profiles in the symmetry plane z/H=0 on the slant surface and wake region of the Ahmed body. LES results (solid curve), PIV results (empty circles) and results of Lienhart et al. (2000) (filled circles)

PIV measurements and LES computations and Lienhart et al. (2000) measurements, respectively. The present results show that the maximum <u'v'> value is found in downstream of the leading edge of the slant where the flow separates. On the other hand, in LES computations and PIV measurements the location of the peak <u'v'> values are appeared somewhat downstream compared to the results of Lienhart et al. (2000). This situation is also observed in the study of Minguez et al. (2008), and they indicated that it is probably due to the upstream flow where the recirculation bubble in the flow separation region interacts with the shear layer shedding from the roof. Deviation in the peak values of <u'v'> between the present LES and PIV results is 1.9%, but the results of LES differ from the results of Lienhart et al.(2000) by 5.4% on the slant. In this region, deviation of the location of the peak <u'v'> values of LES results from the PIV is 20.8% and from the results of Lienhart et al.(2000) is 15.0% in the stream-wise direction.

4.1.2.4. Contours of Velocity Fluctuations and Reynolds Stress Correlations

The contours of stream-wise velocity fluctuations $<u_{rms}>/U$, normal velocity fluctuations $<v_{rms}>/U$, and Reynolds stress correlations $<u'v'>/U^2$ in the vertical planes positioned at z/H=0, 0.34 and -0.34 in the wake region are presented in Figures from 4.1.45 to 4.1.47 in order to identify regions of high velocity fluctuations. The level of turbulence obtained by the LES calculations is in good agreement with the results of the PIV measurements as presented in these figures. The minimum and incremental values of the contours for stream-wise velocity fluctuations, $<u_{rms}>/U$ and for normal velocity fluctuations, $<v_{rms}>/U$ are the same and equal to 0.02 and 0.02, respectively. The minimum and incremental values of Reynolds stress correlations, $<u'v'>/U^2$ are ±0.003 and 0.003, respectively. The solid and dashed lines here represent the positive and negative Reynolds shear stress contours, respectively. The peak values of positive and negative Reynolds stress contours indicate regions under high fluctuations. These regions are located on the slant surface and in the near wake region of the Ahmed body where shear layers and shedding vortices emerge. High concentrations of u_{rms}/U and v_{rms}/U contours are

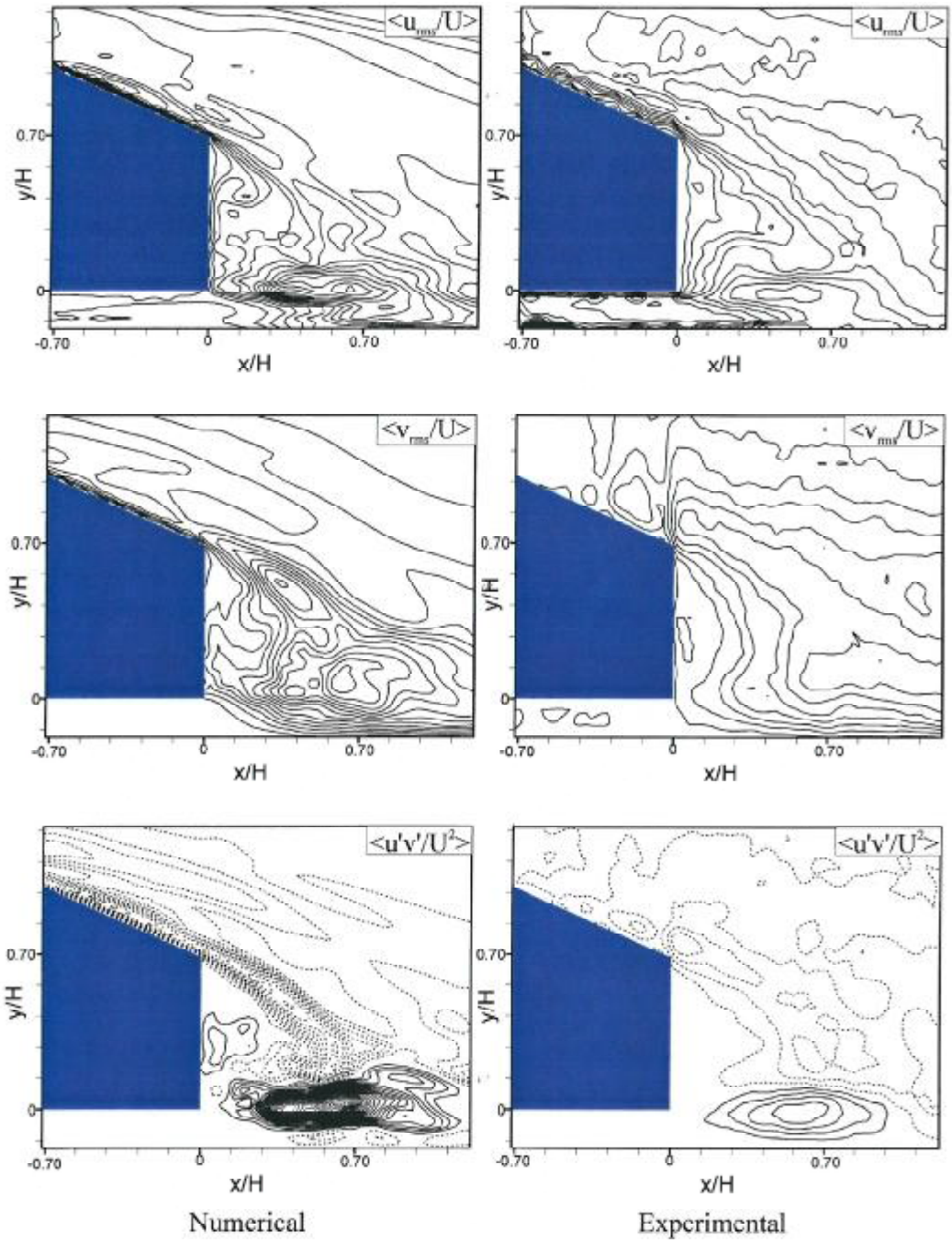

Figure 4.1.45. Contours of streamwise velocity fluctuations $\langle u_{rms}\rangle/U$, normal velocity fluctuations $\langle v_{rms}\rangle/U$, and Reynolds stress correlations $\langle u'v'\rangle/U^2$ in the vertical symmetry plane for z/H=0 in the wake region. Minimum and incremental values of rms of velocity components are $[\langle u_{rms}\rangle/U]_{min}=0.02$, $\Delta[\langle u_{rms}\rangle/U]=0.02$,$[\langle v_{rms}\rangle/U]_{min}=0.02$, $\Delta[\langle v_{rms}\rangle/U]=0.02$ and Reynolds stresses correlations are $[\langle u'v'\rangle/U^2]_{min}=\pm0.003$, $\Delta[\langle u'v'\rangle/U^2]=0.003$, respectively

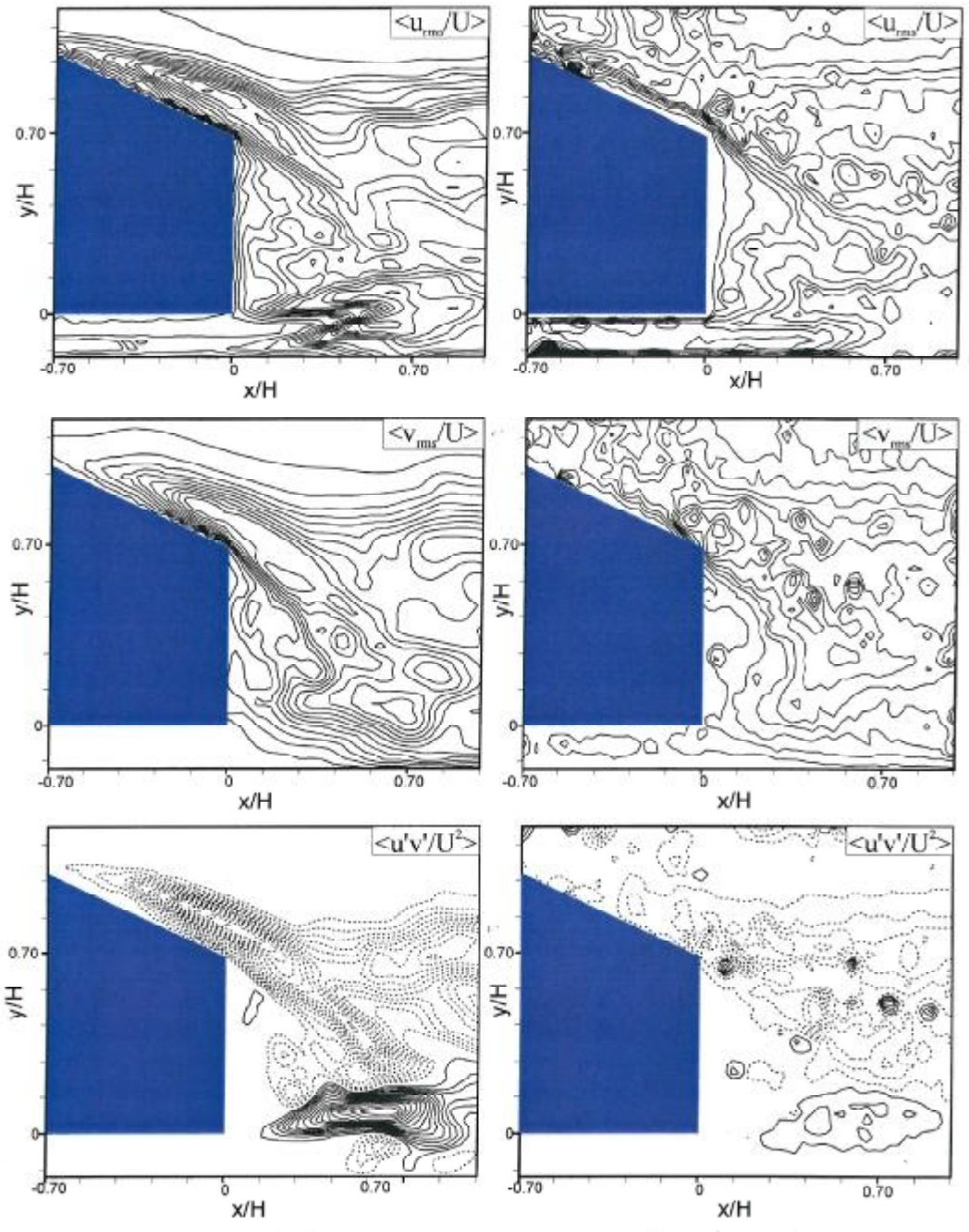

Figure 4.1.46. Contours of streamwise velocity fluctuations $\langle u_{rms}\rangle/U$, normal velocity fluctuations $\langle v_{rms}\rangle/U$, and Reynolds stress correlations $\langle u'v'\rangle/U^2$ in the vertical xy-plane for z/H=0.34 in the wake region. Minimum and incremental values of rms of velocity components are $[\langle u_{rms}\rangle/U]_{min}=0.02$, $\Delta[\langle u_{rms}\rangle/U]=0.02$, $[\langle v_{rms}\rangle/U]_{min}=0.02$, $\Delta[\langle v_{rms}\rangle/U]=0.02$ and Reynolds stresses correlations are $[\langle u'v'\rangle/U^2]_{min}=\pm 0.003$, $\Delta[\langle u'v'\rangle/U^2]=0.003$, respectively

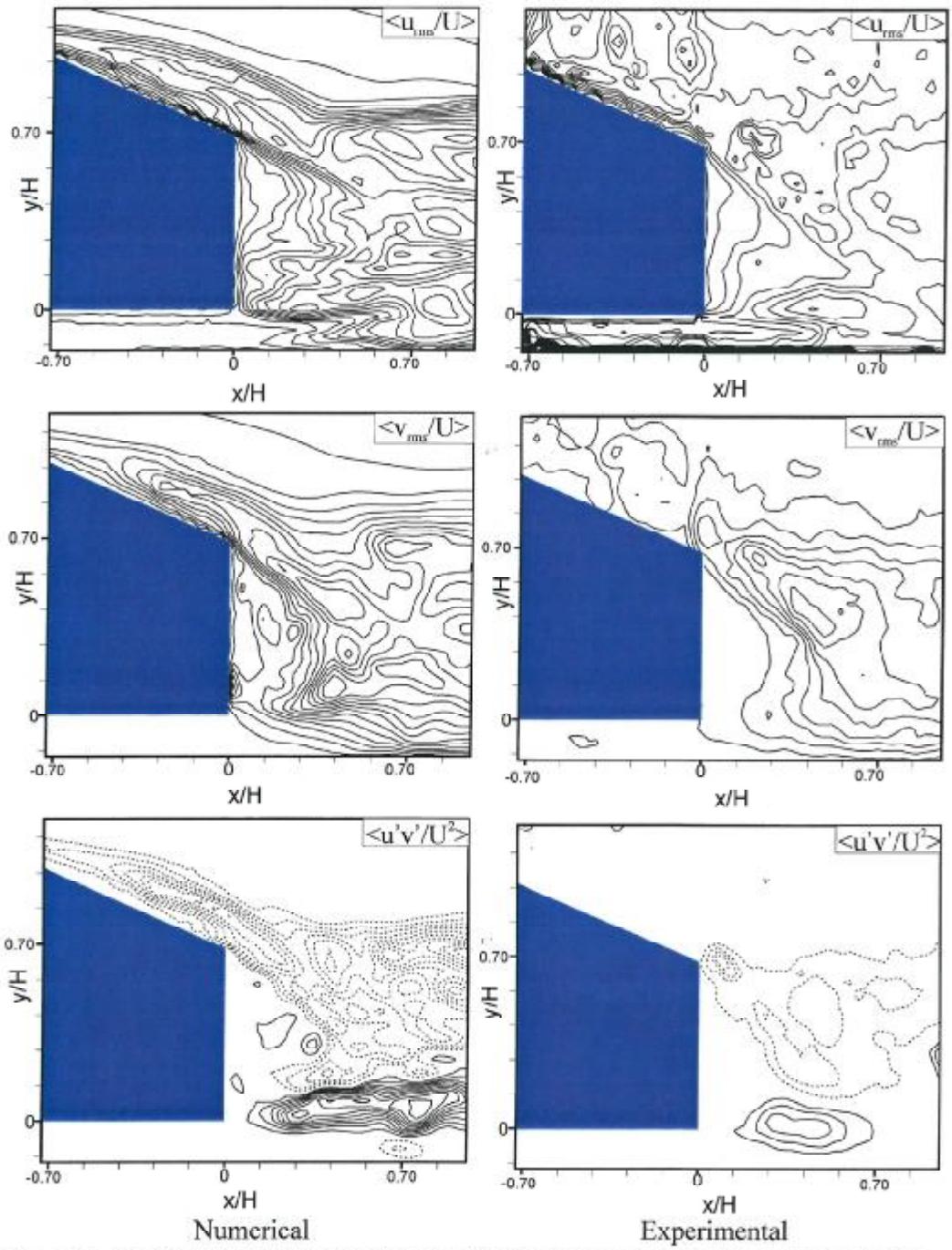

Figure 4.1.47. Contours of streamwise velocity fluctuations $\langle u_{rms}\rangle/U$, normal velocity fluctuations $\langle v_{rms}\rangle/U$, and Reynolds stress correlations $\langle u'v'\rangle/U^2$ in the vertical xy-plane for z/H=-0.34 in the wake region. Minimum and incremental values of rms of velocity components are $[\langle u_{rms}\rangle/U]_{min}$=0.02, $\Delta[\langle u_{rms}\rangle/U]$=0.02, $[\langle v_{rms}\rangle/U]_{min}$=0.02, $\Delta[\langle v_{rms}\rangle/U]$=0.02 and Reynolds stresses correlations are $[\langle u'v'\rangle/U^2]_{min}$=0.003, $\Delta[\langle u'v'\rangle/U^2]$=0.003, respectively

located in the proximity of the slant surface and along the upper-body and under-body shear layer in the wake region of Ahmed body. The highest amplitude of u_{rms}/U and v_{rms}/U appear immediately adjacent to the downstream side of the saddle point in all figures.

4.1.2.5. Trace Lines

Trailing vortices, the span-wise separation region, reattachment lines and foci which are visible flow structure on the rear slant surface of Ahmed body in both numerical and experimental results issued in the literature are also visible in the present LES calculations and PIV measurements. According to the previous literature, on the rear slant surface of the Ahmed body, the flow tends to separates after the beginning of the slant surface and then flow tend to reattach. Beside these, the flow separates at the lateral edges of the slant surface resulting in two large counter-rotating cone-like trailing vortices that spread farther in the wake (Minguez et al, 2008). On the other hand, as it is seen in Figure 4.1.48 (a) and (b), there are differences between the topology of the flow observed in the present LES results and in the LES results of Krajnovic and Davidson (2004). In the present LES, the Reynolds number employed is nearly ten times lower than the Reynolds number employed in the study of Krajnovic and Davidson (2004). The fluid flow coming from the upstream separates along NBL and reattach through PBL_1 and PBL_2 on the slant surface in the present LES as shown in Figure 4.1.48. Between NBL and PBL_1 and PBL_2, there is highly unsteady and complex flow structures. From NBL, the fluid particles move downstream toward the PBL_1 and PBL_2 and upstream toward the edge at the beginning of the slant surface. In the study of Krajnovic and Davidson (2004) there is additional PBL between the beginning of the slant surface and NBL. This flow structure is not observed in the present study. Additionally, a lot of saddle points are observed on the NBL. Minguez et al. (2008) and Spohn and Gillieron (2002) observed that flow recirculation appears divided into two bubbles, symmetrically located around the symmetry plane. A similar flow features are also observed in the present LES calculations. In the separated flow region on the slanted

surface, one stable and one unstable focuses with NBL and PBL are observed on each side of the symmetry plane, z/H=0. Downstream on the slanted surface between two lateral edge, there is highly unsteady flow region. This highly unsteady separated flow region is also observed in the visualization of the instantaneous flow in the work of Spohn and Gillicron (2002) and in the LES calculations of Krajnovic and Davidson (2004). In the present study, unlike to the results of Krajnovic and Davidson (2004), positive bifurcation lines in the outer part of the separated flow region on the slanted surface does not meet. However negative bifurcation lines in the inner part meet each other. According to Spohn and Gillieron (2002), unsteadiness in this flow region is caused by oscillations of the trailing vortices themselves and their interactions with vortices shed from the front. On the other hand, Krajnovic and Davidson (2004) indicated that the interaction between hairpin vortices is the reason for the high levels of unsteadiness in the lower part of the slanted surface because trailing vortices to be relatively steady, with their cores remaining at approximately the same position for a long period of time. Negative bifurcation lines, NBL_1, NBL_2 and the positive bifurcation lines, PBL_3, PBL_4 close to both right and left edges of the slanted surface are presented in Figure 4.1.48(a). Formation of longitudinal trailing vortices on the lateral edges of the slanted surface with the contribution of upstream flow can be observed in this figure. The streamlines coming from the upstream flow on the lateral surfaces of the body are first parallel with the stream-wise direction of the flow and then they are oriented upward toward the lower end of the lateral slanted edge. Furthermore, they enter above the slanted surface and continue to rotate around the trailing vortex core.

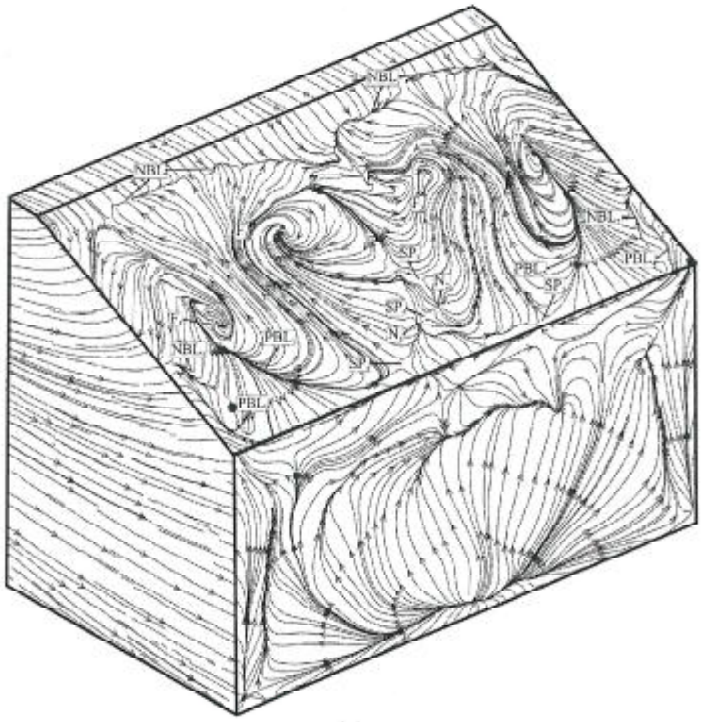

(a)

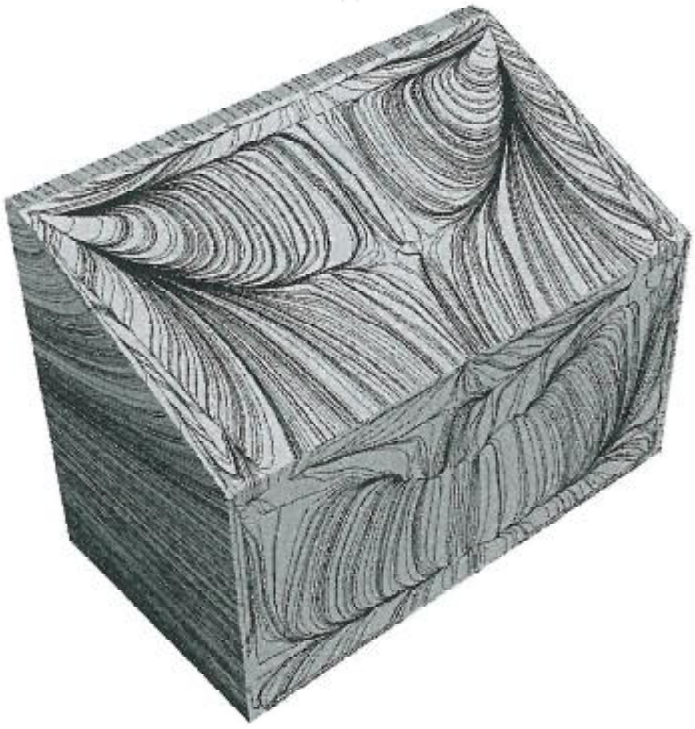

(b)

Figure 4.1.48. Time-averaged trace lines on the rear slanted surface of the Ahmed body. (a) Results of the present LES calculations and (b) Results of LES calculations of Krajnovic and Davidson (2004)

4.2. INSTANTANEOUS VELOCITY FIELD AND FLOW VISUALIZATION

This section presents instantaneous flow fields and flow visualization images to illustrate unsteady characteristics of flow structures around the Ahmed body. Our LES simulations and PIV measurements of flow characteristics around the Ahmed body show complex time-dependent and three-dimensional flow features as presented in figures throughout this section.

Figures from 4.2.1 to 4.2.3 depict instantaneous velocity vectors map, V the patterns of streamlines, ψ and the corresponding vorticity contours, ω obtained by using the PIV measurements and the LES calculations at the front part of the body in the vertical symmetry plane, z/H=0 for instants of t=18, 20.4s and 22.8 seconds. Separated flow estimated in our numerical investigation show vortical structures similar to Kelvin-Helmholtz vortices at the front part of the body as shown in Figures 4.2.1 to 4.2.3. Similar flow behaviour was also observed by Spohn and Gillieron (2002) at the Reynolds number of $Re_H=8x10^3$ in their experimental study. The instantaneous velocity vectors map, V and the corresponding streamlines, ψ clearly present that the swirling patterns of flow streams are evident on the roof surface of the model. These circulatory flow patterns interact severely with the surface of the model in random mode. The time-averaged flow data of experimental and numerical results presented in Figures 4.1.1 and 4.1.9 indicate that reattachment occurs at a distance of x/H=0.426 and 1.815 from the frontal leading edge of the body for the PIV measurements and the LES calculations, respectively. On the other hand, examining the animation of 350 instantaneous velocity vector fields of the PIV measurements we can figure out that the location of the reattachment point moves in forward and backward directions. When compared to the time-averaged flow, in the instantaneous flow structures, additional vortices along the roof of the body are observed. As mentioned in previous sections, character of the flow around the front part of the body depends on the Reynolds number and its curvature. Flow separates after the leading edge of the body and swirling flow patterns occur in this separated flow region. Contours of vorticity, ω corresponding this flow region, show that the

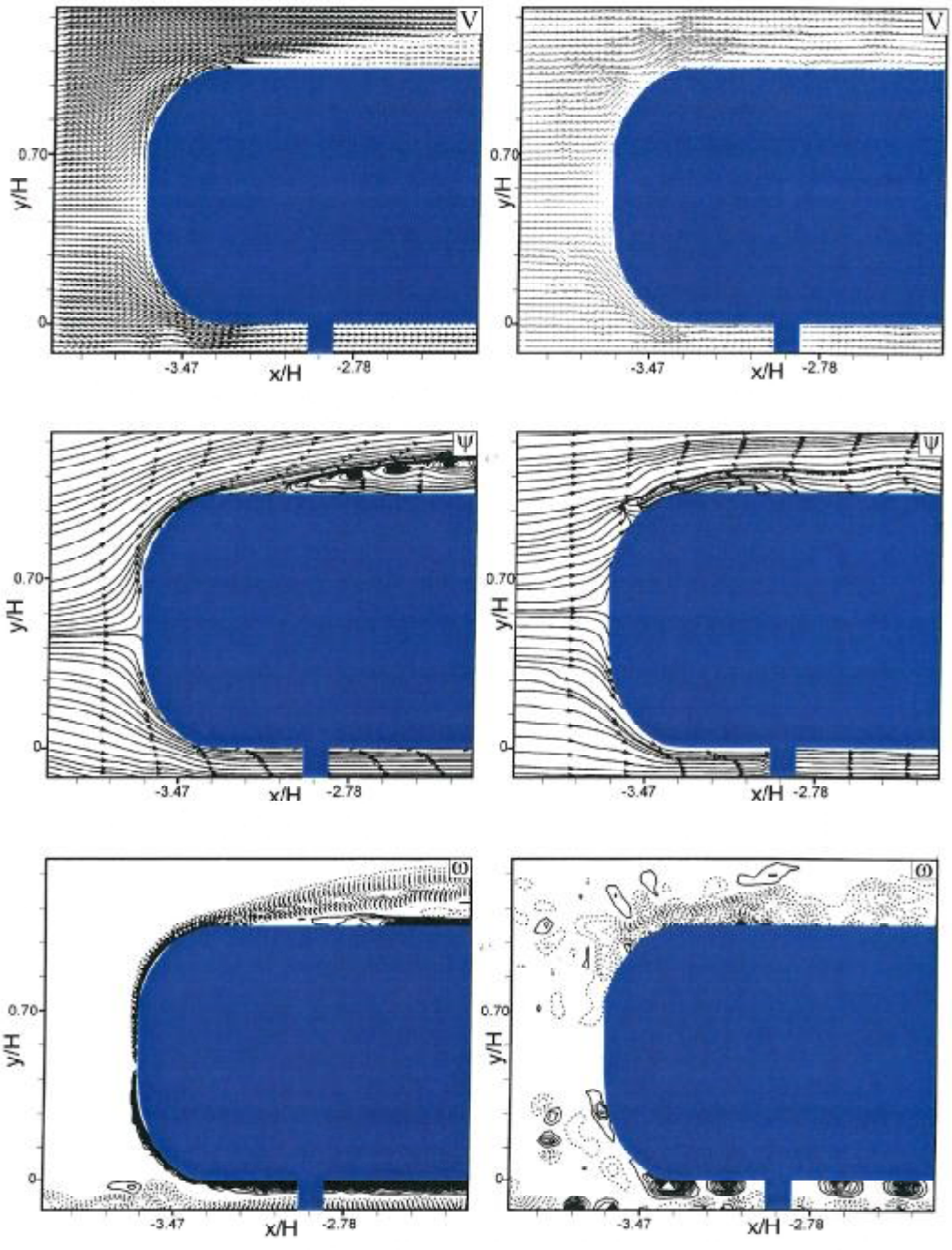

Numerical Experimental

Figure 4.2.1. Patterns of instantaneous velocity vectors map V, streamlines ψ and vorticity contours ω in the vertical symmetry plane (z/H=0) for instant of 18s. Minimum and incremental values of vorticity are $\omega_{min}=\pm 5s^{-1}$ and $\Delta\omega=5s^{-1}$, respectively

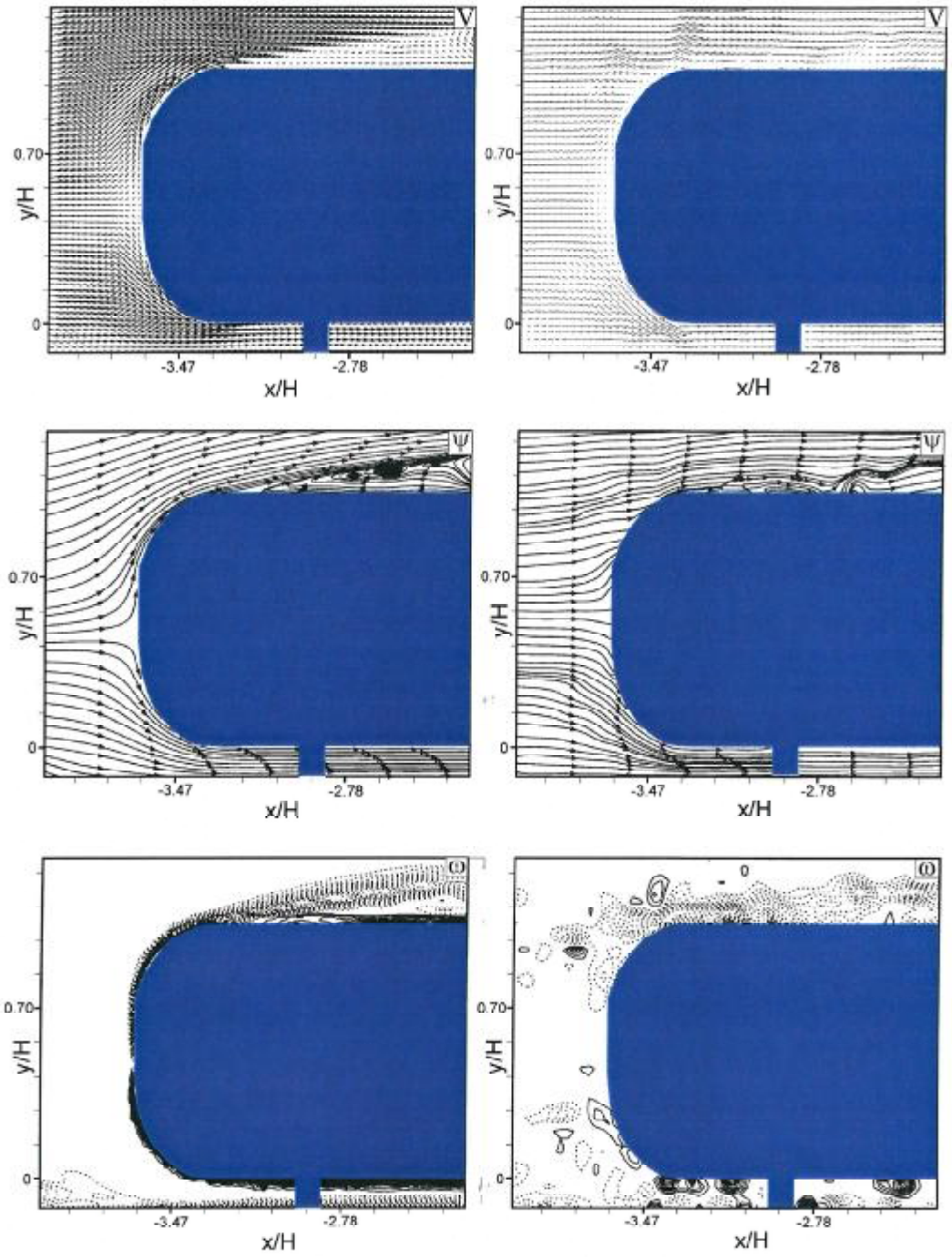

Figure 4.2.2. Patterns of instantaneous velocity vectors map V, streamlines ψ and vorticity contours ω in the vertical symmetry plane (z/H=0) for instant of t=20.4s. Minimum and incremental values of vorticity are $\omega_{min}=\pm 5s^{-1}$ and $\Delta\omega=5s^{-1}$, respectively

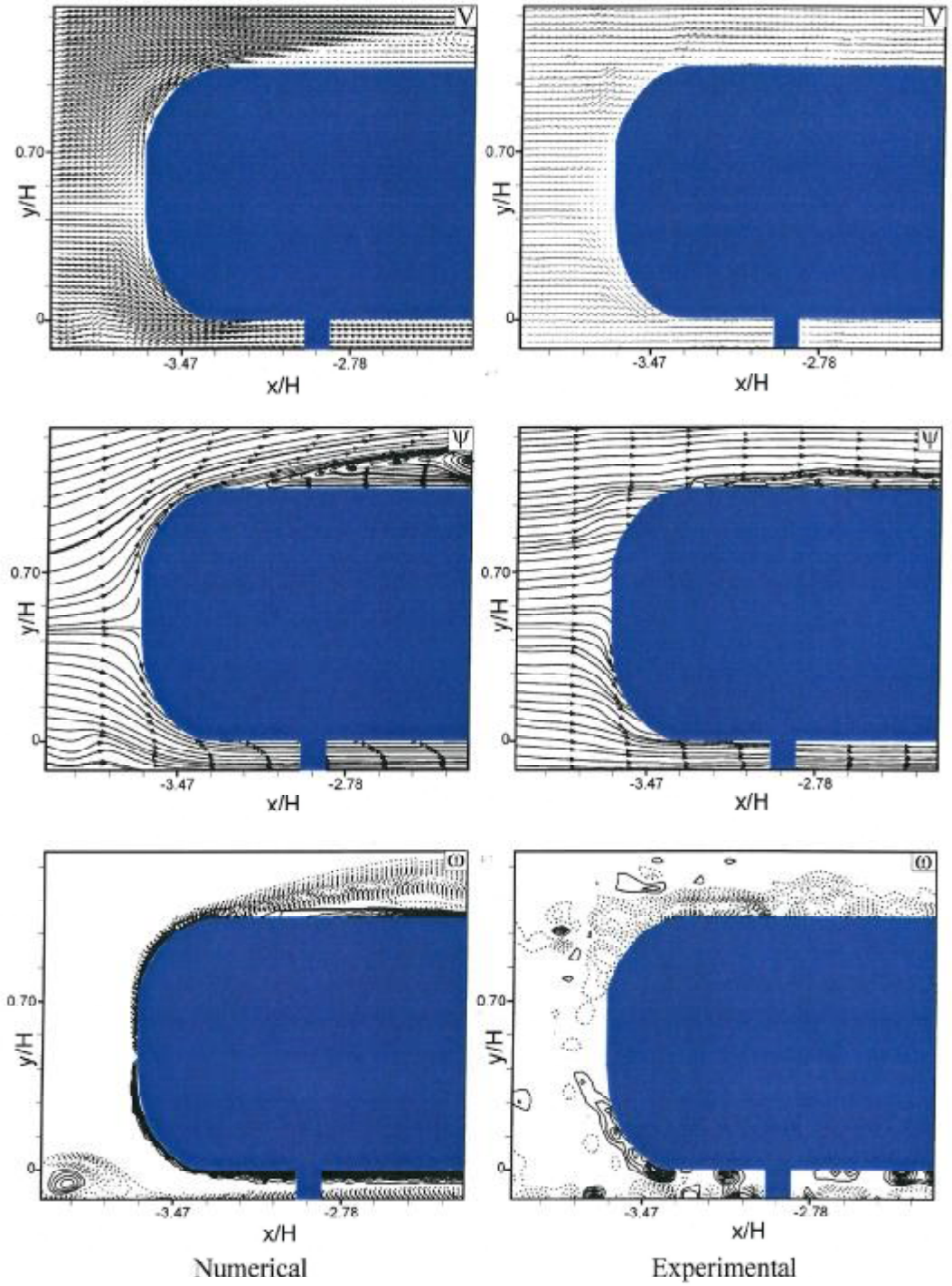

Figure 4.2.3. Patterns of instantaneous velocity vectors map V, streamlines ψ and vorticity contours ω in the vertical symmetry plane (z/H=0) for instant of t=22.8s. Minimum and incremental values of vorticity are $\omega_{min}=\pm 5s^{-1}$ and $\Delta\omega=5s^{-1}$, respectively

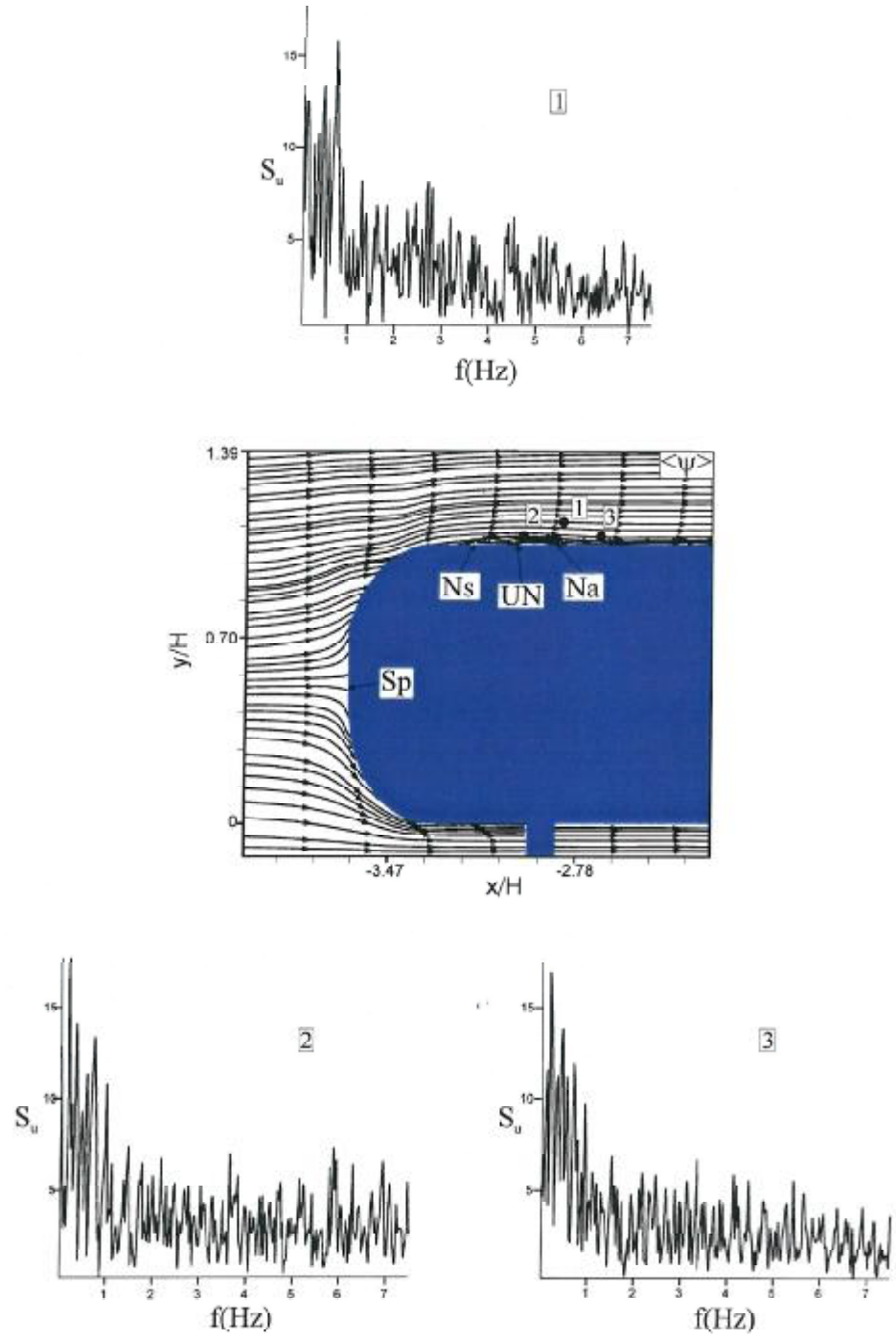

Figure 4.2.4. The spectrum of experimentally obtained streamwise velocity fluctuations for selected points in the vertical symmetry plane, z/H=0 at the front part of the Ahmed body

concentration of vortices occurs along the shear layer. Vibration and noise due to the strong interactions between these unsteady flow structures and upper surface of the body is observed. The strength of these vortices depends on the curvature of the front face of the body. Rounding of these sharp corners degrades the level of the vorticity strengths is widely accepted. The separation at the body front is characterized by a bubble inducing an unsteady recirculation region. Minguez et al. (2008) found that this bubble pulsates at a Strouhal number equal to 0.15, whereas the transverse vortices related to the Kelvin–Helmholtz-like instability within the separated shear layer over the recirculation travel at a Strouhal number one order of magnitude larger. In PIV measurements, it is found that the dominant frequency of 0.21 which leads to Strouhal number equal to 0.07 exist on the upper surface of the front part of the Ahmed body as a result of the spectral analysis of the stream-wise velocity fluctuations as presented in Figure 4.2.4.

The instantaneous flow structures in the wake region downstream of the Ahmed body in the vertical symmetry plane, z/H=0 are shown in Figures from 4.2.5 to 4.2.7 for instants of t=20, 20.6 and 21.1 seconds. The distributions of velocity vectors, V the patterns of streamlines, ψ and the corresponding vorticity contours, ω in these figures indicate that swirling patterns of velocity vectors take place on the slant and in the near wake regions of the Ahmed body. Furthermore, well defined large-scale swirling patterns of velocity vectors are evident at the bottom edge of the vertical base of the model. Shear layers emanating from the upper-body and lower-body surfaces cause complex flow field consisting of a number of vortices that move randomly in time and space. Two main vortices are developed in the wake of the Ahmed body. One comes from the lower side of the rear wall of the body and the other one comes from the slant surface of the body. As clearly shown in Figures from 4.2.5 to 4.2.7 that positive vortex, V_1 induced in the under body shear layer grows in size elongates and loses its strength. As soon as vortex, V_2 enlarges in size this vortex moves upward and downward in vertical direction in the wake of the body and Vortex, V_2 attenuates further downstream.

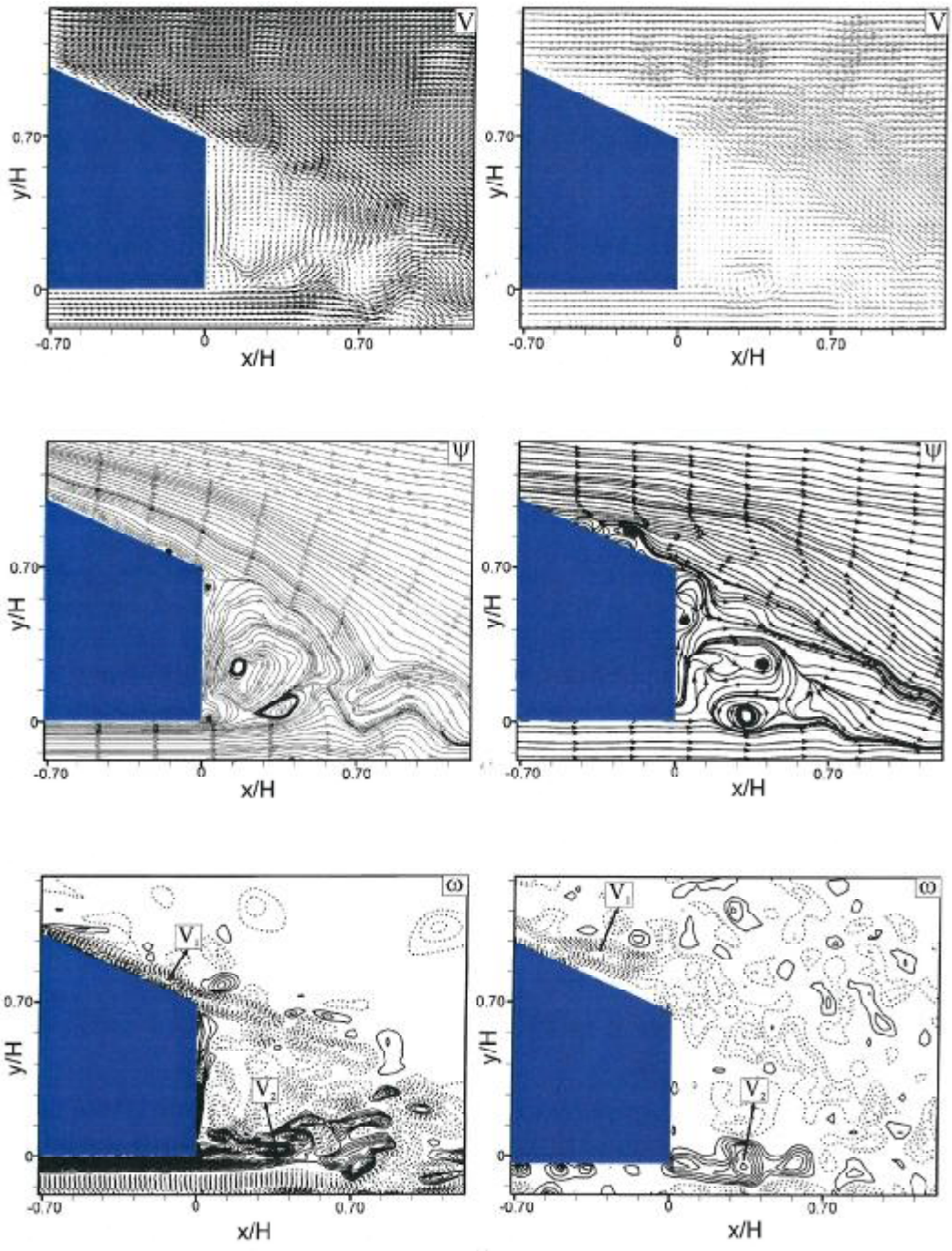

Numerical Experimental

Figure 4.2.5. Patterns of instantaneous velocity vectors map V, streamlines ψ and vorticity contours ω in the vertical symmetry plane (z/H=0) for instant of t=20 s. Minimum and incremental values of vorticity are $\omega_{min}=\pm 5s^{-1}$ and $\Delta\omega=5s^{-1}$, respectively

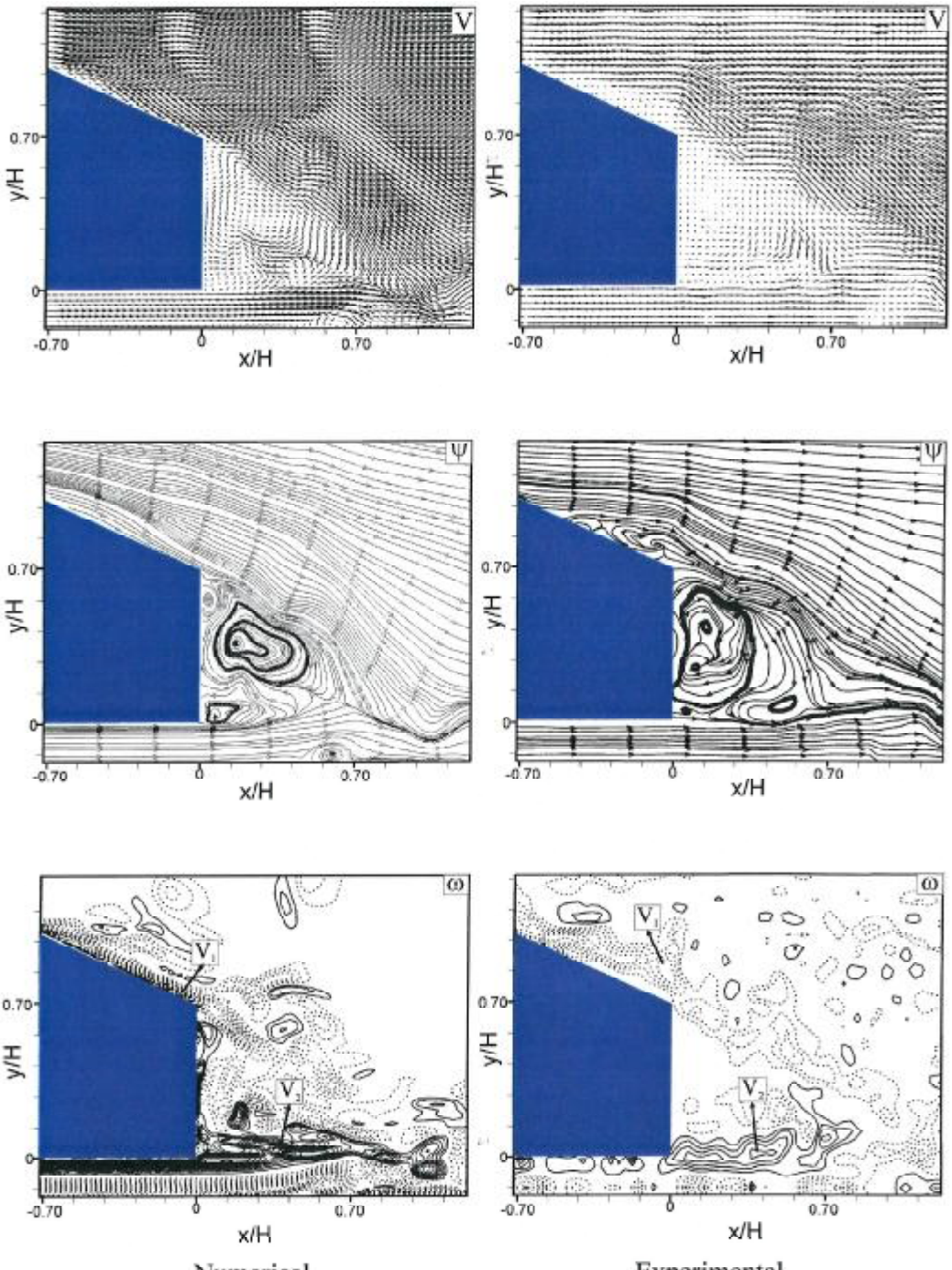

Figure 4.2.6. Patterns of instantaneous velocity vectors map V, streamlines ψ and vorticity contours ω in the vertical symmetry plane (z/II=0) for instant of t=20.6 s. Minimum and incremental values of vorticity are $\omega_{min}=\pm 5s^{-1}$ and $\Delta\omega=5s^{-1}$, respectively

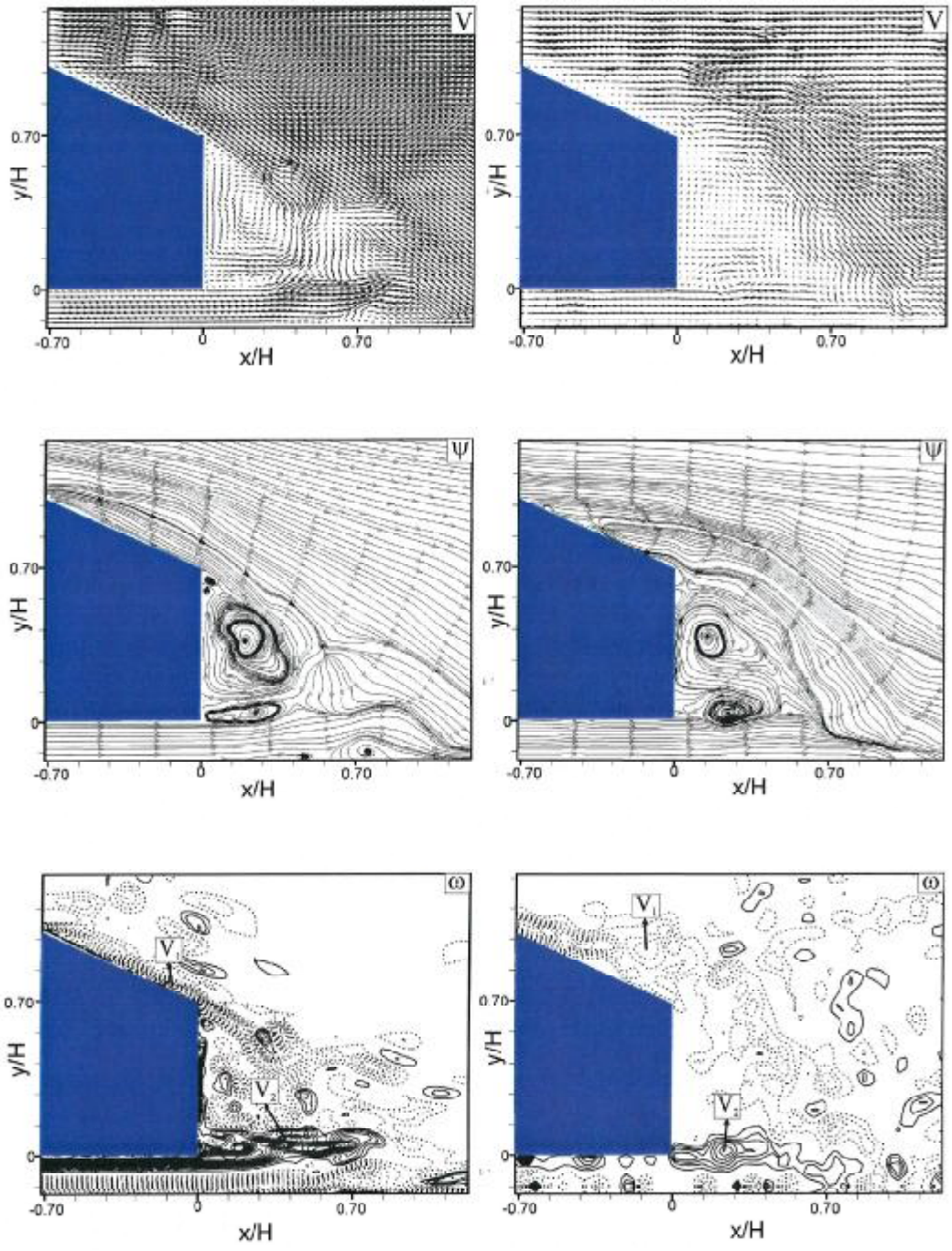

Figure 4.2.7. Patterns of instantaneous velocity vectors map V, streamlines ψ and vorticity contours ω in the vertical symmetry plane (z/H=0) for instant of t=21.1 s. Minimum and incremental values of vorticity are $\omega_{min}=\pm 5s^{-1}$ and $\Delta\omega=5s^{-1}$, respectively

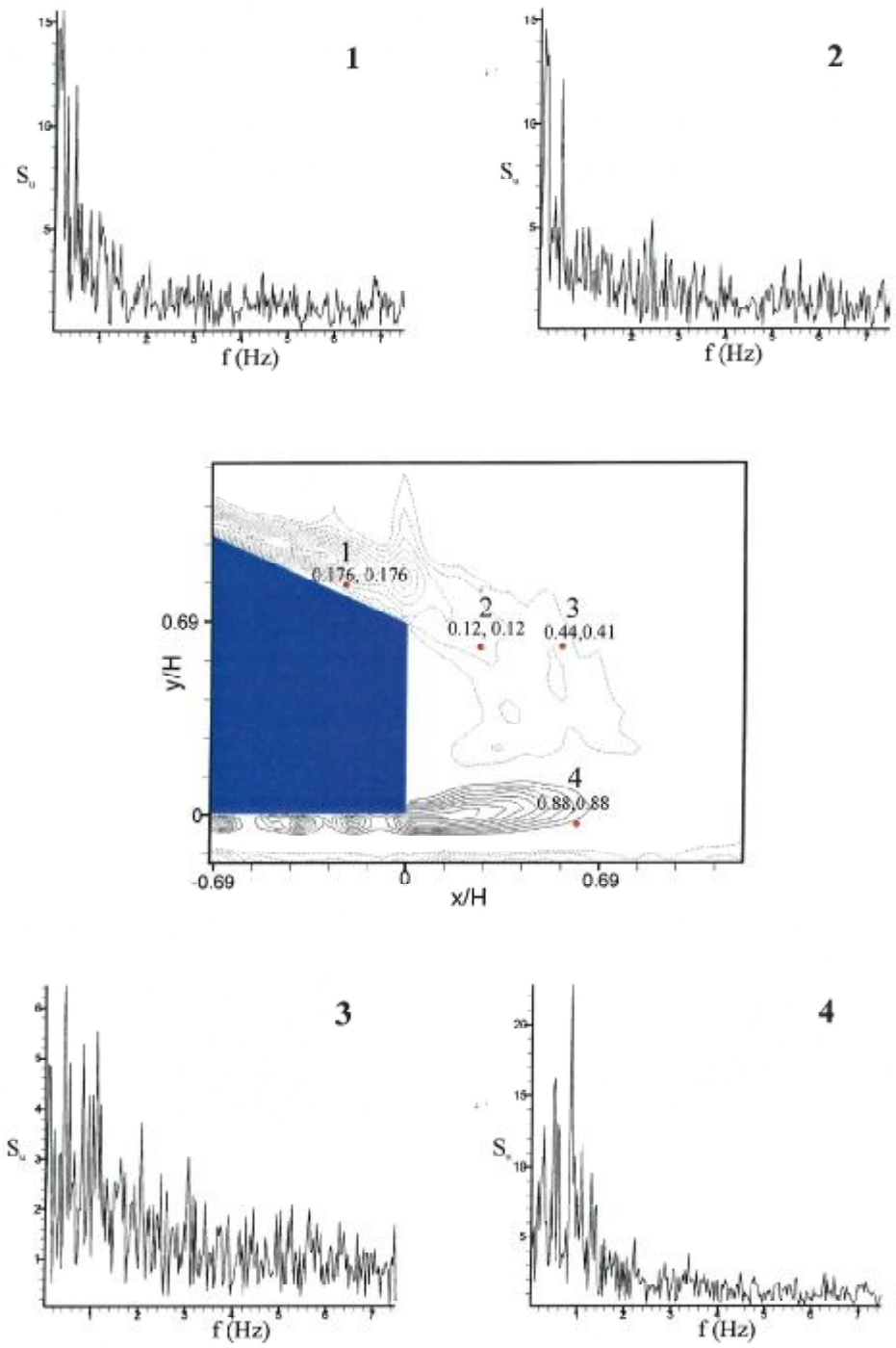

Figure 4.2.8. The spectrum of experimentally obtained streamwise velocity fluctuations for selected points in the vertical symmetry plane z/H=0 in the wake region

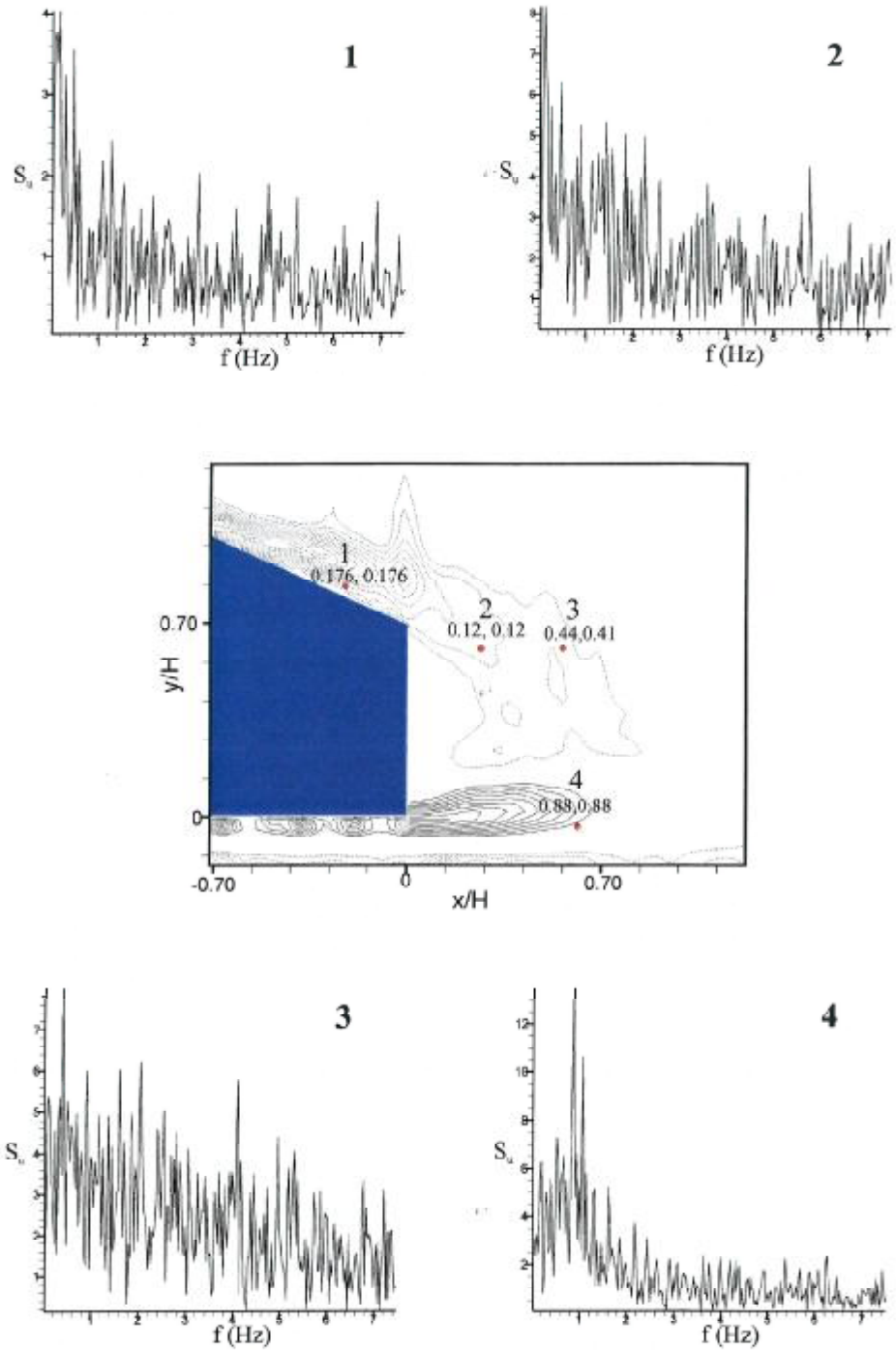

Figure 4.2.9. The spectrum of experimentally obtained normal velocity fluctuations for selected points in the vertical symmetry plane z/H=0 in the wake region

It is known that flow around the Ahmed body is highly turbulent, particularly over the slant, which is confirmed by conducting Fourier analysis of time variations of the stream-wise velocity at different points in the flow. The spectra of the stream-wise and normal velocity fluctuations obtained by applying FFT analysis for four selected points in the vertical symmetry plane are presented in Figures 4.2.8 and 4.2.9. The locations of these selected points are taken as point 1 which is on the slanted surface at x/H=-0.23, y/H=0.83; point 2 which is in the inner part of the upper shear layer at x/H=0.26, y/H=0.60; point 3 which is in the outer part of the upper shear layer at x/H=0.55, y/H=0.60 and point 4 which is in the lower shear layer at x/H=0.61, y/H=-0.03 in the wake region. The dominant frequency in our study was found to be f=0.88 at the fourth point in the lower shear layer which leads to the Strouhal number of St=fH/U=0.31 (based on the model height H and the free steam velocity U) This result corresponds with the numerical result reported by Minguez et al. (2008) as 0.42. Additionally, Figure 4.2.9 shows the spectra of normal velocity fluctuations evaluated at the same locations investigated in Figure 4.2.8. The spectra taken from the upstream locations of the body do not show a dominant frequency, f except at the forth point in the lower shear layer, which also corresponds to the Strouhal number of St=0.31.

Iso-surfaces of second invariant of the velocity gradient, Q defined in equation 4.1 is a useful tool to identify coherent structures in the flow. The multiple vortex system around the Ahmed body can be observed using this technique. This method was used both for mean flow and for instantaneous flow. The iso-surfaces of second invariant of the velocity gradient coloured with axial velocity magnitude are shown in Figures 4.2.10 and 4.2.11.

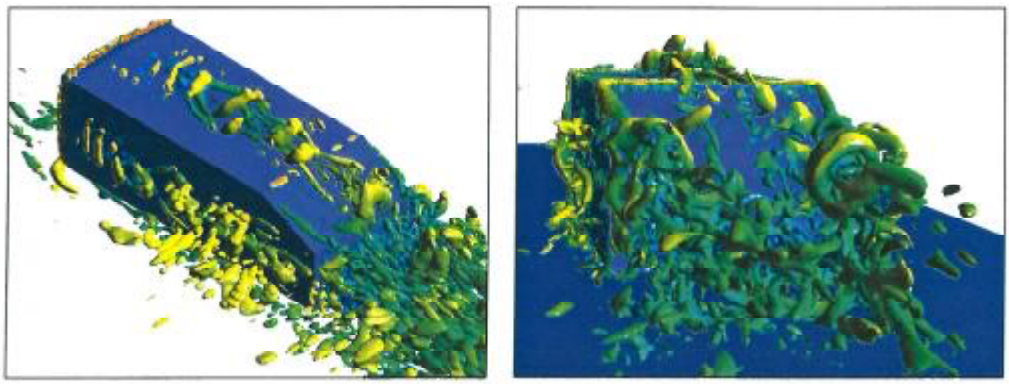

Figure 4.2.10. Iso-surfaces of second invariant of the velocity gradient, Q=0.08 on the left and Q=0.15 on the right

Figure 4.2.10 and 4.2.11 show iso-surfaces of second invariant of the velocity gradient. These figures illustrate the presence of large-scale vortices in the recirculation zones throughout the Ahmed body. Figure 4.2.10 gives a perspective view and Figure 4.2.11 depicts three sequential instants in time (t=19, 21, 23 seconds) respectively. Horseshoe vortex and a secondary corner vortex in front of the Ahmed body are visible in Figure 4.2.10. The lifespan of lateral vortices from front to the rear of the lateral surface of the obstacle can be traced. It can be seen that large span-wise vortex tubes are generated on the upper surface of the Ahmed body, which grow and then become similar to the horseshoe vortex on the slant surface. Furthermore, vortex tubes that wrap the counter-rotating vortices coming from the lateral sides can be observed. The interaction of the trailing vortices coming from the lateral side of the slant surface with the smaller horseshoe vortices coming out from the upstream of the flow provides helical structures in the wake of the body.

On the slant surface of the body hairpin vortices coming out from the upper surface travel in the stream-wise direction and break up when they meet other hairpin vortices at the region of the reattachment. These meetings result in a large number of collisions and make this region of the flow very unsteady. As indicated by Krajnovic and Davidson (2005), the unsteady character of the flow in the lower part of the slant is not a direct consequence of the trailing vortices, but the result of their indirect influence on the hairpin vortices making them change their paths and interact with the other hairpin vortices.

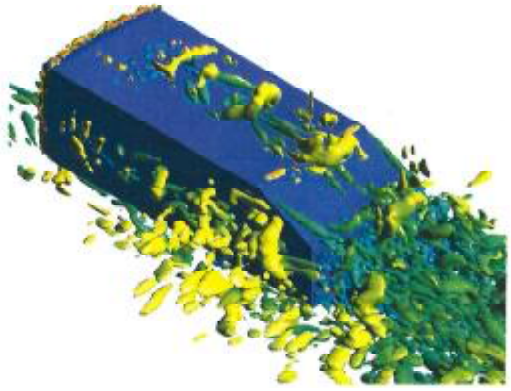

(a)

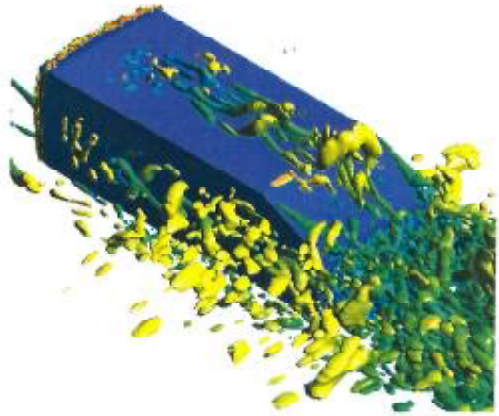

(b)

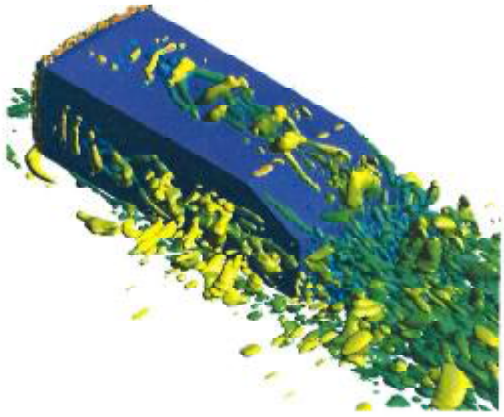

(c)

Figure 4.2.11. Iso-surfaces of second invariant of the velocity gradient, Q=0.08 for instants of (a) t=19 s, (b) t=21 s and (c) 23 s

4.3. PRESSURE FIELD

4.3.1. Surface Pressure

Pressure coefficient distribution on the surface of the Ahmed body obtained from the LES calculations are presented in Figure 4.3.1. Pressure coefficient distribution results at the rear part of the Ahmed body are also compared with previous literature data in Figure 4.3.2. For the calculation of pressure coefficient, Krajnovic and Davidson (2005) took static pressure in undisturbed flow upstream at the inlet close to the left lateral wall of the channel at y=2F/3 (where F denotes channel height) as a reference pressure. In the present simulations, we also employed mean pressure value at point y=2F/3 as the reference pressure.

As seen in Figure 4.3.1., the highest pressure regions occur on the front face of the Ahmed body and on its stilts. The magnitude of pressure coefficients contours decrease as the flow goes through the frontal leading edges. After the flow reaches its lowest pressure coefficient value near the frontal leading edge of the body, recovery in pressure coefficient which correspond to the separated flow region, is observed. On the upper surface of the Ahmed body, before the beginning of the slanted

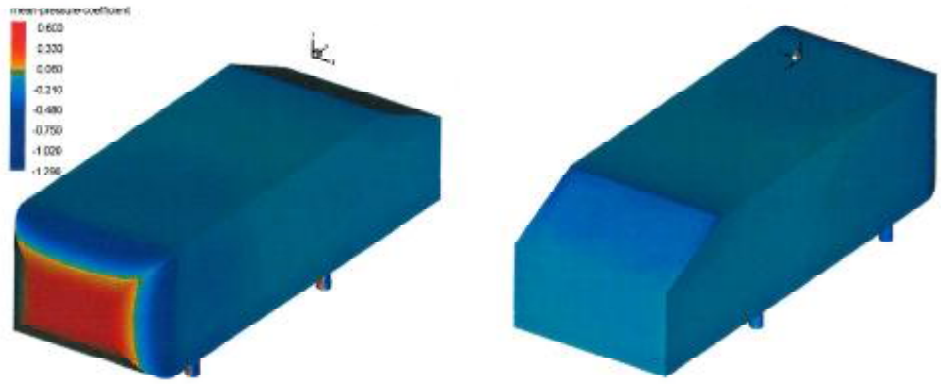

(a) (b)

Figure 4.3.1. Distribution of the pressure coefficient on the Ahmed body

surface, magnitude of the pressure coefficient again decreases. It is found that the lowest pressure regions occur on the Ahmed body near the frontal leading edges and

near the beginning edge of the slant surface which are associated with the acceleration of the flow. Two longitudinal vortices form from the lateral edges of the slant surface corresponding with the low pressure regions in the flow as shown in Figure 4.3.1.

The pressure coefficient distribution on the rear part of the model obtained from LES computations are presented in Figure 4.3.2 and compared with the previous studies. Structures of the pressure coefficient distribution on the rear slant and vertical surface are generally in agreement with the related literature. However, significant differences are observed on the slant surface of the body where imprint of the separation region is more tentative in the present LES computations. Lower Reynolds number employed in the present simulations may be reason for this result. In addition, the imprint of the longitudinal trailing vortices can be observed with the aid of the low pressure imprint on the side of the slant surface. Fares (2006) stated that the pressure level in the separation region is the determining factor of the total drag of a vehicle. In present LES simulation average pressure coefficient value found on the slant surface is bigger than the corresponding average pressure coefficient values found in the results of Lienhart and Becker (2003) and Fares (2006) as presented in Figure 4.3.2.

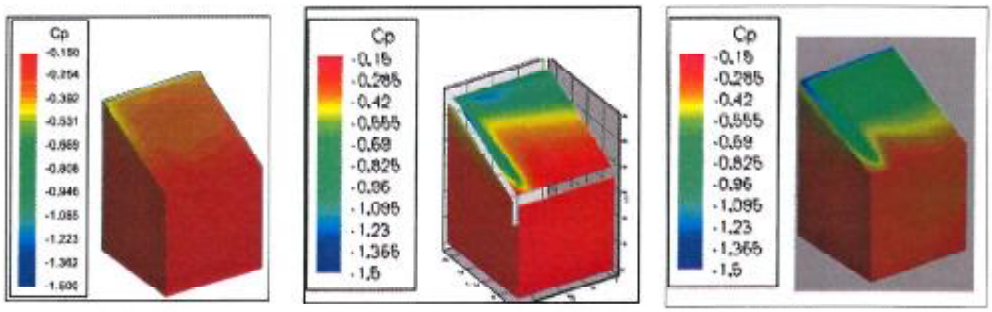

a) b) c)

Figure 4.3.2. Comparison of pressure coefficient distribution on the rear surface of the Ahmed body for (a) LES simulation, (b) Lienhart and Becker (2003) and (c) Fares (2006) (Only half of the geometry are shown)

Another way of investigating pressure distribution characteristics around the Ahmed body is to present mean surface pressure coefficient, $\langle C_p \rangle_t$ profiles on the body. Comparison of the time-averaged pressure coefficient, $\langle C_p \rangle_t$ profiles with

experimental results of Lienhart and Becker (2003) on the rear slanted and the rear vertical surfaces for three planes (z/H=0, z/H=0.31, and z/H=0.625) are presented in Figure 4.3.3. Although, Lienhart and Becker (2003) measured the distribution of the pressure coefficient on the rear part of the Ahmed body, they did not measure the drag coefficient of corresponding flow. In the study of Lienhart and Becker (2003), Reynolds number employed was 768000. In general, shapes of the mean pressure coefficient $\langle C_p \rangle_t$ profiles revealed in our numerical simulation are in good agreement with the experimental results. However, main difference between our numerical results and experimental results of Lienhart and Becker (2003) is in the magnitude of mean pressure coefficient, $\langle C_p \rangle_t$ as presented in Figure 4.3.3.

The distribution of the time averaged surface pressure coefficients along the rear slanted surface is shown in Figure 4.3.3 (a). Present numerical $\langle C_p \rangle_t$ results are in good agreement with the experimental $\langle C_p \rangle_t$ results between approximately x/H=−0.3 and x/H=0 for positions z/H=0 and z/H=0.31. This good agreement between numerical and experimental results is not seen for position, z/H=0.625. For -0.74<x/H<-0.3, it is found that present numerically calculated pressure coefficient, $\langle C_p \rangle_t$ results show difference with the experimental $\langle C_p \rangle_t$ results of Lienhart and Becker (2003) in all positions. Rapid decrease in pressure coefficient $\langle C_p \rangle_t$ is observed after the leading edge of the slanted surface as declared by previous literature. Location of dip point on profiles at which value of pressure coefficient $\langle C_p \rangle_t$ is minimum, is found nearly at x/H=−0.698 for all positions. Although the location of dip point found in our simulation is in good agreement with the numerical results of Krajnovic and Davidson (2005), it shows large difference in the magnitude of pressure coefficient $\langle C_p \rangle_t$. This dip point locations form somewhat further in the stream-wise direction in the experimental results of Lienhart and Becker (2003). Although the magnitude of present numerical results show difference with experimental results, their pressure gradient is in good agreement with them especially after the location at which dip point value occur.

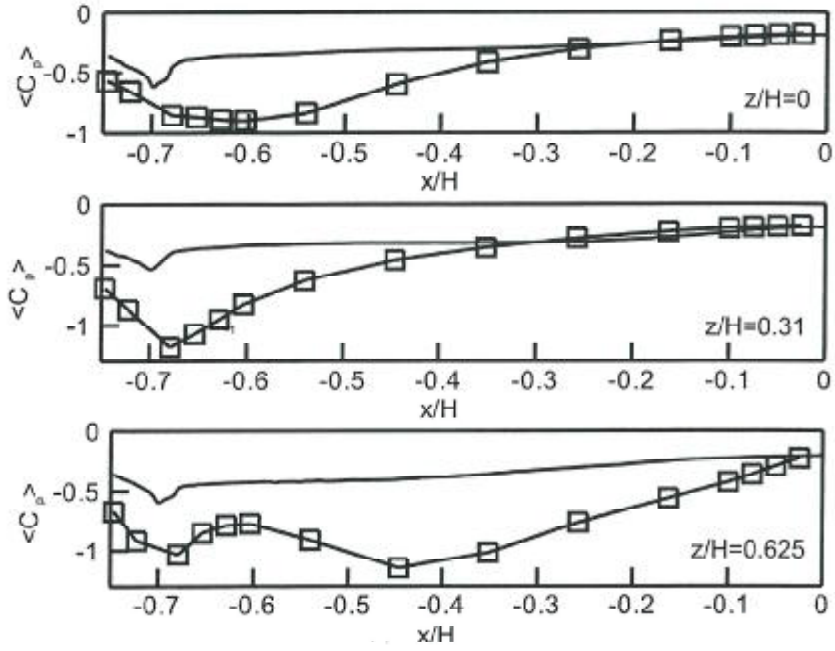

(a)

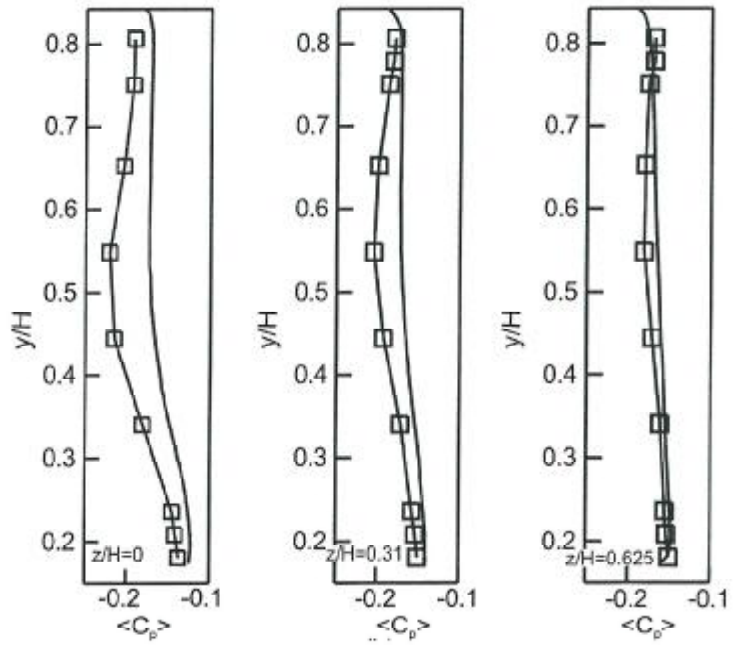

(b)

Figure 4.3.3. Distribution of time-averaged surface pressure coefficients in three planes, z/H=0, z/H=0.31 and z/H=0.625. Profiles are plotted along (a) slanted surface (b) rear vertical surface. The present numerical results (solid curve), experimental results of Lienhart and Becker (2003) (line with symbols)

In the separated flow region, recovery in pressure coefficient $\langle C_p \rangle_t$ values in LES calculation is faster than the results of previous literature.

Mean pressure coefficients, $\langle C_p \rangle_t$, on the rear vertical surface are presented for three vertical planes (z/H=0, z/H=0.31, and z/H=0.625) in Figure 4.3.3 (b). General trends of numerically computed mean pressure coefficient, $\langle C_p \rangle_t$, profiles are in good agreement with experimental results of Lienhart and Becker (2003) for all positions, showing a hill at the upper and lower parts of the vertical surface and a valley at the mid part of the vertical surface as shown in Figure 4.3.3(b). Agreement between the $\langle C_p \rangle_t$ values of numerical and experimental results become better as the positions change from z/H=0 to z/H=0.625. Numerical and experimental profiles presented for the case of z/H=0.625 have the best agreement with each other. Present numerical simulation predicted higher values of mean pressure coefficients along the entire length of the surface for all positions.

4.3.2. Iso-Surfaces of Pressure

To visualize large-scale coherent structures, contours of mean pressure coefficient are also a useful tool. In Figures 4.3.4 and 4.3.5, contours of mean pressure coefficient are presented in the transversal yz-planes for positions x/H=-0.69, -0.56, -0.42, -0.28, -0.14, 0, 0.28, 0.69, 1.04, 1.39, 1.74 and 2.43 through the slant surface and wake region downstream of the body. In these figures, main flow structures such as recirculation zone behind the body, longitudinal vortices emanating from lateral sides of the slant are well captured. Development of the counter-rotating vortices in the wake region can be observed through positions x/H=0 to 2.431. Positions from x/H=-0.694 to 0.347, formation and development of longitudinal vortices emanating from lateral sides of the slant surface can be confirmed. On the slant surface, two symmetrical vortex structure just around the symmetry plane of the body are visible from positions x/H=-0.417 to 0. A pair of two dominant counters rotating trailing vortices downstream of the model in the wake region are easily observed in positions

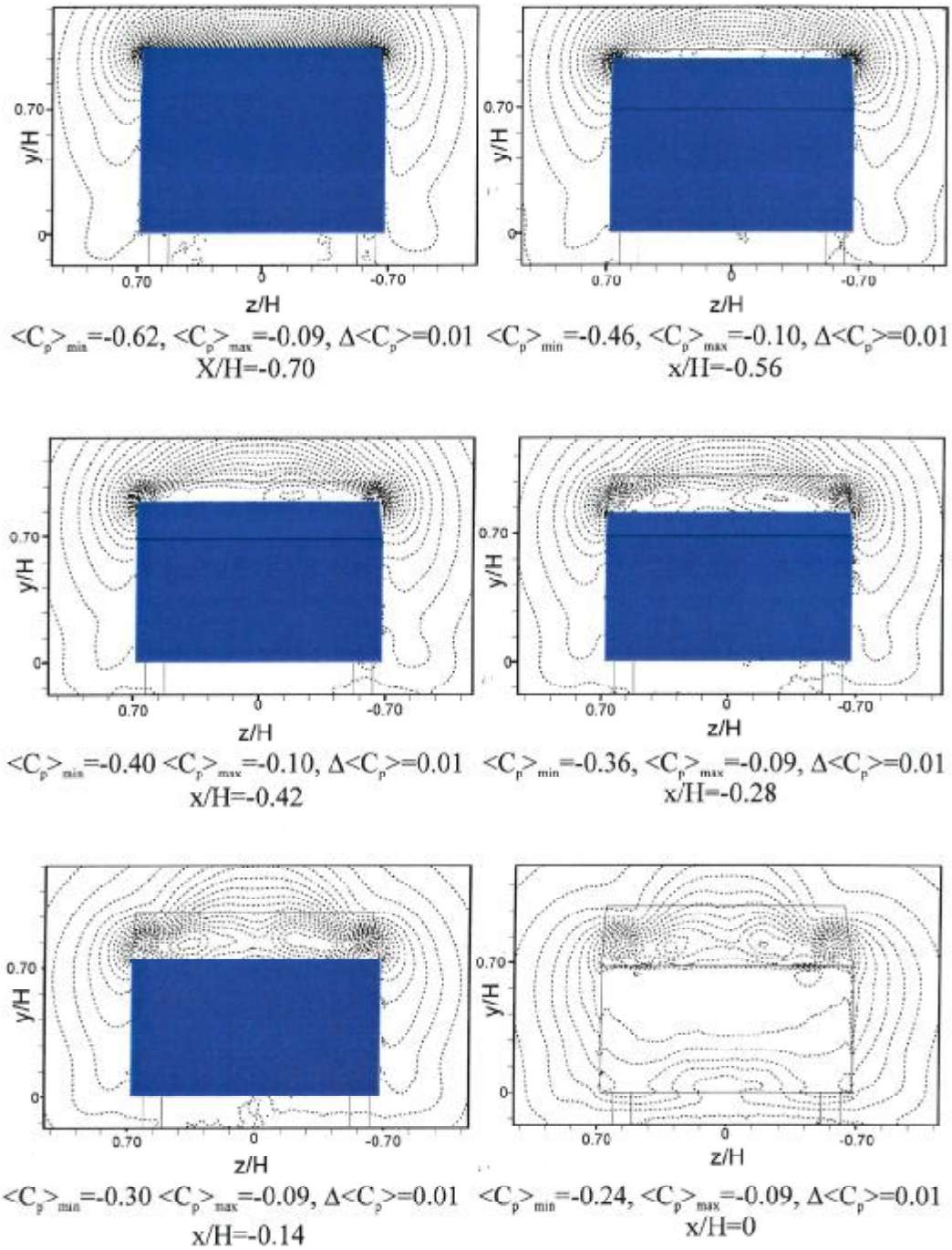

Figure 4.3.4. Patterns of mean pressure coefficient contours $<C_p>$ in different transversal yz-planes through the slant surface of the Ahmed Body

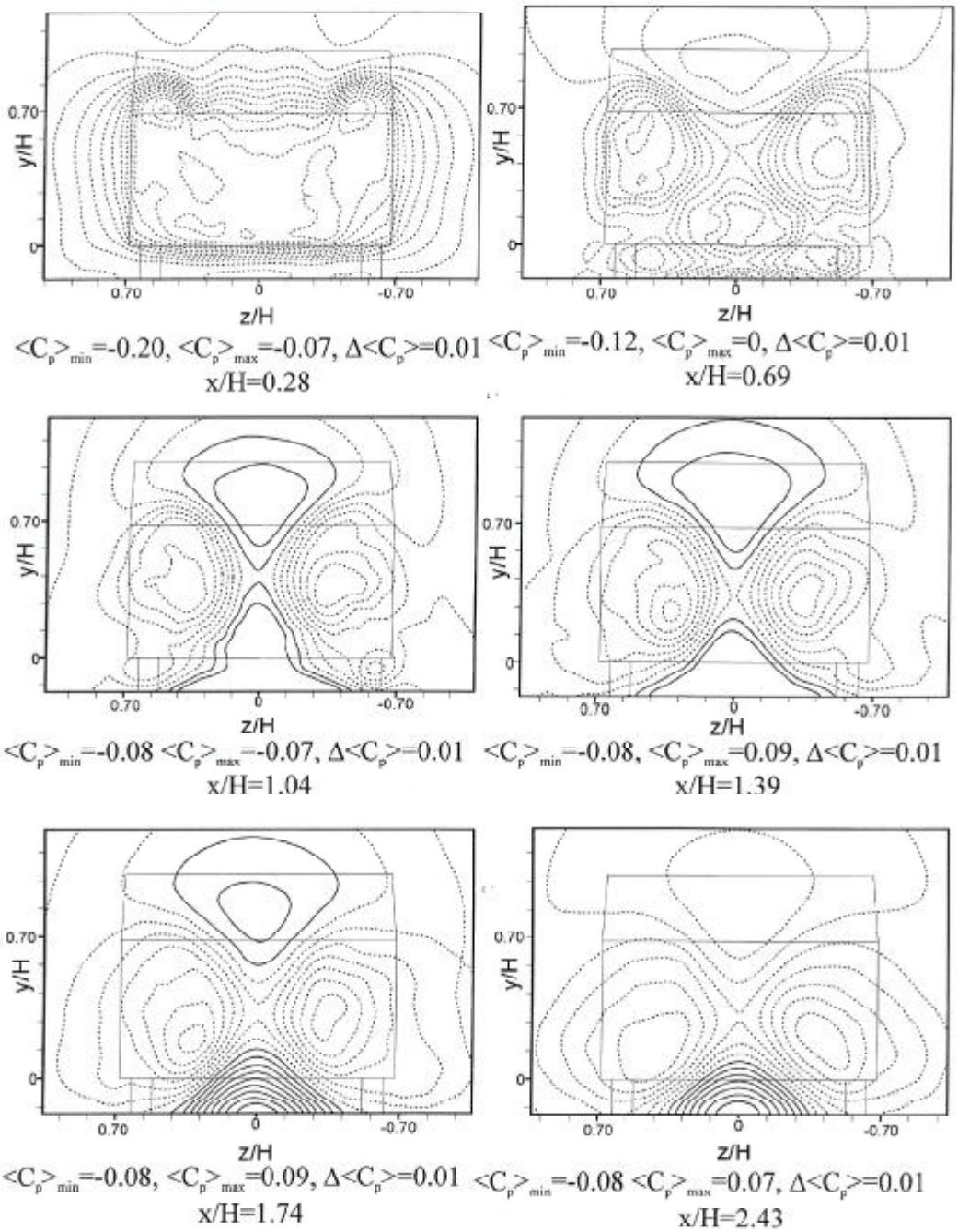

Figure 4.3.5. Patterns of mean pressure coefficient contours $\langle C_p \rangle$ in different transversal yz-planes through the wake region downstream of the Ahmed Body

between x/H=0.694 and 1.389. From location x/H=1.042 to downstream of the flow positive pressure coefficient region at the upper and lower part of the flow occur.

4.3.3. Drag Forces

The time history of the aerodynamic drag force coefficient was computed as $C_D=F/0.5\rho U_\infty^2 A$. Here ρ is density; F drag force due to the surface pressure and wall shear stress and A is the frontal cross sectional area. Results of numerically computed aerodynamic drag coefficients and their comparison with the experimental values are given in Table 4.3.1. Krajnovic and Davidson (2005) stated that, there is uncertainty in the comparison of their LES results with the experimental data of Ahmed et al. (1984), because Ahmed et al. (1984) did not give reference pressure employed in their study explicitly. Therefore, comparison of their results should be used only as an indication of the magnitude of the contributions of the integrated pressure on the front, rear slant, and rear vertical surfaces to the total pressure drag. They also stated that Ahmed et al. (1984) measured pressure drag only at three angles of the rear slant surface as 5°, 12.5°, and 30°. These values were then used to interpolate pressure drag for all angles between 0° and 30°. This causes an additional difficulty in comparing numerical results with the experimental results of Ahmed et al. (1984).

Time-averaged drag coefficients obtained from LES calculations are higher than the value of drag coefficient reported in the results of Ahmed et al. (1984) as presented in Table 4.3.1. The result of numerically computed drag force coefficient is not very satisfactory, because its estimated value are greater than the value reported in the literature. In this study, Reynolds number of the flow is nearly 80 times lower than the Reynolds number employed in the study of Ahmed et al. (1984). In fact, there is no experimental study conducted to measure drag force coefficient of the Ahmed body at low Reynolds number as aimed in the present study (Re=14830). Thus, we cannot find an opportunity to compare present numerically computed drag force coefficient with experimentally measured drag force coefficient at the same Reynolds number. In the present case, as explained in previous sections, vortex

structures formed as the result of flow detachments and then large separated flow regions occurred on the upper and lateral surfaces at the front of the body have striking effect on the flow structures formed at the rear part of the body. Besides, the counter-rotating vortices observed in this study on the slant surface of the body are weaker than those reported in previous studies.

Table 4.3.1. Comparison of time-averaged drag force coefficient and its components on rear slant, C_S, rear vertical, C_B, frontal, C_K, lateral, bottom, upper and stilts surfaces.

	Pressure Coefficient	Viscous Coefficient	Total Coefficient	Ahmed et al. (1984)
Rear Slant Surface (C_S)	0.0943	0.000319	0.0946	0.152
Rear Vertical Surface (C_B)	0.100	0	0.100	0.070
Frontal Surface (C_K)	0.158	0.0283	0.187	0.020
Lateral, Bottom and Upper Surfaces	0	0.0455	0.0455	0.054
Stilts	0.0174	0.00350	0.0209	-
Total	0.370	0.0776	0.448	0.296

According to the previous literature (Ahmed et al. (1984) and Krajnovic and Davidson (2005) conducted at high Reynolds number, $Re=1.2x10^6$ and $Re= 2x10^5$ respectively), the force on the rear slanted surface, C_S, dominates the total drag force coefficient, followed by the force on the rear vertical surface, C_B. However, in the present study which is conducted at relatively lower Reynolds number ($Re=1.48x10^4$), no drag force coefficients on the surfaces of the Ahmed body was found to be dominant. Contribution of forces on the rear vertical surface, C_B, together with rear slant surface to the total drag force coefficient have the maximum effect. The main difference between the present and previous studies is in the value of the contribution of the force on the front surface of the body to the total force coefficient in which its value in our work is nearly three times higher than the corresponding value in the literature as presented in Table 4.3.1. By comparing values of the components of the drag force coefficients presented in Table 4.3.1, it can be concluded that as the Reynolds number decreases, the effects of forces on the rear slant surface to the total drag force coefficient also decrease and the effects of forces on the front surface to the total drag force coefficient increase.

The time histories of the drag coefficient are presented in Figure 4.3.6. To identify the dominating frequency, f the time histories of the integrated pressure coefficients are Fourier transformed into the Fourier domain. It is found that dominating frequency f=0.305 Hz leads to the Strouhal number of St =0.11 as shown in Figure 4.3.7. In a similar way, Krajnovic and Davidson (2005) found two dominating frequencies in the Fourier transform of the drag coefficient signal which correspond to Strouhal numbers of St =0.15 and St=0.26.

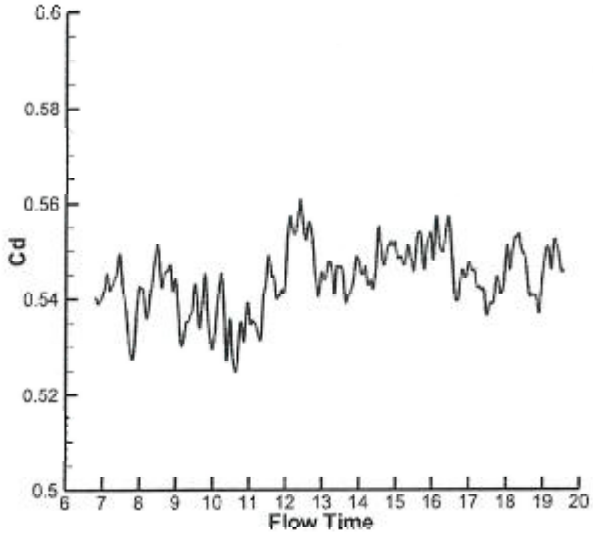

Figure 4.3.6. Drag coefficient history of the model

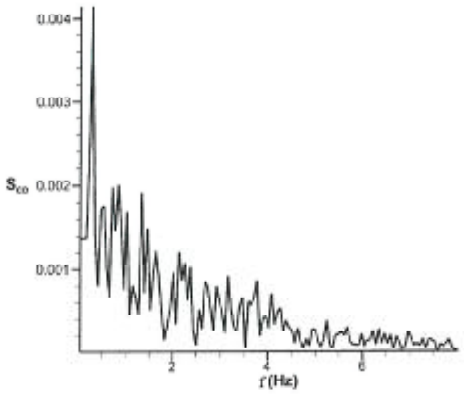

Figure 4.3.7. The spectrum of drag coefficient of the model

5. CONCLUSION AND RECOMMENDATIONS

The aim of the present study is to investigate characteristics of flow structures around the ground vehicles with the aid of Ahmed body using both experimental and numerical methods. The present investigation focuses on a number of fundamental phenomena, which are formation and development of large-scale separation and recirculation regions, a complex wake flow, long trailing vortices and the interaction of boundary layer flows occurred around the ground vehicles. These phenomena are inspected both qualitatively and quantitatively using Large Eddy Simulation (LES) method and the Particle Image Velocimetry (PIV) technique. In accordance with this purposes, ¼ scale Ahmed body having 25° slant angle is employed. The Reynolds number based on the body heights, H and the free stream velocity, U was about $Re_H=1.48x10^4$. Investigations were conducted in two parts. In the first part of the study, particle image velocimetry (PIV) technique was used for the measurement of the instantaneous velocity fields around the Ahmed body. Measurements were performed at several planes which were selected to highlight the aerodynamic characteristics of the body. In the second part of the study, the LES method was used to resolve the flow structures around the Ahmed body, numerically. The instantaneous and time-averaged velocity vector maps, vorticity contours, streamline topology and turbulence characteristics of the flow fields were presented and discussed in detail. Comparison of the mean and turbulent quantities of the present LES calculation and PIV measuring results with some open literature data at different locations over the slant, in the wake and at the front part of the Ahmed body are presented. Most of the flow features around the vehicle model were well predicted, such as the formation of trailing vortices, separation and circulatory flows. The main conclusions driven from the present study are summarized as follow.

Flow is separated and then reattaches after the leading edges of the front part of the body and hence a separated flow regions are formed both on the upper and lateral surfaces. Distances of the separation point from the frontal leading edge on the upper surface of the body in the vertical symmetry plane, z/H=0, are founded as x/H=0.167 in the numerical computations and x/H=0.108 in the experimental

measurements. In the present study, differently from previous literature which are conducted at higher Reynolds numbers, larger separated flow regions observed on the front part of the Ahmed body. Two trailing vortices form at each side of the upper lateral edges of the body. One of them is on the horizontal (roof) side of the edge and the other one is on the vertical side of the edge. These trailing vortices are seen on the transversal plane between the positions of x/H=-2.93 and -2.24. Furthermore, another pair of trailing vortices is also developed around each lower lateral edge of the body and they exist along the body length. Comparing the time-averaged flow with the instantaneous flow structures additional vortices along the roof of the body are observed. Separated flow estimated in the numerical investigations show counter rotating longitudinal vortices linked by transversal vortices similar to the Kelvin- Helmholtz vortices. The separation at the body front is characterized by a bubble that induces an unsteady recirculation region. It is found that the dominant frequency of f=0.21 which correspond to Strouhal number of St=0.07 exist on the upper surface of the front part of the Ahmed body as the result of the present PIV measurements. It can be seen that large span-wise vortex tubes are generated on the upper surface of the Ahmed body, which grow and then becomes similar to the horseshoe vortex on the slant surface.

Main flow structures such as recirculation zone behind the body, longitudinal vortices emanating from lateral sides of the slanted surface are well captured. Development of the counter-rotating vortices in the wake region can be observed through positions x/H=0 to 2.43 in both results of velocity field and results of pressure field. Positions from x/H=-0.69 to 0.35, formation and development of longitudinal vortices emanating from lateral sides of the slant surface can be confirmed. On the slant surface, two symmetrical large vortex structure just around the vertical symmetry plane of the body are visible in positions between x/H=-0.417 and 0. Pair of two dominant counter rotating trailing vortices downstream of the model in the wake region are easily observed in positions between x/H=0.69 and 1.39. The flow recirculation region formed downstream of the body is composed of two counter-rotating vortices in the symmetry plane, z/H=0. Size and centre location of LES calculations agree well with PIV measurements. The spectra of stream-wise

and normal velocity fluctuations show dominant frequency of f=0.88, obtained by using PIV measurements at the same location of x/H=0.61 and y/H=-0.03, in the lower shear layer downstream of the body which corresponds to the Strouhal number of St=fH/U=0.31. This result is consistent with the numerical result of Minguez et al. (2008) which is 0.42. The conformity of the numerical and experimental results obtained in this study through the wake region with the results of previous literature conducted at higher Reynolds numbers shows that qualitative knowledge about the wake flow downstream three-dimensional bluff bodies can be extracted from the flow at much lower Reynolds number.

Although there is good agreement between the flow characteristics revealed from the numerical and experimental studies with the results of previous literature in the wake region downstream of the Ahmed body, the differences are found on the slant surface of the body. Previous studies (Ahmed et al. (1984), Lienhart et al. (2000), Spohn and Gillieron (2002), Gant, 2002, Hinterberger (2004), Krajnovic and Davidson (2005), Fares (2006), Guilmineau (2008), Minguez et al. (2008)) have shown that the flow separates at the top edge of the rear slant, reattaches roughly half-way down the slant and thereafter remains attached due to the presence of strong side-edge vortices. In the present case, as the results of numerical calculations, the flow coming from the upper surface separates after the leading edge of the slant and partly reattach to the slant. Very small recirculation region on the slant surface of the body is observed in the vertical symmetry plane, z/H=0. The present LES calculations predict massive separation at vertical planes at z/H=0.34 and z/H=-0.34 on the slant whereas PIV measurements show no separation at these planes. Vortex structures formed as the result of flow separations and then large separated flow regions occurred on the upper surface at the front of the body are effective on the flow structures formed over the slant of the body. The longitudinal counter-rotating vortices coming from the lateral side of the slant surface are weaker than the previous literature.

Structures of the pressure coefficient distribution on the Ahmed body are generally in agreement with literature. However, significant differences are observed on the slant surface of the body where imprint of the separation region is more

tentative in the present LES simulations. Lower Reynolds number employed in the present simulations may be reason for this result. Main difference between the present numerical results and experimental results of Lienhart and Becker (2003) is in the magnitude of mean pressure coefficient, $\langle C_p \rangle_t$. Although the magnitude of present results shows difference with experimental results, their pressure gradient is in good agreement with them. On the other hand, it is known that the pressure level in the separation region is the determining factor of the total drag of the vehicle. As it is expected, time-averaged drag coefficients obtained from LES calculations are higher than the value of the drag coefficient presented in the results of Ahmed et al. (1984). The result of numerically computed drag force coefficient is not very satisfactory, because its estimated value greater than the values reported in the literature. In this study, the Reynolds number of the flow is nearly 80 times lower than the Reynolds number employed in the study of Ahmed et al. (1984). In fact, there is no experimental study conducting to measure drag force coefficient of the Ahmed body at low Reynolds number as in the present study ($Re=14.8x10^4$). Therefore, we cannot find opportunity to compare present numerically computed drag force coefficient with experimentally measured drag force coefficient at the same Reynolds number. According to the previous literature (Ahmed et al. (1984) and Krajnovic and Davidson (2005) conducted at high Reynolds number, $Re=1.2x10^6$ and $Re= 2x10^5$, respectively), the force on the rear slanted surface, C_S, was found to dominate the total drag force coefficient, followed by the force on the rear vertical surface, C_B. On the other hand, in the present study conducted at relatively lower Reynolds number ($Re=1.48x10^4$), no drag force coefficients on the surfaces of the Ahmed body was found to be dominant. Contribution of forces on the rear vertical surface, C_B, together with rear slant surface to the total drag force coefficient has the maximum effect. Main difference between the present work and previous works is in the value of the contribution of the force on the front surface of the body to the total force coefficient in which its value in our work is nearly three times higher than the corresponding value in the previous literature. it can be concluded that as the Reynolds number decrease, effects of forces on the rear slant surface to the total drag force coefficient also decrease and effects of forces on the

front surface to the total drag force coefficient increase. The spectra of drag coefficient shows dominating frequency of f=0.305 Hz corresponded to the Strouhal number of St =0.11.

5.1. Recommendations for future works

Based on the experimental and numerical investigations carried out in this study, the following recommendations are made for future work.

1. Active or passive flow control techniques should be applied on the Ahmed body to reduce drag force and their effects on the drag can be identified.
2. Investigations of flow structures around the Ahmed body having different slant angles, for example 30^{0} and 35^{0} using computational and experimental methods and comparison of results obtained will be subject of the future study.
3. Detailed studies of the effect of add-on devices, for example mirrors, to the flow structures can be performed by using experimental and numerical methods.
4. Detailed studies of aero-acoustical analysis of flow structures around the Ahmed body can be conducted as future work.

REFERENCES

ADRIAN, R.J., 1988. Statistical properties of particle image velocimetry measurements in turbulent flows. Laser Anemometry in Fluid Mechanics, 115-129.

ADRIAN, R.J., 1991. Particle-Imaging techniques for experimental fluid mechanics. Annual Review of Fluid Mechanics. 23, 261-304.

ADRIAN, R.J., 2005. Twenty years of particle image velocimetry. Experiments in Fluids, 39, 159-169.

AHMED, S.R., RAMM, G., FALTIN, G., 1984. Some salient features of the time-averaged ground vehicle wake. SAE Technical Paper 840300.

ALAM, F., WATKINS, S., ZIMMER, G., 2003. Mean and Time-Varying Flow Measurements on the Surface of a Family of Idealized Road Vehicles. Experimental Thermal and Fluid Science 27 (2003) 639–654.

BARLOW , J.B., GUTERRES, R., RANZENBACH, R., 2001. Experimental parametric study of rectangular bodies with radiused edges in ground effect. Journal of Wind Engineering and Industrial Aerodynamics, Vol. 89, Pages 1291-1309.

BASARA, B. and ALAJBEGOVIC, A., 1998. Steady State Calculations of Turbulent Flow Around Morel Body, The 7th Int. Symp. on Flow Modelling and Turbulence Measurements October 5-7,Taiwan.

BAYRAKTAR, I., 2002. "External Aerodynamics of Heavy Ground Vehicles Computations and Wind Tunnel Testing", PhD Thesis, Old Dominion University.

BEAUDOIN, J. F., CADOT, O., AIDER, J.L., GOSSE, K., PARANTHOEN, P., HAMELIN, B., TISSIER, M., ALLANO, D., MUTABAZI, I., GONZALES, M., WESFREID, J. E., 2004. Cavitation as a Complementary Tool for Automotive Aerodynamics. Experiments in Fluids, Vol. 37, pp. 763–768.

BEAUDOIN, J. F., CADOT, O., AIDER, J.L., WESFREID, J. E., 2006. Bluff-Body Drag Reduction by Extremum-Seeking Control. Journal of Fluids and Structures, 22 (2006) 973–978.

BEAUDOIN, J. F., AIDER, J.L., and WESFREID, J. E., 2006. Drag Reduction of a Bluff Body Using Adaptive Control Methods. Physics of Fluids 18, 085107, (2006).

BEAUDOIN, J. F. and AIDER, J. L., 2008. Drag and Lift Reduction of a 3D Bluff Body Using Flaps. Exp. Fluids, Vol.44, pp. 491–501.

BERNARD, P. S., COLLINS, P. and POTTS, M., 2005. Vortex Method Simulation of Ground Vehicle Aerodynamics. SAE Technical papers, 2005-01-0549.

BRUNEAU, C. H., GILLIÉRON, P. and MORTAZAVI, I., 2008. Passive control around the two-dimensional square back Ahmed body using porous devices.

BRUNEAU, C. H., CREUS, E., DEPEYRAS, D., GILLIÉRON, P. and MORTAZAVI, I., 2010. Coupling Active and Passive Techniques to Control The Flow Past the Square Back Ahmed Body. Computers and Fluids, Accepted Manuscript.

BRUNN, A., NITSCHE, W., 2006. Active Control of Turbulent Separated Flows Over Slanted Surfaces. Int. Journal of Heat and Fluid Flow 27 (2006) 748–755.

BRUNN, A., NITSCHE, W., 2006. Drag Reduction of an Ahmed Car Model by Means of Active Separation Control at the Rear Vehicle Slant. Notes on Numerical Fluid Mechanics and Multidisciplinary Design, Results in Numerical and Experimental Fluid Mechanics V, Vol. 92, p. 249-256.

CANPOLAT, Ç., 2008. Vortex Formation over a Nonslender Delta Wing. MSc. Thesis, Institute of Natural and Applied Sciences, University of Çukurova.

CEYROWSKY, T., BRUCKER, C., SCHWARZE, R., 2009. Unsteady RANS Simulations of Flows Around a Simplified Car Body. EUROMECH Colloquium 509 Vehicle Aerodynamics External Aerodynamics of

Railway Vehicles, Trucks, Buses and Cars Berlin, Germany, March 24–25, 2009.

CHUNG, T., J., 2002. Computational Fluid Dynamics, Cambridge University Press.

D'APOLLONIA, A. S., CONTINI, S., MATHEY, F., DUCRET, Y., 2007. Large Eddy Simulation of a Semi Realistic Vehicle Shape under Crosswind Conditions. 3rd European automotive CFD Conference, EACC 2007.

DAVIDSON, L., 2009. Large Eddy Simulations: How to evaluate resolution. International Journal of Heat and Fluid Flow, 30, 2009, 1016–1025.

DAVIDSON, L., 2011. Fluid mechanics, turbulent flow and turbulence modelling. Lecture notes, Chalmers University of Technology.

DIEDRICHS, B., BERG, M. and KRAJNOVIC, S., 2004. Large Eddy Simulations of the Flow Around High-Speed Trains Cruising Inside Tunnels. European Congress on Computational Methods in Applied Sciences and Engineering, ECCOMAS 2004.

DURST, F., 2008. Fluid Mechanics, An Introduction to the Theory of Fluid Flows, Springer, Berlin.

ENGLAR, R. J., 2001. Advanced Aerodynamic Devices to Improve the Performance, Economics, Handling and Safety of Heavy Vehicles, SAE Technical Paper, 2001-01-2072.

ELANKUMARAN, K., 1997. Numerical Investigation of an Inflatable Aerodynamic Boattail For Tractor-Trailers. MSc. Thesis, p. 58, Texas Tech University.

FLUENT 6.3 User's Guide, Fluent Inc., September 2006.

FARES, E., 2006. Unsteady Flow Simulation of the Ahmed Reference Body Using a Lattice Boltzmann Approach. Computers & Fluids 35 (2006) 940–950.

FRANCK, G. and D'ELIA, J., 2004. CFD modeling of the flow around the Ahmed vehicle model. GiD Conference, North Campus of the Technical University of Catalonia.

FRANCK, G., NIGRO, N., STORTI, M. and D'ELIA, J., 2007. Numerical simulation of the Ahmed vehicle model near-wake. Cuadernos de Matemática y Mecánica.

GILLIÉRON, P., CHOMETON, F., 1999. Modelling of Stationary Three-Dimensional Separated Air Flows around an Ahmed Reference Model. Third International Workshop on Vortex ESAIM, Proceedings, Vol 7, 1999, pp 173-182.

GROSCHE, F.-R. and MEIER, G.E.A., 2001. Research at DLR Gottingen on Bluff Body Aerodynamics, Drag Reduction by Wake Ventilation and Active Flow Control. Journal of Wind Engineering and Industrial Aerodynamics, Vol.89, pp. 1201–1218.

GUILMINEAU, E., 2006. Numerical study of wakes on a simple car model. The Fourth International Symposium on Computational Wind Engineering (CWE 2006), Yokohama, 2006.

GUILMINEAU, E., 2008. Computational Study of Flow Around a Simplified Car Body. J. Wind Eng. Ind. Aerodyn., Vol. 96, pp. 1207–1217.

GÜRLEK, C., 2008. Study of the Flow Around a Bus Model. PhD Thesis, Institute of Natural and Applied Sciences, University of Çukurova.

HAN, T. (1989). Computational analysis of three-dimensional turbulent flow around a bluff body in ground proximity. AIAA Journal 27(9), 1213-1219.

HEMIDA, H., KRAJNOVIC, S., DAVIDSON, L., 2005. "Large-Eddy Simulation of the Flow Around a Simplified High Speed Train Under the Influence of a Cross-Wind", 17th AIAA Computational Fluid Dynamics Conference 6-9 June 2005, Toronto, Ontario Canada, AIAA 2005-5354.

HINTERBERGER, C., GARCIA-VILLALBA, M., RODI W., 2004. "Large eddy simulation of flow around the Ahmed body", The Aerodynamics of Heavy Vehicles: Trucks, Buses and Trains, Lecture Notes in Applied and Computational Mechanics, vol. 19. Springer, Berlin.

HOWARD, R. J. A. and POURQUIE, M., 2002. "Large eddy simulation of an Ahmed reference model", Journal of Turbulence.

HOESSLER, J., BEAUDOIN, J.F. and PEROT, F., 2007. Unsteady Separated Flow Around the Ahmed Body. IUTAM Symposium on Unsteady Separated Flows and their Control, June 18-22, 2007, Corfu, Greece

HUCHO, W.-H., SOVRAN, G., 1993. Aerodynamics of Road Vehicles. Annu. Rev. Fluid Mech. 1993.25 :485-537.

HUCHO, W. H., 1998. Aerodynamics of road vehicles. SAE Publishing, Warrendale, PA.

HUCHO, W.-H., 2009. Important gaps in the science of car aerodynamics. EUROMECH Colloquium 509 Vehicle Aerodynamics External Aerodynamics of Railway Vehicles, Trucks, Buses and Cars Berlin, Germany, March 24-25, 2009.

JAKIRLIC, S., JESTER-ZURKER, R., TROPEA, C. (Eds.), 2001. In: 9th Joint ERCOFTAC/IAHR/QNET-CFD Workshop on Refined Turbulence Modelling.

JENKINS, L.N., 2000. An Experimental Investigation of the Flow Over the Rear End of a Notchback Automobile Configuration. SAE Technical Paper Series, 2000-01-0489.

JIANG, X. and LAI, H., 2009. Numerical techniques for direct and large-eddy simulations, Taylor and Francis Group.

JINDAL, S., KHALIGHI, B., IACCARINO, G., 2005. Numerical Investigation of Road Vehicle Aerodynamics Using Immersed Boundary RANS Approach. SAE International, 05B-419.

KAPADIA, S., ROY, S., VALLERO, M., WURTZLER, K. and FORSYTHE, J. 2003. Detached-Eddy Simulation Over a Reference Ahmed Car Model. Direct and Large-Eddy Simulation-V, Garching, Germany, August 27-29, 2003.

KAPADIA, S., ROY, S., WURTZLER, K., 2003. Detached Eddy Simulation Over a Reference Ahmed Car Model. 41st Aerospace Sciences Meeting and Exhibit, 6-9 January 2003, Reno, Nevada, AIAA-2003-0857.

KARAKUŞ, C., 2007. Investigation of Tip Vortex Formation, Development and Merging Using Particle Image Velocimetry (PIV) Technique. PhD. Thesis, Institute of Natural and Applied Sciences, University of Çukurova.

KEANE, R.D. AND ADRIAN, R.J., 1990. Optimization of particle image velocimeters: I. Double pulsed systems. Measurement Science and Technology, 1;11, 1202.

KEANE, R.D. AND ADRIAN, R.J., 1991. Optimization of particle image velocimeters: II. Multiple pulsed systems. Measurement Science and Technology, 2;10, 963.

KHALIGHI, B., ZHANG, S., KOROMILAS, C., BALKANYI, S. R., BERNAL, L. P., IACCARINO, G., MOIN, P., 2001. Experimental and Computational Study of Unsteady Wake Flow behind a Bluff Body with a Drag Reduction Device. SAE Papers, 2001-01B-207.

KRAJNOVIC, S., DAVIDSON, L., 2000. Flow Around a Three-Dimensional Bluff Body. 9th International Symposium on Flow Visualisation, 2000, 177-10.

KRAJNOVIC, S., DAVIDSON, L., 2001. Large-Eddy Simulation of the Flow Around a Ground Vehicle Body. SAE Paper No. 2001-01-0702.

KRAJNOVIC, S., DAVIDSON, L., 2002. Development Of Large-Eddy Simulation For Vehicle Aerodynamics. Proceedings of IMECE2002, ASME International Mechanical Engineering Congress & Exposition, New Orleans, Louisiana.

KRAJNOVIC, S., 2002. Large-Eddy Simulations for Computing the Flow Around Vehicles, PhD thesis, Department of Thermo and Fluid Dynamics Chalmers University of Technology, Göteborg, Sweden.

KRAJNOVIC, S., DAVIDSON, L., 2002. "Large-Eddy Simulation of the Flow Around a Bluff Body", AIAA Journal, Vol. 40, No. 5.

KRAJNOVIC, S., DAVIDSON, L., 2002. A Test Case For Large Eddy Simulation In Vehicle Aerodynamics. Engineering Turbulence Modelling And Experiments 5, pp. 647-656.

KRAJNOVIC, S., DAVIDSON, L., 2003. Numerical Study of the Flow Around a Bus-Shaped Body. ASME, Journal of Fluids Engineering, Vol. 125, pp 500-509.

KRAJNOVIC, S., DAVIDSON, L., 2004. Large Eddy Simulation Of The Flow Around An Ahmed Body. Proceedings of HTFED04, ASME Heat

Transfer/Fluids Engineering Summer Conference, Charlotte, North Carolina, USA.

KRAJNOVIC, S., DAVIDSON, L., 2004. Large-Eddy Simulation of the Flow Around Simplified Car Model. SAE World Congress, SAE Paper No. 2004-01-0227, Detroit, USA.

KRAJNOVIC, S., DAVIDSON, L., 2005. Influence of floor motions in wind tunnels on the aerodynamics of road vehicles. Journal of Wind Engineering and Industrial Aerodynamics, 93, 677–696.

KRAJNOVIC, S., DAVIDSON, L., 2005. Flow Around a Simplified Car, Part 1: Large Eddy Simulation. September 2005, Vol. 127, p.907-918.

KRAJNOVIC, S., DAVIDSON, L., 2005. Flow Around a Simplified Car, Part 2: Understanding the Flow. September 2005, Vol. 127, p.919-928.

KRAJNOVIC, S., 2009. Large eddy simulation of flows around ground vehicles and other bluff bodies. Phil. Trans. R. Soc. A 2009 367, 2917-2930.

KRAJNOVIC, S., FERNANDES, J., 2010. Numerical Simulation of the Flow Around a Simplified Vehicle Model With Active Flow Control. International Journal of Heat and Fluid Flow, Article in Press.

KOZAKA, E. O., ÖZKAN, G. and ÖZDEMİR, I. B., 2004. Turbulent Structure of Three-Dimensional Flow Behind a Model Car: 1. Exposed to Uniform Approach flow. J. Turbulence 5 (2004) 002.

LANDRETH, C.C. and ADRIAN, J.R., 1989. Measurement and refinement of velocity data using high-image-density analysis in particle image velocimetry. Applications of Laser Anemometry: Proceedings of the 4th International Symposium. Springer Verlag, Berlin, NY, 484-499.

LAWSON, N. J. GARRY, K. P. AND FAUCOMPRET, N., 2006. An Investigation of the Flow Characteristics in the Bootdeck Region of a Scale Model Notchback Saloon Vehicle. Proc. IMechE Vol. 221 Part D: J. Automobile Engineering.

Le GOOD, G. M., and GARRY, K. P, 2004. On the Use of Reference Models in Automotive Aerodynamics. SAE Technical paper series, 2004-01-1308, 2004 SAE World Congress Detroit, Michigan March 8-11, 2004

LIENHART, H., STOOTS, C. and BECKER, S., 2000. Flow and turbulence structures in the wake of a simplified car model (Ahmed model). In DGLR Fach. Symp. der AG STAB DGLR Fach. Symp. der AG STAB, Stuttgart University.

LIENHART, H., BECKER, S., 2003. Flow and turbulence structure in the wake of a simplified car model. SAE Technical Paper 2003-01-0656.

LUDWIEG, H., 1984. Widerstandsreduzierung von Kraftfahrzeugen, DFVLR-Nachrichten Heft 42 Juni, 1984, pp. 46–48.

MADDOX, S., SQUIRES, K. D., WURTZLER, K. E. and FORSYTHE, J. R., 2004. Detached-Eddy Simulation of the Ground Transportation System. The Aerodynamics of Heavy Vehicles: Trucks, Buses, and Trains, Rose McCallen, Fred Browand, James Ross (Eds.), Vol.19, Page 89-104.

MAKOWSKI, F. T. and KIM, S.-E., 2000. Advances in External-Aero Simulation of Ground Vehicles Using the Steady RANS Equations. SAE Technical Paper Series, 2000 World Congress Detroit, Michigan March 6-9, 2000, 2000-01-0484.

MAVURI, S. P. and WATKINS, S., A., 2005. Novel Mirror-Image Technique for Wheel and Ground Simulation in Automotive Wind-Tunnels. 6th World Conference on Experimental Heat Transfer, Fluid Mechanics, and Thermodynamics, April 17-21, 2005, Matsushima, Miyagi, Japan.

McCALLEN, R., FLOWERS, D., DUNN, T., OWENS, J., BROWAND, F., HAMMACHE, M., LEONARD, A., BRADY, M., SALARI, K., RUTLEDGE, W., ROSS, J., STORMS, B., HEINECK, J. T., DRIVER, D., BELL, J., WALKER S. and ZILLIAC, G., 2000. Aerodynamic Drag of Heavy Vehicles (Class 7-8): Simulation and Benchmarking. SAE Technical Paper Series, 2000-01-2209, Government/Industry Meeting Washington, D.C. June 19-21, 2000.

MCCALLEN, R., SALARI, K., ORTEGA, J., BROWAND, F., HAMMACHE, M. , HSU, T., LEONARD, A., CHATELAIN, P., RUBEL, M., ROY, C., DECHANT L., HASSAN, B., ROSS, J., WALKER, S., HEINECK, J.T., YASTE, D., STORMS, B., ENGLAR, R., POINTER, D., 2004. DOE's

Effort to Reduce Truck Aerodynamic Drag – Joint Experiments and Computations Lead to Smart Design. AIAA Fluid Dynamics Conference, Portland, Oregon.

MEYNARD, R., 1983. Measure de champs de vitesse d'ecoulements fluids par analyse de suites d'images obteneues par diffusion d'un fueillet lumineux. Ph.D. Dissertation, Faculte des Science Appliquees, Universite Libre de Bruxelles.

MINGUEZ, M., PASQUETTI, R., SERRE, E., 2008. High-order large-eddy simulation of flow over the "Ahmed body" car model. Physics of Fluids, 20, 095101, 2008.

MOREL, T., 1978. Aerodynamics Drag of Bluff Body Shapes Characteristic of Hatch-Back Cars, SAE Paper 780267.

NISUGI, K., HAYASE, T. and SHIRAI, A., 2004. Fundamental Study of Aerodynamic Drag Reduction For Vehicle With Feedback Flow Control. JSME International Journal, Series B, Vol. 47, No 3.

ORTEGA, J. M., DUNN, T., MCCALLEN, R., SALARI, K., 2002. "Computational Simulation of a Heavy Vehicle Trailer Wake", the United Engineering Foundation, Aerodynamics of Heavy Vehicles: Trucks, Buses, and Trains Conference, Monterey, CA.

POPE, S. B., 2000. Turbulent Flows, Cambridge University Press.

RAFFEL, M., WILLERT, E.C. and KOMPENHANS, J., 1998. Particle image velocimetry. Springer-Verlag Berlin Heidelberg, New York.

RAFFEL, M., CHRISTIAN, E.W., WERELEY, S.T., KOMPENHANS, J., 2007. Particle Image Velocimetry, A Practical Guide. Springer-Verlag, Berlin.

ROBINSON, C. M. E., 2001. Advanced CFD Modelling of Road-Vehicle Aerodynamics. PhD thesis, Institute of Science and Technology of University of Manchester.

ROCKWELL, D. and LIN, J.C., 1993. Quantitative interpolation of complex unsteady flows via high-image density particle image velocimetry. SPIE International Symposium on Optics, Imaging and Instrumentation, San Diego, CA.

ROCKWELL, D., MAGNESS, C., TOWFIGHI, J., AKIN, O. and CORCORANT, T., 1993. High-Image-Density particle image velocimetry using scanning techniques. Experiments in Fluids, 14, 181-192.

RODI, W., FERZIGER, J.H., BREUER, M., POURQUIE, M, 1997. Status of large-eddy simulations: Results of a workshop. J. Fluids Engineering, 2, 248-262, 1997.

RODI, W., 2004. DNS and LES of some engineering flows. Fluid Dynamics Research, 38, 145.

ROUMÉAS, M., GILLIÉRON, P., KOURTA, A., 2008. Separated Flows Around the Rear Window of a Simplified Car Geometry. Journal of Fluids Engineering, Vol. 130.

ROUMÉAS, M., GILLIÉRON, P., KOURTA, A., 2009. Drag reduction by flow separation control on a car after body. *Int. J. Numer. Meth. Fluids* 2009; 60:1222–1240.

ROUMÉAS, M., GILLIÉRON, P., KOURTA, A., 2009. Analysis and control of the near-wake flow over a square-back geometry. Computers & Fluids, 38, 60–70.

SMAGORINSKY, J., 1963. "General Circulation Experiments with the Primitive Equations. I. The Basic Experiment. Month. Wea. Rev., 164, 91-99.

SPOHN, A. and GILLIERON, P., 2002. Flow Separations Generated by a Simplified Geometry of an Automotive Vehicle. In IUTAM Symposium: Unsteady Separated Flows, April 8-12, Toulouse, France.

STRACHAN, R., KNOWLES, K., and LAWSON, N., 2005. Comparisons between CFD and experimental results for a simplified car model in wall proximity. Integrating CFD and Experiments in Aerodynamics, 5-6 September 2005.

STRACHAN, R., KNOWLES, K., and LAWSON, N., 2007. The vortex structure behind an Ahmed reference model in the presence of a moving ground plane. Exp Fluids (2007) 42:659–669.

TENNEKES, H., and LUMLEY, J.L., 1972. A First Course in Turbulence. The MIT Press.

TONDDAST-NAVAEI, A. and SHARP, D. B., 2001. The Use of Particle Image Velocimetry in The Measurement of Sound Fields, Proc. of the International Symposium on Musical Acoustics. 379-382.

TSUBOKURA, M., KOBAYASHI, T., NAKASHIMA, T., NOUZAWA, T., NAKAMURA, T., ZHANG, H., ONISHI, K., OSHIMA, N., 2009. Computational Visualization of Unsteady Flow Around Vehicles Using High Performance Computing. Computers & Fluids, 38, 981–990.

TSUBOKURA, M., NAKASHIMA, T., KITAYAMA, M., IKAWA, Y., DOH, D.H., KOBAYASHI, T., 2010. Large Eddy Simulation on the Unsteady Aerodynamic Response of a Road Vehicle in Transient Crosswinds. International Journal of Heat and Fluid Flow, Article in Press.

URUBA, V., HLADIK, O., 2009. On the Ahmed Body Wake. Colloquium FLUID DYNAMICS, Prague, October 21 - 23, 2009.

VAN DAM, G. P., 1999. Recent experience with different methods of drag prediction. Progress in Aerospace Sciences 35 (1999) 751-798.

VERZICCO, R., FATICA, M. IACCARINO, G. and MOIN, P., 2002. Large Eddy Simulation of a Road Vehicle with Drag-Reduction Devices. AIAA Journal Vol. 40, No. 12, December 2002.

VINO, G., WATKINS, S., MOUSLEY, P., WATMUFF, J. and PRASAD, S., 2004. The Unsteady Near-Wake of a Simplified Passenger Car. 15th Australasian Fluid Mechanics Conference, Sydney, Australia.

VINO, G., WATKINS, S., MOUSLEY, P., WATMUFF, J., PRASAD, S., 2005. Flow Structures in The Near-Wake of The Ahmed Model. Journal of Fluids and Structures, 20, 673–695.

WESSELING, P, 2001. Principles of Computational Fluid Dynamics. Springer.

WOOD, R. M., BAUER, S. X. S., 2003. Simple and Low-Cost Aerodynamic Drag Reduction Devices for Tractor-Trailer Trucks, SAE Paper No. 2003-01-3377.

WOOD, R. M., 2004. Impact of Advanced Aerodynamic Technology on Transportation Energy Consumption, SAE Paper No. 2004-01-1306.

CIRRICULUM VITAE

Tural TUNAY was born on May 07, 1978 in Adana. He graduated from Adana Atatürk High School in 1995 and enrolled in the Mechanical Engineering Department of Çukurova University in the same year. He graduated from Çukurova University as a mechanical engineer in July 2000. He received his master of science degree from the Mechanical Engineer Department of Çukurova University in 2002. He had commenced the studies leading to the degree of Doctor of Philosophy in 2002 at the Mechanical Engineering Department of Çukurova University. He had been employed as a research assistant in the Mechanical Engineering Department of Çukurova University between 2001 and 2002. He has been employed in Adana İl Özel İdaresi as an engineer since 2005.